



UNIVERSITÉ CATHOLIQUE DE LOUVAIN
ÉCOLE POLYTECHNIQUE DE LOUVAIN
ICTEAM ELECTRICAL ENGINEERING

Highly-sensitive CMOS capacitive biosensors towards detection of single bacterial cell in electrolyte solutions

Numa Couniot

Thesis submitted in partial fulfillment
of the requirements for the degree of
Docteur en Sciences de l'Ingénieur

Dissertation committee:

Prof. **Denis Flandre** (UCL, Belgium), Supervisor

Prof. **Laurent Francis** (UCL, Belgium), Supervisor

Dr. **Aryan Afzalian** (TSMC, Belgium)

Prof. **Mohamad Sawan** (Ecole Polytechnique de Montreal, Canada)

Prof. **Sven Ingebrandt** (Hochschule Kaiserslautern, Germany)

Prof. **David Bol** (UCL, Belgium), President

September 2015

To my parents
To Amandine
To Baptiste

Contents

Acknowledgements	i
Abstract	iii
Publications	v
List of Acronyms	ix
List of Symbols	xvii
Introduction	1
1 State of the art of bacterial detection	7
1.1 Fundamentals of bacteriology	7
1.1.1 Definitions and implications	7
1.1.2 Bacterial morphology	7
1.1.3 Growth and reproduction	9
1.1.4 Immune mechanisms against bacteria	9
1.1.5 Staphylococcus spp.	11
1.2 Traditional methods for pathogen detection	12
1.2.1 Culture	13
1.2.2 ELISA	13
1.2.3 PCR	14
1.2.4 MALDI-TOF MS	14
1.3 Biosensors for pathogen detection	15
1.3.1 Transducers	15
1.3.2 Sample handling	20
1.3.3 Selectivity means	22
1.3.4 Readout interfaces	24
1.3.5 Figures of merit	24
1.4 Summary	29
2 Capacitive and label-free detection of bacterial cells	31
2.1 Impedance spectroscopy	31
2.1.1 Principle	31
2.1.2 Impedance representation	32
2.1.3 Electrochemical cells	33
2.1.4 Electrode designs	33
2.1.5 Electrode materials	33

2.1.6	Surface- versus volume-based impedimetry	34
2.1.7	Performance comparison	35
2.1.8	Recommandations	37
2.1.9	Sensor modeling	39
2.1.10	Chapter innovations	42
2.2	Sensor modeling	44
2.2.1	Sensor design and fabrication	44
2.2.2	Behavior in simple electrolyte	45
2.2.3	Behavior in electrolyte with bacterial cells	56
2.3	Lytic enzymes as selectivity means	65
2.3.1	Principle	65
2.3.2	Experimental validation	66
2.3.3	Advantages and limitations	68
2.4	Optimization of the sensitivity	70
2.4.1	Implementation of 2D numerical simulations	70
2.4.2	Fitting with experiments and analytical model	77
2.4.3	Impact of charges	78
2.4.4	Optimization of the insulating layer	79
2.4.5	Optimization of the electrolyte	81
2.4.6	Influence of the bacterial cell	84
2.4.7	Optimization of metric properties	86
2.4.8	Impact of the electrode thickness	89
2.4.9	Impact of the electrode width	89
2.4.10	Sensitivity optimization	90
2.5	Conclusions	91
3	Bacterial attraction by electrokinetic effects	93
3.1	State of the art	93
3.1.1	Theory of electrokinetic forces	93
3.1.2	Theory of natural forces	98
3.1.3	Scaling laws	99
3.1.4	Electrode designs, materials and voltages	100
3.1.5	Key applications in bacteriology	101
3.1.6	Electrokinetics with impedance sensing of bacteria	103
3.1.7	Chapter innovations	106
3.2	Chip design and microfabrication	107
3.3	Analytical models	108
3.4	Numerical simulations	109
3.5	Electrokinetic phenomena	110
3.6	Impedance sensing with electrokinetics	116

3.7	Comparison to the state of the art	119
3.8	Conclusions	120
4	CMOS readout interfaces for capacitive biosensors	121
4.1	State of the art	121
4.1.1	CMOS technology	121
4.1.2	Co-integration of CMOS and sensors	122
4.1.3	Capacitive interfaces	128
4.2	A CFC for bacterial sensing in conductive buffers	136
4.2.1	Motivations	136
4.2.2	System architecture	136
4.2.3	Experimental validation	140
4.2.4	Comparison with relevant works	144
4.2.5	Conclusions	145
4.3	A biosensor array towards single bacterium sensing	147
4.3.1	Motivations	147
4.3.2	Challenges of in-pixel capacitance conversion	148
4.3.3	Implementation	149
4.3.4	Experimental validation	157
4.3.5	Comparison with relevant works	164
4.3.6	Conclusion	165
4.4	Conclusions	166
	Conclusions and perspectives	167
	Bibliography	178
A	Protocols and setups	197
A.1	Sensor microfabrication	197
A.2	Materials	201
A.3	Bacterial handling	202
A.4	CMOS chip fabrication, post-processing and encapsulation	204
A.5	Measurement setup	205
B	Programs	209
B.1	Matlab algorithm for automatic bacterial counting	209
B.2	PIVlab for bacterial speed extraction	209

C	Mathematical developments	211
C.1	Analytical expression of the sensitivity to bacteria	211
C.2	Linear versus exponential sensitivity	213
C.3	Analytical models of electrokinetic effects with passivated electrodes	213
D	Supplementary results	219
D.1	2D-to-3D sensitivity conversion	219
D.2	Characterization of the permittivity of different solutions	220
D.3	Performance comparison between reference and CFC IDEs	220
D.4	CFC inverter sizing	222
D.5	Temperature impact on CFC	223
D.6	Characterization of the biosensor array	224

Acknowledgements

This thesis was conducted over 4 continuous years of research, during which intensive work has converted some speculative hypotheses to robust scientific results. Failures in some research directions were compensated by achievements in others, and the encouragements from the many following people were thus really important for me.

First, I would like to express my deepest thanks to Prof. Denis Flandre, my main advisor, for its assistance in imagining and defining this PhD thesis topic. I will remember the passion, expertise, availability, motivation and trust that he has manifested since the begin of my master thesis. In particular, I could always count on him to carefully read my papers, to advise me on professional choices, and to trust me in difficult situations, especially the funding of a second CMOS run after that the first has failed. Also many thanks to my second advisor, Prof. Laurent Francis, for its availability, advises, enthusiasm and enjoyable discussions. I am also grateful to the FNRS to have funded my project.

Second, I would like to thank Prof. Mohamad Sawan, Prof. Sven Ingebrandt and Dr. Aryan Afzalian who gratefully accept to become members of my PhD Jury. Their careful readings and interesting remarks have provided substantial improvements of the thesis. A special thank to Dr. Aryan Afzalian, who has closely followed this project for a long time; first as assistant of my master thesis and then as a member of my support committee. The enthusiastic discussions and laughs shared with him were really a good time. Also my profound gratitudes to Prof. David Bol for having led the Jury and for all the work that we performed together on the *Sunpixer* project.

In an interdisciplinary topic such as this thesis, it is critical to establish reliable, strong and efficient relationships with scientists working in complementary research fields. I was very fortunate to meet Thomas Vanzieleghem after that my colleague Nicolas André has talk about my research during a badminton game! From that moment, every borders previously encountered in Biology were cleared and an amazing collaborative work started. Many thanks to Thomas for the long hours of ardent discussions on the fundamentals of Biology, for our mutual trust, and for the friendship that follows. I also want to thank Prof. Jacques Mahillon for allowing an electrical engineer to handle biological stuffs

in its laboratory. In addition, I want to express my sincere thanks to Jamal Badir and Prof. Jean-Luc Gala of CTMA in Woluwe for their welcome, trust and help. Besides the Biology field, I also would like to thank Prof. Laurent Jacques, Prof. Christophe de Vleeschouwer and Prof. Danielle Vanhoenacker for their availability to discuss about signal processing and electromagnetism related to my work.

I also would like to thank my office colleagues, Jonathan Rasson, Olivier Poncelet, Lamia El-Fissi and Nancy Van Overstraeten, for their friendship, the many laughs and the hot croissants at each good news. A special thanks to Olivier who made most of my ALD depositions. Also many thanks to my friends Pierre-Antoine Haddad, Maxime Gilliaux, Daniel Vergeylen and Augustin Cosse for their constant encouragements! There are also many other people in our ICTEAM department who helped me and shared memorable moments with me during this thesis, especially Nicolas André, André Crahay, Isabelle Dargent, Sylvain Druart, Constantin Dutu, Geoffroy Gosset, Valeriya Kilchytska, Guillaume Pollissard, Christian Renaux, Gilles Scheen, Pascal Simon, David Spôte, Thomas Walewyns, Miloud Zitoud.

Finally, I would like to sincerely thank my wife Amandine for its continuous encouragements and love during these four years, and for our wonderful little child Baptiste she gave me during this thesis. She is a marvellous wife! Also many thanks to my family, my parents, my brother, my godmother and my in-laws who have continuously encouraged me and been interested by the topic of this thesis.

Numa

Abstract

For centuries, bacterial cells have been one of the major causes of human diseases, and are still responsible for several millions of deaths every year. Rapid detection and identification of pathogens in clinical, food or water samples is an important prerequisite step to establish a diagnosis and prevent the disease propagation. This thesis investigates how capacitive biosensors can be used for rapid, selective and sensitive pathogen detection in various biological buffers. Their integration with microfluidics, electrokinetics and CMOS technology is provided towards miniaturized and affordable lab-on-chips for point-of-care diagnosis tools.

The first part of the thesis studies the capacitive transduction, based on Al/Al₂O₃ interdigitated microelectrodes (IDEs). Real-time detection of *Staphylococcus epidermidis* in low-conductive solutions is experimentally shown, and explained by a comprehensive analytical model of the transducer. An innovative selectivity principle using lytic enzymes is then presented and shown to selectively detect of *S. epidermidis* among *Enterococcus faecium* cells in synthetic urine. Thanks to numerical simulations using Poisson-Nernst-Planck equations, the capacitive biosensor parameters are eventually optimized towards the maximal sensitivity.

The second part of the thesis investigates the use of electrokinetic effects to attract bacterial cells on the surface of capacitive biosensors. By using an annular-ring macroelectrode encompassing the IDEs, short and long-range trapping of *S. epidermidis* were observed and attributed to contactless dielectrophoresis and electrothermal flow, respectively. At 63 MHz precisely, a resonance effect related to device connectors was found to dramatically increase the trapping of *S. epidermidis* lowering the detection limit by two orders of magnitude. Analytical models and numerical simulations are provided to explain the observed phenomena.

The last part of the thesis focuses on the design of two analog circuits to interface on-chip capacitive biosensors in a 0.25- μ m CMOS technology. The first is a capacitance-to-frequency converter working up to 575 MHz which demonstrates sensitivity to bacterial cells in high-conductive solutions. The second is a 16 \times 16 capacitive biosensor array featuring micrometer-sized pixels to lower the absolute number of detectable bacteria to ca. 7. The innovative pixel architecture uses a capacitance-to-voltage converter followed by a gain stage to boost the sensitivity.

In conclusion, capacitive biosensors towards bacteria detection have extensively been studied in this thesis, first starting from the transduction principles and then integrating them into advanced electrokinetic and electronic systems. The innovations provided in this thesis offer interesting perspectives for the next generations of capacitive biosensors targeting point-of-care diagnosis of bacterial cells.

Publications

Journal articles:

- **N. Couniot**, A. Afzalian, N. Van Overstraeten-Schlögel, L.A. Francis, D. Flandre. *Capacitive biosensing of bacterial cells: sensitivity optimization, submitted*
- **N. Couniot**, L.A. Francis, D. Flandre. *Resonant dielectrophoresis and electrohydrodynamics for high-sensitive impedance detection of whole-cell bacteria, Lab-on-chip, In Press*
- **N. Couniot**, G. de Streel, F. Botman, A. Kuti Lusala, D. Flandre, D. Bol. *A 65-nm 0.5-V DPS CMOS Image Sensor with 17-pJ/frame.pixel and 42-dB Dynamic Range for Ultra-Low-Power SoCs, IEEE JSSC, in Press*
- **N. Couniot**, L.A. Francis, D. Flandre. *A 16 × 16 CMOS Capacitive Biosensor Array towards Detection of Single Bacterial Cell, IEEE TBCAS, In Press*
- **N. Couniot**, A. Afzalian, N. Van Overstraeten-Schlögel, L.A. Francis, D. Flandre. *Capacitive biosensing of bacterial cells: analytical model and numerical simulations, Sensors & Actuators B: Chemical, 211, pp. 428-438, 2015*
- **N. Couniot**, D. Bol, O. Poncelet, L. A. Francis, and D. Flandre, *A Capacitance-to-Frequency Converter with On-Chip Passivated Microelectrodes for Bacteria Detection in Saline Buffers up to 575 MHz, IEEE TCAS II: Express briefs, 62(2), pp. 159-163, 2015*
- **N. Couniot**, T. Vanzieleghem, J. Rasson, N. Van Overstraeten-Schlögel, O. Poncelet, J. Mahillon, L.A. Francis, D. Flandre. *Lytic enzymes as selectivity means for label-free, microfluidic and impedimetric detection of whole-cell bacteria using ALD-Al₂O₃ passivated microelectrodes, Biosensors and Bioelectronics, 67, pp. 154-161, 2015*
- N. Van Overstraeten-Schlögel, O. Lefèvre, **N. Couniot**, D. Flandre. *Assessment of different functionalization methods for grafting a protein to an alumina-covered biosensor, Biofabrication, 6(3), p. 035007, 2014*

- **N. Couniot**, D. Flandre, L.A. Francis, A. Afzalian. *Signal-to-noise ratio optimization for detecting bacteria with interdigitated micro-electrodes*. Sensors & Actuators B: Chemical, 189, pp. 43–51, 2013.
- **N. Couniot**, A. Afzalian, D. Flandre. *Scaling laws and performance improvements of integrated biosensor microarrays with multi-pixel per spot*. Sensors & Actuators B: Chemical, 166-167, pp. 184–192, 2012.

Conference proceedings:

- D. Bol, G. de Streel, F. Botman, A. Kuti Lusala, **N. Couniot**, *A 65-nm 0.5-V 17-pJ/frame.pixel DPS CMOS Image Sensor for Ultra-Low-Power SoCs achieving 40-dB Dynamic Range*, VLSI, Hawaii, 2014
- N. André, G. Pollissard, **N. Couniot**, P. Gérard, Z.S. Ali, F. Udrea, L.A. Francis, D. Flandre, *A Silicon-on-Insulator Platform Functionalized By Atomic Layer Deposition for Humidity Sensing. International Meeting on New Sensing Technologies and Modelling for Air-Pollution Monitoring*, EuNetAir, Portugal, 2014
- **N. Couniot**, D. Bol, O. Poncelet, L. A. Francis, and D. Flandre, *A very high frequency capacitance-controlled oscillator for improved biosensing in high-salt solutions*, Biosensors conference, Australia, 2014
- **N. Couniot**, T. Vanzielegem, J. Rasson, N. Van Overstraeten-Schlögel, O. Poncelet, J. Mahillon, L. A. Francis, and D. Flandre, *Real-time, label-free and selective impedimetric detection of bacteria using CMOS-compatible microelectrodes in a fluidic cell*, Biosensors conference, Australia, 2014
- N. André, G. Pollissard, **N. Couniot**, P. Gérard, Z.S. Ali, F. Udrea, L.A. Francis, D. Flandre, *Harsh Environment Water Vapour Sensing Platforms in SOI Technology. CMOS Emerging Technologies Research Symposium*, CMOS Emerging Technologies Research Symposium, France, 2014

- J. Rasson, **N. Couniot**, N. Van Overstraeten, L.A. Francis, D. Flandre, *Biofunctionalization of a biosensor for an improved detection of Staphylococcus aureus*, IEEE EMBS, Belgium, 2013
- N. Van Overstraeten-Schlögel, O. Lefèvre, **N. Couniot**, D. Flandre, *A magnetic-based approach for improving the specificity and sensibility of electronics biosensors in diagnostic field*, IEEE EMBS, Hawaii, 2012
- **N. Couniot**, N. Van Overstraeten, L.A. Francis, D. Flandre, *Bacteria detection with interdigitated microelectrodes: noise consideration and design optimization*, Euroensors, Poland, 2012
- A. Afzalian, **N. Couniot**, D. Flandre, *Detection Limit of ultra-scaled Nanowire Biosensors*, SISPAD, USA, 2012
- **N. Couniot**, N. Van Overstraeten, L.A. Francis, D. Flandre, *Simulation of noise due to random configurations of biomolecules on capacitive biosensors*, IEEE EMBS, Belgium, 2011

Patents:

- D. Bol and **N. Couniot**, "Image Sensors", Patent EP14 152 504.8
- D. Bol and **N. Couniot**, "Image Sensors", Patent EP14 152 508.9

List of Acronyms

AAI	Aqua Ad Iniectabilia
Ab	Antibody
AC	Alternating Current
AC-EO	AC-Electroosmosis
ADC	Analog-to-Digital Converter
ALD	Atomic Layer Deposition
ATCC	American Type Culture Collection
ATP	Adenosine Triphosphate
BSA	Bovine Serum Albumin
BWA	Biological Warfare Agent
c-DEP	Contactless DEP
C2f	Capacitance-to-Frequency Conversion
C2V	Capacitance-to-Voltage Conversion
CB	Charge-Based
CBCM	Charge-Based Capacitance Measurement
CCO	Current-Controlled Oscillator
CDS	Correlated Double Sampling
CE	Counter Electrode
CFC	Capacitance to Frequency Converter
CFU	Colony Forming Unit
CM	Clausius-Mossoti
CMOS	Complementary Metal Oxide Semiconductor
CP	Charge Pump

CQFP	Ceramic Quad Flatpack
CS	Clinical Samples
CV	Cyclic Voltammetry
D	Differential
DC	Direct Current
DDS	Delta-difference sampling
DEP	Dielectrophoresis
DEPIM	Dielectrophoretic Impedance Measurement
DFi	Dark Field
DI	Deionized
DL	Double Layer
DNA	Deoxyribonucleic Acid
DR	Dynamic Range
DRS	Delta-Reset Sampling
ECS	Electrical Capacitance Spectroscopy
EDC	1-(3-Dimethylaminopropyl)ethylcarbodiimide hydrochloride
EDL	Electrical Double Layer
EHD	Electrohydrodynamics
EIS	Electrochemical Impedance Spectroscopy
EK	Electrokinetics
ELISA	Enzyme-Linked Immunosorbent Assay
ENFET	Enzyme Field-Effect Transistor
EO	Electroosmosis
EP	Electrophoresis

EPA	Electropermeabilization
EPA-DEPIM	Electropermeabilization-assisted dielectrophoretic impedance measurement
EPS	Extracellular Polymeric Substances
ET	Electrothermal
EU	European Union
EWD	Electrowetting-on-Dielectric
FEM	Finite Element Method
FET	Field-Effect Transistor
FoM	Figure of Merit
FPN	Fixed-Pattern Noise
FR	Flow Rate
FRA	Frequency Response Analyzer
FTIR	Fourier Transform Infrared Spectroscopy
GCE	Glassy Carbon Electrodes
GCS	Gouy-Chapman-Stern
GDP	Gross Domestic Product
HDL	Highest Detectable Level
HF	High Frequency
HMDS	Hexamethyldisilazane
HRP	Horseradish Peroxidase
i-DEP	Insulator-based DEP
IA	Impedance Analyzer
IC	Integrated Circuit
IDAM	Interdigitated Array Microelectrode

IDC	Interdigital Capacitors
IDE	Interdigitated Electrodes
IFC	Impedance Flow Cytometry
iLoD	Intrinsic Limit of Detection
IM	Impedance
IMFET	Immunological Field-Effect Transistor
IP	Isoelectric Point
IPA	Isopropyl Alcohol
IPE	Ideal Polarisable Electrode
IR	Infrared
ISE	Ion-Selective Electrode
ISFET	Ion-sensitive field-effect transistor
ITO	Indium-Tin Oxide
J-ET	Joule-heating Electrothermal
L-ET	Light-induced Electrothermal
LB	Lysogeny Broth
LbL	Layer-by-Layer
LF	Low Frequency
LFi	Light Field
LO	Local Oscillator
LoC	Lab on Chip
LoD	Limit of Detection
LoQ	Limit of Quantification
LPF	Low-Pass Filter

LSV	Linear Sweep Voltammetry
MAb	Monoclonal Antibody
MALDI-TOF MS	Matrix-Assisted Laser Desorption Ionisation Time-of-Flight Mass Spectroscopy
MEA	Multi-Electrode Arrays
MEMS	Microelectromechanical Systems
MF	Medium Frequency
MIE	Metal-Insulator-Electrolyte
MOSFET	Metal-Oxide-Semiconductor Field-Effect Transistor
MP	Magnetic Particle
MRSA	Meticillin-Resistant <i>Staphylococcus Aureus</i>
MST	Maxwell Stress Tensor
n-DEP	Negative Dielectrophoresis
NA	Not Available
ND	Non-Differential
NI	National Instrument
NP	Nanoparticle
OD	Optical Density
p-DEP	Positive Dielectrophoresis
PAb	Polyclonal Antibody
PBS	Phosphate Buffered Saline
PCB	Printed Circuit Board
PCR	Polymerase Chain Reaction
PDMS	Polydimethylsiloxane
PE	Plasma-Enhanced

PFD	Phase-Frequency Detector
pH	Potential Hydrogen
PLL	Phase-Locked Loop
PoC	Point of Care
PoCT	Point of Care Tests
PPB	Potassium Phosphate Buffer
PZC	Point Zero of Charge
QCM	Quartz Crystal Microbalance
qPCR	Quantitative Polymerase Chain Reaction
RBC	Red Blood Cell
RE	Reference Electrode
RMS	Root Mean Square
RNA	Ribonucleic Acid
RPM	Revolutions Per Minute
RT	Room Temperature
SAM	Self-Assembled Monolayer
SAW	Surface Acoustic Wave
SC	Switched Capacitor
SNR	Signal-to-Noise Ratio
SPAD	Single-Photon Avalanche Diode
SPE	Screen-Printed Electrode
SPQC	Series Electrode Piezoelectric Quartz Crystal
SPR	Surface Plasmon Resonance
sp./spp.	Species

T	Transistor
TIA	TransImpedance Amplifier
TIE	Triangular Impedance Extraction
TMA	Trimethylaluminum
TN	Temporal Noise
TSA	Trypticase Soy Agar
TSB	Tryptic Soy Broth
TSM	Transverse Shear Mode
TWV	Triangular Waveform Voltage
USA	United State of America
UV	Ultra-Violet
XLD	Xylose Lysine Deoxycholate
VCO	Voltage-Controlled Oscillator
VHF	Very High Frequency
VNA	Vector Network Analyzer
WE	Working Electrode

List of Symbols

A_e	Electrode surface area	m^2
C	Capacitance	F
C_b	Bacterial concentration	CFU/mL
C_{cyt}	Cytoplasm capacitance	F
C_{DL}	Double layer capacitance	F
C_g	Gate capacitance	F
C_{GC}	Gouy-Chapman capacitance	F
C_{IDE}	IDE capacitance	F
C_{ins}	Insulator capacitance	F
C_{ins}^{lat}	Lateral insulator capacitance	F
C_{inv}	Inverter output capacitance	F
C_{ions}	Electrolyte ionic strength	M
c_m	Negatively-charged ion concentration	mol/m^3
C_{out}^*	Equivalent outer shell capacitance	F
C_{ox}	Oxide capacitance	F
c_p	Positively-charged ion concentration	mol/m^3
C_{pl}	Plasma membrane capacitance	F
C_s	Series capacitance of C_{DL} and C_{ins}	F
C_{sIDE}	Capacitance of the sub-IDE	F
C_{stern}	Stern capacitance	F
C_{sol}	Electrolyte capacitance	F
C_{wall}	Cell wall capacitance	F
D	Ionic diffusion coefficient	m^2/s
d_{bact}	Bacterial diameter	m
d_{cyt}	Cytoplasm diameter	m

d_e	Electrode gap	m
DR	Dynamic range	dB
\vec{E}	Electric field	V/m
\vec{E}_{sol}	Electric field inside the electrolyte	V/m
f	Applied frequency	Hz
F	Faraday constant	C/mol
f_c	Cutoff frequency	Hz
f_{CM}	Clausius-Mossoti factor	-
\vec{F}_{DEP}	Dielectrophoretic force	N
f_{IDE}	Frequency of IDE	Hz
\vec{F}_g	Gravity force	N
FoM_1	Figure of merit #1 for biosensors	CFU
FoM_2	Figure of merit #2 for biosensors	CFU.min
f_{out}	Output frequency	Hz
f_v	Friction coefficient	CVs/m ²
g	Gravity constant	m/s ²
G	Geometrical factor of the IDE 3D geometry	-
g_m	Transistor transconductance	S
H	Factor expressing the frequency dependence of the electric field	-
$\Im\{X\}$	Imaginary part of the complex X	
\vec{I}	Identity tensor	-
I_0	DC current	A
I_d	Transistor drain current	A
I_{on}	Drive current provided by one inverter	A
iS	Intrinsic sensitivity	
\vec{J}_c	Conduction current density	A/m ²

\vec{J}_d	Displacement current density	A/m ²
k	Electrolyte thermal conductivity	W/(m.K)
K	Ratio between 3D and 2D sensitivities	-
K^{th}	Theoretical value of the ratio K	-
K_a	Acidic dissociation constant of oxide	-
K_{ai}	Dissociation constant of anionic groups	-
K_{aj}	Dissociation constant of cationic groups	-
K_b	Basic dissociation constant of oxide	-
k_B	Boltzmann constant	J/K
K_W	Dissociation constant of water	-
L	Transistor channel length	m
L_e	Electrode length	m
M	Factor expressing the physical nature of the electrothermal flow depending on f	-
N_{av}	Avogadro number	-
N_e	Number of electrodes	-
N_{inv}	Number of inverters	-
N_s	Hydroxyl group density of oxide	C/m ²
N_{si}	Anionic group density in cell wall	m ⁻²
N_{sj}	Cationic group density in cell wall	m ⁻²
pKa	Acid dissociation constant	-
q	Unit charge	C
r	Distance from the electrodes	m
R	Resistance	Ω
r_{bact}	Bacterial radius	m
R_{ct}	Charge transfer resistance	Ω
R_{cyt}	Cytoplasm resistance	Ω

Res	Resolution	
R_p	Polarisation resistance	Ω
R_{sol}	Electrolyte resistance	Ω
R_{wall}	Cell wall resistance	Ω
$\Re\{X\}$	Real part of the complex X	
S	Sensitivity	%
S_r	Relative sensitivity	%
S_b	Bacterial density	mm^{-2}
SNR	Signal-to-noise ratio	dB
s_{rt}	Real-time slope	F/s
t	Time	s
T	Temperature	K
t_{detect}	Detection time	s
t_e	Electrode thickness	m
t_{incub}	Incubation time	s
t_{ins}	Insulator thickness	m
\vec{T}_M	Maxwell Stress Tensor (MST)	Pa
t_{pl}	Plasma thickness	m
t_{wall}	Cell wall thickness	m
U_t	Thermal voltage	V
\vec{v}	Particle speed	m/s
\vec{v}_{slip}	Slip velocity in the DL due to EO	m/s
\vec{v}_{DEP}	Particle velocity induced by DEP	m/s
V_0	Amplitude of the DC applied voltage	V
V_a	Amplitude of the AC applied voltage	V
V_{dd}	Supply voltage	V

V_g	Gate voltage	V
V_{sample}	Sample volume	m ³
V_{th}	Transistor threshold voltage	V
Y	Complex admittance	S
Y/ω	Normalized complexed admittance	S
W	Transistor width	m
w_e	Electrode width	m
z	Number of electron unit charges	-
Z	Complex impedance	Ω
$\ Z\ $	Impedance modulus	Ω
Z_{bact}	Bacterial complex impedance	Ω
Z_W	Complex warburg impedance	Ω
Δ_c	Shift based on supernatant conductivity	F
Δ_{rt}	Shift in real-time	F
Δ_w	Shift after wash	F
$\Delta\phi_{DL}$	Voltage drop across the double layer	V
ε	Permittivity	F/m
ε^*	Complex permittivity	F/m
ε_0	Vacuum permittivity	F/m
ε_{bact}	Equivalent permittivity of the bacteria	F/m
ε_{bact}^*	Equivalent complex permittivity of the bacteria	F/m
ε_{ins}	Insulator permittivity	F/m
ε_r	Relative permittivity	-
$\varepsilon_{r,cyt}$	Cytoplasm relative permittivity	-
$\varepsilon_{r,ins}$	Insulator relative permittivity	-
$\varepsilon_{r,out}^*$	Equivalent outer shell relative permittivity	-

$\varepsilon_{r,ox}$	Oxide relative permittivity	-
$\varepsilon_{r,pl}$	Plasma membrane relative permittivity	-
$\varepsilon_{r,sol}$	Electrolyte relative permittivity	-
$\varepsilon_{r,wall}$	Cell wall relative permittivity	-
ε_{sol}	Electrolyte permittivity	F/m
ε_p	Particle permittivity	F/m
ε_{sol}	Electrolyte permittivity	F/m
η	Fluid dynamic viscosity	Pa.s
κ	Cell constant	m ⁻¹
λ_D	Debye length	m
Λ	Empirical factor for electroosmosis	-
θ_Z	Impedance phase	°
ω	Angular frequency	rad/s
μ	Electrophoretic mobility	m ² V ⁻¹ s ⁻¹
ϕ	Electric voltage	V
Ψ_0	Surface potential	V
ρ_{bact}	Mass density of bacterial cells	kg/m ³
ρ_{sol}	Mass density of electrolyte	kg/m ³
ρ_v	Space charge density	C/m ³
$\rho_{v,b}$	Space charge density of bacteria	C/m ³
σ	Electrical conductivity	S/m
σ_{cyt}	Cytoplasm conductivity	S/m
σ_{DL}	Double layer charge	C
σ_n	Noise	V
σ_s	Insulator surface charge	C/m ²
σ_{sol}	Electrolyte conductivity	S/m

σ_{wall}	Cell wall conductivity	S/m
τ	Time constant	s
ξ	Zeta potential	V
$[X]$	Molar concentration of the species X	M

Introduction

Context

For centuries, bacterial cells have been one of the major causes of human diseases. They are still responsible for several millions of deaths every year. A subset of the main harmful bacterial infections includes pneumonia, tetanus, meningitis, tuberculosis, cholera, syphilis, anthrax and botulism. To cure such infections, it is critical to identify the responsible pathogen prior to elaborate a therapeutic answer with appropriate antibiotics [1]. Detecting the presence of pathogens in food [2], recreational water [3], hospitals [4], etc. is also critical to prevent the propagation of diseases [5]. Nowadays however, conventional methods to identify pathogens require the isolation of a single bacterial colony, obtained after a time-consuming culturing step lasting several days [6]. Detrimental impacts on the health care system can result from this long delay [1, 5]:

- When hesitating between diagnoses of bacterial or viral infections, doctors are tempted to prescribe antibiotics. Indeed, failure to do so can possibly threaten the patient life in case of bacterial infection. However, antibiotics are useless for viral infections and thus favour the proliferation of resistant strains, that could strongly impact the patient immunity and healthcare costs in future years.
- In case of sepsis (bacterial infection in blood) or meningitis (bacterial infection in brain), death can occur within hours so that an immediate response is required. Broad-spectrum antibiotics are thus typically given in the early stage of the disease, destroying the gut flora and enhancing the development of resistant bacteria.
- Epidemics cannot be efficiently struggled from the beginning. Besides the human disasters of potential pandemics, the associated costs can often achieve several percent of a state GDP.

When not exterminated, pathogens can further group together into clusters surrounded by a polymer substance to form a biofilm, which protects them from external aggressions [7].

For all these reasons, recent developments have focused towards rapid detection of pathogen bacteria directly in the original matrix, thus bypassing the time-consuming culturing step [6, 8–10]. These diagnosis platforms are called *biosensors* and combine a transduction system (optical, electrochemical, acoustic, etc.) with selective bioreceptors (anti-

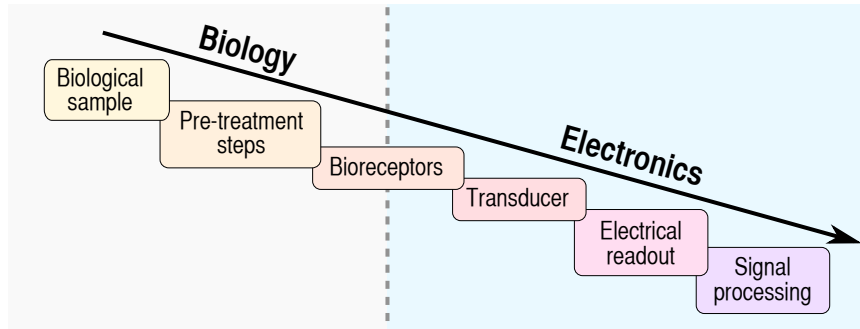


Figure 1 – The different steps involved in a biosensing chain.

bodies, enzymes, etc.) at the milli, micro or even nanometer level to target the detection of a specific bacterial species. Besides their initial objective to reduce the analysis time, biosensors also intend to be portable, miniaturized and low-cost. Based on such biochips, point-of-care tests (PoCT) could be deployed [1] and potentially revolutionize the health care system, and more particularly the personalized medicine.

Because they combine biology with electronics, biosensors are complex systems involving several steps (see Fig. 1) which all need to be optimized with regards to each others:

1. The *biological sample*, also called the *matrix*, is the original infected body fluid (blood, urine, saliva, etc.).
2. The *pre-treatment steps* are performed on the biological sample to get rid of parasitic biospecies such as cells or proteins, and concentrate bacteria in a smaller volume, thus increasing their apparent concentration. It is certainly the most important step to enhance selectivity and sensitivity in the biosensing chain [11, 12].
3. The *bioreceptors*, such as antibodies, enzymes, etc., provide the biosensor with the ability to detect specific bacteria, which is called the selectivity. Bioreceptors are either grafted on the sensor surface [13] or dispensed through the sample volume [14]. Their optimization is critical to increase the sensitivity and avoid false positives and false negatives.
4. The *transducer*, also called the *sensor*, converts a physical parameter related to the presence of bacteria, such as the weight, emitted light, dielectric properties or charges, into an electrical output

quantity, such as voltage, current, capacitance or resistance. Its optimization is usually directed towards the maximal sensitivity.

5. The *electrical readout interface* amplifies the transducer output and convert it into a readable analog or digital signal for further processing by computing units. Especially complex when interfacing multiple biosensors disposed in an array, this block is very important regarding the signal amplification and noise reduction.
6. The *signal processing* consists in analyzing the output data to establish a diagnostics. Used to compare the output with negative and positive controls, different techniques can further reduce the limit of detection and the risk of false positive and negatives [15].

Thesis objectives

As previously explained, biosensors seem to be the most appropriate devices to address point-of-care detection of bacterial cells. Biosensing systems can be very diversified, as each box in Fig. 1 features dozens of possibilities depending on the chosen application. This thesis will focus on capacitive biosensors, mainly because of their scalability and straightforward integration with the Complementary Metal-Oxide-Semiconductor (CMOS) technology, which provides routes towards mass deployment of low-cost biochips. As such biosensors have already shown promising results for bacterial detection, this thesis will aim at extending and optimizing their use in liquid buffers. The overall goal aims at designing a device able to specifically sense small concentrations of bacteria in complex and real media, such as urine. The main scientific challenges addressed in this thesis can be formulated as follows:

How to specifically sense bacteria at concentration of 10^6 CFU/mL with capacitive biosensors in less than 30 min?

How to accurately model and simulate capacitive biosensors with bacteria towards their optimization?

How to combine capacitive biosensors with electrokinetic phenomena for efficient bacterial volume trapping?

How to sense bacteria in physiological buffers featuring electrical conductivity larger than 1 S/m?

How to detect of a single adherent bacterial cell?

Used as a general model for bacteria in this thesis, *Staphylococcus* species were chosen because of the urgent need for efficient detectors to struggle nosocomial infections [16] and because our lab has previously demonstrated expertise with these bacteria [17]. Their spherical shapes also facilitate models and simulations. The thesis is divided into 5 chapters, each one proposing innovative solutions to the above mentioned challenges related to the capacitive detection of bacteria in solution:

- The Chapter 1 first establishes a general state of the art, reviewing the fundamentals of bacteriology, the conventional methods and existing biosensors for bacterial detection.
- The Chapter 2 studies the transduction properties of capacitive biosensors in simple electrolytes with and without bacterial cells. An extensive analysis comprises and compares analytical models, numerical simulations and experimental data. The achieved performance are finally compared to the literature. This chapter proposes four innovative solutions to the four following challenges:
 1. *Real-time sensing of bacteria in low-conductive electrolytes:* experimental results with capacitive biosensors have highlighted an innovative detection principle based on changes of the medium capacitance [18].
 2. *Avoiding effects of non-specific bindings in complex matrixes:* an innovative method using lytic enzymes at the volume level has been proposed and demonstrated for selective detection of *S. epidermidis* in urine buffer, also containing *E. faecium* [18].
 3. *Modeling the frequency-dependent complex sensor impedance:* a complete model based on cutoff frequencies has been developed for the capacitive biosensor without and with bacteria [19], providing a detailed physical understanding.
 4. *Estimation of the maximal sensitivity in different conditions:* numerical simulations based on the Poisson-Nernst-Planck equations have been implemented to optimize different key parameters in the biosensing system [19, 20].
- The Chapter 3 investigates how the detection limit of the capacitive biosensor used in Chapter 2 can be improved by two orders of magnitudes using electrokinetic forces. The achieved performances

are compared to the literature and further discussed with regards to analytical models and numerical simulations. With regards to the literature, this chapter proposes two innovative solutions to the following challenges:

1. *Decreasing the detection limits of capacitive biosensors:*
an innovative macroelectrode design encompassing the capacitive biosensor described in Chapter 2 enables the attraction of whole-cell bacteria on the sensing surface thanks to three combined electrokinetic effects [21]:
 - surface trapping by contactless-dielectrophoresis,
 - volume trapping by Joule-heating electrothermal effect,
 - electromagnetic resonance effect induced by the device.
 2. *Understanding the impact of the insulator on electrokinetics:*
innovative analytical models and numerical simulations, based on the Maxwell Stress Tensor, have been developed to understand the impact of the insulator on bacterial attraction speed and electrokinetic forces, versus the applied frequency [21].
- The Chapter 4 studies CMOS analog circuits to interface capacitive biosensors used in Chapters 2 and 3. More particularly, the readout interfaces aim at bringing additional functionalities, hardly achievable without using CMOS: sensing in high-conductive buffers and sensing few bacteria. Experimental results are compared to analytical models, numerical simulations and state of art. Three innovations are proposed to solve the three following issues:
 1. *Sensing of bacterial cells in high-conductive solutions:*
impedance spectroscopy at frequencies larger than 100 MHz has been performed thanks to a CMOS capacitance-to-frequency converter with on-chip capacitive sensors, and demonstrates sensitive detection of bacteria in physiological buffers [22].
 2. *Lowering the absolute number of detectable bacteria:*
a 16×16 CMOS capacitive biosensor array with small sensing area ($\sim 14 \mu\text{m} \times 16 \mu\text{m}$) has been implemented and demonstrated for real-time detection of bacterial cells, with a detection limit of ca. 7 bacterial cells per pixel [23].
 3. *Optimizing interfaces of capacitive biosensor inside pixels:*
an innovative architecture based on the charge sharing prin-

ciple followed by a subthreshold gain stage has been proposed to interface capacitive biosensors within tiny pixels [23].

- Eventually, the Chapter 4.4 summarizes the main conclusions and results obtained in this thesis, and investigates the most interesting prospects for future research directions and applications.

CHAPTER 1

State of the art of bacterial detection

1.1 Fundamentals of bacteriology

1.1.1 Definitions and implications

Belonging to prokaryotic microorganisms, bacterial cells are unicellular microorganisms without nuclei. With sizes not exceeding few micrometers, they can be found in soil, water, plants and animals. While most of them are beneficial to the human life (e.g. *probiotics*) or harmless, some can cause infectious diseases and are thus qualified as *pathogenic*. The term *virulent* refers to a high degree of severity for the disease [24]. Being summarized for the human body in Fig. 1.1, infectious diseases represent approximately 40% of the worldwide infections [25]. The most known infections include pneumonia, tetanus, meningitis, tuberculosis, cholera, syphilis, anthrax and botulism and originate from the presence of *Streptococcus pneumoniae*, *Clostridium tetani*, *Neisseria meningitidis*, *Mycobacterium tuberculosis*, *Vibrio cholerae*, *Treponema pallidum*, *Bacillus anthracis* and *Clostridium botulinum*, respectively. On the other hand, the bacteria which are mostly involved in the food industry are *Escherichia*, *Listeria* and *Salmonella* spp. [2]. Some pathogens, such as *Bacillus anthracis*, *Brucella melitensis* and *Yersinia pestis* [25], are also considered as biological warfare agents (BWA) due to their virulence and resistance in various environments.

1.1.2 Bacterial morphology

Bacteria are diversified microorganisms presenting various characteristics at different levels. In this section, the shapes, structures, interactions with environment and physical properties of bacteria are described.

Shapes: the *cocci*, *bacilli*, *vibrio*, *spirilla* and *spirochaetes* bacteria denotes spherical, rod-shaped, comma-shaped, spiral-shaped and coiled-shaped bacteria, respectively. The bacteria size is typically comprised between 0.5 and 5 μm .

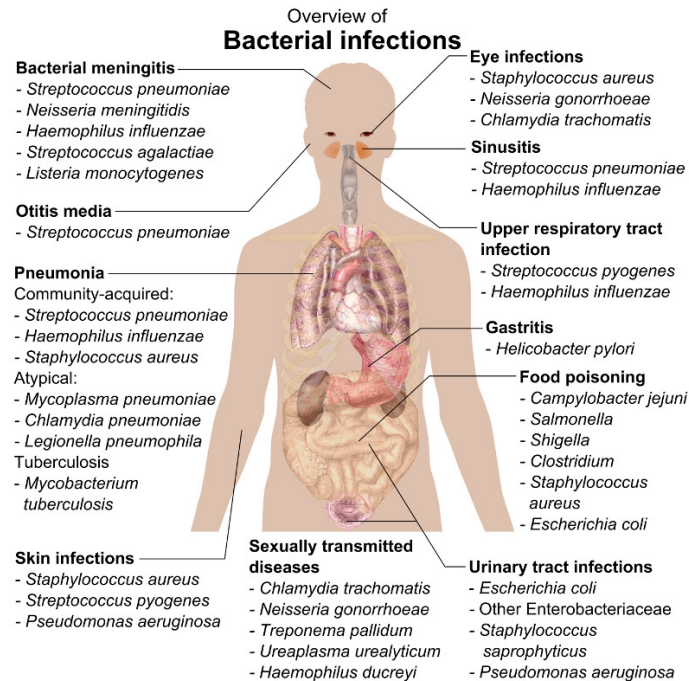


Figure 1.1 – Main bacterial infections in the human body [26].

Structures: the main component of the bacterial cell is the cytoplasm, which contains the nucleoid carrying genetic information. It is surrounded by the plasma membrane, acting as a barrier to regulate nutrients, proteins, and other biological species. For *Gram-positive* bacteria presenting a violet coloration under Gram staining, the outer shell is a thick layer of peptidoglycan, called the *cell wall*. For *Gram-negative* bacteria presenting a pink coloring, the cell wall is thinner and is englobed in an additional outer membrane.

Interactions with environment: external structures such as Flagella, Fimbriae and Glycocalyx provide motility, attachment to surfaces and protection against aggressions. Bacterial cells are further able to form clusters on solid surfaces and secrete extracellular polymeric substances (EPS), called the *slime*, to facilitate their interactions, bindings and protection against external aggressions [27]. The combination of bacterial cluster with EPS matrix is called a *biofilm*, which is responsible for many chronic infections in hospitals.

Physical properties: most bacteria feature an isoelectric point (IP) between pH 0.7 and pH 4.7 [28], which corresponds to the pH where the bacterial charge is zero. They are thus typically negatively charged in physiological buffers of pH 7.4. Gram-positive and -negative bacteria are typically modelled by spherical or rod-like particles surrounded by two or three shells, each layer having different conductivity and permittivity [29, 30]. Composed mostly of water, the mass density of bacteria is ca. 1200 kg/m^3 , given a slow sedimentation speed of ca. 100 nm/s .

1.1.3 Growth and reproduction

Under optimal conditions of temperature, oxygen and nutrients, bacterial cells can divide themselves into two clone daughter cells, achieving division rates down to 10 min [31]. Four phases characterize the bacterial growth. First, bacteria experiences a *lag phase* for several hours, adapting themselves to the nutrient medium. Afterwards, the *exponential phase* denotes the bacterial division at the highest possible growth rate. When available nutrients limit the fast growth, bacterial cells undergo a stress state known as the *stationary phase*. Eventually, the *death phase* occurs when bacteria cannot sustain in the medium empty of nutrients.

To quantify the number of viable bacteria in a liquid volume, diluted amounts of the sample are seed on Petri dishes and cultured overnight. The number of culture colonies is then estimated on the most readable Petri dish and converted in *colony forming unit* (CFU) per mL, according to the dilution factor and seed volume. To compare with *fM-pM-nM* concentrations involved for biomolecule detection, 10^6 CFU/mL corresponds to a concentration of 1.6 fM, assuming that one mole of bacteria is constituted by $6.022 \cdot 10^{23}$ individual bacteria.

1.1.4 Immune mechanisms against bacteria

When infected by pathogen bacteria, the human body can deployed several protection mechanisms to eliminate the threat. The most common means involved recognition and destruction of pathogens by white blood cells, presenting specific detection sites called *antibodies*. Other identification and destruction units exist, such as *lytic enzymes*, *bacteriophages* and *microbial peptides*. External action through *antibiotics*, the major medicine against bacterial infections, is also possible. A brief description of these agents is provided hereafter.

Antibodies (Ab) enable immune cells to bind pathogens in a specific way. They are secreted by plasma cells, a type of white blood cells, and can be found either in soluble form or bound on B-cells membranes. Two kinds of antibodies can be identified according to their selectivity. *Monoclonal antibodies* (MAb) confer a high level of selectivity by recognising a specific antigen or epitope, but are very expensive. In contrast, *polyclonal antibodies* (PAb) are more affordable but recognize multiple epitopes localized on the same antigens, thus having a less pronounced selectivity [13]. Produced from animals, antibodies can be used to diagnose diseases because their presence in body liquids is an indicator of the body fight against the involved disease.

Lytic enzymes have the ability to lyse bacterial cells by destroying their outer shells, either in specific way or not. Found in saliva, tears and breast milk, *lysozymes* are the first kind of lytic enzymes that kill most bacteria unspecifically. A second type is bacteriophage lytic enzymes, also called *endolysins* or *lysins*, that selectively break bonds in the thick cross-linked peptidoglycan of the bacterial outer shell [32]. Produced by bacteria itself, *autolysins* are the third category of lytic enzymes which are tightly controlled by bacteria for cell wall rearrangements during cell division. Finally, in some cases, evolution has driven bacteria to develop lytic enzymes to eliminate species competing for a specific environmental niche. This is notably the case for *Staphylococcus simulans*, which produces *lyso-staphin*, a peptidoglycan hydrolase active against almost all *Staphylococcus* species. Lytic enzymes have regain interest in the struggle against multidrug-resistant strains of bacteria [32].

Bacteriophages are viruses that specifically infect target bacteria by injecting their genetic material in their host, after destroying their cell wall using *endolysins*. They are found in various locations of the human body such as the mouth and skin and also in food eaten by humans. In some cases, they are used as an alternative to antibiotics.

Antimicrobial peptides are biomolecules able to kill Gram-negative and -positive bacteria, but preferably bind on negatively charged organisms [33]. It is considered as a substitute to antibiotics, since bacterial resistance against antimicrobial peptides is almost inexistent [33].

Antibiotics are synthetic or natural biomolecules that typically block

the bacterial growth, either by preventing the cell wall formation (e.g. *Penicillin*) or by inhibiting the synthesis of nucleic acids (e.g. *mitomycin*). Other more complex mechanisms exist.

1.1.5 *Staphylococcus* spp.

Staphylococcus spp. are anaerobic Gram-positive bacteria which are mainly known for their implication in nosocomial infections, i.e. infections indirectly acquired during hospitalisation.

Staphylococcus aureus is the most pathogenic form and is considered as one of the eight pathogens of public health importance in European Union (EU) [34]. Responsible for many severe infections such as skin infections, pneumonia, endocarditis and sepsis, *S. aureus* typically inhabits nasal cavities, has a gold aspect, forms "bunch of grapes" clusters and can be resistant to most antibiotics, as observed for the *Methicillin-resistant Staphylococcus aureus (MRSA)*. Most *S. aureus* are coagulase-positive, i.e. their surfaces are coated by coagulase reacting with blood to form a fibrin protection. By the secretion of staphylococcal enterotoxins [35], *S. aureus* is also known to be responsible for staphylococcal food-poisoning outbreaks, which is the second source of foodborne diseases in France with ca. 2000 cases between 2001 and 2003 [36]. It is considered that 30 to 50% of the population has carried *S. aureus* one time in their life, while 20% are long term carriers [37]. In USA, half million people are yearly infected by *S. aureus*, among which a fifth by the MRSA [37]. Similarly in EU, 18% of the *S. aureus* carriers presents the MRSA form in 2013, ranging from 0% (Iceland) to 65% (Romania) [34]. As recently pointed out [34], the MRSA percentage has decreased between 2010 and 2013 in several EU countries despite the increase of other antibiotic-resistance species, such as *Escherichia coli*, *Klebsiella pneumoniae*, *Pseudomonas aeruginosa* and *Acinetobacter*.

Another opportunistic pathogenic form is *Staphylococcus epidermidis*, a negative-coagulase *Staphylococcus* sp., that presents a white colour contrasting with the gold colour of *S. aureus*. Naturally found on the skin, *S. epidermidis* was previously considered as a non-pathogenic contaminant in blood samples from hospitalized patients [4, 16]. However, *S. epidermidis* is now considered as a major source of nosocomial bloodstream infection due to its ability to colonize and form early stage biofilms in vascular catheters, cerebrospinal shunts, prosthetic joints and prosthetic cardiac valves [4, 38]. The extensive use of broad-spectrum antibiotics also promotes the rise of multidrug-resistant *S. epidermidis*.

Table 1.1 – Detection levels required for pathogens in various matrix.

Matrix	Physical state	Involved bacteria	Infection threshold	Ref.
Blood	Liquid	<i>S. aureus</i> & <i>E. coli</i>	< 1 CFU/mL	[39]
Cheese	Solid	<i>S. aureus</i>	10 ⁴ CFU/g	[40]
Drinking water	Liquid	<i>E. coli</i>	1 CFU/100 mL	[41]
General food	Solid	<i>S. aureus</i>	10 ⁵ CFU/g	[36]
Mastitis	Liquid	<i>S. aureus</i>	10 ³ CFU/mL	[42]
Raw milk	Liquid	<i>S. aureus</i>	2·10 ³ CFU/mL	[40]
Urine	Liquid	<i>E. coli</i> (50%), <i>S. aureus</i>	10 ⁵ CFU/mL	[43]

Table 1.2 – Conventional methods for the detection of bacterial cells.

	Culture	ELISA	PCR	MALDI-TOF
Complexity	Very low	High	Very high	Very high
Cumbersomness	Very low	Low	High	High
Cost	Very low	High	Very high	High
LoD	1 CFU/mL	10 ⁵⁻⁶ CFU/mL	10 ¹⁻² CFU/mL	10 ⁵⁻⁶ CFU/mL
Analysis time	> 2 days	> 1 day	1-2 h	10 min
Selectivity	Very high	High	Very high	High
Reference	[6]	[6]	[6]	[44]

1.2 Traditional methods for pathogen detection

The rapid identification of responsible pathogens is considered as a key step to cure diseases, as it can reduce the patient mortality, healthcare costs and the proliferation of multidrug-resistant bacteria [1]. Diagnosis affects more than 60% of treatment decisions, while it accounts for only 2% of healthcare costs [1]. Research in pathogen detection mostly focuses on the food industry (38%), the clinical area (18%) and the water and environment system (16%), where involved pathogens are *Salmonella* (33%), *Escherichia coli* (27%), *Listeria* (14%), *Campylobacter* (11%) and *Legionella* (7%) [6]. The typical infection thresholds for various matrixes are summarized in Table 1.1.

For all these reasons, several methods have been developed to identify responsible pathogens in clinical, food and environmental samples (Fig. 1.2). The four prominent methods are the *culture*, *enzyme-linked immunosorbent assay* (ELISA), *polymerase chain reaction* (PCR) and *Matrix-assisted laser desorption ionization time-of-flight mass spectroscopy* (MALDI-TOF MS). Their advantages and drawbacks are detailed hereafter, and summarized in Table 1.2.

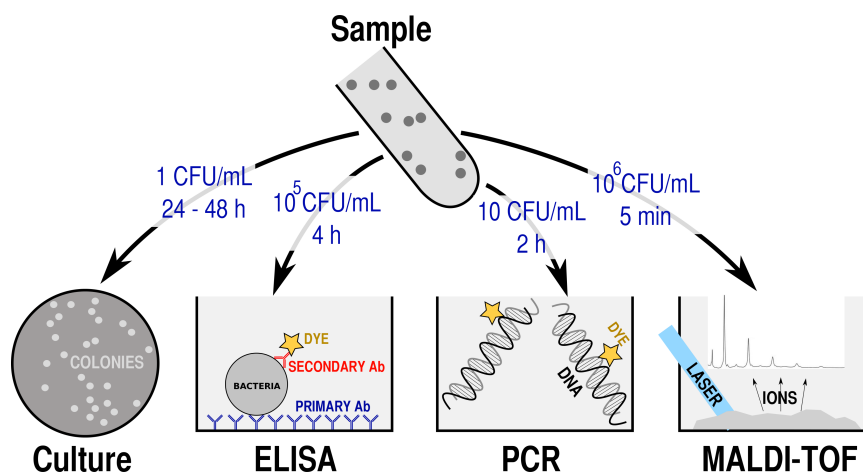


Figure 1.2 – Schematic representation of four conventional techniques for identification of bacterial cells.

1.2.1 Culture

Considered as the gold standard since the 19th century [40], the culture is the oldest method used for bacterial identification. It is based on the transfer of microorganisms from their initial medium to a solid or liquid culture medium to favour their growth, lasting from one day (e.g. *Staphylococci* and *Escherichia* species) to nine or fifteen days (*Campylobacter* and *Tuberculosis*) in optimal conditions of temperature, oxygen and nutrients [6]. For direct bacterial identification, growth media can be selective such as the Xylose lysine deoxycholate (XLD) agar where only *Salmonella* spp. can develop. When using non-selective growth media such as Lysogeny broth (LB) or Tryptic Soy Broth (TSB), additional optical screening methods such as colorimetry is required to identify the involved bacteria based on a single colony [45]. Despite the long analysis time, this method provides the best sensitivity, selectivity and screening for viability and resistance to antibiotics.

1.2.2 ELISA

The enzyme-linked immunosorbent assay (ELISA) uses interactions between antigens on a bacterial surface and related antibodies [6], in *sandwich*, *direct* and *competitive* ways. The sandwich ELISA is the most common method and starts by a bacterial incubation of more than two

hours on a surface functionalized with *primary antibodies*. Afterwards, the surface is extensively washed and incubated ca. two hours with *secondary antibodies* labeled with fluorophores, e.g. cyanine dyes Cy5, or colorimeter dies, e.g. horseradish peroxidase (HRP). The fluorescence or colorimetric level is then measured to quantify the presence of target bacteria. When dealing with samples of bacterial load $< 10^{5-6}$ CFU/mL [6], a one-day pre-enrichment step is often required.

1.2.3 PCR

The polymerase chain reaction (PCR) is based on the nucleic acid amplification of the bacterial DNA, contained in the cytoplasm and obtained after cell lysis. The DNA amplification is obtained after successive cycles, each consisting in denaturation, annealing and extension in this order. These three procedures require different temperatures, whose cooling steps explains the typical assay duration of 2 h. Once DNA concentration in the sample is sufficient, the bacterial identification is typically performed by gel electrophoresis. To avoid this additional step, real-time PCR directly identifies the fluorescence intensity from specific dyes attached to replicated DNA during the exponential amplification. Since cross-contamination must be avoided, the purity of the sample is a key requirement and requires qualified personnels [25, 40].

1.2.4 MALDI-TOF MS

Commercialized in the early 1990s, matrix-assisted laser desorption ionization time-of-flight mass spectroscopy (MALDI-TOF MS) is a fast, relatively-expensive and largely adopted technique for rapid bacterial identification. The mass fingerprint of the ions comprised in target bacteria are compared to a reference database and enables the accurate identification of bacterial strains found in the sample [46]. When starting from bacterial colonies of 10^{4-6} CFU [44] decomposed by acidic MALDI matrix into proteins and peptides [47], only 5 to 15 minutes are required for the simultaneous identification of 16 to 384 samples [44]. One drawback of MALDI-TOF MS is the inefficient distinction between Gram-positive bacteria [46], mostly between *Streptococci* and *Staphylococci* [48]. For relatively-simple matrixes such as urine, the analysis can be directly performed on the pellets resulting from the direct centrifugation of the sample [44]. In this case, the total analysis time is strongly reduced thanks to the avoidance of the culturing step.

1.3 Biosensors for pathogen detection

As previously described, most methods for identification of bacteria in liquid samples require time-consuming steps such as pre-enrichment or DNA amplification. Analysis time would benefit from getting rid of these steps and detecting bacterial cells directly in their initial samples. The use of micro and nanotechnology goes in this direction, and promises the development of sensitive, selective and compact *biosensors* that can revolutionize the personalized medicine [1].

A biosensor can be defined as "*a compact analytical device incorporating a biological or biologically-derived sensing element (such as an enzyme, antibody, microbe or DNA) either integrated within or intimately associated with a physicochemical transducer*" [49]. This broad definition highlights that biosensors can be distinguished on their kind of transducer, recognition element, sample handling and readout interface. Next sections described each category with regards to bacterial detection.

1.3.1 Transducers

The transducer converts the presence of bacteria atop the sensor into a physical signal, typically proportional to their number. The electrochemical, optical and acoustic transducers are the three most popular transducers for bacteria sensing [25]. Their performances are compared in Table 1.3, especially for the detection of *S. aureus*.

Electrochemical transducers

Electrochemical transducers consist of electrodes applying electrical stimuli to the liquid sample to monitor its electrochemical answer. The electrical response can be promoted by electrochemical reactions of additional redox mediators. Depending on signals, electrochemical transducers can be categorized into four categories [64]:

- *Potentiometry* measures the DC voltage between an indicator and a reference electrode [65], whose value depends on electrochemical reactions produced by the applied DC current. The measured potential is typically proportional to the logarithm of the ion activity, but hardly achieves a steady-state value and strongly depends on the electrolyte ionic strength. A detection limit of $8 \cdot 10^2$ CFU/mL of *S. aureus* after only 20 min was achieved thanks to covalent functionalization of carbon nanotubes with aptamers [50].

Table 1.3 – Comparison between several kinds of biosensors for bacterial detection.

	Method	Medium	Bacteria	Selectivity	LoD	Time	Ref.
Electrochemical	Potent.	PBS	<i>S. aureus</i>	Aptamers	$8 \cdot 10^2$ CFU/mL	20 min	[50]
	Voltam.	milk	<i>S. aureus</i>	RbIgG	$4 \cdot 10^2$ CFU/mL	90 min	[51]
	Voltam.	milk	<i>S. aureus</i>	Ab-ELISA	1 CFU/g	18 h	[52]
	Voltam.	GM.	<i>S. aureus</i>	Antibiotics	$7 \cdot 10^2$ CFU/mL	3 h	[53]
	EIS	PBS	<i>S. aureus</i>	Ab-SAM	10^2 CFU/mL	2 h	[54]
	EIS	PBS	<i>S. aureus</i>	Ab-SAM	10 CFU/mL	NA	[55]
	EIS	PBS	MRSA	PCR	10 nM	~ 2 h	[56]
	EIS	PBS	<i>S. aureus</i>	Ab	10^2 CFU/mL	NA	[57]
	ISFET	NaCl	Salmonella	Ab	100 CFU/mL	1h	[58]
Optical	SPR	PBS	<i>S. aureus</i>	Ab	10^5 CFU/mL	NA	[59]
	SPR	PBS	MRSA	Bacterioph.	10^3 CFU/mL	20 min	[60]
	Colorim.	CS	MRSA	PCR+NP	500 ng amplic.	NA	[61]
	Fluoresc.	SELEX	<i>S. aureus</i>	Ap.+MP+NP	1 CFU/mL	1.5 h	[37]
Ac.	SAW	PBS	wc <i>E. coli</i>	Ab-SAM	10^6 CFU/mL	1 h	[62]
	SPQC	Milk	<i>S. aureus</i>	Ap.	41 CFU/mL	1 h	[63]

GM: growth medium; NP: nanoparticle; MP: magnetic particle; Ap.: aptamers; NA: not available

Ac.: Acoustic; CS: Clinical samples; amplic.: amplicon; SELEX buffer: see [37].

- *Voltammetry* measures a DC current generated after applying a DC potential on an electrochemical cell comprising working, auxiliary and reference electrodes, thanks to a potentiostat [65]. In linear sweep voltammetry (LSV), a potential that linearly increases with time is applied on the working electrode while cyclic voltammetry (CV) denotes the same potential function but in a cyclic way. The CV method is the most popular electrochemical technique, because of its reproducibility and ability to perform simultaneous observation of the oxidation and reduction peaks [65]. *Amperometry* is a fixed-potential voltammetry, with an applied voltage larger than the redox potential. With screen-printed electrodes featuring covalent immobilization of RbIgG, a detection limit of $3.7 \cdot 10^2$ CFU/mL was obtained for *S. aureus*, with a total detection time of ca. 90 min and a limited dynamic range of ca. 35 dB [51]. Indirect detection of 1 CFU/g of *S. aureus* in milk samples and after 18 hours was performed by amperometry monitoring O_2 released after the addition of hydrogen peroxide on a sandwich-ELISA assay [52]. Another indirect detection of *S. aureus* based on glucose consumption and antibiotic screening was reported by flow-injected amperometric measurements, showing a detection limit of $6.5 \cdot 10^2$ CFU/mL after 3 hours [53].

- *Electrochemical impedance spectroscopy* measures the AC impedance of the electrochemical cell, by applying a frequency-dependent AC voltage or current of small amplitude [65]. The mass transport and reaction kinetics can be estimated at low frequency, the electrical double layer (DL) at medium frequency, the ohmic resistance at high frequency and solution capacitance at very-high frequency. *Conductimetry* is a particular case of impedance spectroscopy aiming at measuring the conductance, which is impacted by ion release following an enzymatic reaction or a bacterial ion exchange. The largest sensitivity is obtained with differential measurements [64]. For *Staphylococcus* species, R_{ct} analysis in the low frequency range was shown to achieve a detection limit of 10^{1-2} CFU/mL *S. aureus* after ca. 2 hours thanks to self-assembled monolayers (SAM) with anti-*S. aureus* antibodies [54, 55]. Strategies can also encompass bacterial lysis for subsequent PCR analysis [56] or increased number of fragments binding to the biofunctionalized surface [57].
- *Charge sensing* with ion-sensitive field-effect transistors (ISFET), which can sense analyte charges and more generally the local pH [64]. Detection limit of 100 CFU/mL of whole-cell *Salmonella* was achieved in one hour using carbon nanotube FET [58]. However, most works with ISFET focus on the detection of specific DNA strands obtained after bacteria lysis [66] and on the sequencing capability using sensor arrays such as the ion torrent technology [67] that has demonstrated genome sequencing of *E. coli*. The use of such array for detection of whole-cell bacteria remain challenging because of trapped charges mismatch on the FET floating gates that introduce fixed-pattern noise (FPN) between pixels [68, 69].

Optical transducers

Optical biosensors are the most widespread biosensors. They measure the light intensity emitted from labels or bacteria themselves, and exist in various forms depending on the emitted spectrum and physical principle:

- *Surface plasmon resonance* (SPR) consists in measuring minute changes of the biolayer refractive index or thickness, thanks to excitation of surface plasmons [59], when bacterial cells bind on the surface. The main challenges for detection of whole-cell bacteria are the exponential decaying of the electromagnetic field in

the solution and the background noise induced by the change in temperature and sample composition. SPR sensors can employ prism couplers, grating couplers, optical fibers and integrated optical waveguides [59]. A detection limit of 10^7 CFU/mL of *S. aureus* in PBS was achieved in direct assay, while 10^5 CFU/mL was obtained in sandwich assay [59]. When combined with bacteriophage, a detection limit of 10^3 CFU/mL was reached after 20 min of incubation for MRSA detection [60].

- *Colorimetry* is based on the colorimetric reaction induced by an indirect physical parameter related to the bacterial concentration. For instance, colorimetric pH indicator slightly changes its colour when CO_2 is released during the growth of bacterial cells [25]. In this case, the selectivity depends exclusively on the growth medium selectivity. A recent work has demonstrated that combining PCR with gold nanoparticles enables a direct colorimetric identification of MRSA, with detection limits expressed in term of amplicon mass comparable to the state of the art, but with one day less [61].
- *Fluorescence spectroscopy* consists in measuring the light intensity emitted from fluorescent labels bound to target bacteria. Fluorophores, quantum dots and gold nanoparticles (NP) are the most used labels. NP are typically preferred because they are brighter, do not photobleach and enable a ratiometric readout [70]. For detection of *Staphylococcus* spp., nanoparticles, magnetic particles and aptamers can be combined in a clever way to amplify by three orders of magnitude the fluorescence intensity of a given *S. aureus* concentration, achieving single cell detection within 1.5 h [37].
- *Fourier Transform Infrared (FTIR) spectroscopy*, also known as vibrational spectroscopy [71], is a fingerprinting method that can use to identify intact bacteria from a single colony [72]. The technique can also be used during growth to estimate the number of viable bacteria present in a sample [73]. From the FTIR database and the use of Raman spectroscopy, it is possible to discriminate the involved bacterial sp. [40]. It is a simple, compact and affordable technique, but requires a pre-enrichment step [72].
- *Bioluminescence* relies on the ability of certain enzymes to emit photons as the result of their chemical reaction [25]. Two techniques using bacteriophages were reported for bacterial detection.

The first aims at infecting bacteria with pre-encoding luciferase bacteriophages to confer them light emission. The second method specifically lyses bacteria with bacteriophages to observe the ATP bioluminescence provided by the ionic cytoplasm content [25]. For both methods, high selectivity and distinction between viable and non-viable bacteria are guaranteed, but the detection time exceed several hours for a detection limit of 10^{4-5} CFU/mL.

Acoustic transducers

The converse piezoelectric effect, i.e. the generation of an acoustic wave when a piezoelectric material is stimulated by an electric field, is the foundation of acoustic transducers [74]. They can be described as very high sensitive balance, weighting biological cells through the measured frequency shift. However, acoustic biosensors face extreme sensitivity to all kinds of perturbation on the electric field path, and also face electric field attenuation when working in liquid [74]. Depending on the wave travelling direction, two main principles can be identified: the surface acoustic wave (SAW) and the transverse shear mode (TSM), also called quartz crystal microbalance (QCM). Selectivity is typically provided by immobilizing receptors on the sensor surface.

For QCM, the stimuli frequency is generally limited between 5 and 30 MHz [74] owing to the propagation through the material volume. For detection of *Staphylococcus* spp., most QCM transducers are nucleic acid biosensors requiring an initial bacterial lysis [75] but whole-cell detectors were also reported by coating the surface with antibodies [76] or indirectly by monitoring the infected milk coagulation [77], achieving $\sim 2 \cdot 10^2$ CFU/mL in 6 hours.

Thanks to the wave propagation in surface, SAW transducers feature larger operating frequencies between 30 and 500 MHz, justifying their broader used [74, 78]. To the best knowledge of the author, no SAW sensor were reported for the detection of whole-cell *Staphylococcus* spp., but detection limit of 10^6 CFU/mL within 1 hour was reported for whole-cell *E. coli* [62]. A recent work combining aptamers and graphene atop gold electrodes connected in series with piezoelectric quartz crystal (SPQC) demonstrates detection of 41 CFU/mL of *S. aureus* in one hour [63].

1.3.2 Sample handling

The way to deliver and handle the bacterial sample to the biosensor is often a key feature to reach high performance. For bacterial detection, the sample load can be as small as 10 CFU/mL while the volume above microsensors can be smaller than 1 μL , making binding events very hypothetical. For this reason, preconcentration steps and delivering methods are extremely important, as detailed hereafter.

Preconcentration steps

- *Centrifugation* enables to concentrate most bacterial cells contained in a liquid sample on the form of a solid pellet at the bottom of the centrifugation tube, after 5 min at around 5000 g. The remaining liquid above the pellet is called the *supernatant*, and is typically replaced by a simpler medium having a smaller volume (e.g. 100 μL instead of 1 mL). The new mix thus features a larger effective bacterial concentration. In addition, the resuspension medium is typically chosen with regards to the sensor operating regions [79]. Unfortunately, the centrifugation method is not selective.
- *Immunomagnetic separation* also forms a bacterial pellet by applying a magnetic field across the solution to attract magnetic beads conjugated to bacteria [80, 81]. It is also possible to use integrated coils to attract conjugates directly on the sensor [82]. Unlike centrifugation that requires moving parts, immunomagnetic separation is relatively simple, can be miniaturized and can further serve as a selectivity means when magnetic beads are functionalized.
- *Electrokinetic forces* are forces exerted on bacterial cells when the sample is subject to DC or AC voltages [83]. They can be used to attract bacteria on a region of interest, which is typically the sensing part [84, 85] or a separate microfluidic channel [86]. As they strongly depend on the dielectric properties of the bacteria and electrolyte, their optimization is notably more complex than centrifugation and immunomagnetic separation, but the concentration factors can achieve two to three orders of magnitude [84]. Electrodes can be avoided by inserting insulating beads in the sample to attract bacterial cells thanks to the generated electric field gradients [87], which is called the *DC insulator-based dielectrophoresis (iDEP)*.

- *Droplet confinement* enables the isolation and manipulation of single bacterial cell in nanoliter droplets thanks to digital microfluidics, improving the apparent concentration by several orders of magnitudes [88]. More information is provided in the next section.

Sample-delivering methods

- *Reservoir tanks* generally have an open side in contact with air, and can take various forms: a large volume (> 300 mL) beaker where impedance biosensors are immersed [89], wells of a 96-well plate each containing a sensor [90], Eppendorf tubes with external optical transducer [61], miniaturized tanks with mixing capabilities [91] and aperture atop the sensing part of a chip defined either with epoxy resist [92] or with a mounted tube [93]. Single drops of several thousands μL can also be dispensed directly on the sensor surface [94], but including preferably a closable lid to prevent evaporation [79] and the subsequent change of the analyte concentration. It is therefore preferable to perform a single measurement just after immersing the sensor and avoid real-time monitoring.
- *Continuous-flow microfluidics* deals with the manipulation of small volume samples, including mixing, pumping and separation in *flow cells*. The micrometer size gives rise to high surface-to-volume ratios, laminar flow and high transport rates for heat and mass [95]. Furthermore, the evaporation is almost inexistent in a closed microfluidic system and shear forces are better controlled. Most transducers can be integrated in a pL-nL microfluidic chamber, whose dimensions should be optimized with regards to convective and diffusive flows to trap most bacteria in the channel volume [96]. It is possible to perform wafer-scaled electrical measurements with a mobile microfluidic setup, called *microfluidic probe*, to automate biosensors measurements [97]. Many studies involving detection of *Staphylococcus* spp. use continuous-flow microfluidics [54, 78, 89].
- *Digital microfluidics*, also called *droplet-based microfluidics*, enables the manipulation and control of individual pL- μL droplets thanks to the electrowetting-on-dielectric (EWD) method [98, 99]. Compared to continuous-flow microfluidics, digital microfluidics enables huge miniaturization, fast heat and reaction transfer rates, integration capability, reusability, synchronization, individual droplet

control, evaporation control and energy efficient droplet actuation without undesirable capillary flows, moving parts (e.g. valves, pumps, etc.), patterned channels and reagent wasting. For *S. aureus* detection, fluorescence detection of $2 \cdot 10^5$ CFU/mL in 1-nL droplets of growth medium has been achieved after 2.8 hours of incubation, which was faster by 1.5 hours compared to the use of 1-mL droplets [88]. Digital microfluidics with 1-nL drops has also been implemented on sensor arrays including single-photon avalanche diodes (SPADs) to perform quantitative polymerase chain reaction (qPCR) on a 364-base sequence of *S. aureus* [100].

1.3.3 Selectivity means

Despite that the transducer transforms the presence of adherent bacteria into a physical signal, it has no ability to distinguish one sp. from another. Biological recognition elements, such as *antibodies*, *lytic enzymes*, *bacteriophages*, *microbial peptides* and *DNA strands* (see Section 1.1.4), must be added in the biosensing system to provide selectivity to a target bacterial cell. The example of sepsis, involving blood samples containing 1 CFU/mL of *S. aureus* (cfr Table 1.1) among more than ca. 10^9 red blood cells/mL, illustrates the extreme difficulty of the task. Selectivity can be provided to the sensor either through a surface or volume-based method, as described hereafter.

Surface-based methods

In surface-based methods, the transducer is covered by *bioreceptors*, also called *probes* or the *affinity-based layer*, so that only target bacteria can theoretically bind the sensor surface. As a result, the sensor signal is necessarily attributed to them. However, several drawbacks can be identified. First, the capture percentage is relatively low since only bacteria in close vicinity to the surface bind to the affinity-based layer [96]. Second, the imperfect bioreceptor selectivity and coverage result in bindings of undesirable biological cells, which are called *non-specific adsorptions* or *background noise* [101]. Despite *differential measurements*, *antifouling agents* or *blocking agents* such as bovine serum albumin (BSA) [102, 103], this effect still increases the number of false positives. In microfluidics, non-specific adsorption is further magnified by the high surface-to-volume ratio [102]. Third, the affinity-based layer typically suffers from low stability over time, low reproducibility and

low robustness to shear forces produced by the pipetting or microfluidic flow [104]. In microfluidics, it is recommended to functionalize the sensor surface before the encapsulation, otherwise the entire channel (not only the sensor) would be covered by bioreceptors which strongly decreases the sensitivity. However, bioreceptors can be denatured by the annealing step, which is typically required to seal the fluidic package. Multiplexed biosensors using the *microarray* technology can be defined by patterning spots with specific bioreceptors thanks to a spotter. To graft bioreceptors such as *antibodies* or *enzymes* on a sensor surface, two main methods are used for bacterial sensing:

- *Physical adsorption*, also called *physisorption*, denotes the incubation of bioreceptors directly on the naked sensor surface. Demonstrating good detection levels with antibodies for *S. aureus* in dry condition [17] and *Escherichia coli* in low-conductive buffers [105], this method yet suffers from antibody denaturation and poor coverage, uniformity, reproducibility and robustness to wash [102].
- *Self-assembled monolayers* (SAM) is the building of chemical groups, called *cross-linkers*, on the naked sensor surface to provide a covalent link with chemical terminations of bioreceptors [106, 107]. For instance, impedimetric biosensors use antibody-terminated SAM to enhance sensitivity and selectivity, e.g. towards *S. aureus* detection [57, 108]. It is also possible to covalently immobilize bacteriophages on an electrode surface thanks to EDC chemical processing of the surface [109], to subsequently capture and digest *E. coli* in a selective way that releases ion in the outer medium.

The same principles stand for called *aptamers*, which are DNA or RNA molecules synthetically produced to provide high specificity to target bacteria (pico or nanomolar affinity) [37, 110]. Other methods such as *Layer-by-layer* (LbL) assembly [111] or polymer coating [104] exist.

Volume-based methods

In contrast to surface-based selectivity, bioreceptors are spread through the whole sample volume and thus increase the number of interactions. If the transducer is not able to quantify the number of bioreceptor-bacteria conjugates in the whole volume, e.g. through UV-vis spectrophotometer evaluating the global colorimetric intensity [61], conjugates are concentrated on the sensor surface thanks to magnetic Ab-

nanoparticles [79, 94]. It is also possible to use lytic enzymes and bacteriophages for high-selective impedimetric detection of bacteria [112]. In the first case, the bacterial growth is inhibited in a media containing bacteriophages, which decreases the ion release sensed by conductimetry [113]. In the second case, lytic enzymes such as *lysostaphin* have also been used to fragment *S. aureus* cells into small pieces to increase the biomass binding on the sensor surface [57].

1.3.4 Readout interfaces

The type of readout interface strongly depends on the transducer. For optical transducers, cumbersome and costly setup are required since both microscopes and high-resolution lenses must be included with a CMOS or CDD image sensor. The setup can be miniaturized, but lenses and alignment settings are still required [114].

For electrochemical transducers, bulky analyzers or potentiostats are typically used in research but miniaturized electronic circuits smaller than few mm² have recently been reported for commercial applications, on the same chip [115, 116] or not [117] as the sensor.

The measurement of acoustic sensors can be performed using oscillators, vector voltmeters or network analyzers [78]. Because vector voltmeters are 10 to 100 times less sensitive than other techniques and oscillators do not provide information about the voltage amplitude and can present distortion, the best method is the use of network analyzers giving a complete characterization of the device impedance.

1.3.5 Figures of merit

To compare different kinds of biosensors, it is crucial to quantify their performances based on various figures of merit (FoM), characterizing many key aspects of biosensing such as sensitivity, detection time and selectivity. An exhaustive list of FoM is provided hereafter and classified into three distinct categories: the transducer performance, the bioreceptor performance and the portability/implantability performance.

Transducer performance:

- The *limit of detection* (LoD), also sometimes incorrectly called the sensitivity, is the minimal detectable concentration of bacterial cells, contained in the initial sample and expressed in CFU/mL.

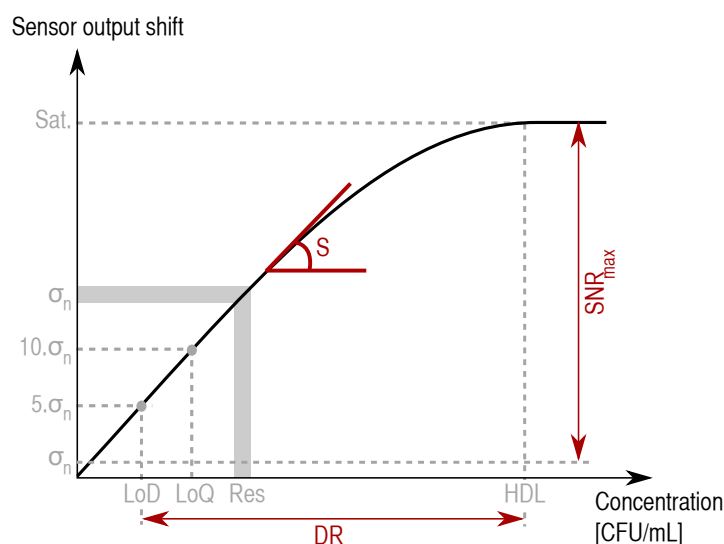


Figure 1.3 – Schematic representation of the sensor output shift versus the bacterial concentration, highlighting the limit of detection (LoD), the limit of quantitation (LoQ), the highest detectable level (HDL), the noise floor (σ_n), the saturation signal (Sat.), the dynamic range (DR), the maximal signal-to-noise ratio (SNR_{max}), the sensitivity (S) and the resolution (Res).

This critical concentration corresponds to a shift of the electrical output larger than the noise by a factor 5 [118], which concurs to a signal-to-noise ratio (SNR) of 14 dB. The output shift is the difference between output and blank signals, the last obtained preferably from sample containing other bacteria than the target one [103]. For surface-based biosensors, this thesis defines an *intrinsic limit of detection* (iLoD) which denotes the minimal surface coverage, given in % or in number of bacteria per mm^2 , or minimal physical quantity required for detection, given in F for instance in the case of capacitive biosensors.

The *limit of quantization* (LoQ), used sporadically, is the minimal quantifiable concentration of bacterial cells and corresponds by definition to an output electrical shift 10 times larger than the noise [118, 119], which is equivalent to a SNR of 20 dB.

- The *sensitivity* (S) is the change of the sensor output per unit variation of the bacterial concentration or the number of adherent bacteria, thus expressed in $F/(CFU/mL)$ or $F/(\# \text{ bacteria})$

for capacitive biosensors. It corresponds to the slope of the sensor output characteristics (Fig. 1.3). This thesis also defines an *intrinsic sensitivity* (iS) quantifying the change of the sensor output per unit variation of the sensor physical input, e.g., expressed in V/F in the case of a capacitance-to-voltage conversion.

- The *dynamic range* (DR) is the range of detectable bacterial concentrations spanning from the LoD to the highest detectable level (HDL), often defined as the bacterial concentration saturating bioreceptors [103]: $DR \triangleq 20 \cdot \log_{10}(\frac{HDL}{LOD})$ [dB]. The DR is important in applications requiring the quantification of the bacterial concentration. The sensor output corresponding to the HDL is the saturation level (*Sat.* in Fig. 1.3).
- The *detection time*, also called *steady-state response time* and *transient response time* [64], is the analysis time needed to obtain a stable biosensor output starting from the initial collection of the biological sample. It encompasses the durations of sample conditioning, pre-concentration steps and the *response time* of the transducer itself. The biosensor can be used either in *endpoint* or *real-time* modes. The first involves the steady state, defined as the time needed to achieve 90% of the stable biosensor value [64]. In opposite, *real-time* monitoring is faster thanks to averaging capabilities and can further provide useful kinetic information. The detection time is also strongly impacted by the kind of detection, *direct* [94, 108, 120] or *growth-based* [89, 121, 122].
- The *resolution* (*Res*), also called the *precision*, is the minimal error expressed in CFU/mL on the bacterial concentration, which is associated to the sensor noise σ_n resulting from electrical and biological noise sources [123].
- The *maximal signal-to-noise ratio* (SNR_{max}) is the ratio between saturation and noise levels at the sensor output: $SNR_{max} \triangleq 20 \cdot \log_{10}(\frac{Sat.}{\sigma_n})$ [dB]. This figure of merit is occasionally used, especially when optimizing the sensor parameters [123, 124].
- In this thesis, two *figures of merit* (FoM) have been introduced: $FoM_1 \triangleq LoD \cdot V_{sample}$ and $FoM_2 \triangleq LoD \cdot V_{sample} \cdot t_{incub}$, where *LoD* is the limit of detection, V_{sample} the sample volume and t_{incub} the incubation time. FoM_1 denotes the minimal detectable number of bacteria in CFU contained in the sample (whatever its volume).

To account for the incubation time, FoM_2 is the multiplication of FoM_1 by the incubation time, and is expressed in CFU.min.

Bioreceptor performance

- *Selectivity*, often preferred to the *specificity* term [125], is the sensor ability to detect a *target* bacterial cell in a sample containing many *background* components such as proteins, viruses and other bacteria. Typically provided by biological species such as antibodies, enzymes or DNA (see Section 1.1.4), selectivity is very challenging as already explained in Section 1.3.3. Closely linked to the selectivity, the *matrix complexity* also limits biosensing performance [45] and depends on the matrix physical nature (liquid, solid or semisolid), chemical properties (ionic strength, permittivities, ion composition, etc.), microbial and parasitic compositions (red blood cells, proteins, etc.). Another related terminology is the biosensor *reproducibility*, which denotes the sensor-to-sensor variability typically dominated by the random binding of biological species on random positioned bioreceptors at the sensor surface [123].
- *Labeling* consists in grafting fluorophores [25], magnetic beads [81] or enzymes [61] on the surface of target bacteria to improve the biosensor sensitivity and selectivity [103]. However, it is at the expense of larger detection time, cost and complexity in sample handling. *Label-free* biosensors do not use such bacteria labeling.
- The *robustness* and *stability under flow* of the bioreceptor layer is very important in microfluidic applications and in systems requiring intense washing procedures, such as ELISA. In most biosensing applications, the sensor is used few minutes and then discarded so that the affinity-based layer typically withstands biofouling and keeps biological reaction kinetics identical [64].
- *Multiplexing* is the ability to detect several bacterial spp. within a sample by using a single biochip. It is typically achieved by dividing the chip area into several biosensing regions that are differently functionalized [116], to form a *microarray* or *biosensor array*. Multiplexing can provide tremendously decreased cost and sample volume, especially important for point-of-care bacterial detection [1].

- The *distinction between viable and non-viable bacteria* is critical for pathogen detection since non-viable bacterial cells are not pathogen. Dealing with viable bacteria only, the culturing step can be combined with impedance-based measurements to estimate the viable concentration of bacteria [81, 122]. Other techniques using dielectrophoresis [126] or aptamers [110] also enable the separation or direct detection of viable bacteria.

Portability and implantability performance

- The biochip *power consumption*, expressed in W, is critical in portable and implantable biosensing applications [127]. It is generally dominated by the transducer and the readout interface, which must be designed accordingly.
- The *biostability* and the *lifetime* of the biochip, which are closely related to the *robustness* and *stability under flow* previously described, are crucial for long-term applications where the sensor surface must withstand biological liquids during hours or days. Electrochemical corrosion of the surface material including the affinity-based layer must be sufficiently slow compared to the expected operating time of the biosensor.
- The *biocompatibility* denotes the biosensor ability to keep the biological sample clean and unaltered [64], avoiding the release of pollutants by the sensor itself. It is particularly important for in-vivo applications where inappropriate biocompatibility can promote toxicity, mutagenicity, carcinogenicity, thrombogenicity or immunogenicity [64].
- The *integration* and *miniaturization* capabilities have important consequences on the biosensor *size*, *portability* and *cost*. The integration is related to the inclusion of signal processing and readout units around the biosensor, by using e.g. microcontrollers and wireless modules. Both integration and miniaturization are drastically enhanced by using the CMOS technology, delivering multiplexed and $< 1 \text{ cm}^2$ biochip including the integrated readout [67]. Such technology also offers dramatic cost reduction for high production volumes. Finally, the biochip miniaturization also strongly reduces *sampling* (e.g. blood) and *reagent* (e.g. antibodies) volumes, decreasing cost and improving the simplicity and easiness of the diagnosis test.

- The *sample preparation* and all other steps requiring manipulation must be discarded or automated for achieving portable or implantable devices. For detection of pathogens, most biosensors either perform DNA detection after cell lysis, requiring on-chip heating. The detection of *whole-cell* bacteria, also called *intact* bacteria [72], is much simpler to integrate.
- *Single-usability*, opposite to *reusability*, denotes the fact that the biosensor must be discarded after a single use [64]. For point-of-care diagnosis tools, most applications present single-use biosensors, assimilated to consumables, mounted on a reusable readout instrument such as glucometers commercially available [128]. Implants are also single use to avoid contamination and technical failures.

1.4 Summary

In this first chapter, we have reviewed the main issues related to detection of pathogen bacteria, focusing on the case of *Staphylococcus* species. The four main conventional detection techniques (culture, ELISA, PCR and MALDI-TOF MS) have been described and compared to biosensors, which are attractive bio-devices combining a transducer with a biological recognition element and targeting faster bacterial detection.

Among those biosensors, electrochemical transducers using impedance spectroscopy have the unique advantage of enabling label-free techniques, extreme miniaturization and system integration, while keeping competitive performances (see Table 1.3). In most cases, these devices can be considered as capacitive biosensors, since either the recognition or insulating layer atop metal electrodes makes the impedance mostly capacitive. In the next chapter, a complete analysis of capacitive biosensors towards bacterial detection is thus proposed.

CHAPTER 2

Capacitive and label-free detection of bacterial cells

In this chapter, the capacitive transduction involving bacteria atop passivated interdigitated microelectrodes (IDEs) is studied. In Section 2.1, a review of impedance spectroscopy for bacterial detection is provided. In Section 2.2, measurements of the fabricated IDEs in electrolytes with and without bacterial cells are analyzed with regards to an established analytical model [18, 19]. In Section 2.3, an innovative selectivity principle using lytic enzymes is experimentally demonstrated [18]. Finally in Section 2.4, numerical simulations are implemented to optimize the sensor parameters towards maximal bacterial sensitivity [19, 20].

2.1 Impedance spectroscopy

2.1.1 Principle

Impedance spectroscopy consists in applying an AC voltage of amplitude V_0 and frequency f on one electrode and reading at the other the generated AC current characterized by an amplitude I_0 , phase θ and fundamental frequency f . Because the system can be assumed perfectly linear when $V_0 \ll U_t$ [129], where $U_t = \frac{k_B T}{q} \simeq 26$ mV is the thermal voltage, the complex impedance in phasorial form between electrodes is:

$$Z(\omega) \triangleq \frac{V_0 \cdot e^{j\omega t}}{I_0(\omega) \cdot e^{j\omega t + \theta(\omega)}} = \frac{V_0}{I_0(\omega)} \cdot e^{-j\theta(\omega)} \quad (2.1)$$

where $\omega \triangleq 2\pi f$ is the angular frequency. In biosensing applications, minute changes of the complex impedance $Z(\omega)$ are monitored when biological species bind between electrodes, and two transduction mechanisms must be distinguished. The first is the *electrochemical impedance spectroscopy* (EIS) benefiting from electrochemical reactions between biological species and the electrolyte medium, which are often amplified by *redox probes* [130] such as $[\text{Fe}(\text{CN})_6]^{3-/4-}$ [131], also called *electroactive species*. In this case, the electron transfer through *faradaic electrodes* is quantified through the charge transfer resistance R_{ct} [131].

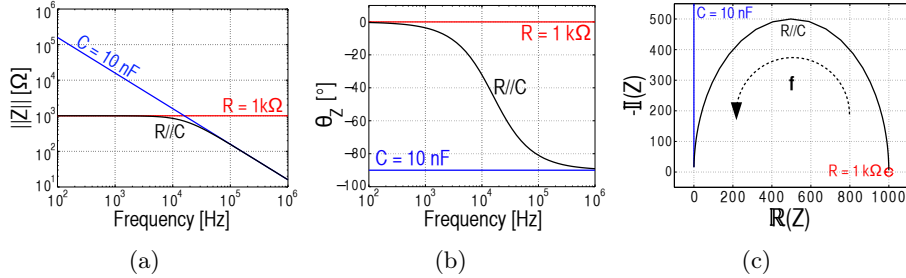


Figure 2.1 – Representation of the complex impedance $Z(\omega)$ for a 1-k Ω resistance R , a 10-nF capacitance C and the parallel association of both: (a)(b) Bode plots of the impedance modulus $\|Z\|$ and phase θ_Z versus the applied frequency f and (c) Nyquist plot of the opposite imaginary part of $Z(\omega)$ versus its real part.

When no electron transfer occurs at solid-electrolyte interface, the electrodes are called *non-faradaic* and the sensing information is mainly contained in the dielectric properties of the system. This *electrical impedance spectroscopy*, also called *electrochemical capacitance spectroscopy* (ECS) [131], thus involves no electrochemical reactions.

2.1.2 Impedance representation

Two graphical representations of the complex impedance $Z(\omega)$ are typically used and come from two possible decompositions of $Z(\omega)$:

$$Z(\omega) = \|Z(\omega)\| \cdot e^{j\theta_Z(\omega)} \quad (2.2)$$

$$= \Re\{Z(\omega)\} + j\Im\{Z(\omega)\} \quad (2.3)$$

Based on Eq. 2.2, *Bode plots* represent the impedance modulus $\|Z(\omega)\|$ and phase $\theta_Z(\omega)$ in function of the frequency f (Figs. 2.1(a) and 2.1(b)). The *Nyquist plot*, also called the *Cole-Cole plot*, is based on Eq. 2.3 and represents the opposite imaginary part $-\Im\{Z(\omega)\}$ of $Z(\omega)$ in function of its real part $\Re\{Z(\omega)\}$ (Fig. 2.1(c)). Although the spectral information provided by Bode plots is more consistent, Nyquist plots better represent time constants and are suitable for frequency-independent parameters such as R_{ct} in EIS using redox probes [94].

In biosensing applications, minute changes of $Z(\omega)$ occur so that the logarithmic representation of $\|Z(\omega)\|$ is not very practical. Because capacitive biosensors mostly exhibit capacitive behaviors, it is more suitable to represent the *normalized admittance* modulus $\|Y(\omega)/\omega\|$ expressed in F instead of $\|Z(\omega)\|$, where the complex admittance is de-

defined as $Y(\omega) \triangleq 1/Z(\omega)$. The phase analysis remains essential to attest the dominant behavior, either resistive as $\theta_Z > -45^\circ$ or capacitive as $\theta_Z < -45^\circ$.

2.1.3 Electrochemical cells

To perform impedance measurements, three key components are required: an *electrochemical cell*, an *impedance analyzer* and optionally a *potentiostat*. For EIS involving electrochemical reactions, it is critical to control the electrolyte potential to have reproducible results [132]. The impedance is measured between a *counter* (CE) and a *working* electrode (WE), while a *reference* electrode (RE) maintains a constant potential in the electrolyte thanks to a potentiostat [57, 121, 130, 133–136]. In the case of non-faradaic electrodes, the solution potential does not necessarily need to be controlled since no electrochemical reactions occur. As a result, a two electrode system is sufficient to probe the system impedance [54, 79, 84, 86, 89, 94, 120, 137–141].

2.1.4 Electrode designs

Most systems use miniaturized planar electrodes, that provide better performance than large-scale electrodes such as 3D centimeter-scaled glassy electrodes [142]. *Interdigitated electrodes* (IDEs), also called *interdigitated array microelectrodes* (IDAM) or *interdigital capacitors* (IDCs), are two large sets of electrodes disposed in a comb fashion. Fabricated by standard microfabrication techniques [103], IDEs have typically micrometer- [108] or nanometer- [143, 144] scale width and gap, thus benefiting from large capacitance values and active area. With circular [89, 139] or rectangular [120, 138] shapes, IDEs have been widely used for bacterial detection [79, 89, 90, 94, 108, 120, 145]. *Screen-printed electrodes* are another notable electrode design for EIS and typically comprise a centimeter scale disk WE surrounding by a circular ring CE and by a small RE [146].

2.1.5 Electrode materials

Electrodes are typically made in noble metals such as gold (Au) [57, 79, 89, 94, 108, 120, 122, 134, 135, 138, 140, 147–149] and platinum (Pt) [84, 86, 137], because of their inertness and biocompatibility in solution [92]. Other resistant materials such as chromium (Cr) [105, 150] can also be used. Thanks to its conductivity, transparency, stability and

polarizability, indium-tin oxide (ITO) is also an attractive material to build electrodes [130, 133]. Carbon electrodes are interesting as well to easily build chemical organic links with biomolecules [109, 110, 142, 146]. However, most of these materials cannot straightforwardly be used in standard CMOS process since they are considered as contaminant [151] or highly expensive. Despite complexity and cost, post-process steps can still be used to pattern gold electrodes atop CMOS chips [92, 139].

In opposite, the last CMOS metal layer in aluminum can be used for patterning electrodes, but then requires a passivation layer grown by microfabrication (SiO_2 [82, 152], Si_3N_4 [153, 154], Al_2O_3 [155], Ta_2O_5 [156], TiO_2 [157], $\text{TiO}_2/\text{ZrO}_2$ [157], etc.) to act as protective coating against electrochemical corrosion of the underneath aluminum [158]. In particular, the passivation by a thin biocompatible [159] Al_2O_3 layer has shown to fulfil capacitive biosensing of bacteria [17] or proteins [160] in dry conditions. Since Al_2O_3 withstands corrosion in water during several days [161], Al_2O_3 passivated biosensors can be used in short analysis time [162–165].

2.1.6 Surface- versus volume-based impedimetry

Impedance detection can target suspended bacterial cells in the electrolyte (i.e. volume-based) or captured bacterial cells at the sensor surface (i.e. surface-based).

The volume-based method is called impedance flow cytometry (IFC), and enables an accurate counting and statistical size analysis of a large number of cells (> 10.000 in less than 2 min [166]) flowing through two planar electrodes patterned at the top and bottom of the channel [167–169]. Mostly used for large cells [170], IFC can be extended for bacterial cells by scaling down the microfluidic channel to $\simeq 10 \mu\text{m}$ [166], by sheathing the sample with oil [171] or by using resonance effects [169]. Its main disadvantage is the inability to selectively distinguish one bacteria from another, despite some promising works that show slight differences of the dielectric footprints [169, 172].

The surface-based method uses planar electrodes designed atop a solid substrate, in order to detect bacterial cells that progressively adhere the sensor surface thanks to the microfluidic flow [145]. The main disadvantage of this method is that many cells flowing atop the sensor are lost. However, selectivity can be easily obtained by functionalizing the sensor surface, e.g. with antibodies.

2.1.7 Performance comparison

An exhaustive comparison of significant works on impedance detection of bacterial cells in solution is provided in Table 2.1. As explained in Section 2.1.6, only surface-based methods can be used for selective detection of bacterial cells. Therefore, this section deals only with this kind of sensors. The detection limit (LoD) must be compared by considering the detection time and the incubated bacterial volume. Extremely small bacterial loads of 1-100 CFU/mL are generally obtained at the expense of large detection time and/or incubated volumes [54, 57, 122, 134, 150]. In this case, growth-based methods can further provide screening between viable and non-viable bacterial cells [89, 122, 137]. Surface functionalization and electrokinetic effects can also improve the LoD, at a given volume and detection time. The way the bacterial sample is delivered to the sensor, e.g. immersion, microfluidic flow, pipetting, agitation, etc., is also an important factor to improve the bacterial binding on the sensor surface.

Most impedance biosensors use two-electrode systems without redox mediators (see Table 2.1). In high-conductive buffers such as pure PBS ($\sigma_{sol} \sim 1.8$ S/m), the impedance analysis mainly relies on minute changes of the double layer capacitance C_{DL} [89, 120] or charge-transfer resistance R_{ct} [57, 110, 130, 133, 135, 146], when the electrolyte comprises redox probes $\text{Fe}(\text{CN})_6^{3/4-}$. In low-conductive buffers such as 0.1 M mannitol solution characterized by an electrical conductivity $\sigma_{sol} \sim 100$ $\mu\text{S}/\text{m}$, the solution resistance R_{sol} is typically used for bacterial sensing [79, 84, 86, 94, 105, 122, 137, 138, 150]. This thesis reports innovative bacterial sensing using both R_{sol} and the medium capacitance C_{sol} , in low-conductive [18, 21] and high-conductive buffers [22].

Selectivity is typically provided by antibodies grafted on the sensor surface either by physisorption [105, 120, 130, 135, 146] or atop a self-assembled monolayer (SAM) [54, 57, 108, 133, 134, 138]. When grafted on magnetic or nanoparticle beads [79, 86, 94], they can act throughout the sample volume and improve the LoD. Besides antibodies, antimicrobial peptides [140, 148], bacteriophages [109] and aptamers [110] can also provide selectivity when grafted on the sensor surface. In this thesis, a new selectivity means is introduced with lytic enzymes [18].

Eventually, most works report detection of whole-cell viable bacteria while others detect peptidoglycan fragments after bacterial lysis [57], heat-killed bacteria [133] or the lyse process itself [105, 150].

Table 2.1 – Performance comparison of relevant works on microscopic impedimetric detection of bacteria in solution, sorted chronologically. Blue-highlighted results are those reported in this thesis.

Princ.	Medium	Bacteria	Selectivity	Electrode	LoD	Time	Vol.**	FoM ₂	Ref.
<i>R_{sol}</i> *	0.1 M mannit.	<i>wc-E. coli</i>	-	Pt IDE (2E)	10 ⁵ CFU/mL	10 min	130 mL	1.3·10 ⁸ CFU·min	[84]
<i>R_{sol}</i>	Tris-Gly-Dext	<i>v-L. innocua</i>	-	Pt IDE (2E)	10 ⁷ CFU/mL	2h	5.27 mL	6.3·10 ³ CFU·min	[137]
<i>R_{ct}</i>	PBS (R)	<i>hk-E. coli</i>	SAM-Ab	ITO (3E)	6·10 ³ CFU/mL	> 1 h	50 μL	1.8·10 ⁴ CFU·min	[133]
<i>R_{sol}</i>	0.1%-peptone	<i>wc-E. coli</i>	SAM-Ab	Gold IDE (2E)	10 ⁵ CFU/mL	5 min	20 mL	10 ⁷ CFU·min	[138]
<i>R_{ct}</i>	PBS (R)	<i>wc-E. coli</i>	Ab	ITO (3E)	10 ⁶ CFU/mL	NA	20 μL	NA	[130]
<i>R_{sol}</i> *	DI water	<i>wc-L. monoc.</i>	M-Ab	Pt IDE (2E)	7·10 ⁵ CFU/mL	2 h	40 μL	3.4·10 ⁶ CFU·min	[86]
<i>C_{DL}</i>	0.1% peptone	<i>wc-E. coli</i>	SAM-Ab	Cr IDE (2E)	10 ⁴ CFU/mL	10 min	30 mL	3·10 ⁶ CFU·min	[108]
<i>R_{sol}</i> *	DI water	<i>l-E. coli</i>	-	Cr IDE (2E)	10 ² CFU/mL	3 h	90 mL	1.6·10 ⁶ CFU·min	[150]
<i>C_{DL}</i> *	DI water	<i>wc-E. coli</i>	-	Gold IDE (2E)	5·10 ³ CFU/mL	NA	NA	NA	[147]
<i>R_{sol}</i> *	0.1 M mannit.	<i>l-E. coli</i>	Ab	Cr IDE (2E)	10 ⁶ CFU/mL	10 min	5 mL	5·10 ⁷ CFU·min	[105]
<i>R_p</i>	PBS	<i>wc-E. coli</i>	b-Ab SAM	Gold (3E)	10 CFU/mL	1 h	200 μL	1.2·10 ² CFU·min	[134]
<i>R_{sol}</i>	0.1 M mannit.	<i>wc-E. coli</i>	MNP-Ab	Gold IDE (2E)	7.4·10 ⁴ CFU/mL	35 min	2 μL	5.2·10 ³ CFU·min	[94]
<i>C_{DL}</i>	PBS	<i>wc-E. coli</i>	biot-Ab	Gold IDE (3E)	10 ⁴⁻⁵ CFU/mL	40 min	1 mL	4·10 ⁵ CFU·min	[120]
<i>R_{sol}</i>	YPLT	<i>v-E. coli</i>	-	Gold IDE (2E)	8 CFU/mL	14 h	NA	NA	[122]
<i>R_{sol}</i>	DI water	<i>wc-S. typhim.</i>	M-Ab	Gold IDE (2E)	3.5·10 ⁶ CFU/mL	30 min	20 μL	2.1·10 ⁶ CFU·min	[79]
<i>R_{ct}</i>	SM-buffer	<i>wc-E. coli</i>	Bacterioph.	SPCE (3E)	10 ⁴ CFU/mL	20 min	50 μL	10 ⁴ CFU·min	[109]
NA	PBS	<i>wc-E. coli</i>	Peptides	Gold IDE (2E)	10 ³ CFU/mL	15 min	NA	NA	[148]
<i>C_{por.}</i>	PBS	<i>wc-S. aureus</i>	SAM-Ab	Nanomem. (2E)	10 ² CFU/mL	3 h	170 μL	3·10 ³ CFU·min	[54]
<i>R_{ct}</i>	DPBS (R)	<i>wc-S. typhim.</i>	SAM-apt.	GNP-SPCE (3E)	600 CFU/mL	1 h	30 μL	10 ³ CFU·min	[110]
<i>C_{DL}</i>	TSB	<i>v-S. epiderm.</i>	-	Gold IDE (2E)	8.5·10 ⁵ CFU/mL	10 h	350 mL	2·10 ¹¹ CFU·min	[89]
<i>R_{ct}</i>	Milk (R)	<i>wc-L. innoc.</i>	SAM-EL	Gold SPE (3E)	10 ⁵ CFU/mL	20 min	5 μL	10 ⁴ CFU·min	[149]
<i>R_{ct}</i>	PBS (R)	<i>wc-S. pyogen.</i>	Biot-Ab	Gold SPE (3E)	10 ⁴ CFU/mL	30 min	10 μL	3·10 ³ CFU·min	[135]
<i>R_{ct}</i>	Milk (R)	<i>wc-B. melit.</i>	Ab	GNP-SPCE (3E)	4·10 ⁵ CFU/mL	1.5 h	15 μL	5.4·10 ⁵ CFU·min	[146]
<i>R_{ct}</i>	PBS (R)	<i>l-S. aureus</i>	SAM-Ab	Gold (3E)	10 ² CFU/mL	10 min	200 μL	2·10 ² CFU·min	[57]
NA	PBS	<i>wc-L. monoc.</i>	Peptides	Gold IDE (2E)	10 ³ CFU/mL	20 min	20 μL	4·10 ² CFU·min	[140]
<i>C_{sol}</i>	PBS 1:1000	<i>wc-S. epider.</i>	Lytic enz.	Al/Al ₂ O ₃ IDE (2E)	5·10 ⁶ CFU/mL	20 min	20 μL	2·10 ⁶ CFU·min	[18]
<i>R_{sol}/C_{sol}</i>	PBS	<i>wc-S. epider.</i>	-	Al/Al ₂ O ₃ IDE (2E)	10 ⁷ CFU/mL	20 min	5 μL	10 ⁶ CFU·min	[22]
<i>C_{sol}</i> *	PBS 1:1000	<i>wc-S. epider.</i>	-	Al/Al ₂ O ₃ IDE (2E)	2·10 ⁵ CFU/mL	10 min	50 μL	10 ⁵ CFU·min	[21]

*: using electrokinetics; **: sample volume; (R): w/ redox probes; v: viable; wc: whole-cell; l: lysed; hk: heat-killed; Ab: Antibody; EL: endolysin
3E: three-electrode cell; 2E: two-electrode cell; M: magnetic bead; NP: nanoparticle; DPBS: Dulbecco PBS; SPCE: screen-printed carbon electrode

2.1.8 Recommendations

As it will be demonstrated in Section 2.2.2, impedance spectroscopy is extremely sensitive to the electrical conductivity σ_{sol} of the electrolyte (both at low and medium frequencies with C_{DL} and R_{sol}). Without labels, it is therefore impossible to directly predict the bacterial concentration from a single measurement since two samples with identical bacterial loads but different conductivities would result in different signals. The sensor signal must thus be compared to an appropriate control value, which is often the source of errors.

Typical misinterpretations found in literature

To show how biosensors response to the bacterial concentration, most works use successive dilutions of a bacterial sample. The electrical conductivity of these samples can be different in some cases and great care must be paid to avoid drawing wrong conclusions:

- As obtained by diluting successively the bacterial culture (e.g. $\sigma_{sol} = 1.3$ S/m for LB medium) into a reference buffer (e.g. $\sigma_{sol} = 1.8$ S/m for PBS) [79, 108, 134, 138], the dilutions present different conductivities of 1.3, 1.75 and 1.7995 S/m for dilution factors of 1, 10 and 1000. With regards to the reference buffer, it corresponds to apparent sensitivities of 27, 2.7 and 0.027% that logarithmically decrease with the dilution factor and might suggest that the sensor correctly responds to the bacterial concentration, even if it is not the case. In [134] for instance, the sensor is not able to distinguish between *E. coli* and *S. epidermidis* despite the antibody layer, probably because the sensor responds to σ_{sol} instead of the number of captured bacteria.
- After centrifugation or magnetic separation of the culture sample, the supernatant is discarded and the pellet typically resuspended in a low-conductive reference buffer (e.g. 0.1 M mannitol with $\sigma_{sol} \simeq 100$ μ S/m) [79, 84, 94, 120, 137]. The problem is that a small amount of ions, e.g. released from bacteria burst after centrifugation, vortexing or osmotic shock [173], is sufficient to significantly perturb the small electrolyte conductivity to $\sigma_{sol} = 150$ μ S/m. When performing dilutions of 1:1000, 1:10 and 1:1 in the reference solution, the related conductivities are 100.1, 105 and 150 μ S/m, corresponding to sensitivities of 0.05, 5 and 50% with

regards to the reference buffer. Of course, these sensitivities are indirectly linked to the number of bacteria, but strongly vary with experimental conditions, procedures and contaminations. It is thus preferable to manually adjust the conductivity to a fixed value for each bacterial dilution [105]. This effect is almost inexistent when high-conductive reference buffers are used.

To avoid these artefacts, it is possible to use five control techniques which are more accurate and reliable, as detailed hereafter.

Control using an independent buffer

To avoid the cumbersome and time-consuming centrifugation step, the sensor covered with bacteria can be washed and measured in a reference buffer. The obtained value is then compared with the blank response initially acquired in the same reference buffer [54, 148]. In this case, it is critical to ensure that measurements are performed at the equilibrium and without ionic contamination of the reference buffer between the two measurements. It is also possible to avoid the comparison with the blank response [146], but then the response can possibly be biased.

Control using a functionalization-free sensor

A simple and robust method consists in using two sensors sized identically, but with different functionalizations. Both sensors contact the same sample, but while the first reacts specifically to the target bacteria, the second reacts with no bacteria [57, 105, 140]. Differential measurements thus strongly reduce artefacts from electrolyte conductivity, but with an efficiency depending on the initial sensor mismatch. Differential measurements on electrodes with different dimensions, targeting either volume or surface sensing, can also be used to remove artefacts.

Control by optical means

Not suitable for point-of-care and compact sensors, optical monitoring of the sensor surface can nevertheless be performed in laboratory during electrical sensing to assess the binding of bacteria [84, 105, 174]. In this case, electrical shifts can be directly correlated to the number of captured bacteria. However, it does not fully remove the risk of misinterpretation with σ_{sol} because the sensor can be more sensitive to it than to bacteria.

Control by growth

When the sensor is immersed in a culture media with bacteria, the conductivity change by ion release during the growth phase is an indirect way to assess the presence of bacterial cells and requires no control [86, 89, 122], since the medium is not replaced during the whole real-time experiment. However, a selective method should be used to assess that the growth originates from the target bacteria.

Control using the sample supernatant

The supernatant obtained after centrifugating the bacterial sample accounts for ions released by bacteria at the previous centrifugation step. Especially important for low conductive samples, it presents a similar conductivity to the final resuspended bacterial sample. The supernatant can thus be used as the reference buffer to perform successive dilutions.

2.1.9 Sensor modeling

To understand and optimize impedance sensors, models and simulations have been proposed in the literature and summarized in this section.

Interfacial properties and Randles circuit

When solid materials are immersed in electrolytes, charge redistribution occurs (Fig. 2.2(a)). A single monolayer of hydrated ions with diameter a , called the *Stern layer*, builds up at the interface and is characterized by a total charge σ_0 . Furthermore, a diffusing *Gouy-Chapman layer* with a negative charge (σ_{DL}) decays along a distance λ_D , called the *Debye length* or the *Double layer thickness*:

$$\lambda_D \simeq \sqrt{\frac{\varepsilon_{sol} U_t}{2FC_{ions} \cdot 10^3}} \quad (2.4)$$

with ε_{sol} the electrolyte permittivity, U_t the thermal voltage, F the Faraday constant and C_{ions} the ionic strength expressed in Molar concentration. The given expression of λ_D holds only when local potentials are smaller than U_t , because only in this case the Poisson-Boltzmann equation can be linearized [175]. The Stern and Gouy-Chapman layers define the *Gouy-Chapman-Stern* (GCS) model of the *electrical double layer* (DL), whose potential distribution decays from surface Ψ_0 and zeta ξ potentials to a neutral equilibrium in bulk electrolyte (Fig. 2.2(b)).

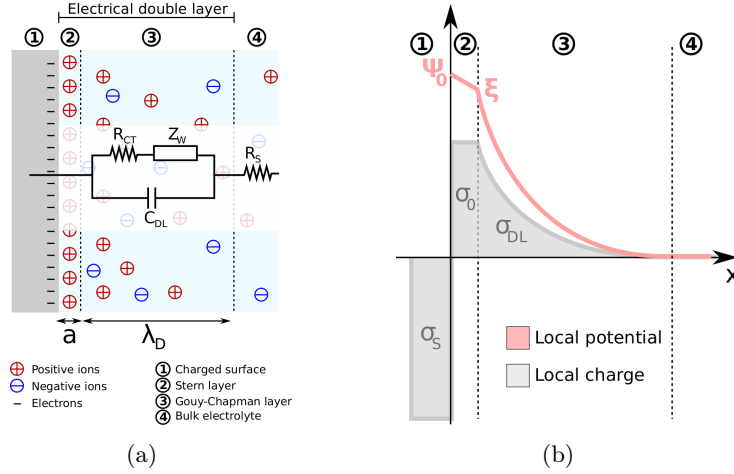


Figure 2.2 – (a) Schematic representation and equivalent electrical model of the solid-electrolyte interface. R_{CT} is the charge transfer resistance, Z_W the Warburg impedance, C_{DL} the double layer capacitance and R_S the electrolyte resistance. (b) dependence of the local charge and potential with the distance. Ψ_0 is the surface potential, ξ is the zeta potential, σ_s the charge of the solid material, σ_0 the charge in the Stern layer and σ_{DL} the charge within the electrical double layer.

To fix idea, typical values of λ_D are 1 nm, 3 nm, 10 nm and 30 nm in electrolytes with C_{ions} of 100 mM, 10 mM, 1 mM and 0.1 mM, respectively. When considering a Al_2O_3 layer with $8 \cdot 10^{18}$ hydroxyl groups/ m^2 as immersed in an electrolyte [176], the buildup surface charge σ_S features a density of 0.04 C/m^2 at pH 7.4, with a maximal value of 1.28 C/m^2 at extreme pH. Because $\sigma_S = -(\sigma_0 + \sigma_{DL})$, the corresponding surface potentials Ψ_0 are approximately 47 and 218 mV, respectively.

The spectral behavior of the DL is given by *Randles circuit*, which models the faradaic interface with a *charge transfer resistance* R_{CT} , *Warburg impedance* $Z_W(\omega)$, solution resistance R_S and DL capacitance C_{DL} (Fig. 2.2(a)), resulting from the series association of the Stern C_{stern} and Gouy-Chapman C_{GC} capacitances:

$$C_{DL} \triangleq (C_{stern}^{-1} + C_{GC}^{-1})^{-1} \quad (2.5)$$

$$\simeq \frac{a + \lambda_D}{\varepsilon_{sol}} \quad (2.6)$$

This capacitance features a non-linear relationship with the electrical potential [177]. Also, due to the high electrolyte permittivity ($\varepsilon_{sol} \simeq 80 \cdot \varepsilon_0$) and small values of λ_D ($\simeq 1 \text{ nm}$) at saline condition ($\sigma_{sol} \simeq 1.8 \text{ S/m}$),

C_{DL} is extremely large ($> 70 \mu\text{F}/\text{cm}^2$ [103]). The charge transfer resistance R_{ct} , also called the *polarisation resistance* R_p at the equilibrium [65], characterizes the current flow generated by electrochemical reactions [65]. Also related to electrochemical reactions, $Z_W(\omega)$ characterizes the ion diffusion through the DL [65] and features an inverse relationship with f [178]: $Z_W(\omega) \simeq \frac{A\sqrt{2}}{\sqrt{\omega}}$, where A is a constant. For non-faradaic interfaces, no DC current flows through the solid-electrolyte interface. As a result, R_{CT} and Z_W can be discarded [177] and the interface simply consists in C_{DL} in series with R_S .

Global complex impedance

In addition to interfacial properties, the impedance between two electrodes immersed in an electrolyte also depends on the electrode design [143, 179, 180], the possible passivation layer atop metal electrodes [181, 182] and the dielectric properties of the bulk electrolyte, electrode substrate and bacterial cells [94, 143]. For the design point of view, the cell constant κ of IDEs composed of N_e planar electrodes (negligible thickness) of length L_e , gap d_e and width w_e is given by [179]:

$$\kappa \simeq \frac{1}{(N_e - 1)L_e} \cdot \frac{2K(k)}{K(\sqrt{1 - k^2})} \quad (2.7)$$

with $k \triangleq \cos(\frac{\pi}{2} \cdot \frac{w_e}{d_e + w_e})$ and $K(k) \triangleq \int_{t=0}^{t=1} \frac{dt}{\sqrt{(1-t^2)(1-k^2t^2)}}$. The electric field confinement at the electrode surface is another key concept to ensure that bacteria induce the largest modification of electric lines. It is estimated to 73% in a layer of thickness $0.4 \cdot d_e$ when $d_e = w_e$ [143].

For unpassivated electrodes, the LF impedance is dominated by the DL capacitance C_{DL} and charge transfer resistance R_{ct} , while volume resistance R_{sol} and capacitance C_{sol} govern at HF [143]. When passivated, the electrodes feature higher impedance values at LF and lower sensitivities to surface processes [181–183]. The best sensitivity is thus found at HF where volume effects dominate [182]. Surface functionalization can be considered as electrode passivation, slightly reducing the LF capacitance of impedance sensors [143] because SAMs feature insulating properties with small relative permittivities of $\simeq 2.7$ [184, 185].

Finally, bacterial cells are typically modelled by a two- or three-shell representation, depending on their Gram staining, where each shell features different dielectric properties [30, 186, 187]. To account for it in the electrode system, complex equivalent models can be used but often serve only as a qualitative representation [145].

Numerical simulations

To assess experimental data, most works perform an arbitrary fitting of lumped parameters contained in the equivalent electrical model [145]. This mostly enables to qualitatively understand the physical sensing principle, but hardly to optimize the sensitivity. For this reason, 2D or 3D electrostatic simulations are used to accurately quantify the sensitivity to bacteria depending on their random positions on the 3D electrode topology [180], their number [180, 188] and the thickness of the passivation layer [181]. Such simulations have also been implemented to analyze the impact of the applied frequency on the sensor impedance [189] and sensitivity [190–192], but only for nanometer-scale biomolecules.

2.1.10 Chapter innovations

The work developed in the next sections of this chapter provides several notable innovations compared to the established state of the art:

- Bacteria detection in low-conductive solutions is demonstrated in microfluidic channel with Al microelectrodes covered with a thin Al_2O_3 layer, extending their use from dry [17] to liquid conditions [18]. An innovative detection principle based on the monitoring of the medium capacitance C_{sol} at HF is presented, bypassing the sensitivity drop at LF owing to the insulating layer [18].
- A new selectivity method based on lytic enzymes is proposed [18]. Free of selective surface functionalization and centrifugation steps, the whole procedure is simple, straightforward, reproducible and enables the direct flow of real matrix samples. Furthermore, it strongly reduces the effect of non-specific adsorption of bacteria or biomolecules.
- An innovative setup enabling simultaneous real-time optical and electrical monitoring of the microfluidic-encapsulated sensor was built [18]. Electrical phenomena can thus accurately be linked to bacteria binding, and considerably decreasing the risk of the misinterpretations explained in Section 2.1.8.
- A comprehensive analytical model is established for the metal-insulator-electrolyte (MIE) interface with and without bacterial cells, providing an analysis based on cutoff frequencies [19]. Furthermore, the maximal sensitivity and the impact of metallic access lines are evaluated.

- Numerical simulations are developed in coupled electrostatic and AC domains with 2D Poisson-Nernst-Planck equations to account for ion transport, geometry effects, charges and multi-shell dielectric representation of bacterial cells [19]. Thanks to these simulations, the sensitivity to bacterial cells is more accurately estimated, the impact of oxide and bacterial charges is quantified and various sensor parameters are optimized.

The chapter is organized as follows. In Section 2.2, the fabricated sensor is measured in electrolyte with and without bacterial cells, and results are explained with regards to an established analytical model. In Section 2.3, the selective principle using lytic enzymes is described, experimentally demonstrated, and compared to other techniques. Finally in Section 2.4, numerical simulations are developed to optimize the various parameters involved in the system towards maximal sensitivity to bacterial cells.

2.2 Sensor modeling

2.2.1 Sensor design and fabrication

The capacitive sensor consists of a circular shape of passivated interdigitated microelectrodes (IDEs) with a diameter of $250\ \mu\text{m}$ and electrode width and space of $2\ \mu\text{m}$ and $4\ \mu\text{m}$, respectively (Fig. 2.3(a)). The circular shape was chosen to fit with the area of a dispensed drop and to provide uniform electric fields with a surrounding macroelectrode, as shown in Section 3.2. A similar but rectangularly shaped IDEs with $250\text{-}\mu\text{m}$ electrode length was also designed, and thus features a sensing area 27 % larger. No reference electrode is used because electrochemical reactions are almost inexistent (no redox mediator, small applied voltages and no DC current through the insulating layer).

Built atop a transparent Pyrex substrate, the microelectrodes are made in aluminum and covered by a 33 nm-thick atomic-layer-deposited (ALD) Al_2O_3 layer, acting as a protective coating against corrosion in biological solution [161, 162]. Provided by thick photoresist walls and PDMS cap, a 1 mm-wide, 5 mm-long and $300\ \mu\text{m}$ -thick microfluidic channel is defined (Fig. 2.3(b)). The total channel volume is $1.5\ \mu\text{L}$, while the volume above the sensor is only 15 nL. The microfabrication process is detailed in Appendix A.1.

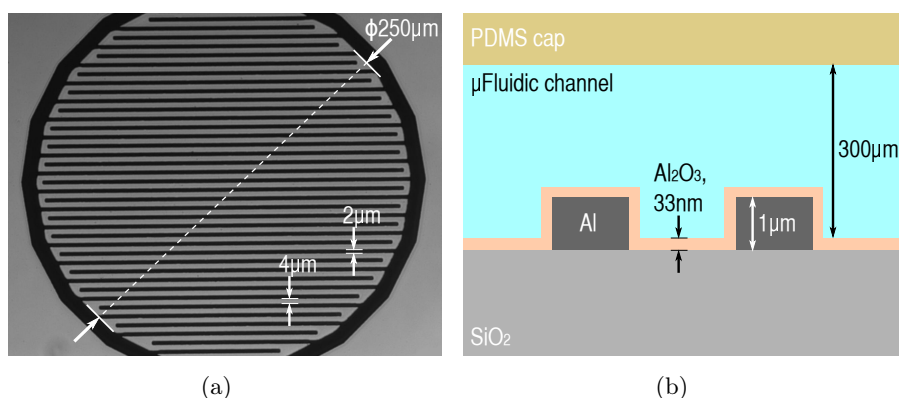


Figure 2.3 – (a) Sensor microphotograph and (b) schematic cross-section (not at scale) of the encapsulated sensor.

2.2.2 Behavior in simple electrolyte

In this section, the analytical model of the microelectrodes immersed in electrolyte is first established to provide a physical understanding of the sensor, before discussing subsequent experimental results. All used parameters and notations are provided in Table 2.2.

Analytical model

The AC device behavior is represented by a system of linear capacitors and resistors, whose key part resides in the series combination of C_{ins} , C_{DL} , and the parallel association of R_{sol} and C_{sol} (Fig. 2.4(a)). It is also usual to place C_{sol} in parallel to the series combination of C_{DL} and R_{sol} [145], but this does not change the global complex impedance at electrolyte conductivities larger than 1 mS/m. Since the interface is non-faradaic, Warburg impedance and charge-transfer resistance can be neglected [177]. Expressions of the surface capacitances can be simplified by the capacitance formula between two-parallel plate conductors:

$$C_{ins} \simeq \frac{\varepsilon_0 \varepsilon_{r,ins}}{t_{ins}} \cdot (N_e - 1) A_e \quad (2.8)$$

$$C_{DL} \simeq \frac{\varepsilon_0 \varepsilon_{r,sol}}{\lambda_D} \cdot (N_e - 1) A_e \quad (2.9)$$

where t_{ins} is the insulator thickness, $\varepsilon_{r,ins}$ the insulator relative permittivity, $\varepsilon_{r,sol}$ the electrolyte relative permittivity, $A_e \simeq (t_e + \frac{w_e}{2}) \cdot L_e$ the electrode area, N_e the total number of electrodes and λ_D the Debye length whose expression is given by Eq. 2.4. All relative permittivities are assumed frequency-independent since the model operates below 1 GHz (see Appendix D.2 for justification). The electric field inside the double layer (DL) is assumed sufficiently small ($< 10^7$ V/m) to keep the DL relative permittivity identical to $\varepsilon_{r,sol}$ [192]. Based on values given in Table 2.2, $\lambda_D \simeq 24$ nm and $C_{DL}/C_{ins} \simeq \frac{t_{ins}}{\lambda_D} \cdot \frac{\varepsilon_{r,sol}}{\varepsilon_{r,ins}} \simeq 12$ so that the insulator capacitance C_{ins} dominates in series with C_{DL} . The DL is then screened by the insulator layer for all $C_{ions} > 0.16$ mM, since λ_D decreases at higher ionic strength making C_{DL}/C_{ins} larger than 12. The medium conductance $G_{sol} \triangleq R_{sol}^{-1}$ and capacitance C_{sol} can be expressed as the sum of the capacitance between parallel conductors of thickness

Table 2.2 – Physical parameters used for the equivalent electrical model. PBS 1:1000 is considered for the electrolyte and Al/Al₂O₃ microelectrodes for the IDEs.

	Symbols	Descriptions	Values	Units
Box	$\varepsilon_{r,ox}$	Oxide relative permittivity	3.9	-
	C_{ox}	Oxide capacitance	-	F
Insulator	t_{ins}	Insulator thickness	33 nm	m
	$\varepsilon_{r,ins}$	Insulator relative permittivity	9	-
	C_{ins}	Insulator capacitance	-	F
	C_{ins}^{lat}	Lateral insulator capacitance	-	F
Electrode	L_e	Electrode length	250 μm	m
	w_e	Electrode width	2 μm	m
	t_e	Electrode thickness	1 μm	m
	d_e	Electrode gap	4 μm	m
	N_e	Total number of electrodes	39	-
	A_e	Electrode surface area	-	m ²
Electrolyte	C_{ions}	Electrolyte ionic strength	0.16 mM	M
	$\varepsilon_{r,sol}$	Electrolyte relative permittivity	80	-
	σ_{sol}	Electrolyte conductivity	1.8 mS/m	S/m
	λ_D	Debye length	-	m
	$C_{sol} - R_{sol}$	Electrolyte capac. and resistance	-	F- Ω
	C_{DL}	Double layer capacitance	-	F

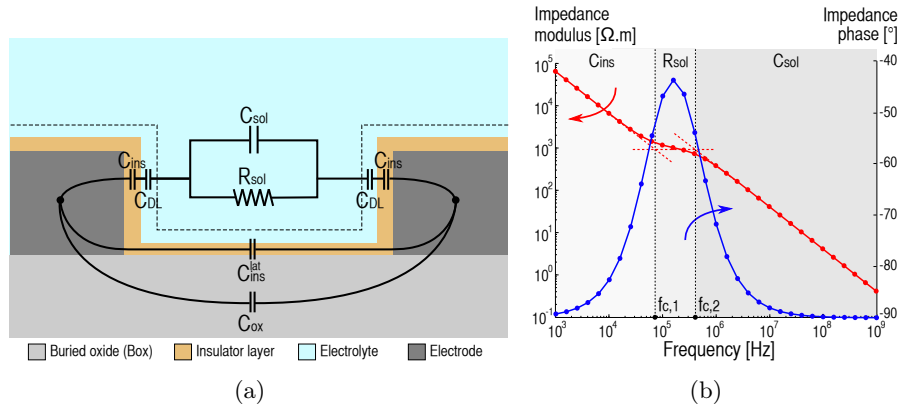


Figure 2.4 – Device in contact with simple electrolyte: (a) schematic representation (not at scale) of the equivalent model with lumped elements and (b) Bode diagrams of the impedance based on the analytical model given in (a).

t_e and the planar capacitance between half electrodes of width $w_e/2$:

$$C_{sol} \simeq \frac{\varepsilon_0 \varepsilon_{r,sol}}{d_e} \cdot (N_e - 1) A_e G \quad (2.10)$$

$$G_{sol} \simeq \frac{\sigma_{sol}}{d_e} \cdot (N_e - 1) A_e G \quad (2.11)$$

where $G \triangleq \frac{t_e + d_e \cdot K(\sqrt{1-k^2}) / (2K(k))}{t_e + w_e/2}$ is a geometric constant with parameters $k \triangleq \cos(\frac{\pi}{2} \cdot \frac{w_e}{d_e + w_e})$ and $K(k) \triangleq \int_{t=0}^{t=1} \frac{dt}{\sqrt{(1-t^2)(1-k^2t^2)}}$ given in [179]. For the electrode geometry given in Table 2.2, the constant G is equal to 1.28. Based on Eq. 2.8 to 2.11 and on the fact that C_{DL} is screened by C_{ins} , the system is characterized by two cutoff frequencies (Fig. 2.4(b)):

$$f_{c,1} = \frac{1}{2\pi \cdot R_{sol}(C_{ins}/2)} \simeq \frac{1}{\pi} \cdot \frac{t_{ins}}{d_e} \cdot \frac{\sigma_{sol}}{\varepsilon_0 \varepsilon_{r,ins}} \cdot G \quad (2.12)$$

$$f_{c,2} = \frac{1}{2\pi \cdot R_{sol} C_{sol}} \simeq \frac{1}{2\pi} \cdot \frac{\sigma_{sol}}{\varepsilon_0 \varepsilon_{r,sol}} \quad (2.13)$$

In parallel to the impedance formed by C_{ins} , C_{DL} , C_{sol} and R_{sol} , the system also comprises the oxide capacitance C_{ox} and lateral insulator capacitance C_{ins}^{lat} .

$$C_{ox} \simeq \varepsilon_0 \varepsilon_{r,ox} \cdot \frac{K(\sqrt{1-k^2})}{2K(k)} \cdot (N_e - 1) L_e \quad (2.14)$$

$$C_{ins}^{lat} \simeq \frac{\varepsilon_0 \varepsilon_{r,ins}}{d_e} \cdot (N_e - 1) t_{ins} L_e \quad (2.15)$$

The lateral insulator capacitance C_{ins}^{lat} can be neglected in parallel, since $C_{ox}/C_{ins}^{lat} = \frac{\varepsilon_{r,ox}}{\varepsilon_{r,ins}} \cdot \frac{d_e}{t_{ins}} \cdot \frac{K(\sqrt{1-k^2})}{2K(k)} \approx 20.5$. At $f < f_{c,1}$, the impedance is dominated by $(C_{ins}/2)$ and the oxide capacitance C_{ox} can be neglected in parallel since $C_{ox} \simeq 0.003 \cdot C_{ins}$. At frequencies larger than $f_{c,2}$, the capacitance C_{sol} dominates and $C_{ox} \simeq 0.03 \cdot C_{sol}$ is sufficiently small compared to C_{sol} for being neglected in parallel. Between $f_{c,1}$ and $f_{c,2}$, the impedance is governed by R_{sol} and C_{ox} can again be neglected at such frequencies, since $f < f_{c,2} = \frac{1}{2\pi \cdot R_{sol} C_{sol}} \ll \frac{1}{2\pi \cdot R_{sol} C_{ox}}$. In conclusion, C_{ox} can always be neglected and the frequency must be larger than $f_{c,1}$ to sense volume properties (R_{sol} , C_{sol}) instead of surface properties (C_{ins}). Also, $f_{c,1}$ and $f_{c,2}$ both depend on the electrolyte conductivity, but not their ratio:

$$\frac{f_{c,2}}{f_{c,1}} \simeq \frac{1}{2} \cdot \frac{\varepsilon_{r,ins}}{\varepsilon_{r,sol}} \cdot \frac{d_e}{t_{ins}} \cdot \frac{1}{G} \quad (2.16)$$

To achieve a predominance of the resistive level R_{sol} between $f_{c,1}$ and $f_{c,2}$, i.e. a larger $f_{c,2}/f_{c,1}$ ratio, the electrode gap d_e and the insulator thickness t_{ins} must be enlarged and reduced, respectively. For low-salt buffers such as phosphate buffered saline (PBS) diluted 1:1000 by volume in deionized (DI) water and characterized by $\sigma_{sol} = 1.8$ mS/m, typical values are $f_{c,1} = 76$ kHz, $f_{c,2} = 405$ kHz and $f_{c,2}/f_{c,1} = 5.3$. For high-conductive saline buffers such as pure PBS with $\sigma_{sol} = 1.8$ S/m, the cutoff frequencies are three orders of magnitude larger, i.e., $f_{c,1} = 76$ MHz and $f_{c,2} = 405$ MHz, but their ratio is kept unchanged. Depending on the required range of frequency set by the electrical readout and target application (surface versus volume sensing), an electrolyte with an appropriate conductivity must be chosen. Also, d_e and t_{ins} must be chosen for a suitable $f_{c,1}$.

Matching between experimental data and analytical model

For experimental measurements in following paragraphs, the setup used is described in Appendix A.5. When considering PBS 1:1000 as indicated for the analytical model in Table 2.2, the experimental normalized admittance $\|Y/\omega\|$ and impedance phase θ_Z show good fitting with the analytical models, especially at frequencies larger than 10 kHz (Fig. 2.5). The factor used to link 2D and 3D $\|Y/\omega\|$ values is $K \triangleq \frac{\|Y/\omega\|_{exp}}{\|Y/\omega\|_{sim}} = 7.21$ mm, evaluated at 1 MHz and very close to the theoretical value of the total electrode length $L_e \cdot (N_{eff} - 1) \simeq 7.25$ mm, where $N_{eff} \triangleq \left(1 + 2 \sum_{i=1}^{(N_e-1)/2} \sqrt{1 - \left(\frac{2i}{N_e-1}\right)^2}\right) \simeq 30$ is the effective number of electrodes of length L_e in the circularly shaped IDE. The 28-% drop of $\|Y/\omega\|$ at LF and the phase bump around 10 kHz comes from metal accesses, as detailed in next paragraphs. The transition $\frac{C_{ins}}{2} \rightarrow \frac{G_{sol}}{\omega} \rightarrow C_{sol}$, mentioned in the previous paragraph, is clearly observable and similar to that reported in [190] and to the $\frac{C_{DL}}{2} \rightarrow \frac{G_{sol}}{\omega} \rightarrow C_{sol}$ transition of unpassivated electrodes simulated in [189].

Dry versus immersed sensor

The sensor impedance strongly depends on the medium phase (gas or liquid). For air ($\varepsilon_{r,sol} = 1$ and $\sigma_{sol} \simeq 5 \cdot 10^{-15}$ S/m), the impedance phase remains around -90° between 1 kHz and 1 MHz, with discrepancies between 100 Hz and 1 kHz because $\|Z\|$ exceeds the LCR intrinsic limit of 1 G Ω (Fig. 2.6). The complex impedance is thus mostly capacitive

and dominated by the parallel association of C_{ox} and the small $C_{sol} \propto \varepsilon_{r,sol}$, since C_{ins} can be neglected because $f_{c,1} \simeq 0.2 \mu\text{Hz}$.

When immersed in DI water ($\varepsilon_{r,sol} = 80$ and $\sigma_{sol} \simeq 50 \mu\text{S/m}$), the complex impedance is similar to the one in PBS 1:1000 (see Fig. 2.5) since only σ_{sol} is modified. Compared to the air, the impedance modulus in DI water is one to two orders of magnitude smaller because of the

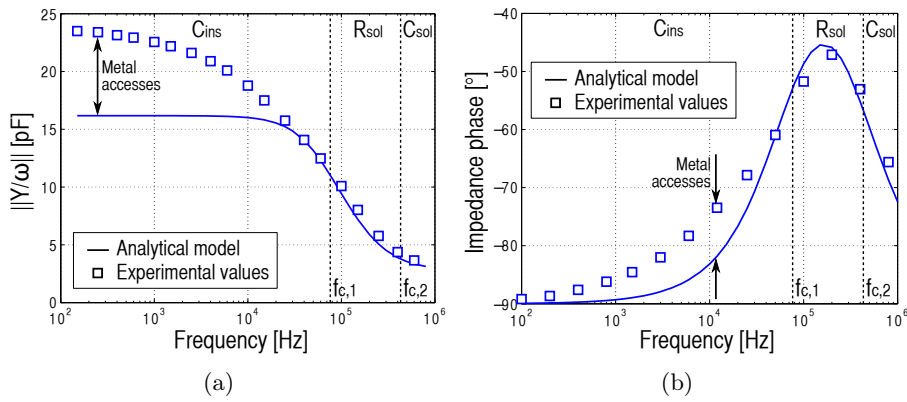


Figure 2.5 – Comparison between experimental measurements and the analytical model in PBS 1:1000 for (a) the normalized admittance $\|Y/\omega\|$ and for (b) the impedance phase θ_Z . The factor K between 2D and 3D is equal to 7.21 mm.

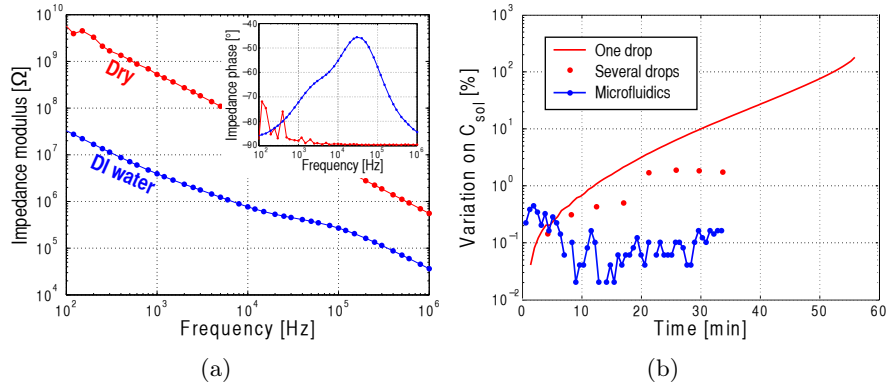


Figure 2.6 – (a) Experimental impedance modulus and phase of a rectangular IDE in dry condition and with DI water. (b) Experimental temporal variation of C_{sol} extracted at 1 MHz when one 5- μL drop of DI water is deposited, several 5- μL drops are successively pipetted every ~ 5 min and continuous flow is applied through a microfluidic channel.

larger $C_{sol} \propto \varepsilon_{r,sol}$ value and the dominance of C_{ins} at LF. As shown in Fig. 2.6(b), the sensor is more or less subject to liquid evaporation, depending on the immersion method. When a single $5\text{-}\mu\text{L}$ drop is pipetted atop the sensor surface, the temporal drift on C_{sol} is exponential and reaches 10% after 30 minutes. In contrast, pipetting several $5\text{-}\mu\text{L}$ drops every 5 minutes limits the error to 2%, while a continuous microfluidic flow suppresses temporal drifts, as only noise of 0.1% is measured.

Impact of the metallic connections to IDEs

Metallic accesses contact the IDEs to electrical pads, located outside the microfluidic channel. When they are parallel to each other (Fig. 2.7(a)), access lines can couple to each other, decrease the LF impedance modulus by 60% and add a cutoff frequency around 1 kHz (Fig. 2.7(b)).

To explain this effect, metal accesses are modeled with two equivalent electrical circuits (Fig. 2.7(a)). On one hand, the part covered with a passivation layer such as KMPR photoresist (see Appendix A.1) for sealing and electrical isolation from the electrolyte results in a passivation capacitance C_{pass} . The large distance between tracks and the small permittivity of the passivation material makes C_{pass} dominating in series with $C_{ins,p} \gg C_{pass}$ and then being neglected in parallel with C_{ins} ,

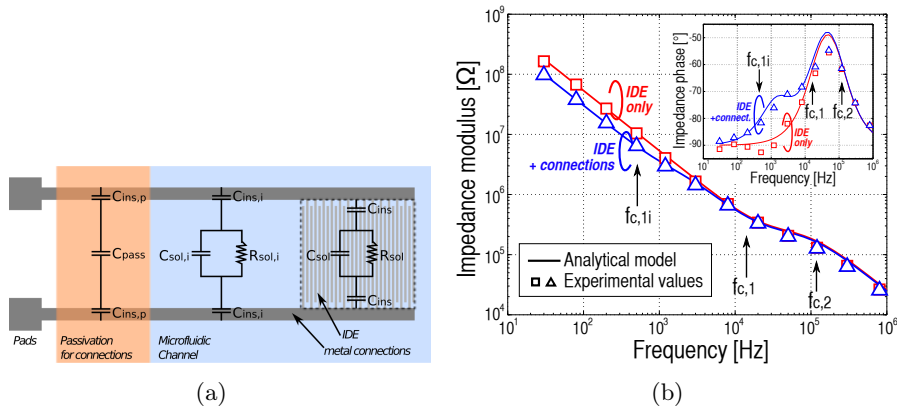


Figure 2.7 – Impact of access lines: (a) schematic top view (not at scale) of the metal connections to the rectangular IDE and (b) comparison between experimental and analytical values of $\|Z\|$ and θ_Z . The impedance analyzer has been calibrated with electrical probes positioned in the air (IDE + connections), or positioned on an open structure having the same access lines as the IDE structure (IDE only).

G_{sol} or C_{sol} . On the other hand, the unpassivated area has a similar equivalent circuit with $C_{ins,i}$, $R_{sol,i}$ and $C_{sol,i}$ as the IDE (Fig. 2.7(a)). Because the distance between access lines is significantly larger than the electrode gap ($\sim 250 \mu\text{m}$ versus $4 \mu\text{m}$), $G_{sol,i} \triangleq R_{sol,i}^{-1}$ and $C_{sol,i}$ are two orders of magnitude smaller than $G_{sol} \triangleq R_{sol}^{-1}$ and C_{sol} , respectively. The cutoff frequency $f_{c,1i} = \frac{1}{2\pi R_{sol,i}(C_{ins,i}/2)}$ is thus two orders of magnitude smaller than $f_{c,1}$ and explains the shape change of the impedance phase around 1 kHz in Fig. 2.7(b). Because $f_{c,1i} < f < f_{c,1}$, the inequality $\omega C_{ins} < 2 \cdot G_{sol,i} < \omega C_{ins,i}$ holds and explains why $R_{sol,i}$ dominates ($C_{ins,i}/2$) in series and ($C_{ins}/2$) in parallel, resulting in a more resistive behavior of the impedance. Below $f_{c,1i}$, the impedance is given by the parallel association of $C_{ins,i}$ and C_{ins} , explaining the larger capacitance due to access lines. At $f > f_{c,1}$, the impact of access lines is considerably reduced because R_{sol} and C_{sol} largely dominate in parallel their counterparts $R_{sol,i}$ and $C_{sol,i}$, both two orders of magnitude smaller, respectively.

Impact of the electrolyte conductivity

Tenfold dilutions of pure PBS in DI water present ionic strengths ranging from $16 \mu\text{M}$ to 160 mM , characterized σ_{sol} from $180 \mu\text{S/m}$ to 1.8 S/m and identical $\varepsilon_{r,sol}$ as DI water. When pipetted atop the sensor, these solutions induce resistive levels R_{sol} inversely proportional to σ_{sol} (Fig.

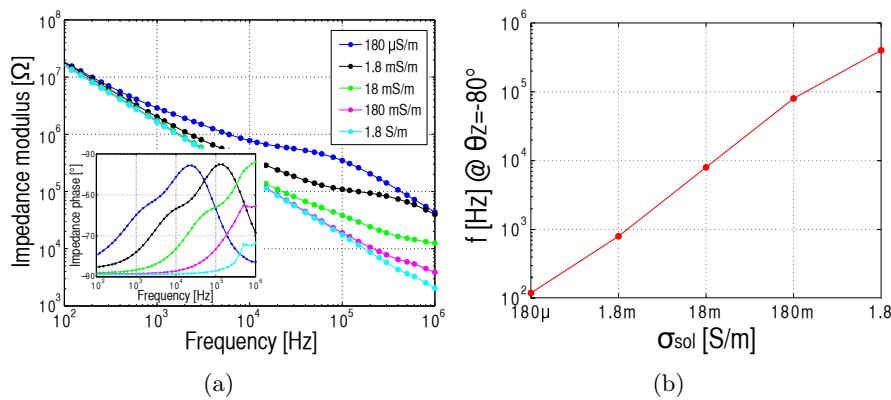


Figure 2.8 – (a) Experimental impedance modulus and phase of the circularly shaped IDE in successive PBS dilutions featuring different σ_{sol} . (b) Evolution of the measured frequency at which $\theta_Z = -80^\circ$ with the electrolyte conductivity σ_{sol} .

2.8(a)), as expected from Eq. 2.11. Similarly, the frequency shift at the phase equal to -80° , evolving as $f_{c,1}$ and $f_{c,2}$, increases linearly with σ_{sol} (Fig. 2.8(b)), as expected from Eqs. 2.12 and 2.13. At sufficiently HF which is only visible for $\sigma_{sol} \leq 1.8$ mS/m in Fig. 2.8(a), the dominant capacitance is insensitive to σ_{sol} while the capacitance at LF slightly depends on σ_{sol} through the contribution of C_{DL} (see Eq. 2.9).

Impact of the electrolyte permittivity

Four solutions listed in Table 2.3 with different $\varepsilon_{r,sol}$ and small σ_{sol} are applied atop the sensor. As expected from Eq. 2.10, C_{sol} extracted at 1 MHz linearly varies with $\varepsilon_{r,sol}$ (Fig. 2.9(b)), while R_{sol} confirms its inverse proportionality to σ_{sol} . At LF, the complex impedance is less subject to variation of $\varepsilon_{r,sol}$ because of the screening from the insulator layer.

Table 2.3 – Physical properties of the solutions under test.

Solutions	$\varepsilon_{r,sol}$	σ_{sol}
IPA	18	6 $\mu\text{S}/\text{m}$
Acetone	21	20 $\mu\text{S}/\text{m}$
Methanol	33	30 $\mu\text{S}/\text{m}$
Aqua ad iniectionabilia (AAI)	80	150 $\mu\text{S}/\text{m}$

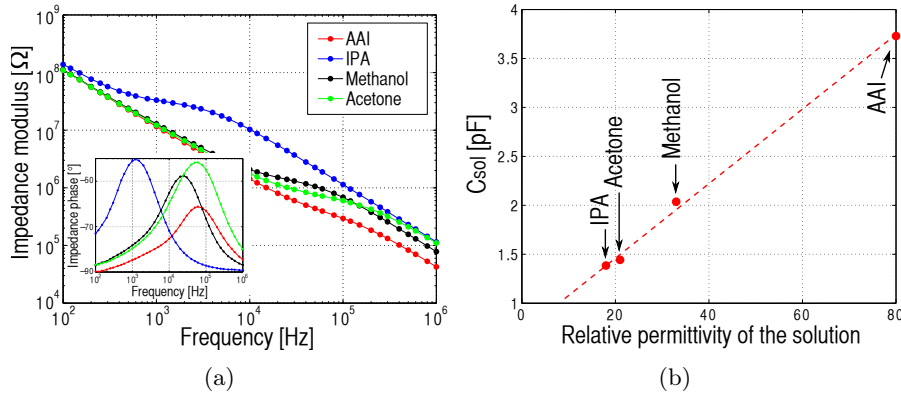


Figure 2.9 – (a) Experimental impedance modulus and phase of the circularly shaped IDE in four solutions of different $\varepsilon_{r,sol}$ and σ_{sol} and (b) the related evolution of the solution capacitance C_{sol} at 1 MHz with $\varepsilon_{r,sol}$.

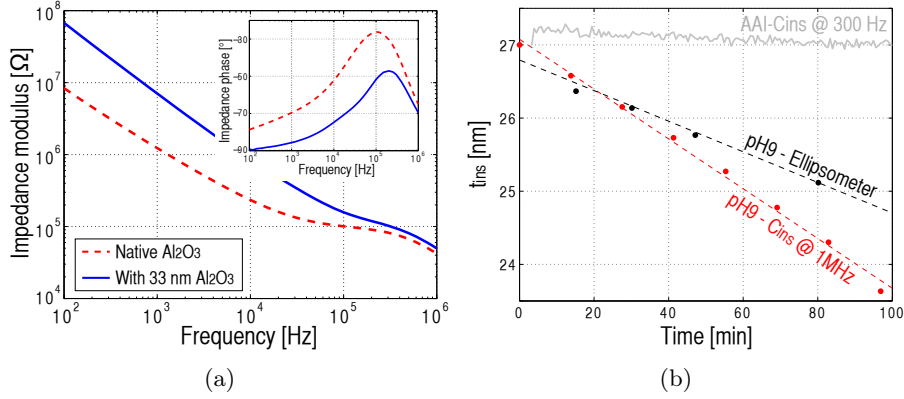


Figure 2.10 – (a) Experimental impedance modulus and phase of a circularly shaped IDE in PBS 1:1000 with native Al₂O₃ and 33-nm thick Al₂O₃ deposited by ALD. (b) Experimental temporal evolution of t_{ins} in pH9 solution containing boric acid, comparing impedimetric and ellipsometer measurements. A control with non-corrosive AAI solution is provided ($\Delta t_{ins} \simeq 0$ as checked by ellipsometry).

Impact of the insulating layer

When increasing the insulator thickness (t_{ins}), the LF capacitance strongly decreases (Fig. 2.10(a)) since C_{DL} becomes screened by the smaller capacitance C_{ins} in series. The LF impedance modulus of the natively oxidized IDE ($t_{ins} \simeq 4$ nm) features measured values ca. 8 times smaller compared to the one with 33 nm of Al₂O₃, which corresponds to the ratio between respective thicknesses. In addition, the resistive level is more apparent because $f_{c,1} \propto t_{ins}$ is more separated from $f_{c,2}$, which is also highlighted by the higher impedance phase (-27° versus -47°) of the native Al₂O₃ layer. At 1 MHz, the slight decrease of the capacitance with larger insulator thicknesses (Fig. 2.10(a)) arises because of the larger contribution of $C_{ins} \propto t_{ins}^{-1}$ in series with C_{sol} .

In the case of most biological buffers, Al₂O₃ withstands electrochemical corrosion when immersed during several hours. However, it has been demonstrated that the Al₂O₃ layer is strongly degraded after an immersion of several days [161]. To describe and analyze this possible etching effect on the sensor response, real-time variations of t_{ins} caused by an etchant consisting of a pH 9 solution containing boric acid H₃BO₃ ($\sigma_{sol} \simeq 0.8$ S/m) has been monitored at LF, where C_{ins} dominates. An etch rate of 0.19 Å/min of an 27-nm thick ALD-Al₂O₃ layer immersed in the etchant is characterized by ellipsometry (Fig. 2.10(b)), while impedance measurements at 1 MHz (C_{ins} dominates because of the large

σ_{sol}) of the capacitive biosensor in a microfluidic channel gives approximately of 0.34 Å/min. In comparison, the control of the impedance at 300 Hz with AAI (C_{ins} dominates because $\sigma_{sol} \simeq 150 \mu\text{S/m}$) did not show any etching. The faster etching rate as monitored electrically comes probably from the microfluidic flow which adds shear forces and permanently renews the etchant.

Impact of the sensor geometry

Several IDEs with different gap d_e and sensor area have been measured in DI water. All lumped elements C_{ins} , R_{sol} and C_{sol} present strong variations with d_e and A_e . In particular, C_{sol}^{-1} features an almost linear dependence with d_e (Fig. 2.11(a)), as expected from Eq. 2.10 because the related decrease of N_e is compensated by a slight increase of G . On the other hand, C_{sol} linearly increases with the sensor area (Fig. 2.11(b)), which is assimilated to $(N_e - 1)A_e$ in Eq. 2.10.

Transient effects

Considering transient transitions between high- and low-conductive solutions, the time for reaching the equilibrium depends on (Fig. 2.12(a)):

- *The kind of transition:* the sensor recovers more quickly an equilibrium value when σ_{sol} increases (i.e. AAI \rightarrow PBS), than the inverse. A factor 2 of difference is observed between the maximal capacitance slope of the two transitions (Fig. 2.12(b)). This can be interpreted by the easiest way to bring ions instead of removing them through a microfluidic flow, whose speed is almost zero at the oxide-electrolyte interface.
- *The flow rate:* renewing a larger volume per minute enables to quicker remove or bring ions uniformly in the microfluidic channel. When the flow rate increases, the capacitance slope is larger (Fig. 2.12(b)) and the transient phase shorter.
- *The frequency:* C_{ins} , R_{sol} and C_{sol} are not equally sensitive to change of σ_{sol} . When PBS is replaced by AAI at 1 MHz, a transition occurs from C_{ins} to C_{sol} , which is almost independent on σ_{sol} , explaining the fast transition (Fig. 2.12(a)). In contrast, the transition at 100 kHz lasts longer because R_{sol} is very sensitive to remaining ions at the electrode surface and in the tube volume, where undesirable diffusive mixing occurs between AAI and PBS.

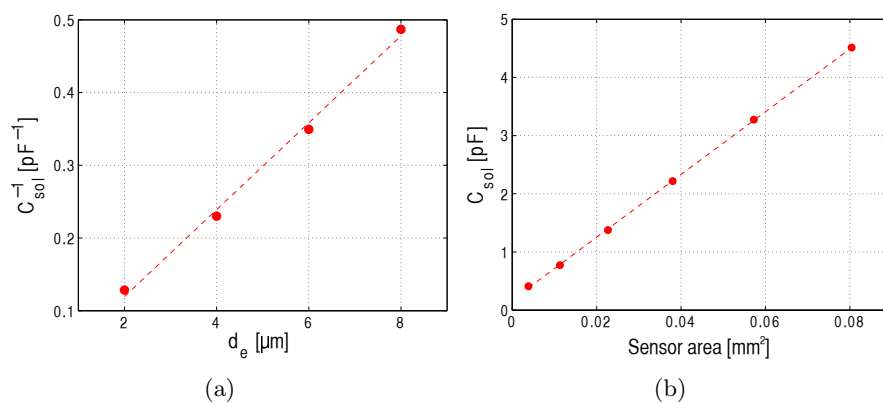


Figure 2.11 – Experimental variation of C_{sol} extracted at 1 MHz in DI water with (a) the electrode gap d_e for rectangular IDEs at fixed area and (b) the total area of the circularly shaped IDEs at fixed electrode gap.

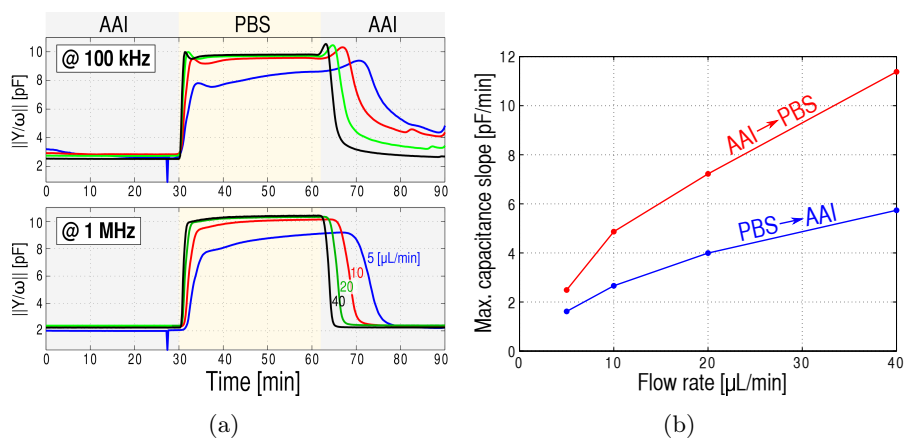


Figure 2.12 – (a) Experimental real-time monitoring of $\|Y/\omega\|$ at 100 kHz and 1 MHz highlighting transitions between AAI, PBS and AAI at different flow rates. (b) The maximal capacitance slopes at 1 MHz versus the flow rate for the transitions AAI → PBS and PBS → AAI.

2.2.3 Behavior in electrolyte with bacterial cells

In this section, an analytical model of the IDE with adherent bacteria is established. Experimental results are then described.

Analytical model

Bacterial cells are composed of several outer shells, two for Gram-positive bacteria and three for Gram-negative bacteria. In this thesis, we mainly focus on Gram-positive bacteria since *S. epidermidis* was used as the reference strain in the experimental procedure. Conclusions can be extended to Gram-negative bacteria since their outer membranes feature similar dielectric properties and thicknesses as plasma membranes (see *Escherichia coli* model in [30]), so that both membranes can be grouped together in one equivalent shell to obtain a similar morphology as Gram-positive bacteria. A multi-shell representation is considered to account for the cytoplasm, plasma membrane and cell wall (Fig. 2.13(a)) whose dielectric values are given in Table 2.4. Because of its ion-penetrability [193], the bacterial cell wall conductivity is proportional to the electrolyte one, i.e. $\sigma_{wall} \simeq 0.4 \cdot \sigma_{sol}$ [194].

The impedance of bacteria is characterized by four cutoff frequencies. The first results from the series connection between C_{pl} and R_{wall} , while the second from the parallel association between R_{wall} and C_{wall} (Fig. 2.13(a)). These cutoff frequencies have little impact on the complex impedance because they express the slight transition between C_{pl} and $C_{out}^* = (C_{pl}^{-1} + C_{wall}^{-1})^{-1}$, formed by the series association of C_{wall} and C_{pl} . The spectrum is thus simplified by the two other cutoff frequencies:

$$f_{cb,1} = \frac{1}{2\pi \cdot R_{cyt}(C_{out}^*/2)} \simeq \frac{1}{\pi} \cdot \frac{(t_{pl} + t_{wall}) \cdot \sigma_{cyt}}{d_{cyt} \cdot \varepsilon_0 \varepsilon_{r,out}^*} \quad (2.17)$$

$$f_{cb,2} = \frac{1}{2\pi \cdot R_{cyt} C_{cyt}} \simeq \frac{1}{2\pi} \cdot \frac{\sigma_{cyt}}{\varepsilon_0 \varepsilon_{r,cyt}} \quad (2.18)$$

where the equivalent relative permittivity of outer shells is $\varepsilon_{r,out}^* = t_{out}^* \cdot \left(\frac{t_{wall}}{\varepsilon_{r,wall}} + \frac{t_{pl}}{\varepsilon_{r,pl}}\right)^{-1} \simeq 34$ with $t_{out}^* \triangleq t_{pl} + t_{wall}$. These cutoff frequencies strongly depend on the bacterial dielectric properties, and therefore on the species. For *Staphylococcus* spp. (Table 2.4), $f_{cb,1}$ and $f_{cb,2}$ are approximately equal to 23 MHz and 200 MHz, respectively. At relatively low frequencies ($f < f_{cb,1}$), the bacterial cell behaves as a large capacitance (C_{pl} or C_{out}^*). However, at larger frequencies, the cytoplasm dominates either in a resistive (R_{cyt}) or a capacitive (C_{cyt}) way.

Table 2.4 – Physical parameters used for the electrical model of the bacterial cell, from the *Staphylococcus* spp. model parameters [30].

Symbols	Descriptions	Values	Units
d_{bact}	Bacterial diameter	1.2 μm	m
d_{cyt}	Cytoplasm diameter	1.2 μm	m
t_{pl}	Plasma thickness	8 nm	m
t_{wall}	Cell wall thickness	20 nm	m
$\varepsilon_{r, cyt}$	Cytoplasm relative permittivity	70	-
$\varepsilon_{r, pl}$	Plasma relative permittivity	16	-
$\varepsilon_{r, wall}$	Cell wall relative permittivity	60	-
σ_{cyt}	Cytoplasm conductivity	0.8	S/m
σ_{wall}	Cell wall conductivity	-	S/m
C_{pl}	Plasma capacitance	-	F
$C_{cyt} - R_{cyt}$	Cytoplasm capac. and resistance	-	F- Ω
$C_{wall} - R_{wall}$	Cell wall capac. and resistance	-	F- Ω
Z_{bact}	Bacterial impedance	-	Ω

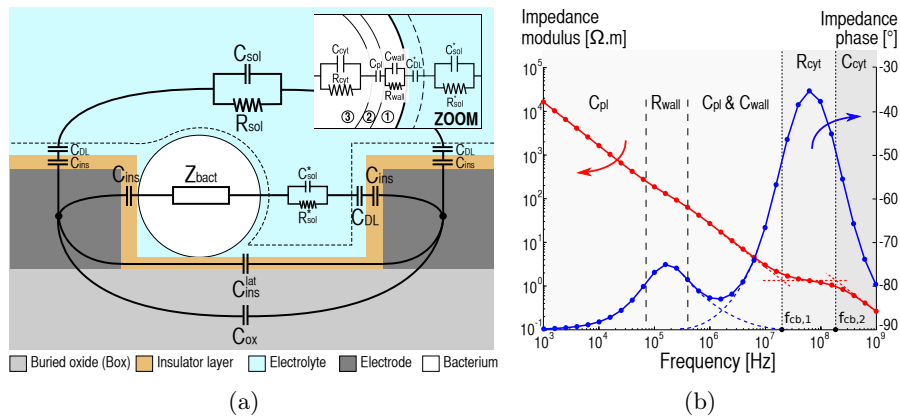


Figure 2.13 – Sensor in contact to the electrolyte with bacteria: (a) schematic representation (not at scale) of the equivalent model with lumped elements, including a zoom where 1,2 and 3 refer to the bacterial cell wall, plasma membrane and cytoplasm, respectively, and (b) Bode diagrams of the bacterial complex impedance.

When we consider both the bacterial cell and the electrolyte, the four main cutoff frequencies must be ordered to understand bacterial effect on the global impedance. In low-conductive buffers ($\sigma_{sol} = 1.8$ mS/m), the order is the following: $f_{c,1} < f_{c,2} < f_{cb,1} < f_{cb,2}$. Below $f_{c,1} \approx 76$ kHz, the impedance is hardly impacted by the bacterial cell since the insulating layer screens both the DL and volume properties. However, large values of C_{pl} , R_{wall} and C_{out}^* can still slightly modify the sensor impedance dominated by C_{ins} . Between $f_{c,1}$ and $f_{c,2}$, the conductive path through electrolyte (R_{sol}) is shortened by the large bacterial capacitance C_{pl} or C_{out}^* , so that the overall volume resistance decreases. For $f_{c,2} < f < f_{cb,1}$, the volume capacitance increases since the capacitive path through the electrolyte is reduced by the large bacterial capacitance C_{out}^* . For $f_{cb,1} < f < f_{cb,2}$, the overall capacitance increases for the same reasons, due to the short circuit behavior of the bacteria cell at these frequencies ($f < f_{cb,2} < \frac{1}{2\pi R_{cyt} C_{sol}}$). Finally, at frequencies larger than $f_{cb,2}$, the overall capacitance decreases since $\varepsilon_{r,cyt} < \varepsilon_{r,sol}$.

For high-conductive buffers such as PBS ($\sigma_{sol} = 1.8$ S/m), the order is different: $f_{cb,1} < f_{c,1} < f_{cb,2} < f_{c,2}$. Again, below $f_{c,1} \approx 76$ MHz, the impedance is hardly impacted by bacteria. Between $f_{c,1}$ and $f_{cb,2}$, bacteria feature a resistive behavior that increases the whole medium resistance since $\sigma_{cyt} < \sigma_{sol}$. At frequencies larger than $f_{cb,2}$, the bacterial capacitive behavior still increases the overall impedance, but by reducing the medium capacitance at $f > f_{c,2}$ since $\varepsilon_{r,cyt} < \varepsilon_{r,sol}$.

The sensitivity to adherent bacterial cells is defined as the relative variation of $\|Y/\omega\|$, in percent:

$$S(\omega) = \left| \frac{\|Y_1(\omega)\| - \|Y_0(\omega)\|}{\|Y_0(\omega)\|} \right| \quad (2.19)$$

where $Y_0(\omega)$ and $Y_1(\omega)$ are the initial and final admittances, before and after bacterial binding, respectively. The maximal sensitivity is defined as $S_{max} = \max_{\omega}\{S(\omega)\}$ and can be used to compare two different conditions independently of ω . To analytically estimate the 2D maximal sensitivity S_{max}^{2D} at $\sigma_{sol} = 1.8$ mS/m, several assumptions are used:

- The optimal frequency f where S_{max}^{2D} is achieved is assumed one order of magnitude larger than $f_{c,2}$, where C_{sol} and C_{ins} dominates (see next sections for justification). When the sensor is free of bacteria, the initial medium capacitance $C_{sol,0}$ is given by Eq. 2.10.
- To estimate the solution capacitance $C_{sol,1}$ in presence of the bacteria, the N_e semi-planar electrodes are each simplified to per-

fect parallel conductors of thickness $(t_e + w_e/2) \cdot G$, gap d_e and length L_e , thus giving the same initial capacitance as Eq. 2.10. Furthermore, the bacterium is simplified by a square box of side $d_{eq} \triangleq (d_{bact} \cdot \sqrt{\pi}/2)$, featuring the same area as spherical bacteria. At the optimal frequency, C_{out}^* dominates the bacterial impedance and the resulting medium capacitance is $C_{sol,1} \simeq \frac{\varepsilon_0 \varepsilon_{r,sol}}{d_e} \cdot (N_e - 1) A_e \cdot (G + P)$, with $P \triangleq \frac{d_{eq}}{t_e + w_e/2} \cdot \frac{1 - 2T}{d_e/d_{eq} - 1 + 2T}$ with $T \triangleq \frac{t_{out}^*}{d_e} \cdot \frac{\varepsilon_{sol}}{\varepsilon_{out}^*} \cdot \frac{d_e}{d_{eq}}$. The complete development is available in Appendix C.1.

The following formula are then obtained for the initial and final admittances: $Y_0(\omega) \simeq j\omega \cdot (2C_{ins}^{-1} + C_{sol,0}^{-1})^{-1}$ and $Y_1(\omega) \simeq j\omega \cdot (2C_{ins}^{-1} + C_{sol,1}^{-1})^{-1}$. Consequently, the maximal sensitivity is approximated to:

$$S_{max}^{2D} \simeq \frac{C_{sol,0}^{-1} - C_{sol,1}^{-1}}{2C_{ins}^{-1} + C_{sol,1}^{-1}} \quad (2.20)$$

$$\simeq \frac{P}{G} \cdot \frac{1}{1 + 2 \cdot \frac{G+P}{Q}} \quad (2.21)$$

with $Q \triangleq \frac{\varepsilon_{r,ins}}{\varepsilon_{r,sol}} \cdot \frac{d_e}{t_{ins}}$. Based on Table 2.2 and 2.4, $G \simeq 1.28$, $T \simeq 0.06$, $P \simeq 0.17$, $Q = 13.6$ and the maximal sensitivity S_{max}^{2D} is equal to 11.2%. In reality, the bacterial cytoplasm resistance never perfectly shortens the sensor capacitance, so that σ_{sol} , $\varepsilon_{r,cyt}$, σ_{cyt} , $\varepsilon_{r,wall}$, σ_{wall} , $\varepsilon_{r,pl}$, σ_{pl} and other metric parameters can still have a slight impact.

Real-time sensing of bacteria

The protocols for the preparation of chemicals and bacterial cells are provided in Appendices A.2 and A.3, while the measurement setup is described in Appendix A.5. Suspensions from 10^6 to 10^9 CFU/mL of stationary-state *S. epidermidis* resuspended in PBS 1:1000 were then injected at 1 $\mu\text{L}/\text{min}$, each followed by a washing procedure with PBS 1:1000 during 5 min at 250 $\mu\text{L}/\text{min}$ followed by 5 min at 125 $\mu\text{L}/\text{min}$. When bacteria bind to the sensor surface, $\|Y/\omega\|$ systematically increases through three successive and different mechanisms (Fig. 2.14):

- The *conductive shift* Δ_c , immediately observed after the injection of the bacterial sample, is attributed to the slight difference of the electrical conductivity σ_{sol} between PBS 1:1000 and bacterial resuspensions in PBS 1:1000 (see Section 2.1.8). Despite its dependence on the bacterial concentration C_b , Δ_c is strongly affected by

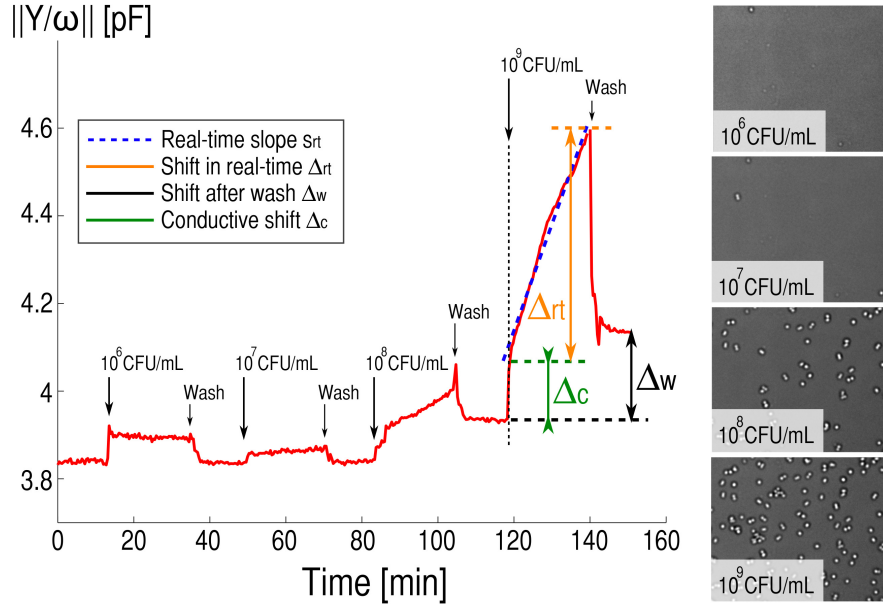


Figure 2.14 – Real time monitoring of $\|Y/\omega\|$ at 1 MHz when increasing *S. epidermidis* concentrations from 10^6 to 10^9 CFU/mL in PBS 1:1000 are flown. Wash steps correspond to flow of sterile 1:1000.

experimental procedures such as manipulation, contamination and temperature (e.g. see the artefact at 10^6 CFU/mL in Fig. 2.14). It is also useless for applications dealing with high-conductive solutions, whose σ_{sol} is hardly impacted by bacterial ion release. For these reasons, bacterial sensing based on Δ_c should be avoided.

- During the next 20 min of bacterial incubation, $\|Y/\omega\|$ continuously grows defining the *real-time slope* $s_{rt} = \frac{\partial \|Y/\omega\|}{\partial t}$ expressed in F/min (Fig. 2.14, dotted blue linear curve). As shown in Fig. 2.15, this slope is correlated to the increase of the number of adherent bacteria counted by a MATLAB[®] algorithm processing successive microscope images (see Appendix B.1). Furthermore, s_{rt} features a fairly linear dependence with the bacterial concentration (Fig. 2.16(a)). Related non-linearities either comes from the saturation of the bacterial surface coverage or from the noise floor of electrical measurements. Defined as the difference between $\|Y/\omega\|$ values after the incubation phase and after the initial conductivity peak, the *real-time shift* Δ_{rt} linearly depends on the bacterial density

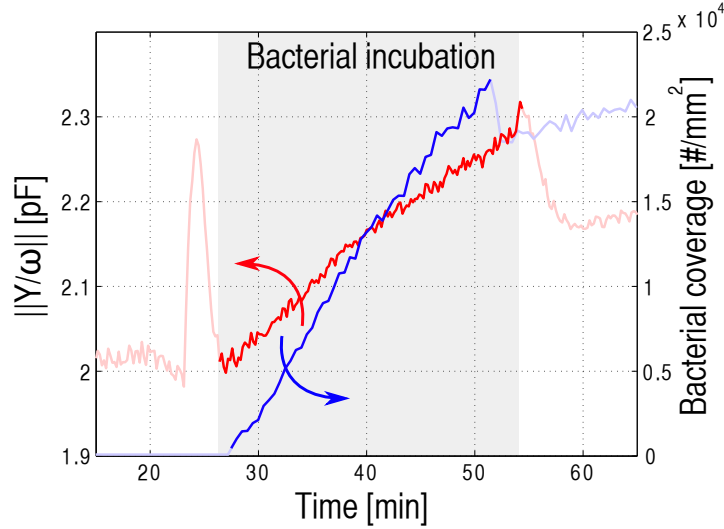


Figure 2.15 – Experimental, real-time and simultaneous electrical (at 1 MHz) and optical monitoring of 10^9 CFU/mL of *S. epidermidis* binding on circularly shaped IDEs ($w_e = 1 \mu\text{m}$).

S_b (Fig. 2.16(b)), featuring $\simeq 228$ aF per bacterium, which is a mean between adherent and non-adherent bacteria. Again however, bacterial sensing using s_{rt} and Δ_{rt} features reduced sensitivity in high-conductive samples, as discussed later.

- After washing the surface with sterile PBS 1:1000 to flush non-adherent bacteria and excessive ions away, $\|Y/\omega\|$ stabilizes at a lower equilibrium value (Fig. 2.14), since in this case only adherent bacteria modify the sensor impedance. This level minus the pre-incubation $\|Y/\omega\|$ value in sterile PBS 1:1000 defines the *shift after wash* Δ_w . A linear dependence between Δ_w and the bacterial surface coverage was experimentally evaluated to $\simeq 101$ aF per adherent bacterium (Fig. 2.16(b)). Because it is measured at equilibrium and under flow with sterile PBS 1:1000, Δ_w is not subject to ion release or contamination and purely originates from dielectric properties of bacteria. This confers high stability and reliability to measurements of Δ_w , and wash procedures can further be used with high-conductive samples. For these reasons, next discussions are only based on Δ_w .

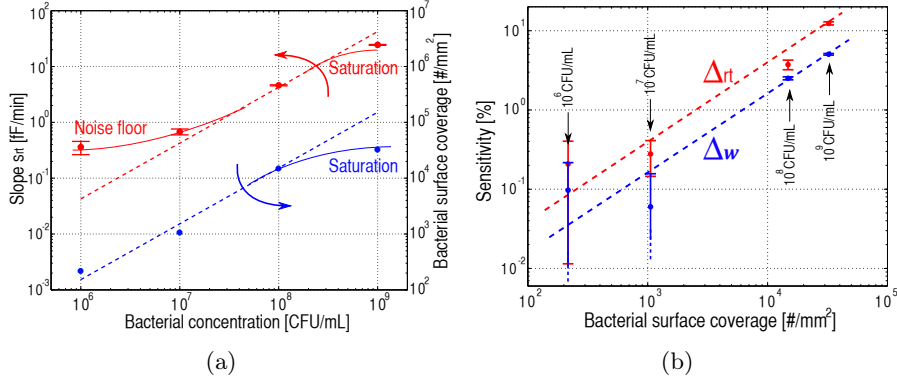


Figure 2.16 – (a) Experimental dependence of the slope s_{rt} measured at 1 MHz and the bacterial surface coverage S_b evaluated from microscope images after an incubation of 20 min with the bacterial concentration C_b . The linear fittings are: $s_{rt} = 4.31 \cdot 10^{-8} \cdot C_b$ and $S_b = 1.5 \cdot 10^{-4} \cdot C_b$. (b) Experimental dependence of the sensitivities based on Δ_{rt} and Δ_w at 1 MHz with the bacterial surface coverage. The linear fittings are: $S_{\Delta_{rt}} = 4 \cdot 10^{-4} \cdot S_b$ and $S_{\Delta_w} = 1.6 \cdot 10^{-4} \cdot S_b$. Error bars represent temporal noise computed on at least 15 successive measurements.

Spectral sensitivity and fitting with the analytical model

The experimental sensitivity $S(\omega)$ to *S. epidermidis* cells present maximal values of $\sim 9\%$ around 1 MHz (Fig. 2.17). As previously explained, lumped parameters R_{sol} and C_{sol} are strongly impacted by the large outer shell capacitance C_{out}^* at such frequency, while the capacitance C_{ins} at LF remains insensitive. The analytical model shows a similar increase at HF, but with an unexpected bump around 10 kHz coming from R_{wall} and C_{pl} . The main reason for this is the non-consideration of the metal accesses in the analytical model. Furthermore, R_{wall} and C_{pl} can possibly be inaccurate, since dielectric parameters given in Table 2.4 do not correspond to the exact *S. epidermidis* strain of this work and the bacterial space charges impact R_{wall} (see Section 2.4.2). On the other hand, the factor $K \triangleq \frac{S_{max}^{3D}}{S_{max}^{2D}} = 0.85$ was used to adjust 2D with 3D sensitivities. This factor is reasonably assumed frequency-independent (see Appendix D.1 for more details). However, the K value is quite far from the theoretical ratio between the 3D and 2D bacteria densities:

$$K^{th} \triangleq \frac{S_b}{1/[d_e \cdot (t_e + \frac{w_e}{2}) \cdot G]} \simeq 0.32 \quad (2.22)$$

The model thus presents only a qualitative fitting to experimental results.

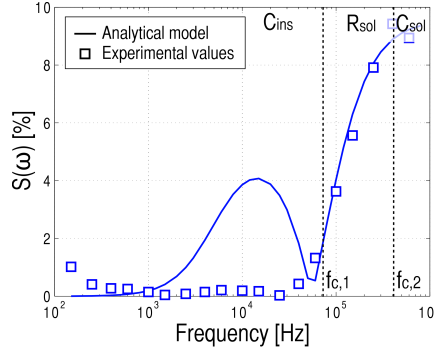


Figure 2.17 – Comparison between spectral sensitivity to *S. epidermidis* in PBS 1:1000 given by the experimental data and by the analytical model. The bacterial surface coverage is $3.2 \cdot 10^4$ bacteria per mm^2 and the adjusting factor K between 2D and 3D is equal to 0.85.

Limit of detection

The readout noise was characterized to $\sigma_n = 1$ fF in optimal conditions. The minimal detectable number of bacteria corresponds to a sensor output of $5 \cdot \sigma_n = 5$ fF, which corresponds to 50 adherent bacteria since $\Delta_w \simeq 101$ aF/bacteria. In this case, $S_b \simeq 707$ bacteria per mm^2 and the minimal bacterial concentration is $C_b \simeq 5 \cdot 10^6$ CFU/mL after 20 minutes of incubation, since $S_b = 1.5 \cdot 10^{-4} \cdot C_b$ (Fig. 2.16(a)). The capture percentage of bacterial cells on the sensor surface is approximately 0.0078 % when considering all bacterial cells flowing in the microfluidic channel during the 20 min of incubation at $1 \mu\text{L}/\text{min}$.

Influence of the electrolyte conductivity σ_{sol}

The Δ_w -based sensing performance in diluted PBS buffers, featuring σ_{sol} spanning from $1.8 \text{ mS}/\text{m}$ to $1.8 \text{ S}/\text{m}$, was performed at fixed coverage of $3 \cdot 10^4$ bacteria/ mm^2 . The mean $\overline{S(\omega)}$ and standard deviation σ_S of the sensitivity $S(\omega) = \Delta_w / \|Y_0/\omega\|$ are obtained through time averaging of at least 10 successive measurements in steady state. When the $SNR = 20 \cdot \log_{10}(\overline{S(\omega)}/\sigma_s)$ [dB] is not considered, maximal sensitivities comprise extremely large error bars (Fig. 2.18, blue bars), unsuitable for accurate interpretation. In contrast, at frequencies maximizing the SNR , sensitivities decrease from 9% to 2% when σ_{sol} increases (Fig. 2.18, orange bars) because C_{ins} screens C_{sol} . The largest sensitivity is thus achieved with low-conductive solutions, at HF.

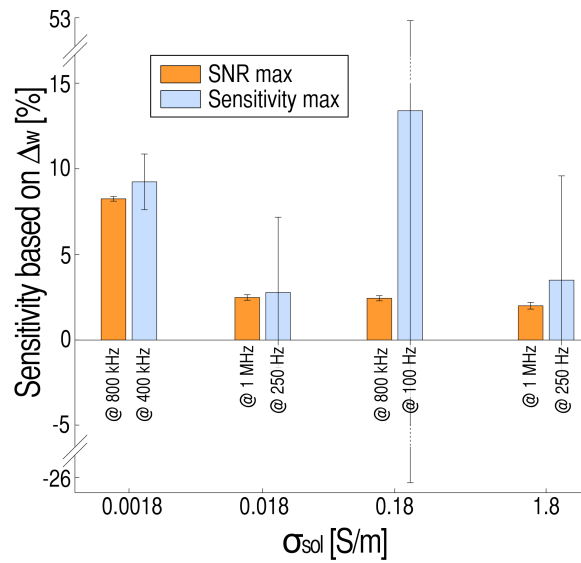


Figure 2.18 – Experimental dependence of the maximal sensitivity and the sensitivity maximizing the SNR with σ_{sol} of the washing solution. Each σ_{sol} condition features the same coverage of $3 \cdot 10^4$ bacteria/mm². Blue bars feature large noise and are therefore not interpretable. Nevertheless, they are included to highlight that the SNR must be taken into account, such as in orange bars. Error bars express temporal noise computed from at least 10 successive measurements of corresponding shifts at steady state.

2.3 Lytic enzymes as selectivity means

This section describes how lytic enzymes can be used along with capacitive biosensors to selectively detect bacteria. The principle is first explained, followed by the discussion of the experimental results. Finally, advantages and limitations of the method are discussed.

2.3.1 Principle

Lytic enzymes provide selectivity to bacteria in complex samples through the following five-step method (Fig. 2.19). First, the matrix sample containing bacterial cells is flown during 20 min on a clean sensor covered with a polydopamine layer, serving as a biological glue [195]. Afterwards, the sensor is washed with low-conductive PBS 1:1000 to fully remove non-adherent species and enable sensitive measurements of $\|Y/\omega\|$ at 1 MHz, as demonstrated in Section 2.2.3. Next, lytic enzymes are flown during 30 min atop the sensor and selectively lyse target bacteria, if present on the sensor surface. A second wash with PBS 1:1000 is then performed to sweep enzymes away before measuring $\|Y/\omega\|$ again. A shift in $\|Y/\omega\|$ occurs between the two measurements only if target bacteria, if present on the sensor surface, have been lysed. An absence of shift means that the surface state is unchanged, i.e. target bacteria are missing from the sensor surface.

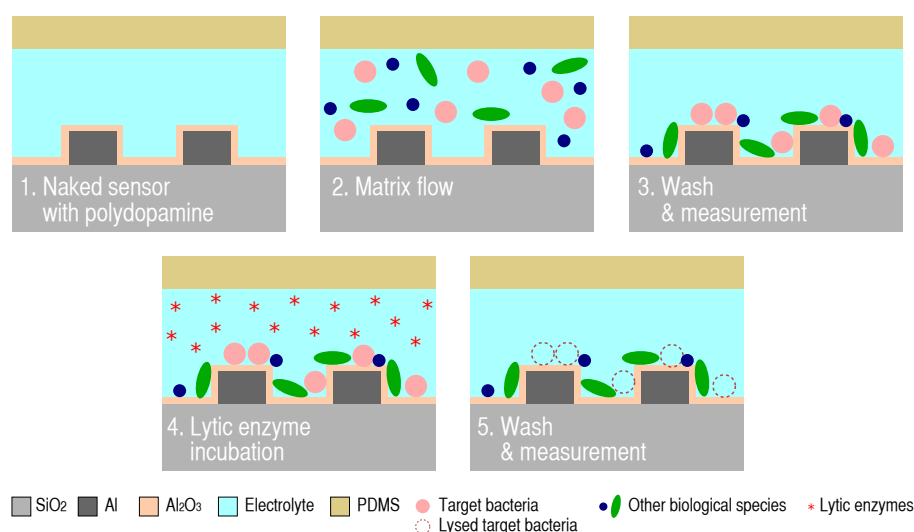


Figure 2.19 – Principle of the selectivity method using lytic enzymes.

2.3.2 Experimental validation

Protocols for chemical preparation and bacterial handling are provided in Appendices A.2 and A.3. The real-time monitoring of $\|Y/\omega\|$ at 1 MHz is provided for the negative control (*E. faecium*, Fig. 2.20(a)), and the test sample (*S. epidermidis* + *E. faecium*, Fig. 2.20(b)), both with synthetic urine as the suspension medium. Because $S(\omega)$ is maximized in low-conductive solutions, only wash parts in PBS 1:1000 are shown.

The shifts Δ_1 and Δ_2 both indicate that adherent *E. faecium* and *S. epidermidis* modify $\|Y/\omega\|$ thanks to their dielectric properties at 1 MHz. They feature significant values compared to the temporal noise computed on at least 10 successive measurements, but notably vary between the three independent sensors because of the different numbers of adherent bacteria (Fig. 2.20(c)). However, when Δ_1 and Δ_2 are normalized by the number of bacteria, *E. faecium* and *S. epidermidis* present reproducible normalized shifts spanning from 52 to 59 aF per bacterium and from 77 to 97 aF per bacterium, respectively (Fig. 2.20(d)). The larger sensitivity to *Staphylococci* may be explained by their dielectric properties, probably increased by a higher ionic cytoplasmic content thanks to the heavily cross-linked cell wall.

After the incubation of lysostaphin which specifically digests *Staphylococcus* cell walls, sensors with only *E. faecium* on the surface showed a slight decrease $\Delta_3 \in [2 \text{ fF}, 21 \text{ fF}]$ of $\|Y/\omega\|$, despite intact *E. faecium* cells as observed optically (Fig. 2.20(a) and 2.20(c)). This slight drop can be attributed to enzymes binding onto the polydopamine layer, which sticks most biomolecules containing aromatic rings [195]. On the other hand, sensors covered with *S. epidermidis* showed a significantly larger decrease $\Delta_3 \in [163 \text{ fF}, 299 \text{ fF}]$ of $\|Y/\omega\|$ (Fig. 2.20(c)), whose large variability results from the different amounts of lysed *S. epidermidis* on the sensor surface, for each experiment. When Δ_3 is divided by the number of lysed bacteria, a reproducible normalized shift spanning from 68 to 88 aF per lysed *S. epidermidis* is obtained.

It is important to note that, despite the almost complete destruction of *S. epidermidis* cells as checked optically (Fig. 2.20(b)), the sensor does not fully recover its initial $\|Y/\omega\|$ value with *E. faecium* only. Our interpretation is that cellular debris (DNA, proteins and peptidoglycan) remains on the sensor surface after cell lysis and interacts with the electric field to cause measurable normalized admittance shifts.

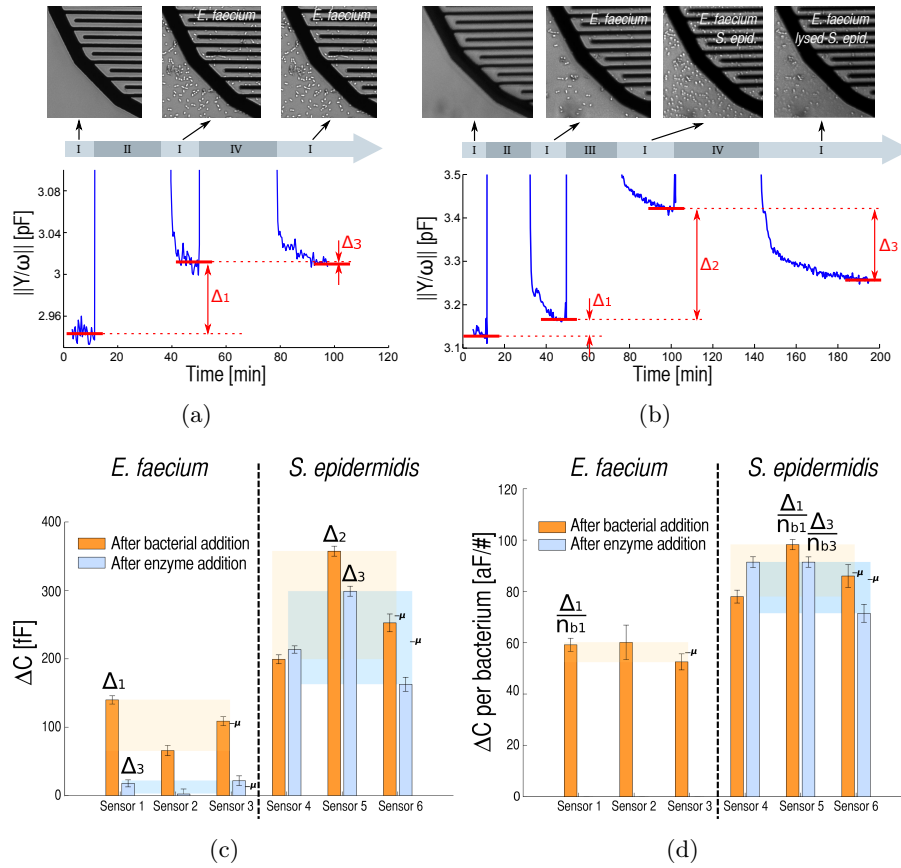


Figure 2.20 – Experimental validation at 1 MHz of the selectivity method based on lytic enzymes: (a) real-time evolution of $\|Y/\omega\|$ for the negative control (*E. faecium* in urine) and (b) for the target sample (*S. epidermidis* + *E. faecium* in urine). The events mentioned in the timeline are: (I) washing with PBS 1:1000, (II) incubating $5 \cdot 10^8$ CFU/mL *E. faecium* in urine, (III) incubating $5 \cdot 10^8$ CFU/mL *S. epidermidis* in urine and (IV) incubating lysozyme. Shifts after wash Δ_1 , Δ_2 and Δ_3 are evaluated after the addition of *E. faecium*, *S. epidermidis* and lytic enzymes, respectively. Reproducibility of three independent sensors at 1 MHz for (c) the absolute capacitive shifts $\Delta C \triangleq \Delta\|Y/\omega\|$ after *E. faecium*/*S. epidermidis* binding (in orange) and after enzyme incubation (in blue), (d) ΔC normalized to the number of bound bacteria after incubation or to the number of destroyed bacterial cells after lytic enzyme incubation. Error bars at each block refer to temporal noise obtained after averaging at least 10 successive temporal measurements on one sensor in a steady-state window. Translucent boxes depict the measurement span in a given condition, with μ the mean value of the 3 sensors.

2.3.3 Advantages and limitations

This innovative selective method presents several advantages:

- The matrix can directly be flown on the sensor without any pre-treatment steps such as centrifugation or dilution. The possible presence of large cells (diameter $> 10 \mu\text{m}$) in the matrix is likely not a problem since they should be washed away by strong shear forces at flow rate of $250 \mu\text{L}/\text{min}$, as confirmed optically with large bacterial cell clusters. A filtration method, e.g., membrane at the channel inlet, could alternatively be added to filter them out.
- The effects of non-specific bindings of bacteria are prevented, while those of biomolecules are limited during the incubation of lytic enzymes. Compared to affinity-based layers, the use of real matrixes is greatly facilitated and requires no centrifugation steps. Compared to antibodies, lytic enzymes are low-cost and can be easily extended to all Gram-positive bacteria (using endolysins).
- Washing with a low-conductive solution enables stable and sensitive detection of the dielectric properties of bacteria.

However, the method still presents some limitations:

- The fluidic setup must be optimized to avoid any cross contamination from high to low-conductive solutions. Osmotic-sensitive bacteria can also burst when subject to osmotic shock, and provide false positives when not being the target bacteria. Due to their thick cell wall ($\sim 30 - 50 \text{ nm}$), Gram-positive bacteria are less subject to this event than Gram-negative ones, having a 2-8 nm-thick cell wall. To resolve these issues, a higher-conductive wash solution can be used, but the electrical frequency should be increased accordingly to keep the same sensitivity (see Chapter 4.2).
- Reproducible cell adhesion on the sensor surface is crucial to avoid false negatives, that can occur if target bacteria do not adhere the surface. Here, a polydopamine layer was used to improve and homogenize bacterial binding. Though other coatings could provide better results, they should be investigated in a separate study.

Importantly, lytic enzymes could hardly be replaced by antibiotics to use the same method towards screening of drug resistance. Indeed, antibiotics stop the bacterial growth and not necessarily destroy their cell walls (see Section 1.1.4 for more details).

Table 2.5 – Performance comparison with relevant works on direct impedimetric detection of bacterial cells in solution

	[108]	[94]	[120]	[79]	This work
t-Bact.	<i>E. coli</i>	<i>E. coli</i>	<i>E. coli</i>	<i>S. typhim.</i>	<i>S. epid.</i>
ctrl-Bact.	-	-	-*	<i>E. coli</i>	<i>E. faecium</i>
Medium	Lettuce	Gr. beef	PBS	DI water	Urine
Pre-treat.	Yes**	Yes**	Yes	Yes	No
Labeling	-	Ab-MP	-	Ab-MP	-
Selectiv.	Ab	Ab	Ab	Ab	Lytic enz.
Material	Gold	Gold	Gold	Gold	Al ₂ O ₃ /Al
w_e/d_e	3/4 μm	15/15 μm	10/10 μm	15/15 μm	4/2 μm
t_e	50 nm	NA	100 nm	NA	1 μm
Encaps. Volume	Immersed 30 mL	Pipetting 2 μL	Pipetting 1 mL	Chamber 25 μL	Microfluidic 20 μL
LOD	10 ⁷ CFU/mL	8 · 10 ⁵ CFU/mL	5 · 10 ⁴ CFU/mL	3 · 10 ⁶ CFU/mL	5 · 10 ⁶ CFU/mL
$t_{det.}$ **	70 min	52 min	50 min	46 min	20 min
Sensitivity	NA	NA	NA	NA	~ 82 aF/#
FoM₂	2.1 · 10 ¹⁰ CFU.min	8.3 · 10 ⁴ CFU.min	2.5 · 10 ⁶ CFU.min	3.4 · 10 ⁶ CFU.min	2 · 10 ⁶ CFU.min
DR	NA	42 dB	106 dB	80 dB	60 dB

t: target; ctrl: negative control; $t_{det.}$: detection time; DR: dynamic range
 *: Control with *S. aureus* and *P. putida* is only shown in a separate ELISA test;
 **: Includes centrifugation, dilution and stomacher steps

Finally, a comparison with some significant works dealing with the direct impedimetric detection of bacteria in solution is provided in Tables 2.1 and 2.5. Our work is the first to use lytic enzymes as a selectivity means, and provides a label-free detection of *S. epidermidis* in a complex matrix (urine) comprising a control bacteria (*E. faecium*), without pretreatment steps. In comparison, works dealing with complex food matrixes [94, 108] first use stomaching to transfer bacteria to a diluent solution, which can be followed by two centrifugation steps and resuspension with magnetic beads [94]. When the functionality is only demonstrated in simple buffers (PBS or DI water) [79, 120], the matrixes need to be centrifuged and the pellets resuspended in such buffers. In addition, most works fail to cross-check the selectivity with another bacteria. The passivated Al/Al₂O₃ electrodes are also more CMOS-compatible than gold electrodes used in [79, 94, 108, 120], and encapsulated in a microfluidic channel to prevent evaporation and facilitate fluid handling. The LoD of 5 · 10⁶ CFU/mL is competitive regarding to other works, by considering the small volume (20 μL) and detection time (20 min). Indeed, the FoM₂ is 2 · 10⁶ CFU·min which is the best FoM₂ after [94], the latter further benefiting from magnetic beads.

2.4 Optimization of the sensitivity

As shown in Section 2.2.2 and 2.2.3, the analytical model is well suited to provide a good physical understanding of the sensor physics, but is unsuitable to accurately quantify the spectral sensitivity to bacterial cells because of the following limitations:

- Lumped elements are represented by simplified expressions (see Eq. 2.8 to 2.11 for instance). Actually, the concentration and curvature of the electric field by the bacterial sphericity and electrode topology result in imprecise estimations.
- The impact of bacteria on the global impedance can hardly be estimated in the spectral domain from a weighted superposition of Fig. 2.4(b) and 2.13(b). Indeed, the bacterial cell replaces a small part of the inter-electrode volume, which completely modifies parallel and series capacitances and resistances in the system. The spherical shape of the bacterial cell further complicates this.
- Despite their impact on the DL thickness, charges at the insulator-electrolyte interface and inside the bacterial cell wall are not considered in the model because of their dependence on the local pH.
- The junction between DLs, atop the insulating layer and around the bacterial cell, cannot be modelled analytically.
- Only AC analysis is considered in the analytical model, despite the possible importance of the equilibrium point.

2.4.1 Implementation of 2D numerical simulations

To solve above limitations and accurately quantify the bacterial sensitivity versus the applied frequency, 2D finite-element simulations of the system depicted in Fig. 2.13(a) were implemented with Comsol Multiphysics[®]. Simulation parameters are summarized in Table 2.6.

Assumptions

Some hypotheses are considered to simplify the numerical simulations:

- PBS 1:1000 is characterized by four ions: the major species Na^+ and Cl^- , and the dissociation of H_2O molecules into H^+ and OH^- . Other ions such as H_2PO_4^- , HPO_4^{2-} and K^+ can be neglected because of their negligible concentrations.

Table 2.6 – Parameters used for 2D numerical simulations.

Symbols	Descriptions	Values	Units
q	Elementary charge	0.19 aC	C
k_B	Boltzmann constant	$1.38 \cdot 10^{-23}$	J/K
T	Temperature	300 K	K
U_t	Thermal voltage ($= k_B T/q$)	26 mV	V
N_{av}	Avogadro number	$6.02 \cdot 10^{23}$	-
K_W	Dissociation constant of water	10^{-14}	-
D	Ionic diffusion coefficient	$1.52 \cdot 10^{-9}$	m ² /s
c_p	Positively-charged ion concentration		mol/m ³
c_m	Negatively-charged ion concentration		mol/m ³
ϕ	Electrical voltage		V
\vec{E}	Electric field		V/m
\vec{J}_c	Conduction current density		A/m ²
\vec{J}_d	Displacement current density		A/m ²
I	Total current through microelectrodes		A
f	Applied frequency	[100, 10 ⁹]	Hz
ω	Angular frequency	$2\pi f$	rad/s
$\pm V_a$	AC voltage on microelectrodes	± 10 mV	V
$[X]$	Molar concentration of the species X		M
σ	Electrical conductivity		S/m
ε	Permittivity		F/m
ρ_v	Space charge density		C/m ³
$\rho_{v,b}$	Space charge density of bacteria	Eq. 2.41	C/m ³
σ_s	Insulator surface charge	Eq. 2.38	C/m ²
N_s	Hydroxyl group density of oxide	$8 \cdot 10^{18} \text{ m}^{-2*}$	m ⁻²
K_a	Acidic dissociation constants of oxide	10^{-10*}	-
K_b	Basic dissociation constants of oxide	10^{-8*}	-
N_{si}	Anionic group density in cell wall	$0 \text{ m}^{-2\dagger}$	m ⁻²
K_{ai}	Dissociation constant of anionic groups	$10^{-9.5\dagger}$	-
N_{sj}	Cationic group density in cell wall	$6 \cdot 10^{16} \text{ m}^{-2\dagger}$	m ⁻²
K_{aj}	Dissociation constant of cationic groups	$10^{-1.8\dagger}$	-

*: Al₂O₃ material parameters [176]; †: *S. epidermidis* model parameters [193].

- The same hydrated diameter is considered for all ions, in order to reduce the number of involved equations. A single diffusion coefficient is thus used and estimated by the Kohlraush law to $D = \frac{\sigma_{sol} U_t}{2q N_{av} C_{ions} 10^3} \simeq 1.52 \cdot 10^{-9} \text{ m}^2/\text{s}$, a value between diffusivities of Na^+ and Cl^- featuring $1.33 \cdot 10^{-9}$ and $2.03 \cdot 10^{-9} \text{ m}^2/\text{s}$, respectively [196]. As a result, positive and negative ions can each be grouped together to form single concentrations c_p and c_m , respectively. It is important to note that, for extremely-diluted electrolytes with $C_{ions} < 1 - 10 \text{ } \mu\text{M}$, H^+ and OH^- ions play a non-negligible role and lead to underestimation of the electrolyte conductivity because of their high diffusion coefficients of $9.3 \cdot 10^{-9}$ and $5.3 \cdot 10^{-9} \text{ m}^2/\text{s}$, respectively.
- Because there is no preferential attraction between H^+ and K^+ , the concentration $[\text{H}^+]$ is set to a fixed part of c_p at each point of the 2D system, which is estimated 100 μm -away from microelectrodes.
- Steric effects in the DL are not modelled. The small AC voltage amplitude (10 mV) indeed guarantees that c_p and c_m do not exceed their maximal physical value ($\sim 200 \text{ M}$ for a 0.2 nm-hydrated diameter), as it has been verified after each simulation. Additional terms could be included in constitutive equations to model steric effects, but the formulation would then become more intricate.
- Only one pair of electrodes are simulated (Fig. 2.13(a)). Coupled effects between non-adjacent electrodes and access lines are thus neglected. These two effects have slight impact on the complex impedance as shown in Fig. 2.7(b), but do not constitute the key sensing part as discussed in Section 2.2.2.
- The system is assumed linear because of the small voltage amplitude ($V_a < U_t$) [129], which is representative to those used in experimental works [79, 120]. The DL thus features a linear dependence with the local potential [197].
- All relative permittivities are assumed frequency-independent since simulations are performed below 1 GHz (see Appendix D.2). On the other hand, the electric field inside the double layer (DL) has been verified by simulations to be sufficiently small ($< 10^7 \text{ V/m}$) to keep the DL relative permittivity identical to $\epsilon_{r,sol}$ [192].

Constitutive equations

Three variables characterize the system depicted in Fig. 2.13(a): the electrical potential ϕ , the positively- and negatively-charged ion concentrations c_p and c_m , respectively. All are expressed as the sum of the electrostatic and AC terms, the latter being expressed as a phasor thanks to the system linearity and the sinusoidal voltage applied on electrodes:

$$\phi = \phi_0 + \phi_a \cdot \mathbb{R}\{e^{j\omega t}\} \quad (2.23)$$

$$c_p = c_{p0} + c_{pa} \cdot \mathbb{R}\{e^{j\omega t}\} \quad (2.24)$$

$$c_m = c_{m0} + c_{ma} \cdot \mathbb{R}\{e^{j\omega t}\} \quad (2.25)$$

where subscripts 0 and a stand for DC and AC, respectively. Once constitutive equations are solved for ϕ , c_p and c_m in equilibrium and AC regimes, the total current density is extracted at each point of the 2D system. The conduction current density is given by $\vec{J}_c = \sigma \cdot \vec{E}$ if the medium conductivity σ is known, or by the continuity equation $\vec{\nabla} \cdot \vec{J}_c = -\partial\rho_v/\partial t$ otherwise. For the displacement current density, the Maxwell formulation gives $\vec{J}_d = j\omega\varepsilon \cdot \vec{E}$, with ε the local medium permittivity. By integrating J_d on the electrode-oxide interface, the total current I through the electrode is obtained:

$$I = I_a \cdot \mathbb{R}\{e^{j\omega t}\} \quad (2.26)$$

The impedance is computed as $Z = V_a/I_a$. Different constitutive equations with ϕ , c_p and c_m must be considered for each medium, which further presents additional surface or space charges. The following parts summarize the related equations for each media.

Conductive and dielectric media : The insulator layer, the buried oxide layer, the bacterial cytoplasm and plasma membrane are characterized by a fixed permittivity ε and conductivity σ , where ϕ is described by the Poisson equation:

$$0 = \vec{\nabla} \cdot \left((\sigma + j\omega\varepsilon) \vec{\nabla}\phi \right) \quad (2.27)$$

$$\vec{J}_c = -\sigma \cdot \vec{\nabla}\phi \quad (2.28)$$

$$\vec{J}_d = -j\omega\varepsilon \cdot \vec{\nabla}\phi_a \quad (2.29)$$

Electrolyte and cell wall : In this case, the mobility of positively- and negatively-charged ions intrinsically determines the electrical conductivity σ . The ion-penetrable bacterial cell wall features an ionic diffusion coefficient equal to 40% of the surrounding electrolyte one [194]. Nernst-Planck equation describes the ion transport [191, 198, 199]:

$$\frac{\partial c_{p,m}}{\partial t} = \vec{\nabla} \cdot \left(D \vec{\nabla} c_{p,m} \pm \frac{D}{U_t} \cdot c_{p,m} \vec{\nabla} \phi \right) \quad (2.30)$$

where the negative sign holds only for negatively-charged ions (i.e. c_m). Four equations are obtained by rewriting these equations at equilibrium (Eq. 2.31) and in AC regime (Eq. 2.32):

$$0 = \vec{\nabla} \cdot \left(\vec{\nabla} c_{p0,m0} \pm c_{p0,m0} \cdot \frac{\vec{\nabla} \phi_0}{U_t} \right) \quad (2.31)$$

$$\frac{j\omega c_{pa,ma}}{D} = \vec{\nabla} \cdot \left(\vec{\nabla} c_{pa,ma} \pm c_{pa,ma} \cdot \frac{\vec{\nabla} \phi_0}{U_t} \pm c_{p0,m0} \cdot \frac{\vec{\nabla} \phi_a}{U_t} \right) \quad (2.32)$$

Thanks to the small applied voltage amplitude, the second-order term $c_{pa,ma} \cdot \frac{\vec{\nabla} \phi_a}{U_t} \cdot e^{j2\omega t}$ can be neglected. The electrical potential in DC and AC is obtained through the Poisson equation knowing that $\rho_v = \rho_{v0} + \rho_{va} \cdot \mathbf{R}\{e^{j\omega t}\}$ with $\rho_{v0} = c_{p0} - c_{m0}$ and $\rho_{va} = c_{pa} - c_{ma}$:

$$\vec{\nabla} \cdot (-\varepsilon \vec{\nabla} \phi_{0,a}) = qN_{av} \cdot (c_{p0,a} - c_{m0,a}) \quad (2.33)$$

For the current densities, \vec{J}_d has the typical formulation while \vec{J}_c is obtained by combining $\vec{\nabla} \cdot \vec{J}_c = -j\omega \rho_{va}$ with Eq. 2.32:

$$\begin{aligned} \vec{J}_c = & -qDN_{av} \cdot \left(\vec{\nabla} (c_{pa} - c_{ma}) + (c_{pa} + c_{ma}) \cdot \frac{\vec{\nabla} \phi_0}{U_t} \right. \\ & \left. + (c_{p0} + c_{m0}) \cdot \frac{\vec{\nabla} \phi_a}{U_t} \right) \end{aligned} \quad (2.34)$$

$$\vec{J}_d = -j\omega \varepsilon \cdot \vec{\nabla} \phi_a \quad (2.35)$$

Insulator-electrolyte interface : Because the insulator is an oxide, hydroxyl groups at the insulator-electrolyte interface are subject to protonation or deprotonation, depending on the local pH value, according to the following chemical reactions [176]:



where $K_a \triangleq [AO^-][H^+]/[AOH]$ and $K_b \triangleq [AOH_2^+][OH^-]/[AOH]$ are the corresponding dissociation constants with values for Al_2O_3 given in Table 2.6. Affecting ion distributions through Eqs. 2.31, 2.32 and 2.33, the surface charge σ_s depends on the pH as shown in Fig. 2.21(a) [176]:

$$\sigma_s = qN_s \cdot \left(\frac{K_b[H^+]^2 - K_aK_W}{K_aK_W + K_W[H^+] + K_b[H^+]^2} \right) \quad (2.38)$$

Bacterial charge : In most electrolytes, the bacterial cell wall of Gram-positive bacteria is negatively charged due to protonation or deprotonation of carboxyle, phosphate and amine groups in the peptidoglycan layer, as expressed by the following chemical reactions [193]:



where HA_1 and B_2 are anionic and cationic groups, respectively, N_{s1} and N_{s2} the corresponding group densities and K_{a1} and K_{a2} their respective dissociation constants. Uniformly distributed in the ion-penetrable cell wall, the bacterial charge is characterized by a space charge density impacting DC and AC ion distributions through Eqs. 2.31 and 2.32 [193]:

$$\rho_{v,b} = \frac{1}{t_{wall}} \cdot \left(\sum_i \frac{-qN_{si}K_{ai}}{K_{ai} + [H^+]} + \sum_j \frac{qN_{sj}[H^+]}{K_{aj} + [H^+]} \right) \quad (2.41)$$

The dependence of $\rho_{v,b}$ with the electrolyte pH is depicted in Fig. 2.21(b). The same method can be used for Gram-negative bacteria by considering their ionic groups on the outer membrane [193].

Convergence issues

The mesh is strongly refined at the insulator-electrolyte interface (~ 0.1 nm) to account for the small thickness (\sim nm) of the DL in saline buffers. To limit the number of nodes in the micrometer-sized system, we use the *boundary layer mesh* tool provided by Comsol Multiphysics[®]. The mesh error on the extracted impedance is approximately 0.01% for the chosen mesh configuration and sensitivity decreases with smaller mesh sizes. Another important geometric feature is the upper and bottom boundary layers of the electrolyte and buried oxide, connected to ground and located far away from electrodes (100 μ m above and 50 μ m below electrodes, respectively).

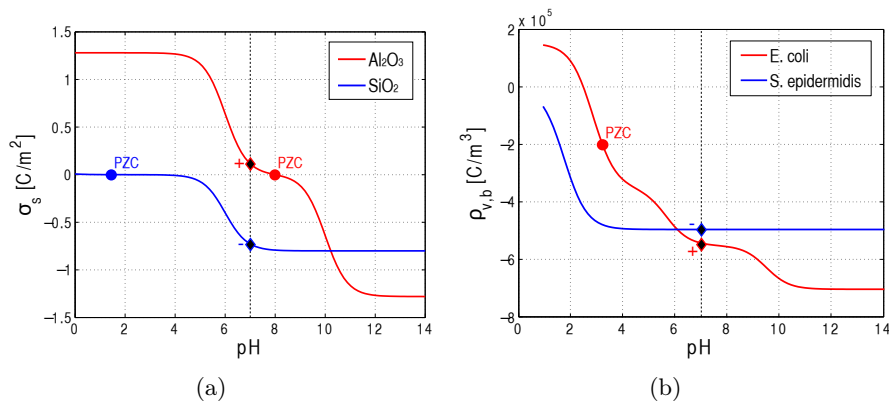


Figure 2.21 – (a) Dependence of the oxide surface charge with the electrolyte pH for Al₂O₃ and SiO₂ insulator layers. (b) Dependence of the bacterial surface charge with the electrolyte pH for *E. coli* and *S. epidermidis* cells. The point zero of charges (PZC) and the pH7 are highlighted.

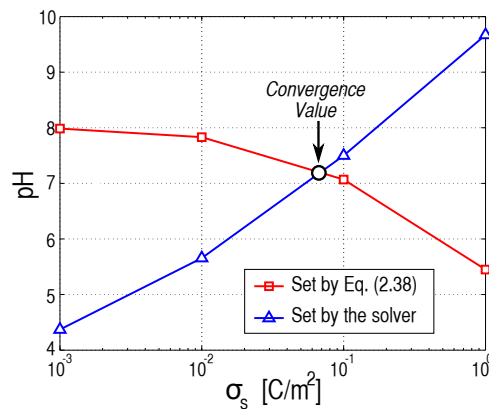


Figure 2.22 – Convergence issue between the oxide surface charge σ_s and the local pH close to the electrode in the electrolyte.

The consideration of the insulator surface charges σ_s can result in convergence difficulties. Indeed, when the local pH decreases (i.e. larger local $[H^+]$), σ_s increases following Eq. 2.38, but positive ions in the electrolyte such as H^+ are repulsed at the same time, increasing the local pH . The solver can thus exhibit difficulties for converging. To address this problem, a bisection method was implemented (Fig. 2.22):

1. The initial pH interval is defined as $[pH_1; pH_2] = [pH_{sol}; PZC_{ins}]$, where pH_{sol} the electrolyte pH and PZC_{ins} is the point zero of charge of the insulator.
2. The system is solved by imposing the σ_s corresponding to pH_2 (see Eq. 2.38). The local pH, denoted pH_{loc} at the insulator-electrolyte interface, is then extracted.
3. If $|pH_2/pH_{loc} - 1| < 0.1\%$, the system has converged. If not, a new pH value $(w \cdot pH_2 + pH_1)/(w + 1)$ is computed by defining w as a weight factor, and attributed to pH_2 if $pH_{loc} > pH_2$ or to pH_1 otherwise. The algorithm then goes on at (2), by using the modified pH value (either pH_1 or pH_2) for σ_s computation.

With the simulation framework now completely defined, the simulation results are first compared to experimental data and analytical model. The impact of oxide and bacterial charges are then described. Finally, the established numerical simulations are used to optimize the sensor towards the maximal sensitivity.

2.4.2 Fitting with experiments and analytical model

Numerical simulations of $\|Y/\omega\|$ in sterile PBS 1:1000 present very close behavior to the analytical model (Fig. 2.23(a)), by using the same factor $K \triangleq \frac{\|Y/\omega\|_{exp}}{\|Y/\omega\|_{sim}} = 7.21$ mm as in Fig. 2.5. The lower $\|Y/\omega\|$ values at LF come from the non-consideration of access lines, as previously explained. To be compared to the experimental results, 2D sensitivities obtained by simulations and by the analytical model were both multiplied by the factor $K \triangleq S_{max}^{3D}/S_{max}^{2D} = 0.58$, which is closer to the theoretical value $K^{th} = 0.32$ than the previous factor $K = 0.85$ used in Fig. 2.17. In this case, the factor K is assumed frequency-independent, which is reasonable as shown in Appendix D.1. As shown in Fig. 2.23(b), numerical simulations provide a better estimation of the sensitivity amplitude than the analytical model on the overall frequency range.

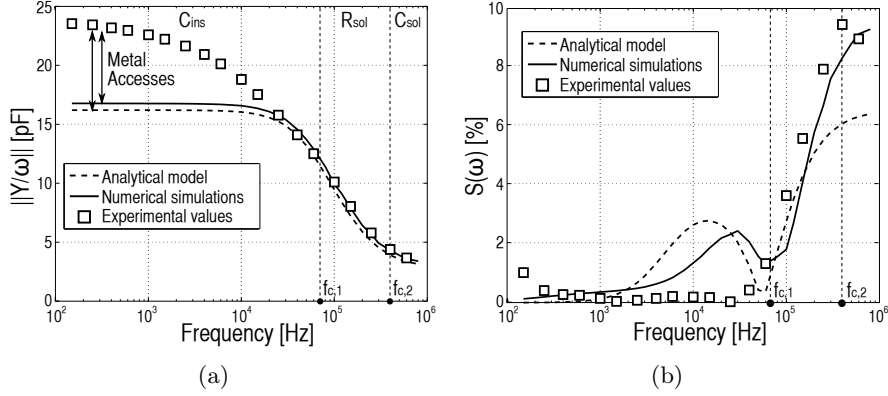


Figure 2.23 – Spectral comparison between analytical model, numerical simulations and experimental data for (a) $\|Y/\omega\|$ in PBS 1:1000 without bacterial cells with an adjusting factor K between 2D and 3D equal to 7.21 mm and (b) $S(\omega)$ with a bacterial surface coverage of $3.2 \cdot 10^4$ *S. epidermidis* per mm^2 in PBS 1:1000, with an adjusting factor K between 2D and 3D equal to 0.58.

2.4.3 Impact of charges

The impact of oxide surface charges σ_s and bacterial space charges $\rho_{v,b}$ on $\|Y/\omega\|$ and $S(\omega)$ is non-negligible. In PBS 1:1000, $\|Y/\omega\|$ is shown to slightly increase at $f < 100$ kHz because of the smaller Debye length λ_D , induced by the larger amount of charges brought by σ_s and resulting in a larger value of the DL capacitance C_{DL} . Indeed, 2D simulations report that the LF capacitance $C_{LF} = \frac{1}{2}(C_{ins}^{-1} + C_{DL}^{-1})^{-1}$ increases from 2.287 to 2.318 nF/m (Fig. 2.24(a)), when the oxide charge density is set to 1.2 mC/m² (corresponding to 9.6 nC/m). Since $C_{DL}/C_{ins} \simeq 12$ (see Section 2.2.2), the C_{LF} increase corresponds to an increase of C_{DL} from 59.46 to 71.91 nF/m, which is reasonable with regards to the oxide surface charge of 9.6 nC/m. As shown in Fig. 2.24(a), the effect is accentuated around 10 kHz because of the lower R_{wall} and higher double layer capacitance values around bacteria due to $\rho_{v,b}$. At HF, the charges do not impact $\|Y/\omega\|$, as expected from previous works reporting the impact of DNA charges only at LF in [199].

When considering the sensitivity $S(\omega)$, the bump around 10 kHz due to C_{pl} is drastically lowered by $\rho_{v,b}$ because of the smaller influence of R_{wall} and the double layer capacitance around bacteria in series with C_{pl} (Fig. 2.24(b)). However, it is slightly compensated by oxide charges σ_s that increase C_{DL} as previously explained. At larger frequencies (> 100

kHz), the smaller R_{wall} value due to $\rho_{v,b}$ increases the apparent C_{out}^* , which is beneficial for $S(\omega)$ since the medium resistive path is more perfectly shortened. This charge analysis should be identical for Gram-negative bacteria, because similar space charge density can be quantified in the outer ion-penetrable layer [193].

2.4.4 Optimization of the insulating layer

Impact on the impedance

$C_{ins} \propto \varepsilon_{r,ins}/t_{ins}$ strongly influences the complex impedance at LF, as previously experimentally shown and analytically explained in Fig. 2.10(a). When considering native Al_2O_3 ($t_{ins} \simeq 4$ nm) and atomic-layer deposited (ALD)- Al_2O_3 ($t_{ins} \simeq 33$ nm), excellent fitting between simulation results and experimental data was obtained (Fig. 2.25(a)). At LF, the measured capacitance is slightly higher than the simulated one because of metal accesses [19]. The impact of the insulator material $\varepsilon_{r,ins}$ should feature an inverse effect as t_{ins} , since $C_{ins} \propto \varepsilon_{r,ins}/t_{ins}$.

Impact on the bacterial sensitivity

Both t_{ins} and $\varepsilon_{r,ins}$ strongly impact the bacteria sensitivity. Numerical simulations show that S_{max}^{2D} always occurs around 1 MHz and decreases for larger t_{ins} (Fig. 2.25(b)). The screening by the insulator layer is indeed amplified at large t_{ins} , where a smaller C_{ins} screens C_{sol} more strongly in series. A fitting on numerical values shows that the maximal sensitivity is inversely proportional to t_{ins} :

$$S_{max}^{2D}(t_{ins}) = \frac{A}{t_{ins} + B} \quad (2.42)$$

where $A = 22$ nm and $B = 97$ nm. If $t_{ins} \ll B$, S_{max}^{2D} is constant and equal to A/B . Otherwise, S_{max}^{2D} decreases as A/t_{ins} . The relationship between S_{max}^{2D} and t_{ins} is confirmed by rewriting the maximal theoretical sensitivity $S_{max}^{2D,th}$ given by Eq. 2.21 in function of t_{ins} :

$$S_{max}^{2D,th}(t_{ins}) = \frac{K_1 P/G}{t_{ins} + K_1} \quad (2.43)$$

where $K_1 = \frac{\varepsilon_{r,ins} \cdot d_e}{2\varepsilon_{r,sol} \cdot (G+P)} \simeq 154$ nm and $P/G \simeq 0.14$, as derived from Section 2.2.3. Compared to fitting values A and B , the theoretical values $K_1 P/G$ and K_1 differ by a factor slightly smaller than 2 because of the

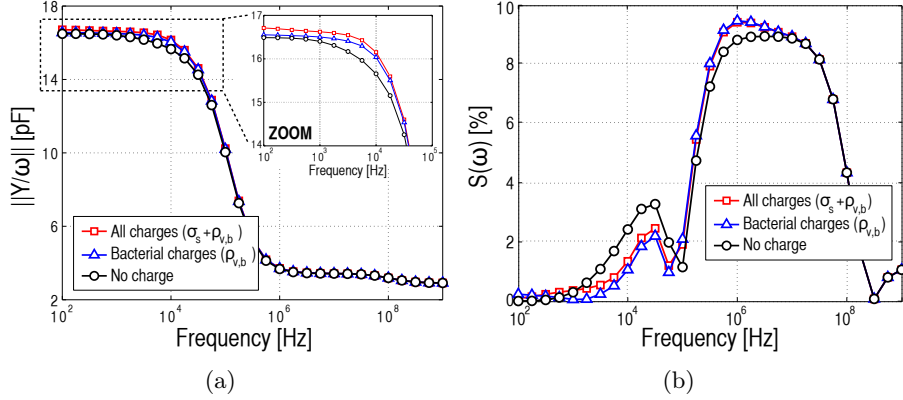


Figure 2.24 – Impact of oxide surface charges σ_s and bacterial space charges $\rho_{v,b}$ on (a) the normalized admittance $\|Y/\omega\|$ and (b) the bacterial sensitivity $S(\omega)$.

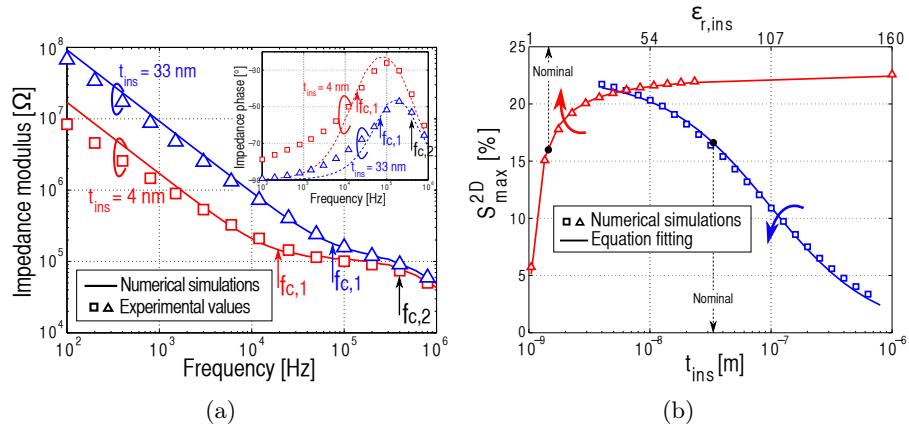


Figure 2.25 – Impact of the insulator layer on the sensor impedance: (a) comparison between numerical simulations and experimental measurements of the impedance modulus and phase in PBS 1:1000 for native Al_2O_3 (~ 4 nm) and ALD-deposited Al_2O_3 (~ 33 nm) layers atop circularly shaped IDEs, respectively. The factor to link 2D with 3D admittance is $K = 7.21$ mm; (b) numerical simulations of S_{max}^{2D} versus t_{ins} (blue curves, at fixed $\epsilon_{r,ins} = 9$) and $\epsilon_{r,ins}$ (red curves, at fixed $t_{ins} = 33$ nm). Eqs. 2.42 and 2.44 are used for the fitting of t_{ins} and $\epsilon_{r,ins}$, respectively.

limitations of the analytical model explained in Section 2.4. For the designer point of view, it is important to note that S_{max}^{2D} loses 0.2% for each supplementary nanometer, for $t_{ins} < 20$ nm. The comparison of typical t_{ins} values of 4 nm, 20 nm, 100 nm and 600 nm gives the following maximal sensitivities, respectively: 22.2%, 18.5%, 11% and 3.4%. The insulator layer must then be as thin as possible, preferably below 30-50 nm, but thick enough for protection against corrosion.

Still obtained around 1 MHz, S_{max}^{2D} is also strongly impacted by $\varepsilon_{r,ins}$ (Fig. 2.25(b)). High-permittivity materials demonstrate larger sensitivities because of the larger C_{ins} values, reducing parasitic series effects with C_{sol} . Excellent fitting with numerical data is obtained with:

$$S_{max}^{2D}(\varepsilon_{r,ins}) = A \cdot \frac{\varepsilon_{r,ins}}{\varepsilon_{r,ins} + B} \quad (2.44)$$

where $A = 0.23$ and $B = 3.5$. For $\varepsilon_{r,ins}$ smaller than B , the maximal sensitivity linearly increases with $\varepsilon_{r,ins}$ to finally reach the constant value A around $\varepsilon_{r,ins} > 50$. Reorganizing Eq. 2.21 shows a similar theoretical expression, with slight differences for constant values:

$$S_{max}^{2D,th} = P/G \cdot \frac{\varepsilon_{r,ins}}{\varepsilon_{r,ins} + K_2} \quad (2.45)$$

where $K_2 = \frac{2(G+P)\varepsilon_{r,sol}t_{ins}}{d_e} \simeq 1.92$. For the designer point of view, three insulating materials with thickness of 33 nm are compared: SiO₂ ($\varepsilon_{r,ins} = 3.9$), Al₂O₃ ($\varepsilon_{r,ins} = 9$) and TiO₂ ($\varepsilon_{r,ins} = 160$). To account for the difference of relative permittivity exclusively, the oxide surface charges are assumed identical to those of Al₂O₃. The corresponding bacterial sensitivities are 12.8%, 17.2% and 23.2%, respectively. The gain of sensitivity is thus significant in the low $\varepsilon_{r,ins}$ values, but slightly declines at high $\varepsilon_{r,ins}$ where C_{DL} dominates C_{ins} in series.

2.4.5 Optimization of the electrolyte

Impact of the relative permittivity $\varepsilon_{r,sol}$

Numerical simulations demonstrate that S_{max}^{2D} is always achieved around 1 MHz and maximized at low $\varepsilon_{r,sol}$ (Fig. 2.26(a)). The large capacitance C_{out}^* between $f_{c,1}$ and $f_{cb,2}$ is indeed better screened when the solution capacitance C_{sol} is reduced. The fitting on numerical data gives:

$$S_{max}^{2D}(\varepsilon_{r,sol}) = \frac{A}{\varepsilon_{r,sol} + B} \quad (2.46)$$

with $A = 29.4$ and $B = 104$. The same form of relationship is obtained from the analytical model:

$$S_{max}^{2D,th}(\varepsilon_{r,sol}) = \frac{K_4 P/G}{\varepsilon_{r,sol} + K_4} \quad (2.47)$$

with $K_4 = \frac{\varepsilon_{r,ins} d_e}{2(G+P)t_{ins}} \simeq 374$. There is a factor 3 of difference with constants from numerical simulations, for the same reasons as previously explained. To our best knowledge, no study reports detection of bacterial cells in solutions of lower $\varepsilon_{r,sol}$, such as acetone ($\sigma_{sol} = 20 \mu\text{S/m}$, $\varepsilon_{r,sol} = 21$), methanol ($\sigma_{sol} = 30 \mu\text{S/m}$, $\varepsilon_{r,sol} = 33$) and ethanol ($\sigma_{sol} = 6 \mu\text{S/m}$, $\varepsilon_{r,sol} = 24$), because bacterial viability can be degraded in such media.

Impact of the electrical conductivity σ_{sol}

Increasing σ_{sol} pushes cutoff frequencies $f_{c,1}$ and $f_{c,2}$ towards higher frequencies, thus expanding the LF range where C_{ins} screens volume properties. The applied frequency must then be increased to achieve the maximal sensitivity, as indicated by arrows in Fig. 2.26(a). At the same time, S_{max}^{2D} decreases at larger σ_{sol} because of the slight difference in ionic content between the bacterial cytoplasm through σ_{cyt} and the surrounding medium through σ_{sol} . The following formula is obtained by fitting numerical data:

$$S_{max}^{2D}(\sigma_{sol}) = A \cdot \left| \frac{\sigma_{sol} - B}{\sigma_{sol} + C} \right| \quad (2.48)$$

with $A = 0.15$, $B = 631 \text{ mS/m}$ and $C = 577 \text{ mS/m}$. The maximal sensitivity is constant and equals to $AB/C \simeq 16.4\%$ when $\sigma_{sol} \ll B, C$. Sensitivity drops 3.4%, 6.2% and 12.4% at electrolyte conductivities of 35 mS/m, 113 mS/m and 356 mS/m, respectively (Fig. 2.26(a)). At physiological condition of $\sigma_{sol} \simeq 1.1 \text{ S/m}$, the capacitive shift becomes negative because the sensing principle now relies on sensing $\varepsilon_{r,cyt} < \varepsilon_{r,sol}$ and $\sigma_{cyt} < \sigma_{sol}$ (see Section 4.2) and the sensitivity reaches 4.4%. In contrast to $\varepsilon_{r,ins}$ and t_{ins} , S_{max}^{2D} cannot be estimated from the analytical model since it assumes operation at HF where only C_{sol} dominates.

The massive sensitivity drop at high electrolyte conductivity explains why many authors used low-conductive buffers, such as deionized water ($\sigma_{sol} = 5.5 \mu\text{S/m}$) [79], PBS 1:1000 ($\sigma_{sol} = 1.8 \text{ mS/m}$) [18, 21, 23], 0.1 M mannitol buffer ($\sigma_{sol} = 200 \mu\text{S/m}$) [94, 105], 0.1% peptone water [108] and tris-glycine-dextrose buffer ($\sigma_{sol} = 1.7 \text{ mS/m}$) [137]. Bacterial

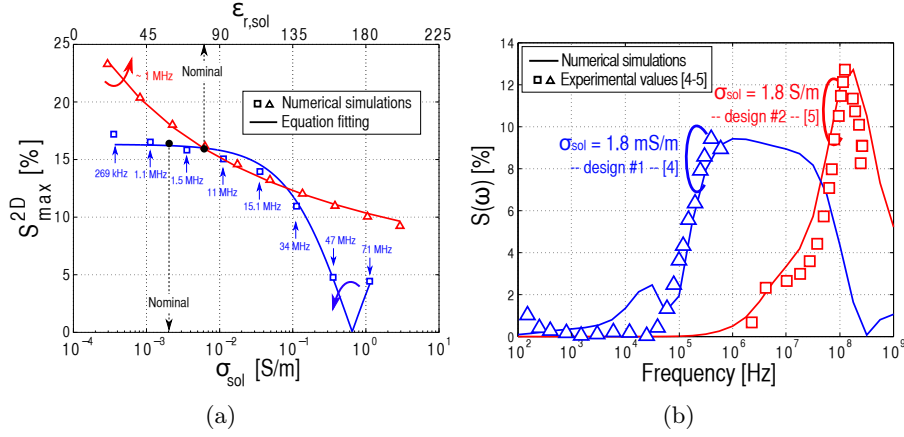


Figure 2.26 – (a) Numerical simulations of S_{max}^{2D} versus σ_{sol} (blue curves, at fixed $\epsilon_{r,sol} = 80$) and $\epsilon_{r,sol}$ (red curves, at fixed $\sigma_{sol} = 1.8$ mS/m). In the case of σ_{sol} , S_{max}^{2D} is achieved at different frequencies indicated by arrows. Eqs. 2.48 and 2.46 are used for the fitting of σ_{sol} and $\epsilon_{r,sol}$, respectively. (b) Comparison of the 3D sensitivity to *S. epidermidis* ATCC 35984 obtained experimentally in sections 2.2.3 (design #1) and 4.2.3 (design #2) with 2D numerical simulations, for two different $\sigma_{sol} = 1.8$ mS/m (PBS 1:1000) and 1.8 S/m (pure PBS). Factors to match 2D to 3D maximal sensitivities are $K_{1.8 \text{ mS/m}} = 0.58$ and $K_{1.8 \text{ S/m}} = 0.89$, respectively.

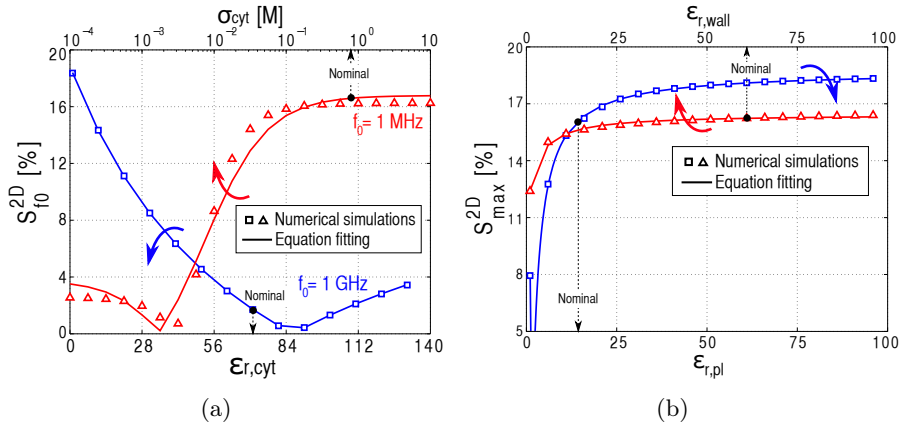


Figure 2.27 – Numerical simulations of $S_{f_0}^{2D}$ and S_{max}^{2D} versus dielectric properties of bacterial cells: (a) σ_{cyt} at fixed $\epsilon_{r,cyt} = 70$ (red curves) and $\epsilon_{r,cyt}$ at fixed $\sigma_{cyt} = 0.8$ S/m (blue curves) at 1 MHz and 1 GHz, respectively, and (b) $\epsilon_{r,wall}$ at fixed $\epsilon_{r,pl} = 16$ (red curves) and $\epsilon_{r,pl}$ at fixed $\epsilon_{r,wall} = 60$ (blue curves). Eqs. 2.49, 2.50, 2.51 and 2.52 are used for the fitting of σ_{cyt} , $\epsilon_{r,cyt}$, $\epsilon_{r,pl}$ and $\epsilon_{r,wall}$, respectively.

detection in saline buffers can be performed by monitoring the change of DL capacitance at LF [120], but it is only possible with non-passivated electrodes. For passivated microelectrodes, bacterial detection in saline buffers can be performed at the very high frequency of ~ 150 MHz, thanks to a dedicated on-chip integrated readout circuit (see Section 4.2). The drop of sensitivity shown in Fig. 2.26(a) is then compensated with smaller electrode gap and width of $1.5 \mu\text{m}$, for an $200\text{-}\mu\text{m}$ sided rectangular IDEs of $1.8\text{-}\mu\text{m}$ metal thickness, as shown by the design #2 in Fig. 2.26(b). Again, numerical simulations demonstrate good fitting with experimental data at the two extreme conductivities. The K factor is larger in the case of the design #2 because of the larger bacterial surface coverage, as explained in Appendix D.3.

2.4.6 Influence of the bacterial cell

Impact of the cytoplasm

The bacterial cytoplasm, composed of the cytosol and cellular substructures, is saline enough to ensure the biological viability of bacteria. The analysis of S_{f_0} at 1 MHz has been preferred to S_{max}^{2D} , because the latter involves different regimes for high and low cytoplasm conductivity. Beyond 30 mS/m , the cytoplasm conductivity σ_{cyt} hardly affects the sensitivity at 1 MHz, which is stuck to a maximal value of 17% (Fig. 2.27(a)). When σ_{cyt} is smaller than 30 mS/m , the sensitivity at 1 MHz drops to extremely low negative sensitivities (2%) because $\sigma_{cyt} < \sigma_{sol}$. The following expression fits relatively well to numerical values:

$$S_{f_0}^{2D}(\sigma_{cyt}) = A \cdot \left| \frac{\sigma_{cyt} - B}{\sigma_{cyt} + C} \right| \quad (2.49)$$

with $f_0 = 1 \text{ MHz}$, $A = 0.17$, $B = 1.7 \text{ mS/m}$ and $C = 7 \text{ mS/m}$. For $\sigma_{cyt} > C$, the sensitivity achieves a maximum value A . In opposite, when $\sigma_{cyt} < B$, the capacitive shift is negative due to the cutoff conductivity B and the sensitivity equals $A \cdot |B/C|$, since the difference between σ_{cyt} and σ_{sol} is not sufficient anymore. To improve the matching with numerical data, quadratic expressions at both the numerator and denominator of $S_{f_0}^{2D}(\sigma_{cyt})$ can be considered, but render physical interpretation much harder.

Besides σ_{cyt} , the cytoplasm relative permittivity $\varepsilon_{r,cyt}$ affects the impedance only at $f > f_{cb,2} \simeq 200 \text{ MHz}$, where the cytoplasm capacitive behavior dominates. For this reason, we extract the sensitivity at 1 GHz.

Numerical simulations show that the largest sensitivity is achieved at small $\varepsilon_{r,cyt}$ values (Fig. 2.27(a)), where the global capacitance decreases. The fitting curve has the following expression:

$$S_{f_0}^{2D}(\varepsilon_{r,cyt}) = A \cdot \left| \frac{\varepsilon_{r,cyt} - B}{\varepsilon_{r,cyt} + C} \right| \quad (2.50)$$

with $f_0 = 1$ MHz, $A = 0.16$, $B = 87$ and $C = 73$. The cutoff permittivity B denotes the limit between negative and positive sensitivity. For $\varepsilon_{r,cyt} < B$, the capacitance decreases after bacterial adhesion as experimentally shown in [22] and the maximal sensitivity reaches $A \cdot |B/C| \simeq 19\%$. For $\varepsilon_{r,cyt} > B$, the capacitance shift is positive and the maximal sensitivity is $A \simeq 16\%$, only achieved at very high $\varepsilon_{r,cyt}$.

Impact of the plasma membrane

Due to its relatively small thickness (~ 8 nm), the plasma membrane does not strongly impact the sensitivity. While its low conductivity $\sigma_{sol} \simeq 1 \mu\text{S/m}$ was not shown to affect the impedance, its low relative permittivity $\varepsilon_{r,pl} = 16$ limits the sensitivity to 17%, compared to the maximal sensitivity of 19% achieved at $\varepsilon_{r,pl} = 80$. However, the worst case occurs at $\varepsilon_{r,pl} \ll 16$ where S_{max}^{2D} drops down to 8% (Fig. 2.27(b)). In this case, C_{pl} becomes so small that the cytoplasm short-circuit is less pronounced. The analytical fitting on numerical values gives the following expression:

$$S_{max}^{2D}(\varepsilon_{r,pl}) = A \cdot \left| \frac{\varepsilon_{r,pl} - B}{\varepsilon_{r,pl} + C} \right| \quad (2.51)$$

with $A = 0.19$, $B = 1.62$ and $C = 0.46$. The largest sensitivity A is achieved at large $\varepsilon_{r,pl}$, while the smallest value is $A \cdot (B/C)$ at low $\varepsilon_{r,pl}$.

Impact of the cell wall

The cell wall is an ion-penetrable peptidoglycan layer composed of a fixed space charge ρ_v , an electrolyte-dependent conductivity σ_{wall} and an intrinsic relative permittivity $\varepsilon_{r,wall}$. The two first parameters are directly dependent on the electrolyte pH and ionic strength C_{ions} , and are therefore not studied in this section. However, $\varepsilon_{r,wall}$ is shown to have similar but attenuated effects as $\varepsilon_{r,pl}$ because of its larger thickness

(Fig. 2.27(b)). A larger $\varepsilon_{r,wall}$ slightly increases the bacterial sensitivity, but in a very limited way, as shown by the following fitting:

$$S_{max}^{2D}(\varepsilon_{r,wall}) = A \cdot \frac{\varepsilon_{r,wall} + B}{\varepsilon_{r,wall} + C} \quad (2.52)$$

with $A = 0.16$, $B = 1.56$ and $C = 2.4$. The maximal sensitivity then spans from $A \cdot (B/C) \simeq 10.4\%$ to $A \simeq 16\%$.

Summary

The sensitivity to bacterial cells comes mostly from the high-conductive property of the cytoplasm. A minimal cytoplasm conductivity is required to guarantee a sufficiently large sensitivity and should typically be one order of magnitude larger than σ_{sol} . Furthermore, the cytoplasm permittivity does not affect the sensitivity, except at very high frequencies ($f > f_{cb,2} \simeq 200$ MHz). Finally, the plasma membrane and the cell wall hardly impact the bacterial sensitivity. As a consequence, the outer membrane of Gram-negative bacteria would not affect the sensitivity and the same conclusions can thus be driven for Gram-negative bacteria.

2.4.7 Optimization of metric properties

The impact of some key parameters of the sensor design and bacterial cells are investigated in this section.

Impact of the bacterial diameter d_e

The sensitivity to bacteria is considerably enhanced with larger diameters d_{bact} (Fig. 2.28(a)). When d_{bact} ranges from $0.4 \mu\text{m}$ to $1.4 \mu\text{m}$, S_{max}^{2D} increases in a seemingly-linear way from 1% to 21%, as already shown by 3D simulations [180]. The following fitting is more accurate and presents very close matching to numerical values:

$$S_{f_0}^{2D}(d_{bact}) = \frac{(d_{bact} - A) \cdot (d_{bact} + B)}{C^2} \quad (2.53)$$

with $f_0 = 1$ MHz, $A = 0.282 \mu\text{m}$, $B = 1.21 \mu\text{m}$ and $C = 3.7 \mu\text{m}$. A given transducer geometry is therefore expected to be more sensitive to large bacterial cells, such as *Escherichia coli*.

Impact of the bacterial top distance

As shown in Fig. 2.28(a), the sensitivity becomes non-negligible when bacteria lie in a 4- μm -thick layer above the sensor. When approaching the electrode surface, $S_{1\text{ MHz}}$ quickly grows to a maximum value of 17% at $d_{b,ox} = 200\text{ nm}$ from electrodes, compared to 14.6%, 11.4%, 4.9%, 1.8% at $d_{b,ox} = 0.5\ \mu\text{m}$, $0.8\ \mu\text{m}$, $1.6\ \mu\text{m}$ and $2.5\ \mu\text{m}$ from electrodes,

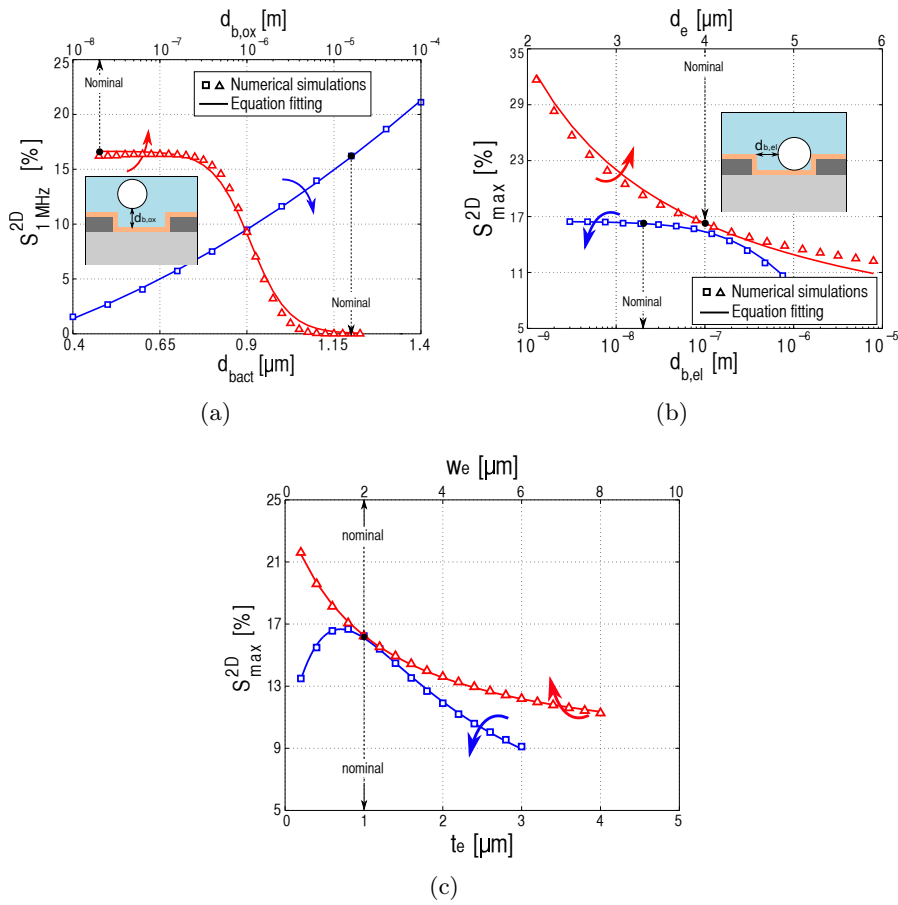


Figure 2.28 – Numerical simulations of $S_{1\text{ MHz}}$ and S_{max}^{2D} versus metric properties, i.e., (a) d_{bact} at fixed $d_{b,ox} = 20\text{ nm}$ (red curves) and $d_{b,ox}$ at fixed $d_{bact} = 1.2\ \mu\text{m}$ (blue curves), (b) $d_{b,el}$ at fixed $d_e = 4\ \mu\text{m}$ (blue curves) and d_e at fixed $d_{b,el} = 20\text{ nm}$ (red curves), (c) t_e (blue curve, at fixed $w_e = 2\ \mu\text{m}$) and w_e (red curve, at fixed $t_e = 1\ \mu\text{m}$). Eqs. 2.53, 2.54, 2.55 and 2.56 are used for the fitting of d_{bact} , $d_{b,ox}$, $d_{b,el}$ and d_e .

respectively. Between 300 nm and 2 μm , the sensitivity is shown to decrease at a rate of $\sim 0.6\%$ each 100 nm. For $d_{b,ox} < 300$ nm, $S_{1 \text{ MHz}}$ is kept identical since only volume properties are monitored at these frequencies, while the cell penetration inside the DL enhances the sensitivity from 0.09% to 0.62% at 1 kHz when $d_{b,ox}$ goes from 300 nm to 20 nm. Based on analytical fitting, $S_{f_0}^{2D}$ is found to be inversely dependent of $d_{b,ox}^2$ at 1 MHz:

$$S_{f_0}^{2D}(d_{b,ox}) = \frac{A^2}{d_{b,ox}^2 + B^2} \quad (2.54)$$

with $f_0 = 1$ MHz, $A = 0.45$ μm and $B = 1.1$ μm . This relationship shows that non-adherent bacterial cells in close vicinity (in this case, $d_{b,ox} < 4$ μm) to the electrode modify the sensor impedance. For this reason, the use of a wash procedure is important to remove them and enable a precise quantification of adherent bacteria only [18].

Impact of the bacterial lateral distance

The position of adherent bacteria between electrodes slightly impacts the sensitivity (Fig. 2.28(b)). When the bacterial cell lies mid-way from the two electrodes, the bacterial sensitivity is at its lowest value (10%). However, when bacteria come closer to one electrode side, the sensitivity increases up to 17%, because of the larger electric field concentration at the electrode edge. Similarly to $d_{b,ox}$, the sharp transition occurs to approximately 300 nm close to the electrode side. The analytical fitting highlights an inverse dependence with $d_{b,el}$:

$$S_{max}^{2D}(d_{b,el}) = \frac{A}{d_{b,el} + B} \quad (2.55)$$

with $A = 0.23$ μm and $B = 1.4$ μm .

Impact of the electrode gap

The last key metric parameter that significantly impacts the bacterial sensitivity is the electrode gap d_e . S_{max}^{2D} evolves from 12% to 42% when d_e spans from 5.9 μm to 1.7 μm (Fig. 2.28(b)). It is important to remind that a smaller d_e can have detrimental impacts on the SNR due to random positions of bacteria between or atop electrodes [180]. The

analytical fitting shows an inverse proportionality with d_e :

$$S_{max}^{2D}(d_e) = \frac{A}{d_e - B} \quad (2.56)$$

with $A = 0.62 \mu\text{m}$ and $B = 0.16 \mu\text{m}$. The highest sensitivity is achieved for the smallest d_e with regards to d_{bact} . For larger electrode gaps, the sensitivity to one bacterial cell falls to zero percent.

2.4.8 Impact of the electrode thickness

Despite most studies are based on planar electrodes, it is possible to gain sensitivity by slightly increasing the electrode thickness t_e . In the case of the *S. epidermidis* cell, an optimal electrode thickness is found at $0.7 \mu\text{m}$ (Fig. 2.28(c)). A smaller thickness places a larger part of the bacterial cell in a region of low electric field, while a larger thickness decreases the percentage of the perturbed volume. The following formula for the maximal sensitivity is found to fit very well the numerical simulations:

$$S_{max}^{2D}(t_e) = A \cdot \frac{t_e + B}{t_e^2 + C \cdot t_e + D^2} \quad (2.57)$$

with $A = 0.30 \mu\text{m}$, $B = 0.38 \mu\text{m}$, $C = 0.4 \mu\text{m}$ and $D = 1.08 \mu\text{m}$. Because $B \simeq C$, the optimum thickness is $t_e^{opt} \simeq D - B = 0.7 \mu\text{m}$, which corresponds to a sensitivity $S_{max}^{2D}(t_e^{opt}) \simeq \frac{A}{2 \cdot (D - B) + CD} = 16.3 \%$. In contrast, ideal planar electrodes ($t_e \simeq 0 \mu\text{m}$) features a sensitivity of $AB/D^2 \simeq 9.7 \%$, which is almost two times smaller than at the optimum electrode thickness. The existence of an optimum thickness only holds when considering that the number of trapped bacteria on the sensor surface is independent of t_e . In opposite, if more bacteria can be trapped thanks to the larger active area brought by higher values of t_e , it is then preferable to increase the electrode thickness [180].

2.4.9 Impact of the electrode width

Choosing an appropriate electrode width w_e is also very important to confine the electric field around the bacterial cell. As shown in Fig. 2.28(c), the electrode width should be minimized to increased the sensitivity to bacteria. The maximal sensitivity features the following dependence with w_e :

$$S_{max}^{2D}(w_e) = A \cdot \frac{w_e + B}{w_e + C} \quad (2.58)$$

with $A = 0.079$, $B = 6.3 \mu\text{m}$ and $C = 2.1 \mu\text{m}$. The maximal sensitivity is then achieved when $w_e \rightarrow 0 \mu\text{m}$ and is equal to $AB/C = 23.7 \%$. On the other hand, whatever the electrode width, the sensitivity cannot be smaller than $A = 7.9 \%$.

Summary

Metric properties strongly impact S_{max}^{2D} . The most predominant factors are the bacterial diameter and the electrode gap. The electrode thickness and width have also non-negligible impacts on the sensitivity, and therefore must not be neglected by the designer. The position of adherent bacteria is shown to slightly alter the sensitivity, as previously reported in [180]. Finally, the sensor can also sense non-adherent bacteria when sufficiently close to the electrodes. It is therefore important to use a wash procedure or reduce d_e to monitor adherent cells only.

2.4.10 Sensitivity optimization

Based on previous sections, it is clear that the device detailed in Section 2.2.1 is not optimal to maximize the sensitivity to bacterial cells. Assuming that the electrolyte and bacteria are fixed by the application, the designer can only tune the device geometry through the electrode gap d_e , thickness t_e and width w_e , as well as the insulator thickness t_{ins} and relative permittivity $\varepsilon_{r,ins}$. Based on analytical expressions (Eqs. 2.42 to 2.56), the sensitivity should be strongly improved with $d_e = 2 \mu\text{m}$, $w_e = 1 \mu\text{m}$, $t_e = 0.7 \mu\text{m}$ and with a TiO_2 insulating layer of thickness $t_{ins} = 10 \text{ nm}$ which features $\varepsilon_{r,ins} = 160$. In addition, the oxide surface charges are given by the following parameters of the site-binding charge model of TiO_2 [200, 201]: $pK_a = 4.94$, $pK_b = 7.4$ and $N_s = 1.8 \cdot 10^{18} \text{ m}^{-2}$. Based on these parameters, the simulation results of the new device achieve a peak sensitivity of 66 % at 1 MHz, which is larger by a factor 4 compared to the nominal sensitivity (16.2 % at 1 MHz) of the device described in Section 2.2.1. The method then demonstrates the significance of considering analytical formula of this study. As verified numerically, the consideration of TiO_2 charges slightly increases the maximal sensitivity by 2 %, compared to the case where charges are evaluated from the site-binding model of Al_2O_3 .

2.5 Conclusions

In this chapter, we have comprehensively studied the use of passivated interdigitated microelectrodes (IDEs) for capacitive biosensing of bacterial cells in a microfluidic channel. These IDEs are CMOS-compatible, miniaturized and feature gaps close to the bacterial diameter.

We have analyzed the complex impedance of IDEs in simple electrolytes, demonstrating the significant impact of the insulator thickness, electrolyte conductivity and permittivity, access lines and transient effects in microfluidic channels [19]. All these effects have been explained with regards to the cutoff frequencies of the established analytical model.

In low-conductive electrolytes containing bacterial cells, we have demonstrated that the normalized admittance $\|Y/\omega\|$ of IDEs linearly increases in real-time with the number of adherent bacterial cells, featuring $\simeq 80 - 100$ aF per adherent bacterium at 1 MHz for the considered electrode geometry [18]. We have also discussed the different sensing methodologies (based on Δ_C , Δ_w , Δ_{rt} and s_{rt}) and the decrease of the sensitivity when the electrolyte conductivity increases. Again, an analytical model has been established and explains the increase of $\|Y/\omega\|$ by the large outer shell capacitance of the bacteria in the considered frequency range [19]. To provide selectivity to one bacterial species, we have proposed an innovative volume-based method using lytic enzymes [18]. Compared to conventional methods using surface coating of antibodies, our method strongly reduces the effects of non-specific adsorption of biomolecules and bacteria, and circumvents pre-treatment steps for real matrixes.

Eventually, 2D numerical simulations have been developed to accurately quantify the sensitivity to bacterial cells versus the applied frequency [19]. Based on Poisson-Nernst-Planck equation, simple expressions for the maximal sensitivity have been obtained in function of each important sensor parameter [20], providing guidelines and tools for the sensor designer.

CHAPTER 3

Bacterial attraction by electrokinetic effects

The main problem with surface-based biosensors is their inability to efficiently trap bacterial cells from the sample volume to the sensor surface. To address this issue, many concentration techniques exist as described in Section 1.3.2. Among them, electrokinetic forces generated by a pair of electrodes enable electrical manipulation of bacterial cells in a liquid sample, while conserving aspects of miniaturization, portability and affordability. In this thesis chapter, a circular ring shaped macroelectrode is integrated around the capacitive biosensor developed in Chapter 2 to direct bacteria from the sample volume towards the sensor surface, and consequently decrease the LoD by two orders of magnitude [21].

The chapter is organized as follows. In Section 3.1, we review fundamentals of electrokinetics including its use towards impedance sensing. In Section 3.2, the design of the passivated electrokinetic electrode is described and the expected electrokinetic effects are studied through analytical models and numerical simulations in Sections 3.3 and 3.4. After describing the observed electrokinetic effects in Section 3.5, their impact on the capacitive sensing of bacteria is detailed in Section 3.6. The achieved performances are eventually compared to the literature in Section 3.7.

3.1 State of the art

In this section, the theory of electrokinetic and natural forces is first reviewed, followed by an analysis of which effect dominates each other. The typical electrode morphologies and some key applications in the field of bacteriology are then described. The combination of impedance sensing with electrokinetics is eventually reviewed.

3.1.1 Theory of electrokinetic forces

Electrokinetics (EK) studies the motion of (bio)particles contained in liquid samples under electrical stimuli applied on electrodes. Different

forces can be identified and sorted into two categories:

- *The forces applied on particles* comprise *electrophoretic* (EP) or *dielectrophoretic* (DEP) forces depending on the spatial uniformity of the electric field.
- *The forces applied on the fluid*, also called *electrohydrodynamic* (EHD) forces, indirectly convey particles thanks to the fluid motion and can be of several types: *electroosmosis* (AC-EO), *electrothermal* (ET) and *buoyancy* forces.

These effects, including *electrolysis* and *boiling*, are all described in next sections for *unpassivated* electrodes in presence of bacterial cells.

Electrophoresis

Electrophoresis (EP) refers to the motion of bacteria, which are typically negatively charged, under uniform electric field in electrolytes. When the DL thickness λ_D is larger than the bacterial radius r_{bact} , the EP force is directly applied on bacteria and moves them at a speed \vec{v} [202]:

$$\vec{v} = \frac{zq\vec{E}_{sol}}{f_v} \triangleq \mu\vec{E}_{sol} \quad (3.1)$$

where f_v is the friction coefficient of the fluid, z the number of electron unit charges, \vec{E}_{sol} the electric field inside electrolyte and μ the electrophoretic mobility. For spherical particles, $f_v = 6\pi\eta r_{bact}$ so that $\mu \simeq \frac{zq}{6\pi\eta r_{bact}}$ with η the fluid dynamic viscosity. When $\lambda_D \ll r_{bact}$, the particle charge is completely screened by counter ions inside the DL so that only the electrolyte ions are conveyed by electrokinetic forces.

Dielectrophoresis

Dielectrophoresis (DEP) causes the motion of bacterial cells in non-uniform electric fields. Depending on the permittivities ε_{sol} and ε_{bact} of the electrolyte and bacteria, the attraction is directed towards regions of high electric field gradients if $\varepsilon_{bact} > \varepsilon_{sol}$ or regions of low electric field gradients if $\varepsilon_{bact} < \varepsilon_{sol}$, which are respectively called *positive* (p-DEP) and *negative dielectrophoresis* (n-DEP) (Fig. 3.1(a)). With AC stimuli, the time-averaged classical dielectrophoretic force $\langle \vec{F}_{DEP} \rangle$ can be analytically expressed as [204, 205]:

$$\langle \vec{F}_{DEP} \rangle = \pi\varepsilon_{sol}r_{bact}^3 \cdot \Re\{f_{CM}(\omega)\} \cdot \vec{\nabla}\{|\vec{E}_{sol}|^2\} \quad (3.2)$$

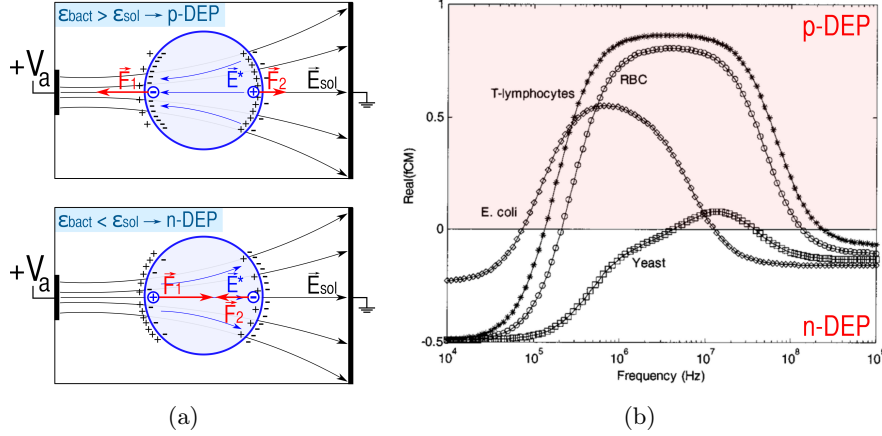


Figure 3.1 – (a) Schematic principle of the dielectrophoresis (DEP) in the cases of $\varepsilon_{bact} > \varepsilon_{sol}$ and $\varepsilon_{bact} < \varepsilon_{sol}$. The electric field lines and applied forces are highlighted. (b) Comparison between Clausius-Mossotti factors f_{CM} of yeast, bacterial cells (*E. coli*), red blood cells (RBC) and T-lymphocytes [203].

where $f_{CM}(\omega) \triangleq \frac{\varepsilon_{bact}^* - \varepsilon_{sol}^*}{\varepsilon_{bact}^* + 2\varepsilon_{sol}^*}$ is the Clausius-Mossotti (CM) factor expressed in function of the complex permittivities $\varepsilon^* \triangleq \varepsilon + \sigma/j\omega$ of the electrolyte and bacteria (Fig. 3.1(b)). At LF, only the conductive properties matter ($\varepsilon^* \simeq \sigma/j\omega$) while permittivities dominate at HF ($\varepsilon^* \simeq \varepsilon$). Particles undergo p-DEP in the frequency range where $\Re\{f_{CM}(\omega)\} > 0$, and n-DEP otherwise. Based on Eq. 3.2 and on the friction factor f_v , the mean speed of particles subjected to \vec{F}_{DEP} at a distance r from the electrodes can be estimated to [206]:

$$\langle \vec{v}_{DEP} \rangle \simeq \frac{r_{bact}^2 V_a^2 \varepsilon_{sol} \cdot \Re\{f_{CM}(\omega)\}}{3\pi^2 \eta r^3} \quad (3.3)$$

where V_a is the amplitude of the AC voltage applied on electrodes. The DEP speed is thus high for large particles $r_{bact} \sim \mu\text{m}$, which are close to microelectrodes (where r is very small). The attraction is short-range since $\vec{v}_{DEP} \propto r^{-3}$ and is thus not suitable for diluted samples. When more accurate expressions are required, the Maxwell stress tensor (MST) \vec{T}_M can be integrated on the particle outer shell [205, 207]:

$$\langle \vec{F}_{DEP} \rangle = \int \langle \vec{T}_M \rangle \cdot \vec{n} d\Gamma \quad (3.4)$$

$$= \int \frac{\Re\{\varepsilon_{sol}^*\}}{4} \cdot \left(\vec{E} \vec{E}^* + \vec{E}^* \vec{E} - \|\vec{E}\|^2 \vec{I} \right) \cdot \vec{n} d\Gamma \quad (3.5)$$

where \vec{I} is the identity tensor, $\vec{E} = \vec{E}_0 \cdot e^{j\omega t}$ the phasorial electric field vector, $\vec{T}_M = \mathbb{R}\{\varepsilon_m^*\}[\vec{E}\vec{E} - \frac{1}{2}(\vec{E} \cdot \vec{E})\vec{I}]$ the MST, \vec{n} the normal vector to the bacterial surface and $d\Gamma$ the surface discretization.

Electroosmosis

Electroosmosis (EO) is the fluid motion induced by the displacement of ions within the DL atop electrodes. The phasorial form of the potential drop across the DL can be estimated to [206]:

$$\Delta\phi_{DL} = \frac{V_a/2}{1 + j\omega\tau_1} \quad (3.6)$$

with $\tau_1 = \frac{\pi r C_{DL}}{2\sigma_{sol}} = \frac{\pi r \varepsilon_{sol}}{2\sigma_{sol} \lambda_D}$. Consequently, the slip velocity within the DL at the electrode surface can be approximated to [206]:

$$\langle \vec{v}_{slip} \rangle = \frac{\varepsilon_{sol} V_a^2 \Lambda}{8\eta r} \cdot \frac{\omega^2 \tau_1^2}{(1 + \omega^2 \tau_1^2)^2} \quad (3.7)$$

with $\Lambda = \frac{C_{stern}}{C_{stern} + C_{DL}} \simeq 0.25$ an empirical factor and C_{stern} the Stern capacitance [206]. The action of AC-EO is long-range, since $\langle v_{slip} \rangle \propto r^{-1}$. The strength ratio between AC-EO and DEP is:

$$\frac{\langle \vec{v}_{slip} \rangle}{\langle \vec{v}_{DEP} \rangle} \propto \left(\frac{r}{r_{bact}} \right)^2 \quad (3.8)$$

which shows that AC-EO becomes outclassed by DEP at large particle diameters and close to the electrodes.

Electrothermal flow

Electrothermal (ET) flow is the fluid motion arising from gradients of σ_{sol} and ε_{sol} , caused by a gradient of temperature (T) in the fluid. Depending on its origin, two kinds of ET flows can be distinguished:

- The *Joule-heating electrothermal* (J-ET) flow occurs because of the temperature increase by Joule dissipation [83, 208]. In this case, the Poisson equation states that $-\sigma_{sol} E_{sol,RMS}^2 = k \vec{\nabla}^2 T$ and the temperature gradient is thus approximated to:

$$\vec{\nabla} T = \frac{V_a^2 \sigma_{sol}}{4\pi k r} \cdot \left(1 - \frac{2\theta}{\pi} \right) \cdot \vec{a}_\theta \quad (3.9)$$

with k the electrolyte thermal conductivity and θ the angle formed by the particle with regards to the inter-gap electrode center (see Fig. C.2 for an illustration).

- The *Light-induced electrothermal* (L-ET) flow arises from a temperature increase coming from the microscope light intensity [208, 209]. In this case, the temperature gradient is constant and depends on the light intensity $\vec{\nabla}T = -|\partial T/\partial y| \cdot \vec{a}_y$ [206].

Two different expressions are thus obtained for the fluid speed in the case of J-ET and L-ET [206]:

$$\langle \vec{v}_{J-ET} \rangle \simeq -5 \cdot 10^{-4} \cdot M(\omega, T) \cdot \frac{\varepsilon_{sol} \sigma_{sol} V_a^4}{kr\eta T} \cdot \vec{a}_\theta \quad (3.10)$$

$$\langle \vec{v}_{L-ET} \rangle \simeq 3 \cdot 10^{-3} \cdot M(\omega, T) \cdot \frac{\varepsilon_{sol} V_a^2}{\eta T} \cdot \left| \frac{\partial T}{\partial y} \right| \cdot \vec{a}_y \quad (3.11)$$

where $M(\omega, T) = \frac{1}{1+(\omega\tau_2)^2} \cdot \left[\frac{T}{\sigma_{sol}} \frac{\partial \sigma_{sol}}{\partial T} - \frac{T}{\varepsilon_{sol}} \frac{\partial \varepsilon_{sol}}{\partial T} \right] + \frac{T}{2\varepsilon_{sol}} \frac{\partial \varepsilon_{sol}}{\partial T}$ and $\tau_2 = \frac{\varepsilon_{sol}}{\sigma_{sol}}$. As shown by Eqs. 3.10 and 3.11, the electrothermal flow is mainly long-range and presents two operating modes: at LF ($\omega \ll \tau_2^{-1}$), the first term of $M(\omega, T)$ dominates while $\frac{T}{2\varepsilon_{sol}} \frac{\partial \varepsilon_{sol}}{\partial T}$ prevails at HF ($\omega \gg \tau_2^{-1}$).

Buoyancy

Buoyancy is the fluid motion induced by local gradients $\vec{\nabla}\rho_{sol}$ of the fluid mass density, creating a natural convection through gravitational forces. For fluids contacting electrokinetic electrodes, thermal gradients $\vec{\nabla}T$ are the main origin of $\vec{\nabla}\rho_{sol}$:

$$\langle \vec{v}_{g,max} \rangle = 0.02 \cdot \frac{\partial \rho_{sol}}{\partial T} \cdot \frac{\sigma_{sol} r^2 V_a^2}{\eta k} \cdot \vec{g} \quad (3.12)$$

It only occurs far from microelectrodes (\sim mm).

Boiling

High voltage amplitudes can occasionally generate temperature increases larger than 75°C, producing water boiling when the initial fluid temperature is 25°C [206]. Integrating Eq. 3.9, the temperature shift is [206]:

$$\Delta T(\theta) = \frac{\sigma_{sol} V_a^2}{4k} \cdot \left(\frac{\theta}{\pi} - \frac{\theta^2}{\pi^2} \right) \quad (3.13)$$

Consequently, the maximal temperature increase occurs when $\theta = \frac{\pi}{2}$ and is equal to $\Delta T_{max} = \frac{\sigma_{sol} V_a^2}{16k}$. The minimal voltage amplitude required for boiling the electrolyte is thus equal to: $V_a \simeq 20 \cdot \sqrt{\frac{3k}{\sigma_{sol}}}$. For typical conductivities $\sigma_{sol} = 0.001, 0.01, 0.1$ and 1 S/m, the minimal boiling voltages V_a are 850, 270, 85 and 27 V, respectively.

Electrolysis

Water electrolysis is the transformation of H₂O into O₂ and H₂ molecules, induced by DC or AC electrical currents through the fluid. In DC condition, a voltage of 1.5 V is often sufficient to cause water electrolysis while a significantly higher voltage is required in AC condition. It is typically admitted that an AC voltage amplitude $\|\Delta\phi_{DL}\|$ across the DL of 2 V is sufficient to create electrolysis [206]. Based on Eq. 3.6, the corresponding voltage amplitude is then equal to $V_a = 4\sqrt{1 + (\omega\tau_1)^2}$.

3.1.2 Theory of natural forces

Besides electrokinetic forces, each bioparticle undergoes three other external forces related to the gravity, the thermal noise and the fluid flow.

Gravity

When a particle of density ρ_{bact} is suspended in a medium of density ρ_{sol} , the particle is subject to a gravity force $\vec{F}_g = \frac{4\pi r_{bact}^3}{3} \cdot (\rho_{bact} - \rho_{sol})g \cdot \vec{a}_z$. The particle speed can thus be approximated to [206]:

$$\vec{v}_g = \frac{\vec{F}_g}{f_v} = \frac{2r_{bact}^2}{9\eta} \cdot (\rho_{bact} - \rho_{sol})g \cdot \vec{a}_z \quad (3.14)$$

where $f_v = 6\pi\eta r_{bact}$ is the friction factor, $\rho_{bact} \simeq 1200 \text{ kg/m}^3$ and $\rho_{sol} \simeq 1000 \text{ kg/m}^3$ (see Section 1.1.2).

Brownian motion

Brownian noise refers to random particle displacements induced by temperature and evaluated to [206]:

$$\Delta x = \sqrt{\frac{2k_b T}{3\pi r_{bact} \eta}} \cdot t \quad (3.15)$$

where t is the elapsed time. This displacement can be assumed negligible for large particles such as bacterial cells ($r_{bact} \sim \mu\text{m}$).

Stokes forces

The laminar microfluidic flow, which is generated by mechanic pumping, indirectly moves bioparticles through Stokes forces according to a Poiseuille's speed profile. In this thesis, these forces can be considered negligible as electrokinetic forces are experimentally observed far larger.

3.1.3 Scaling laws

As explained in Section 3.1.1, the different electrokinetic effects depend on many key parameters, such as the applied frequency f , the bacterial diameter r_{bact} , the electrolyte conductivity σ_{sol} , the bacteria-electrode distance r and the AC voltage amplitude V_a . Inspired from [206], some key scaling tendencies are now described for unpassivated electrodes.

At low σ_{sol} and f , AC-EO dominates for most voltages V_a and distances r (Fig. 3.2(a)). However, the DEP remains the main force at micrometer r . At higher f , the AC-EO drops in amplitude and the DEP slightly dominates up to $r \simeq 100 \mu\text{m}$ (Fig. 3.2(b)). By considering

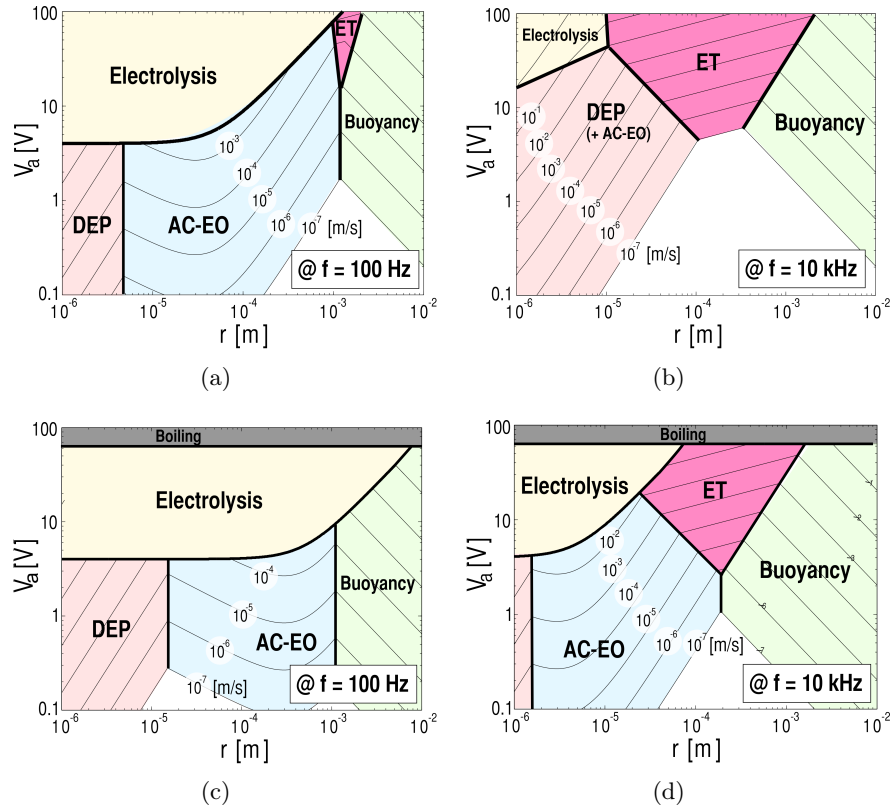


Figure 3.2 – Illustration of dominant electrokinetic effects in function of the voltage amplitude V_a and the distance r between bacteria and electrodes: (a) (b) at $\sigma_{sol} = 1.8 \text{ mS/m}$ and (c) (d) $\sigma_{sol} = 180 \text{ mS/m}$. The electrodes are unpassivated, $r_{bact} = 0.6 \mu\text{m}$, $\eta = 1 \text{ mPa}\cdot\text{s}$, $\varepsilon_{sol} = 80$, $\rho_{sol} = 1000 \text{ kg/m}^3$, $\frac{1}{\varepsilon_{sol}} \cdot \frac{\partial \varepsilon_{sol}}{\partial T} = -0.004 \text{ K}^{-1}$, $\frac{1}{\sigma_{sol}} \cdot \frac{\partial \sigma_{sol}}{\partial T} = 0.02 \text{ K}^{-1}$, $T = 300 \text{ K}$, $k = 0.6 \text{ W}/(\text{m}\cdot\text{K})$. These graphs are inspired from [206].

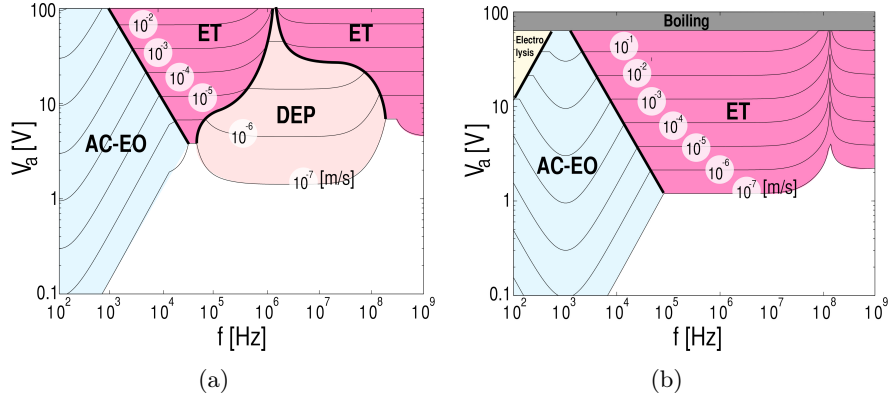


Figure 3.3 – Illustration of dominant electrokinetic effects in function of the voltage amplitude V_a and the applied frequency f between bacteria and electrodes for $r = 50 \mu\text{m}$: (a) at $\sigma_{sol} = 1.8 \text{ mS/m}$ and (b) at $\sigma_{sol} = 180 \text{ mS/m}$. The same parameters as in Fig. 3.2 are used.

larger r and V_a , the ET flow becomes significant. Another representation of these phenomena with f are provided in Fig. 3.3.

When considering larger σ_{sol} , the AC-EO range is shifted to higher distances r and its amplitude slightly reduced (Fig. 3.2(c)). At higher f , the ET flow becomes very important and shrinks the part where AC-EO dominates (Fig. 3.2(d)). Again, the Fig. 3.3 provides another view on dominant electrokinetic phenomena depending on V_a and f .

3.1.4 Electrode designs, materials and voltages

As fully summarized in [204], many different electrokinetic electrode designs exist. Most of them target high electric field gradients with micrometer gaps (see Eq. 3.2) or with special geometric patterns such as spikes or round shapes. The most common designs include castellated electrodes [83, 105] (Figs. 3.4(g) and 3.4(h)), parallel electrodes [126, 147, 210] (Figs. 3.4(a), 3.4(i) and 3.4(j)) or round shaped electrodes [85, 211, 212] (Figs. 3.4(d), 3.4(e) and 3.4(f)). The signals applied on electrodes are basically chosen among the three following possibilities:

- One electrode side is biased with a single AC voltage, the other with ground [83, 105, 126, 210, 211, 213].
- One electrode side is biased with a AC voltage, the other with its copy shifted by 180° in phase [85, 147].

- Quadrupole electrodes are biased with four AC voltages featuring 45°-shifts in phase [214, 215].

Electrodes are typically patterned with resistant metals, without insulators. However, it is possible to intentionally include insulating materials in the two following cases:

- *Contactless DEP* (c-DEP) uses an insulator between the electrolyte and electrodes [213] (Fig. 3.4(b)). Bubble formation, metal fouling and contamination effects are thus prevented, but high voltages $\sim 100 V_{RMS}$ are typically required.
- *Insulator-based DEP* (i-DEP) uses insulating materials to generate local electric field gradients and therefore DC DEP in the electrolyte, without the use of miniaturized electrodes. For instance, insulating microbeads filling the whole fluidic channel height can serve as i-DEP filter retaining bacteria [87], while insulating pillars generating i-DEP can trap bacteria [217] (Fig. 3.4(f)).

3.1.5 Key applications in bacteriology

Electrokinetic effects described in Section 3.1.1 can be used in a wide range of applications [204]. In this section, three main applications in the field of bacteriology are detailed.

Separation between viable and dead bacteria

Because of its dependence on the dielectric properties of the bacterial cells, DEP can be used to separate viable from dead bacteria [126]. It is typically possible in a short range of frequency (around 50 kHz) where viable cells undergo p-DEP while dead cells n-DEP. At lower or higher frequencies, both kinds of cells are subject either to n-DEP or p-DEP, respectively, which renders impossible their differentiation.

Dielectric characterization

For the same reason as previously explained, DEP can also be used to precisely characterize the dielectric properties of each layer forming bacterial cells, such as the cytoplasm, plasma membrane and cell wall [29, 30, 214, 218]. At each frequency, the DEP collection on electrodes is estimated and reflects the Clausius-Mossotti factor f_{CM} . It is thus possible to estimate physical parameters such as $\varepsilon_{r,cyt}$, σ_{cyt} , $\varepsilon_{r,pl}$, $\varepsilon_{r,wall}$

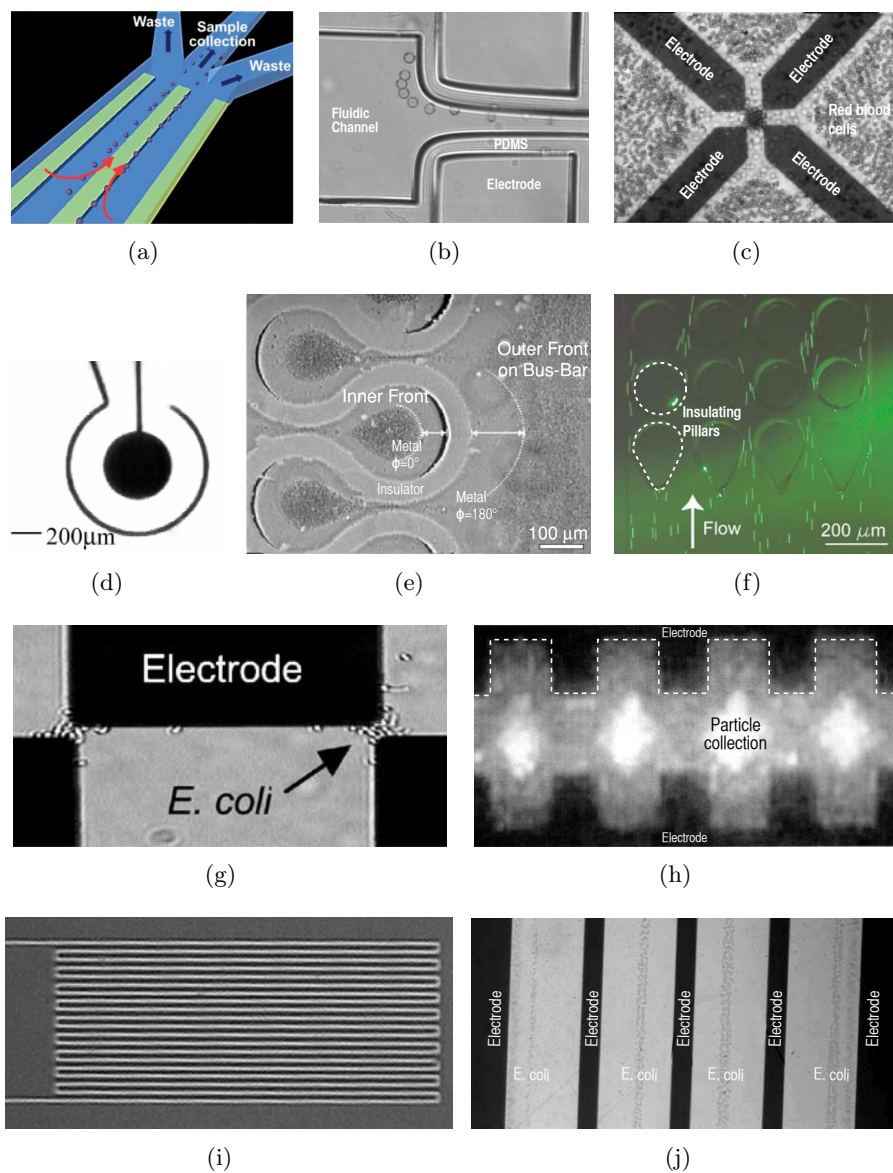


Figure 3.4 – Summary of existing electrode designs for electrokinetic effects: (a) parallel electrodes for particle concentration [210], (b) insulated electrodes for c-DEP [213], (c) quadrupole electrodes [214, 215], (d) central and surrounding electrodes [211], (e) zipper electrodes [85], (f) insulating pillars for i-DEP [212], (g) micrometer gaps with castellated electrodes for DEP [105], (h) castellated electrodes [83], (i) continuous serpentine wire [216] and (j) parallel electrodes [126, 147].

and σ_{wall} , by fitting the experimental collection with an analytical model of the multi-shell bacteria. This technique is sufficiently sensitive to enable a discrimination between isogenic mutants of *E. coli* [218].

Particle trapping

In the field of biosensors, bacterial trapping is certainly the most interesting application of electrokinetic effects. These can either be used individually or combined to each others.

In the first case, p-DEP is the most used electrokinetic force to trap bacterial cells on the edges of micrometer-gap castellated micro-electrodes [84, 105, 150, 174, 219, 220]. However, the ability of AC-EO to focus bacterial cells between two parallel electrodes has also been demonstrated, with additional impedance measurements [147]. Similarly, zipper electrodes focus bacterial cells at the center of a circularly shaped electrode, which can be used as an efficient SPR biosensor since there is no light scattering at the electrode edge [85].

In the second case, combining electrokinetic effects can maximize the trapping range. Short-range DEP and long-range AC-EO can be used together in low-conductive samples by using a serpentine electrode [211, 216]. However, their different relaxation times can lead to incompatibility, since n-DEP can occur in regions of highest AC-EO. To promote p-DEP simultaneously with AC-EO, it is possible to shift f_{CM} towards lower frequencies by increasing $\varepsilon_{r,sol}$ thanks to the addition of ionic molecules [216]. A second possibility consists in combining short-range p-DEP/EP with long-range J-ET to efficiently trap bacteria or viruses in high-conductive buffers [210, 221]. These two methods have currently not been demonstrated along with impedance measurements.

3.1.6 Electrokinetics with impedance sensing of bacteria

Electrokinetics can be used to direct bacterial cells from the sample volume to the surface of impedance sensors, thus serving as a concentration tool and therefore lowering their detection limit. Several established methods exist in the literature:

- The *dielectrophoretic impedance measurement* (DEPIM) consists in trapping bacteria on the edges of castellated electrodes thanks to p-DEP and measuring the subsequent real-time increase of the conductance G_{sol} [84]. Voltage amplitudes and frequency are typically identical for impedance measurements and electrokinetics.

Selectivity is added to DEPIM by using one of the three following methods:

- All bacterial species are first trapped by p-DEP on electrodes. Antibodies are added to stick target bacteria together and a flow is then applied to wash away non-target bacteria [174].
 - Antibodies are added to the bacterial sample to form large clusters of target bacteria by p-DEP between two needles. This solution is then brought atop microelectrodes generating p-DEP, so that only bacterial clusters are trapped [174].
 - Antibodies coat the inter-electrode gap and p-DEP is applied on microelectrodes to trap all bacterial species. After deactivating p-DEP and washing, only target bacteria remain [105].
- The *electropermeabilization-assisted (EPA)-DEPIM* consists in applying brief high-amplitude AC voltages to pierce the membrane of yeast cells [219] or bacteria cells [150], enabling ion release and increasing the sensitivity by two orders of magnitude. Selectivity can also be supplied by surface coating of antibodies [105].
 - The previous methods can be enhanced by patterning a first set of electrodes on one side of the fluidic channel, repelling bacteria by n-DEP towards the impedance sensing electrodes on the other side, which uses DEPIM or EPA-DEPIM for bacteria trapping [220].
 - Splitting electrokinetics and impedance sensing in distinct fluidic chambers enables a separate optimization of their volumes, applied voltages and electrode designs [86]. The first chamber directs and concentrates bacteria by DEP towards the second chamber, where p-DEP retains bacteria on IDEs during a growth phase. The first chamber can also include insulating pillars to trap bacteria by i-DEP [212]. Those are then directed towards the second chamber by deactivating electrokinetics and using flow.
 - Bacterial cells can be concentrated between two electrodes by AC-EO. The LF impedance in DI water can be used for detection of the trapped bacteria [147].

An exhaustive comparison of works combining electrokinetics with impedance sensing of bacterial cells is provided in Table 3.1. Several important comments can be drawn on these works (excluding the study carried out in this chapter):

Table 3.1 – Summary of works combining electrokinetic effects and impedance spectroscopy for whole-cell bacteria detection.

	[84]	[150]	[86]	[147]	[105]	[220]	This work [21]
Bacteria	<i>E. coli</i>	<i>E. coli</i>	<i>L. monocyt.</i>	<i>E. coli</i>	<i>E. coli</i>	<i>E. coli</i>	<i>S. epidermidis</i>
Medium (cond.)	Mannitol (200 $\mu\text{S}/\text{m}$)	DI water (200 $\mu\text{S}/\text{m}$)	DI water (100 $\mu\text{S}/\text{m}$)	DI water (2 mS/m)	Mannitol (200 $\mu\text{S}/\text{m}$)	Mannitol (100 $\mu\text{S}/\text{m}$)	PBS 1:1000 (1.8 mS/m)
Material	Cr/Pt	Cr	EK: Al/SiO ₂ IM: Pt/Ti	Ti/Au	Cr	Cr	Al/Al ₂ O ₃
Elect. width/gap	NA/5 μm	50 $\mu\text{m}/5 \mu\text{m}$	EK: NA/NA IM: NA/NA	40 $\mu\text{m}/20 \mu\text{m}$	50 $\mu\text{m}/5 \mu\text{m}$	50 $\mu\text{m}/5 \mu\text{m}$	EK: 50 $\mu\text{m}/50 \mu\text{m}$ IM: 4 $\mu\text{m}/2 \mu\text{m}$
Principle	DEPIM	EPA-DEPIM	Concentration p-DEP	AC EO	Ab-surfacic EPA-DEPIM	Combined {n/p}-DEP	Resonant cDEP and J-ET
Frequency	100 kHz	100 kHz	100 kHz	100 Hz	100 kHz	n: 1 kHz p: 100 kHz	63 MHz
Voltage	10.7 V_{pp}	DEP: 5 V_{pp} EPA: 20 V_{pp}	16 V_{pp}	2.8 V_{pp}	DEP: 5 V_{pp} EPA: 20 V_{pp}	p-DEP: 5 V_{pp} n-DEP: 20 V_{pp}	14 V_{pp}
Channel volume	NA	15 μL	EK: 400 pL IM: 5.3 nL	NA	15 μL	NA	1 μL
Flow rate*	13 mL/min	0.5 mL/min	1.7 $\mu\text{L}/\text{min}$	NA	0.5 mL/min	0.27 m/s**	5 $\mu\text{L}/\text{min}$
LoD	10 ⁵ CFU/mL	10 ² CFU/mL	7 · 10 ⁵ CFU/mL	5 · 10 ³ CFU/mL	10 ⁶ CFU/mL	NA	10 ⁵ CFU/mL
Incub. time	10 min	3 h	2 h	NA	10 min	NA	20 min
FoM₁	1.3 · 10 ⁷ CFU	9 · 10 ³ CFU	1.4 · 10 ⁵ CFU	NA	5 · 10 ⁶ CFU	NA	10 ⁴ CFU
FoM₂	1.3 · 10 ⁸ CFU-min	1.6 · 10 ⁶ CFU-min	1.7 · 10 ⁷ CFU-min	NA	5 · 10 ⁷ CFU-min	NA	2 · 10 ⁵ CFU · min

DEPIM: Dielectrophoretic impedance measurement; EK: Electrokinetics; EO: Electroosmosis; EPA: Electroporation; IM: Impedance measurement; NA: Not Available; *: during EK incubation; **: flow not available.

- Most works use electrode gaps as close as possible ($\sim 5 \mu\text{m}$) to the bacterial diameter, to increase the short-range trapping by DEP.
- All works report trapping only in low-conductive solutions, where σ_{sol} ranges from $100 \mu\text{S/m}$ to 2 mS/m .
- Most works use low ($\simeq 100 \text{ Hz}$) or medium ($\simeq 100 \text{ kHz}$) frequencies.
- Limits of detection (LoD) range between 10^2 CFU/mL to 10^6 CFU/mL , but strongly depend on the incubation time t_{incub} and flow rate FR . By defining figures of merit $FoM_1 \triangleq LoD \cdot FR \cdot t_{incub}$ and $FoM_2 \triangleq LoD \cdot FR \cdot t_{incub}^2$ (see Section 1.3.5), the absolute detectable number of bacteria ranges from $9 \cdot 10^3 \text{ CFU}$ to $1.3 \cdot 10^7 \text{ CFU}$ and the absolute detectable number of bacteria per min from $1.6 \cdot 10^6 \text{ CFU}\cdot\text{min}$ to $1.3 \cdot 10^8 \text{ CFU}\cdot\text{min}$.

3.1.7 Chapter innovations

In this chapter, we present an innovative design combining contactless IDEs, demonstrated as high-sensitive surface-based capacitive transducers for bacterial sensing (see Chapter 2), with a surrounding passivated macroelectrode enabling multi-range trapping of bacteria in bulk electrolyte thanks to combined cDEP, AC-EO and J-ET effects. At 63 MHz where cDEP and J-ET effects co-exist and are amplified by an electromagnetic resonance effect, a detection limit of 10^5 CFU/mL of *Staphylococcus epidermidis* is achieved within 20 minutes of incubation. Around 10 kHz where AC-EO dominates, the detection limit is $3.5 \cdot 10^5 \text{ CFU/mL}$ of *S. epidermidis* within 20 minutes. Compared to the state of the art reviewed in Section 3.1.6, several key innovations can be identified:

- This work is the first to combine short-range (cDEP) with long-range (AC-EO and J-ET) trapping for an improved bacteria collection on the surface of a capacitive sensor.
- An electromagnetic resonant effect, identified at 63 MHz, greatly enhances the trapping of bacterial cells on the electrode edges by combined cDEP and J-ET effects. This effect is similar to the resonance event reported for quadrupole electrodes [214], but which was not exploited towards impedance sensing.
- An innovative flow-based method is developed to direct bacterial cells, previously captured on the electrode edges at 63 MHz, towards the sensor center.

3.3 Analytical models

This section extends the formulae of DEP, AC-EO and J-ET effects (see Section 3.1.1) to the case of contactless and planar electrodes, thus including a passivated layer in the analysis. The system is assumed two-dimensional and resonance effects that are possibly due to the setup (cables, probes, etc.) are not considered in the following models. Calculation details are provided in Appendix C.3.

When electrodes are passivated with a thin insulating layer, the phasorial form of the electric field \vec{E}_{sol} exerted in the electrolyte between electrodes becomes frequency-dependent:

$$\vec{E}_{sol}(\omega, r) = \frac{V_a}{\pi r} \cdot H(\omega, r) \cdot \vec{a}_\theta \quad (3.16)$$

$$H(\omega, r) \triangleq \frac{1}{1 + 2 \cdot \left(\frac{\varepsilon_{sol}}{\varepsilon_{ins}} + \frac{\sigma_{sol}}{j\omega\varepsilon_{ins}} \right) \cdot \frac{t_{ins}}{\pi r}} \quad (3.17)$$

where ω is the angular frequency, V_a the amplitude of the applied AC voltage, r the distance from electrodes, ε_{sol} and σ_{sol} the permittivity and conductivity of the electrolyte, ε_{ins} and t_{ins} the permittivity and thickness of the insulating layer. The bacterial speed produced by cDEP is given by:

$$\langle \vec{v}_{DEP} \rangle \simeq \frac{r_{bact}^2 \varepsilon_{sol} \Re\{f_{CM}(\omega)\} \cdot V_a^2}{3\pi^2 \eta \cdot \left(r + 2 \frac{\varepsilon_{sol} t_{ins}}{\varepsilon_{ins} \pi} \right)^3} \cdot \frac{-\vec{a}_r}{[1 + Q(\omega, r)^2]^2} \quad (3.18)$$

where $Q(\omega, r) \triangleq \frac{2\sigma_{sol} t_{ins}}{\omega(r\varepsilon_{ins}\pi + 2\varepsilon_{sol} t_{ins})}$, r_{bact} is the bacteria radius, η the dynamic viscosity of the electrolyte, $f_{CM}(\omega) \triangleq \frac{\varepsilon_{bact}^* - \varepsilon_{sol}^*}{\varepsilon_{bact}^* + 2\varepsilon_{sol}^*}$ the frequency-dependent Clausius-Mossotti factor, ε_{sol}^* and ε_{bact}^* the complex permittivities of the electrolyte and bacteria. By assuming the same permittivity in the DL as in the electrolyte, the slip velocity of AC-EO atop electrodes depends on the voltage drop across the DL and is given by:

$$\langle \vec{v}_{AC-EO} \rangle \simeq \frac{V_a^2 \omega^2 \varepsilon_{sol} \Lambda \vec{a}_r}{8\eta (C_{DL}/C_s)^2 r} \cdot \frac{(\tau_1 + \tau_2)\tau_1 + \omega^2 \tau_1^2 \tau_2^2}{\left[\omega^2 \tau_1^2 + (1 + \omega^2 \tau_1 \tau_2)^2 \right]^2} \quad (3.19)$$

with $\tau_1(\omega) \triangleq \frac{\pi r C_s / (2\sigma_{sol})}{1 + \omega^2 \tau_2^2}$ the system time constant, $\tau_2 \triangleq \frac{\varepsilon_{sol}}{\sigma_{sol}}$ the electrolyte time constant, $C_{DL} = \varepsilon_{sol} / \lambda_D$ and $C_{ins} = \varepsilon_{ins} / t_{ins}$ the DL and insulator 2D capacitances, $C_s = [C_{DL}^{-1} + C_{ins}^{-1}]^{-1}$ the series capacitance of C_{ins} and C_{DL} and $\Lambda = \frac{C_{stern}}{C_{stern} + C_{DL}} \simeq 0.25$ an empirical factor accounting

for the Stern capacitance C_{stern} [206]. For the J-ET flow, the temperature gradient ∇T comes from the Poisson equation and is a function of ω , r , V_a , $H(\omega, r)$ and θ . The following expression is obtained for the bacteria speed under J-ET:

$$\langle \vec{v}_{J-ET} \rangle \simeq -5 \cdot 10^{-4} \cdot M(\omega, T) \cdot \frac{\varepsilon_{sol} \sigma_{sol} V_a^4 \|H(\omega, r)\|^4}{kr\eta T} \cdot \vec{a}_\theta \quad (3.20)$$

where $M(\omega, T) \triangleq \frac{1}{1+(\omega\tau_2)^2} \cdot \left[\frac{T}{\sigma_{sol}} \frac{\partial \sigma_{sol}}{\partial T} - \frac{T}{\varepsilon_{sol}} \frac{\partial \varepsilon_{sol}}{\partial T} \right] + \frac{T}{2\varepsilon_{sol}} \frac{\partial \varepsilon_{sol}}{\partial T}$ and k is the electrolyte thermal conductivity. The parameter values corresponding to the experimental conditions are summarized in Table 3.2. It is important to note that the complex permittivity ε_{bact}^* of bacteria accounts for a two-shell bacteria representation with parameters given in Table 2.4.

Table 3.2 – Parameters used for analytical models of electrokinetic effects.

Parameter	Description	Value
η	Fluid dynamic viscosity	10^{-3} Pa.s [206]
σ_{sol}	Electrolyte conductivity	1.8 mS/m
ε_0	Vacuum permittivity	$8.85 \cdot 10^{-12}$ F/m
ε_{sol}	Electrolyte permittivity	$80 \cdot \varepsilon_0$
ε_{ins}	Insulator permittivity	$9 \cdot \varepsilon_0$
t_{ins}	Insulator thickness	33 nm
C_{stern}	Stern capacitance	0.007 F/m ² [206]
T	Temperature	300 K
V_a	AC voltage amplitude	7 V
k	Electrolyte thermal conductivity	0.6 W/(m·K)
r_{bact}	Bacteria diameter	0.6 μ m
r	Distance from the electrodes	50 μ m
$\frac{1}{\sigma_{sol}} \frac{\partial \sigma_{sol}}{\partial T}$	Electrolyte conductivity variation with temperature	0.02 K ⁻¹ [206]
$\frac{1}{\varepsilon_{sol}} \frac{\partial \varepsilon_{sol}}{\partial T}$	Electrolyte permittivity variation with temperature	-0.004 K ⁻¹ [206]

3.4 Numerical simulations

2D finite-element method (FEM) simulation of cDEP was performed with Comsol Multiphysics[®]. The IDEs are simplified by a single plain electrode at virtual mass (since $50 \text{ mV} \ll 7 \text{ V}$), while a AC potential of 14 V_{pp} is applied on the macroelectrode. Similarly to Section 3.3, resonance effects are not included in the simulations. A single bacterial cell, modeled as a two-shell representation of *Staphylococcus* spp. (see Table

2.4), is located between the macroelectrode and the IDEs, 50 μm atop the electrode surface. The phasorial form of Maxwell equations is used to solve the electrical potential, by neglecting ion transport involved in the DL. To extract the dielectrophoretic force \vec{F}_{DEP} , the most accurate method consists in integrating the Maxwell Stress Tensor (MST) [207] on the boundary between bacterial cell wall and electrolyte [205]:

$$\vec{F}_{DEP} = \int \langle \vec{T}_M \rangle \cdot \vec{n} d\Gamma \quad (3.21)$$

$$= \int \frac{\Re\{\varepsilon_{sol}^*\}}{4} \cdot \left(\vec{E}_{sol} \vec{E}_{sol}^* + \vec{E}_{sol}^* \vec{E}_{sol} - \|\vec{E}_{sol}\|^2 \vec{I} \right) \cdot \vec{n} d\Gamma \quad (3.22)$$

where \vec{I} is the identity tensor, \vec{E}_{sol} the phasorial form of the electric field, $\vec{T}_M = \Re\{\varepsilon_{sol}^*\} [\vec{E}_{sol} \vec{E}_{sol} - \frac{1}{2} (\vec{E}_{sol} \cdot \vec{E}_{sol}) \vec{I}]$ the MST, \vec{n} the normal vector to the bacterial surface and $d\Gamma$ the surface discretization.

3.5 Electrokinetic phenomena

In this section, the electrokinetic phenomena experimentally observed with the device depicted in Fig. 3.5(a) are described and explained with regards to analytical models and numerical simulations. The measurement setup is fully described in Appendix A.5 and the bacterial handling in Appendix A.3. The bacteria speed is directly extracted from the movies taken with the inverted microscope, thanks to the *PIVlab* program as described in Appendix B.2.

Description of the experimental electrokinetics

When applying a sinusoidal stimuli of 14 V_{pp} whose frequency ranges from 1 kHz to 100 MHz, two distinct electrokinetic effects have been observed at different frequency ranges:

- Comprised between ca. 1 kHz and 50 kHz in PBS 1:1000, the first electrokinetic effect brings bacterial cells from the bulk volume to the sensor centre (Figs. 3.6(a) and 3.6(b)). The attraction is maximal at 1 kHz, featuring mean and maximum speeds of 5 $\mu\text{m/s}$ and 57 $\mu\text{m/s}$, as computed by *PIVlab* (Fig. 3.7(a)). This effect was strongly attenuated in PBS 1:100 and almost inexistent in PBS 1:10 and pure PBS.

- From ca. 50 kHz to 80 MHz in PBS 1:1000, bacteria are rather trapped on the sensor and macroelectrode peripheries thanks to combined short and long-range attractions, featuring vortexes directing bacterial cells from the bulk volume to the chip surface (Figs. 3.6(c) and 3.6(d)). At 63 MHz precisely (called the *resonance frequency*), the bacteria speed dramatically increases both at the surface and volume levels. The mean and maximal bacterial speeds were 28 $\mu\text{m/s}$ and 116 $\mu\text{m/s}$ at 63 MHz, which is approximately 5 times larger in average compared to the 1-kHz effect (Fig. 3.7(a)). The surface trapping was steadily more attenuated in PBS 1:100 and PBS 1:10, and eventually vanished in pure PBS. The volume motion through the whole channel depth was identical in PBS 1:100, but reversed and slightly stronger in PBS 1:10 and PBS. The resonance frequency was kept identical from PBS 1:1000 to PBS, and comprised between 58 and 63 MHz for all measured devices (more than 10).

Physical explanation of the observed electrokinetic effects

To physically understand which electrokinetic forces are involved in the two effects previously described, the analytical expressions of the bacterial speed without resonance effects (see Section 3.3) are compared for cDEP, AC-EO and J-ET at two electrical conductivities $\sigma_{sol} = 1.8$ mS/m and 180 mS/m, corresponding to PBS 1:1000 and PBS 1:10 (Fig. 3.8(a) and 3.8(b)). As the absolute value of bacteria speed is considered in these figures, the sharp transitions simply correspond to sign changes, i.e. bacteria move in the opposite direction. Light-induced electrothermal flow (L-ET) was not considered since bacterial attraction was experimentally independent of the light intensity from the inverted microscope. Four cases must be distinguished:

- *Case 1 - $f < 20$ kHz and $\sigma_{sol} = 1.8$ mS/m:* AC-EO effects dominate with a slight n-DEP force (Fig. 3.8(a)), confirming streamlines driving bacterial cells towards rest position in the sensor center as shown in Fig. 3.6(a) and 3.6(b), similarly to [85].
- *Case 2 - $f < 20$ kHz and $\sigma_{sol} = 180$ mS/m:* the low-frequency forces are inexistent because of the screening by the insulator, making AC-EO decreasing as ω^2 and J-ET/cDEP as ω^4 (Fig. 3.8(b)).

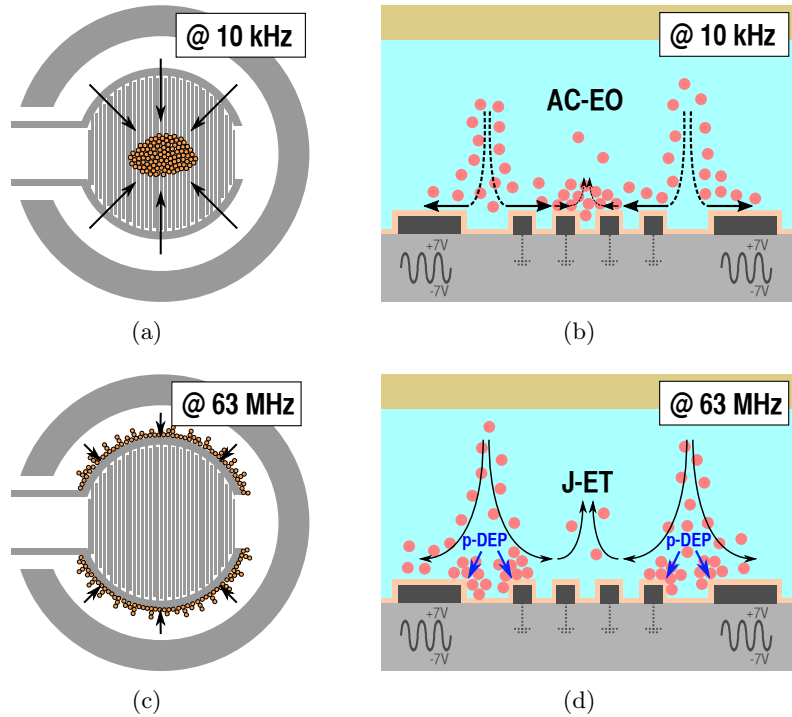


Figure 3.6 – Schematic representation of the observed electrokinetic effects: (a)(b) AC-EO at 10 kHz and (c)(d) combined p-DEP and J-ET at 63 MHz.

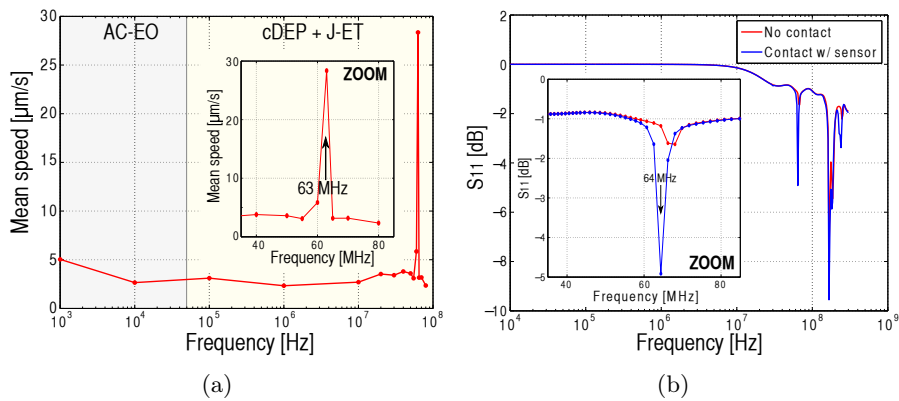


Figure 3.7 – (a) *PIVlab* experimental extraction of the mean speed of *S. epidermidis* versus the applied frequency when macroelectrodes are biased by a 14-V_{pp} sinusoidal voltage. (b) Experimental measurement of the S_{11} parameter of the BNC cables and electrical probe alone and in contact with the macroelectrode immersed in PBS 1:1000 without bacteria, while the IDEs are grounded.

- *Case 3* - $20 \text{ kHz} < f < 100 \text{ MHz}$ and $\sigma_{sol} = 1.8 \text{ mS/m}$: bacterial cells are theoretically directed by cDEP and J-ET (Fig. 3.8(a)), which is driven by the temperature gradient of ε_{sol} in the $M(\omega, T)$ expression. At the resonance frequency of 63 MHz, both effects are amplified but more strongly for J-ET since $\langle \vec{v}_{J-ET} \rangle \propto V_a^4$ while $\langle \vec{v}_{DEP} \rangle \propto V_a^2$ (more details in the next paragraph). Consequently, these surface (cDEP) and volume (J-ET) effects act in a rather equal strength on bacterial cells, enhancing their trapping on the sensor and macroelectrode peripheries as shown in Figs. 3.6(c) and 3.6(d).
- *Case 4* - $20 \text{ kHz} < f < 100 \text{ MHz}$ and $\sigma_{sol} = 180 \text{ mS/m}$: J-ET strongly dominates and is now driven by the temperature gradient of σ_{sol} , thus with an inverse direction compared to the case where $\sigma_{sol} = 1.8 \text{ mS/m}$. The cDEP forces still attract bacterial cells on sensor and macroelectrode peripheries, but at a shorter range than in electrolyte with $\sigma_{sol} = 1.8 \text{ mS/m}$ (because the force is smaller in amplitudes). This confirms experimental observations previously reported.

It is important to note that the bacterial speed is theoretically larger around 10 MHz than at 63 MHz, for both $\sigma_{sol} = 1.8$ and 180 mS/m (see Figs. 3.8(a) and 3.8(b)). The device geometry in Fig. 3.5(a) could then potentially be engineered to shift the resonance frequency down to 10 MHz in order to further maximize the bacterial speed at the resonance. To do so, a complete model of the sensor and setup measurement including all parasitics resistances, capacitances and inductances should be established. It is also possible to replace the complex measurement setup by a miniaturized PCB with a discrete inductance $\sim 5 - 10 \mu\text{H}$ to modulate the resonance frequency.

Origin of the resonance effect at 63 MHz

To understand the origin of the resonance effect, the S_{11} parameters of the BNC cables and electrical probe alone and in contact with the macroelectrode were measured when the microfluidic channel was filled with PBS 1:1000 without bacteria and the IDEs were grounded. The absorption peak of 1.6 dB at 67 MHz was shown to strongly increase to 4.9 dB at a shifted frequency of 64 MHz when the macroelectrode was contacted by the electrical probe (Fig. 3.7(b)). On one hand, the 4.9-dB reduction of $S_{11} \triangleq \frac{Z_1 - Z_0}{Z_1 + Z_0}$ occurs because the probed impedance Z_1 is not purely

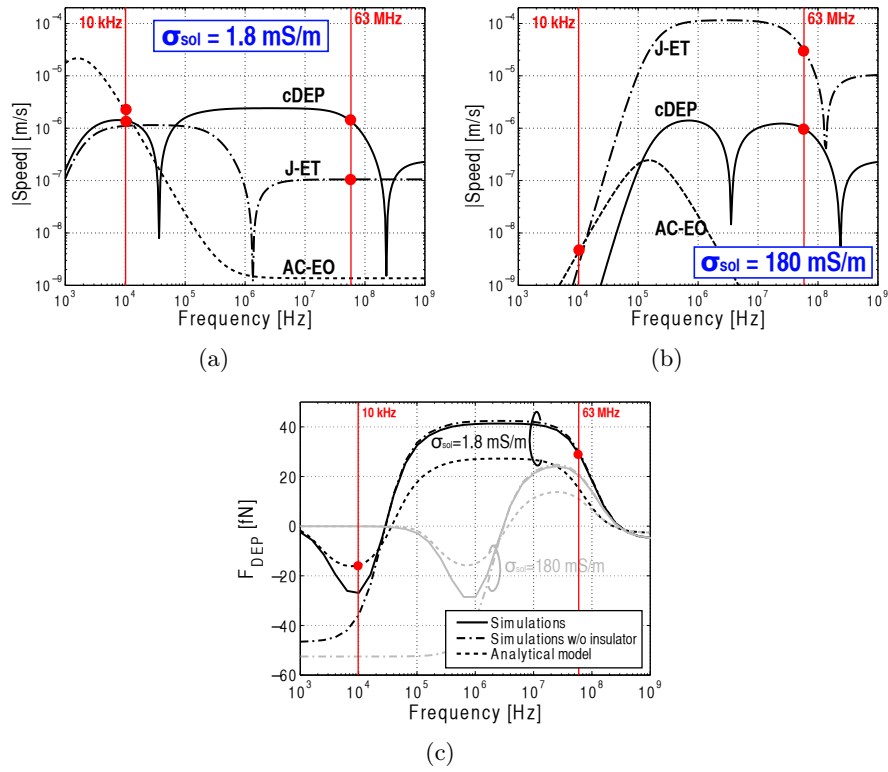


Figure 3.8 – (a)(b) Spectral comparison between bacterial speed absolute values driven by contactless dielectrophoresis (cDEP), Joule heating electrothermal (J-ET) and AC-electroosmosis (AC-EO) at $\sigma_{sol} = 1.8 \text{ mS/m}$ and 180 mS/m without modelling the resonance effect. (c) Spectral comparison between dielectrophoretic forces \vec{F}_{DEP} from the analytical model and numerical simulations for $\sigma_{sol} = 1.8 \text{ mS/m}$ and 180 mS/m , including the insulator or not, without modelling resonance effect.

imaginary and features a modulus closed to the VNA input impedance $Z_0 = 50 \Omega$ at 64 MHz. On the other hand, the 64-MHz value corresponds to the resonance frequency between the macroelectrode-IDEs solution capacitance and the parasitic inductance from BNC cables and electrical probe. As a result, the potential difference between the macroelectrode and the IDEs is found to be ca. five times larger, explaining the stronger electrokinetic forces observed around 63 MHz. It is important to mention that the other adsorption peaks above 100 MHz in Fig. 3.7(b) are also due to the setup (cables, probes, etc.). However, it was not possible to measure their impact on the bacterial speed since the function waveform generator (Agilent 33250A) is limited to 80 MHz.

To the author knowledge, a similar resonance effect was only reported once for the study of human erythrocyte electrorotation [214], where the resonance frequency was around 180 MHz and similarly caused by the microelectrode chamber. Instead of being a chamber artefact, this resonance effect could intentionally be produced by adding lumped elements in parallel or in series to the macroelectrode.

Impact of the insulating layer

From Eq. 3.17, it is possible to identify a cutoff frequency introduced by the insulating layer:

$$f_0 = \frac{\sigma_{sol} t_{ins}}{\pi(\varepsilon_{ins} \pi r + 2\varepsilon_{sol} t_{ins})} \quad (3.23)$$

Below f_0 , most of the electric field is contained within the insulating layer so that all electrokinetic effects are screened owing to the low $\|H(\omega, r)\|$ value. This cutoff frequency is approximatively equal to 1.5 kHz at $\sigma_{sol} = 1.8$ mS/m (Fig. 3.8(a)) and 150 kHz at $\sigma_{sol} = 180$ mS/m (Fig. 3.8(b)), showing that the screening range linearly increases with the electrolyte conductivity.

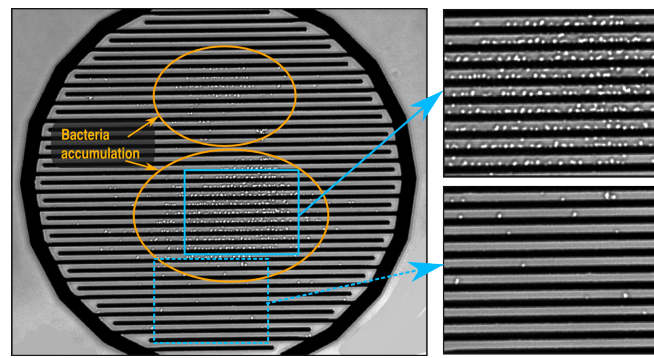
These cutoff frequency values were double-checked by numerical simulations described in Section 3.4 for the dielectrophoretic force (Fig. 3.8(c)). As expected, the analytical model and numerical simulations of \vec{F}_{DEP} fit relatively well especially for the spectral behaviour, with slightly higher magnitudes for simulations because of geometric inaccuracy of the analytical model. At $\sigma_{sol} = 1.8$ mS/m, bacterial cells experience mostly p-DEP between 40 kHz and 200 MHz, while this range is reduced to the 4 MHz–200 MHz interval when $\sigma_{sol} = 180$ mS/m. The spectral behavior of \vec{F}_{DEP} versus the frequency and force amplitudes of dozens fN at $\sigma_{sol} = 1.8$ mS/m and 180 mS/m both correspond to previous reported theoretical and experimental observations [30, 83, 215, 220, 222].

3.6 Impedance sensing with electrokinetics

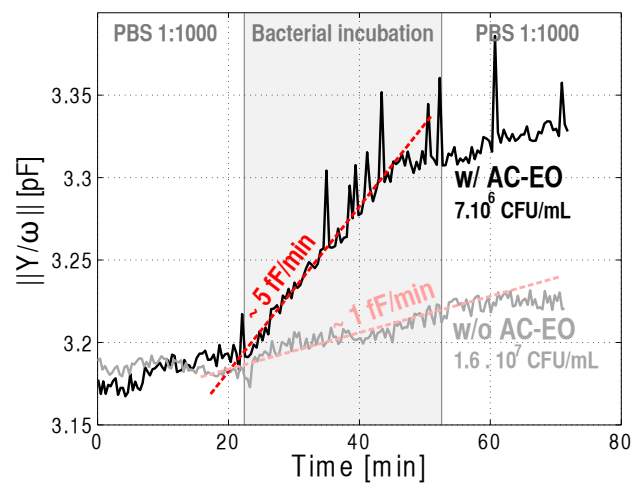
The measurement setup is similar to the previous section but includes an impedance analyzer (see Appendix A.5). The handle of *S. epidermidis* is detailed in Appendix A.3. Sterile PBS 1:1000, bacterial suspension in PBS 1:1000 and sterile PBS 1:1000 were successively incubated at 5 $\mu\text{L}/\text{min}$ in the microfluidic channel, each during more than 20 min. Real-time measurements of the IDEs complex impedance were performed during the whole experiment. Above-mentioned electrokinetic effects were activated 5 min before the bacterial incubation to assess that it does not impact the raw sensor impedance, and lasted until the end of the bacterial incubation to trap most bacterial cells as possible. For the AC-EO effect, the frequency of 10 kHz was chosen instead of 1 kHz for noise consideration on the measured impedance.

At 10 kHz, bacterial cells are progressively trapped in two central regions of the sensor by AC-EO (Fig. 3.9(a)). This asymmetry is most likely due to the macroelectrode opening for IDEs metal accesses as depicted in Fig. 3.5(a). The number of bacteria on the sensor surface linearly increases with time as observed with the inverted microscope, which results in a growth rate of 5 fF/min for $\|Y/\omega\|$ (Fig. 3.9(b)), as the concentration of *S. epidermidis* is $7 \cdot 10^6$ CFU/mL. The peaks in Fig. 3.9(b) are possibly due to momentary presence of large bacterial clusters near the IDEs surface [18] or to the electropermeabilization of some bacterial cells, since their outer shells are overstrained during dozens minutes by a 10-kHz electric field of $0.28 \cdot 10^6$ V_{pp}/m. In comparison, immediate electropermeabilization of *Escherichia coli* were reported to occur at 100 kHz and $4 \cdot 10^6$ V_{pp}/m [150]. For the same sensor without the use of electrokinetics, the $\|Y/\omega\|$ increase is only 1 fF/min for a slightly larger *S. epidermidis* concentration of $1.6 \cdot 10^7$ CFU/mL. A factor 11 of improvement is thus provided by the use of AC-EO to concentrate bacteria on the sensor centre. Since the noise σ_n on $\|Y/\omega\|$ is approximately 1 fF in optimal conditions, the LoD corresponding to $5 \cdot \sigma_n$ is ca. $3.5 \cdot 10^5$ CFU/mL after 20 min of incubation, while the device without EK features a LoD of $3.8 \cdot 10^6$ CFU/mL after 20 min.

At the resonance frequency of 63 MHz, bacterial cells are considerably attracted on the sensor periphery as explained in Section 3.5 and form a thick accumulation layer (Fig. 3.10(a)). However, this layer introduces almost no admittance shift because of its location outside the sensor. To address this issue, the macroelectrode voltage is stopped during few seconds so that bacterial cells in the accumulation layer are released



(a)



(b)

Figure 3.9 – Concentration of bacterial cells on the capacitive sensor at 10 kHz and 14 V_{pp} thanks to AC-EO: (a) microphotograph of the sensor surface after 18 min of bacterial incubation showing two distinct zones of accumulation and (b) real-time normalized admittance $\|Y/\omega\|$ at 1 MHz with and without the application of AC-EO.

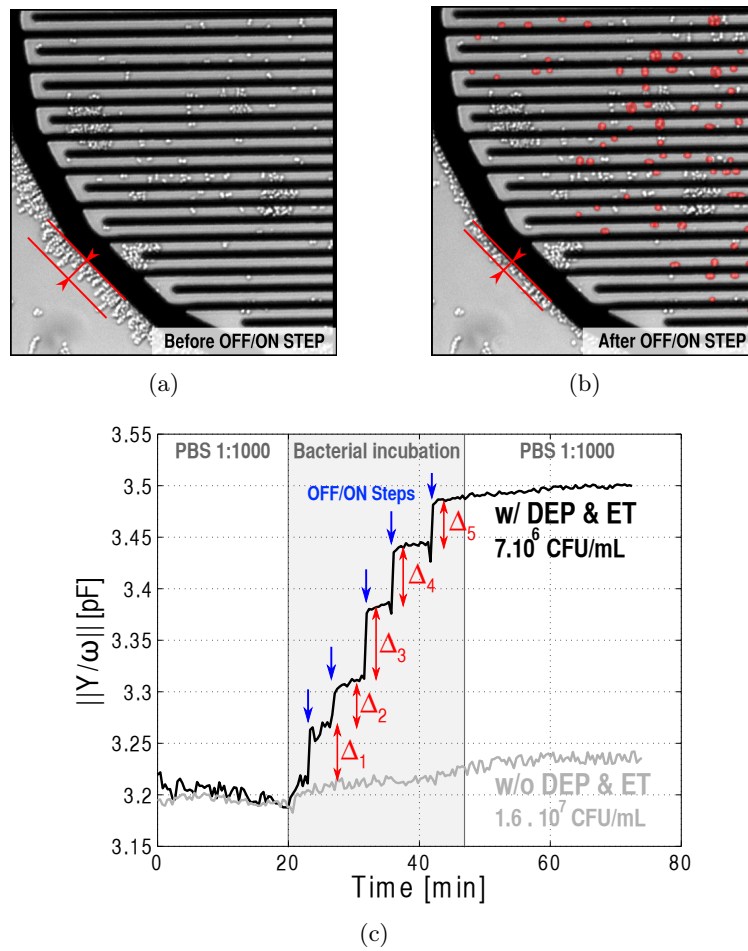


Figure 3.10 – Concentration of bacterial cells on the capacitive sensor at 63 MHz and 14 V_{pp} thanks to a resonant cDEP and J-ET: microphotograph of the sensor surface (a) before and (b) after the deactivation/activation of the macroelectrode voltage that enables bacteria to concentrate on the sensor centre, which corresponds to Δ_2 in (c), and (c) real-time normalized admittance at 1 MHz with successive 5-min cycles of deactivation/activation of cDEP and J-ET.

in the electrolyte and directed above the sensor centre thanks to the microfluidic flow. Once most bacteria are located above the sensor, the macroelectrode voltage is activated again so that bacteria are trapped between the sensor microelectrodes (Fig. 3.10(b)) and instantaneously generate $\|Y/\omega\|$ shifts, as indicated by Δ_1 to Δ_5 in Fig. 3.10(c). The immediate shifts Δ_1 to Δ_5 are approximately equal to 50 fF and spaced 5 min apart, for a *S. epidermidis* concentration of $7 \cdot 10^6$ CFU/mL. As shown in Fig. 3.10(c), the shifts are significantly larger than the reference curve without electrokinetic effects, showing an improvement factor of 38 for a given bacterial concentration. Using the same methodology as previously described, the LoD is approximated to 10^5 CFU/mL after 20 min of bacterial incubation.

3.7 Comparison to the state of the art

Table 3.1 compares the performance obtained in this work with recent studies coupling electrokinetics with impedance-based sensors. In this work, *S. epidermidis* is resuspended in a relatively high conductive electrolyte, i.e. PBS 1:1000 with a conductivity of 1.8 mS/m, while most works deal with *Escherichia coli* or *Listeria monocytogenes* in electrolyte of conductivity close to 200 μ S/m, benefiting from larger electrokinetic forces. Furthermore, our device uses Al/Al₂O₃ electrodes that are more CMOS-compatible than Cr or Au electrodes used in other works. As it will be demonstrated in Chapter 4 [22, 23], the capability to integrate an electrical readout circuit below the Al/Al₂O₃ sensor is a non-negligible advantage that provides significant improvements in term of efficiency, cost and compactness.

Another key difference is the use of two separate electrodes for the sensing and actuating parts. With this choice, both can be optimized for their own purposes: interdigitated microelectrodes for high sensitive surface sensing (see Chapter 2) [18–20, 180] and the macroelectrode for efficient volume trapping. Most works reported in Table 3.1 use the same electrode for both attraction and detection, at the exception of [86] where volume trapping and surface sensing are separated in two successive microfluidic chambers, which is less appropriate than the simultaneous attraction and detection performed in this work. The use of resonance and combined electrokinetic effects to enhance the bacterial trapping is also innovative in the case of impedance sensors, since the resonance effect was only reported for optical monitoring between electrodes [214],

and other impedance sensors exclusively use DEP or AC-EO [84, 86, 105, 147, 150, 220].

Finally, the achieved detection limit of 10^5 CFU/mL after 20 min of incubation is similar to the best values reported by other works [84], but still far from the 10^2 CFU/mL in 3h [150], which is equivalent to 10^3 CFU/mL in 20 min. This strong difference can be explained by the use of a higher flow rate (0.5 mL/min versus $5 \mu\text{L}/\text{min}$). By defining FR as the flow rate and t_{incub} as the incubation time, it is therefore more impartial to compare figures of merit $FoM_1 \triangleq LoD \cdot FR \cdot t_{incub}$ and $FoM_2 \triangleq LoD \cdot FR \cdot t_{incub}^2$ (see Section 1.3.5). As indicated in Table 3.1, this work achieves a FoM_1 of 10^4 CFU, which is similar to the best value of $9 \cdot 10^3$ CFU reported in [150], and a FoM_2 of $2 \cdot 10^5$ CFU·min, which is one order of magnitude better than other works.

3.8 Conclusions

In this chapter, we have developed a device combining circularly shaped interdigitated microelectrodes with a surrounding macroelectrode, respectively used for high-sensitive surface sensing and volume trapping of bacterial cells [21]. At frequencies around 10 kHz, whole-cell *Staphylococcus epidermidis* are directed towards the sensor centre by AC-EO resulting in the linear increase of the sensor capacitance and in a detection limit of $3.5 \cdot 10^5$ CFU/mL after 20 min of incubation. At 63 MHz precisely where positive dielectrophoresis and Joule-heating electrothermal flow dominate, a resonance phenomena due to chamber lumped elements significantly increases the bacterial attraction up to $116 \mu\text{m}/\text{s}$, forming dense bacteria layer on the sensor periphery. By momentarily stopping the macroelectrode voltage and benefiting from the microfluidic flow, bacteria are repositioned on the sensor centre and produce immediate impedance shifts. In this case, the LoD is 10^5 CFU/mL after 20 min of incubation. Modelling of the electrokinetic effects, i.e. the dielectrophoresis, the AC-electroosmosis and the Joule heating electrothermal flow, in presence of the insulating layer is provided and enables a comprehensive understanding of the impact of frequency and conductivity on their respective balance. The device is CMOS compatible, thus enabling system integration, affordability and miniaturisation as shown in the next chapter.

CHAPTER 4

CMOS readout interfaces for capacitive biosensors

To achieve miniaturized, portable and affordable biochips, co-integrating the sensor and readout interface on the same chip is essential. Thanks to the complementary metal-oxide-semiconductor (CMOS) technology, it can provide additional key functionalities that would be hardly achievable without CMOS. In this chapter, we present two readout interfaces designed to specifically address two different problems:

- *Sensing bacteria in high-conductive solutions with passivated microelectrodes*, thanks to a capacitance-to-frequency converter (CFC) working at very high frequency (up to 575 MHz) [22].
- *Sensing single bacterial cells*, thanks to a 16×16 capacitive biosensor array featuring very small pixels of $14 \mu\text{m} \times 16 \mu\text{m}$ [23].

The chapter is organized as follows. In Section 4.1, we review the state of the art of CMOS interfaces for capacitive biosensors. In Section 4.2 and 4.3, we present the CFC and biosensor array described above, respectively.

4.1 State of the art

4.1.1 CMOS technology

Motivations

The complementary metal-oxide-semiconductor (CMOS) technology has been the key enabler for the current revolution of electronics, information and technology. First built in 1959, the *transistor* has seen its number per mm^2 doubled every 18 to 24 months between 1971 and 2010 (which is known as the *Moore's law* [223]), achieving a minimal channel length of 16 nm in 2015. With so small features, integrated circuits (IC) combining millions of transistors, capacitors and resistors on the same chip provide computing, processing and integrating capabilities on sub- mm^2 dies, which are extremely low-cost ($< 1\text{€}$) when massively produced.

Despite its benefit for digital functions, the transistor scaling is not necessarily advantageous for interfacing real analog signals in the world. For this reason, many efforts have been done in the last years to integrate more specialized analog functions, such as RF, passives, high-voltage power, sensors, optoelectronics and biochips, with CMOS technology [224]. This trend is known as the *More than Moore's law*, also called the *More Moore's law*. Particularly, the power of CMOS can be used to interface sensors and microelectromechanical systems (MEMS), enabling calibration, digital interfaces and self-testing on a single chip [225].

CMOS manufacturing process

The CMOS process typically starts from a p-type silicon wafer, where n-well regions are first defined thanks to photolithography and implantation steps. The polysilicon gate is then patterned by photolithography atop an thin gate oxide layer and, thanks to SiO₂ shielding windows, doped drain, source and body transistor terminals are defined by implanting n and p ions. Afterwards, metal contacts for these terminals are proceeded by covering the die with a first metal layer. Eventually, a succession of metal layers is processed on different levels with dielectric separation, enabling routing and connections of transistors.

4.1.2 Co-integration of CMOS and sensors

The power of CMOS is considerably increased when both sensing and readout parts are co-integrated on a single chip. In this case, high-efficient architectures can be designed and miniaturized biodevices can be massively produced at low cost [225]. In this section, the key features regarding the co-integration between sensors and CMOS are described.

Sensor arrays versus single sensor

Readout circuits are usually designed to interface a single sensor [127, 226–229] for versatility and commercial reasons. However, depending on the target application, sensor arrays [67, 82, 92, 116, 139, 158, 230–233, 233–239] can be preferred to single sensor interfaces because of the following advantages:

- Capability to interface a large number of sensors, i.e. thousands [230] to millions [67], with only a limited set of I/Os [139]. Thanks to *active pixels* consisting of dedicated sensing and readout parts, each sensor can be selected and read individually.

- Capability to shrink the sensor area (e.g. down to $5.1\text{-}\mu\text{m}$ pitch [67]), while keeping a large total sensing area by increasing the number of pixels. The small sensing units are thus more sensitive to micro or nanoscale biological species [240].
- Capability for multiplexing, because pixels or pixel clusters can be differently covered by bioreceptors [116]. A single chip can thus target the simultaneous and specific detection of different species in a single sample.

Architecture of sensor arrays

A $N \times N$ biosensor array is composed of several important blocks, to control and interface signals coming from the pixels (Fig. 4.1(a)):

- *Pixels* are the key parts of the biosensor array, containing both a sensing unit and a proper readout circuit. The in-pixel circuit architecture can be various, as detailed in Section 4.1.3.
- *Row and column decoders* enable the row and column selection based on a very limited number of pins, typically $\log_2(N)$.
- *Column amplifiers* are each dedicated to one column and to the corresponding pixel output. Their important function consists in storing reset and signal values, both required to perform the double sampling (see next paragraph).
- The *output driver* typically consists in source followers, which load the output busses to given voltage values. It can be preceded by a multiplexer to reduce the number of outputs [230].

The conversion of analog signals, either expressed in temporal or voltage forms, can be performed at various places. When not performed inside the pixel, the *analog-to-digital conversion* typically occurs inside column amplifiers, either using a single or N *analog-to-digital converters* (ADC) when the speed is a major requirement.

Reducing non-idealities in sensor arrays

One of the major drawbacks of using a sensor array is that all pixels are not exactly identical, especially when pixels are very small, because of non-homogeneity and imperfections of the CMOS process. Even with identical inputs, they can thus figure different output voltages, whose

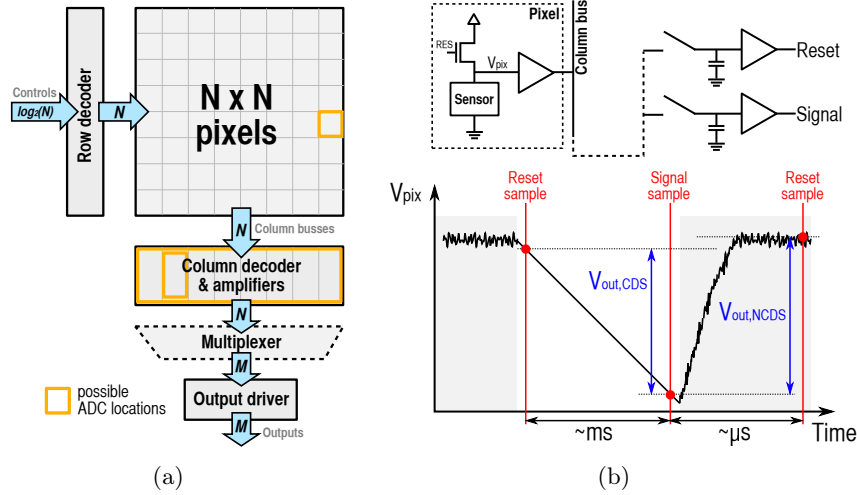


Figure 4.1 – Schematic representation of (a) the architecture of a sensor array, highlighting the possible locations for the analog-to-digital conversion and (b) the principle for the correlated (CDS) and non-correlated (NCDS) double sampling.

variability is called the fixed-pattern noise (FPN). Furthermore, a temporal variability must also be considered between each pixel because of thermal and flicker noises intrinsic to transistors. One common technique to reduce these two imperfections is the *double sampling*, which is widely used in CMOS image sensor [241]. Its principle consists in subtracting reset from signal levels, both sampled at different moments. Depending on these sampling times, two methods exist (Fig. 4.1(b)):

- The *correlated double sampling* (CDS) samples the reset level just after the start of the integration phase. At its end, the signal level is sampled and features the same kT/C noise as the reset level (they are *correlated*), since the reset transistor is cut off during the integration phase. By subtracting these two levels, the pixel mismatch (FPN) and kT/C noise are strongly reduced. However, the CDS requires large hardware resources to store the reset level during the integration phase, which further delays the frame rate.
- The *non-correlated double sampling* (NCDS), also called the *delta-reset sampling* (DRS), consists in first sampling the signal level at the end of the integration phase, before evaluating the reset level when the pixel is subsequently reset. Despite cancelling FPN,

the signal and reset levels are no more correlated so that their subtraction increases the kT/C noise by a factor $\sqrt{2}$. In return, the NCDS timing is much shorter, the flicker noise is reduced and the hardware resources are less important [241].

Differential versus non-differential architectures

To remove parasitics and increase sensitivity of capacitive biosensors, a reference capacitance C_{r0} is typically subtracted from the sensing capacitance $C_s = C_{s0} + \Delta C_s$, with $C_{r0} \simeq C_{s0}$, so that the shift ΔC_s is more easily amplified which significantly improves the sensitivity. Other non-idealities such as temperature and electrolyte conductivity can also be cancelled. The obtention of a reference capacitance $C_{r0} \simeq C_{s0}$ can be obtained in two different ways:

- The *fully differential method* involves a reference electrode of capacitance C_{r0} in contact either with the bacterial sample, in this case the reference electrode is not covered by bioreceptors [139], or with the same solution but without bacteria (thus in a different microfluidic channel) [228, 232]. In both cases, no bacterial cell adheres the electrode and the measured capacitance can be considered as a reference value. This technique is mainly limited by the initial capacitance mismatch.
- The *pseudo-differential method* involves a reference capacitance C_{r0} with a fixed value, independent of the solution properties. In this case, the electrode is typically covered by a thick resist layer and is thus insensitive to the fluid properties [231, 242]. A calibration method is then required since C_{r0} does not respond to the medium properties such as $\varepsilon_{r,sol}$, σ_{sol} , $\varepsilon_{r,ins}$ and t_{ins} (see Section 2.2 and 2.4). Versatility is thus the main issue.

Despite very popular, differential methods are not suitable for biosensor arrays [139, 231, 232] featuring pixels with both sensing and reference capacitances. Indeed, each reference capacitance must provide a local control value in the biological point of view, i.e. be without bacteria. As previously explained, it can be achieved either with a local antifouling coating or a local flow of the same solution but without bacteria. Both approaches are currently not technically feasible when pixels are scaled down to the micrometer size, and the last further requires the possibility to obtain the reference solution from the initial biological sample.

Post-processing and encapsulation issues

The standard CMOS process must slightly be adapted for biosensing applications. Since the topmost Al metal layer is typically used to define the biosensor, a resistant sensing material must be post-processed:

- *Processing the passivation layer:* either the passivation layer is removed atop the sensing regions [82, 235, 243], or the thick passivation layer is kept intact [93, 244].
- *Replacing the whole sensing material:* this is typically used for long-term applications (e.g. several weeks for cell cultivation) but requires more steps including patterning:
 - Removing passivation, depositing a Cr/Au stack layer and liftoff processing to define the area [234].
 - Depositing a Ti/Pt stack layer, structuring it by liftoff process and coating the whole surface by a TiO₂/ZrO₂ stack layer. A thick Au layer is eventually deposited on bondpads, after removing the previous dielectric layer [230].
 - Sputtering a Ti/W/Pt stack layer, patterning it with liftoff process and depositing a SiO₂/Si₃N₄ passivation layer [245].
 - Depositing a Ni/Au stack layer atop opened and passivated regions of the chip. No photolithography step is required since Ni/Au layer does not hold on passivation [92, 234].
 - Depositing Au with photolithography-based patterning after the standard CMOS process [139].

Besides post-processing, encapsulation methods are summarized in Fig. 4.2. In general, wirebonds are protected by epoxy resist to avoid saline solution to short-circuit tracks and corrode them [92, 228, 230, 234, 245, 246]. The most common method involves ring-like glass rings, glued atop CMOS chips or ceramic packages and serving as cultivation or fluidic chambers [67, 226, 230, 245]. More elaborated (micro)fluidic chambers can also be used and pressed atop the chip [139], defined with a direct-write method [228, 246] or with other methods [237]. More exotic encapsulation methods involve cylindrical tubes glued atop the chip [93, 244]. Eventually, it is also possible to deposit a drop of the solution under test [67, 82, 92, 234, 235], by taking into consideration the possible liquid evaporation.

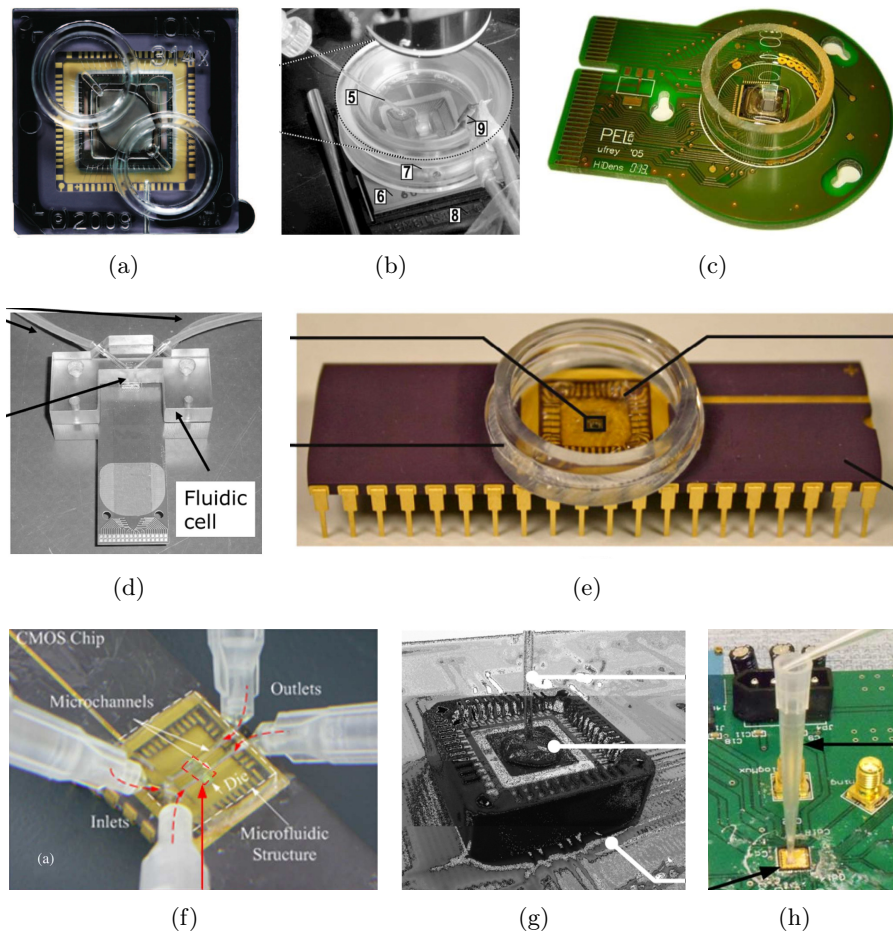


Figure 4.2 – Illustration of the different encapsulation methods for CMOS chips: (a) ceramic package with moulded fluidic lid [67], (b) ceramic package glued atop a cultivation chamber with silicone [230], (c) CMOS chip mounted and wirebonded on a PCB, featuring a glued glass ring [245], (d) CMOS chip mounted and wirebonded on a PCB with a two-chamber fluidic cell [139], (e) DIP ceramic package with a glued well [226], (f) direct-write microfluidic packaging of a ceramic package [228, 246], (g) ceramic package with a drop of solution and electrode wire [92], (h) cylindrical tube fixed and glued atop the chip, which is mounted and wirebonded on a PCB [93, 244]. Most of these works use epoxy resist to protect wirebonds from the solution contact.

Figures of merit

For comparing electrical readout interfaces of capacitive sensors, it is important to enlarge the figures of merit previously defined in Section 1.3.5. In all cases, it is strongly advised to precise *intrinsic* performances, such as the *interface limit of detection* expressed in F, the *interface input range* expressed in F and the *interface sensitivity* in V/F or in Hz/F when the capacitance is converted into a voltage or a frequency, respectively. The *chip area*, *power consumption* and *whether sensing parts are located on-chip* are important figures of merit for readout interfaces. Another critical aspect, which is sporadically mentioned in the literature, is the consideration of a *non-ideal sensing capacitance*, which is more accurately represented by an impedance $Z(\omega)$ including lumped elements with C_{ins} , C_{DL} , R_{sol} and C_{sol} shown in Fig. 2.4(a).

For sensor arrays, it is also very important to report the *number and size of the sensors*, because they indirectly impact the sensitivity, chip area and multiplexing capabilities. Also, *fixed-pattern noise* (FPN) characterizing the output variability must be expressed in V or % of the saturated signal.

4.1.3 Capacitive interfaces

The most popular interfaces of capacitive sensors are summarized in this section. The circuit must be designed to convert the impedance $Z(\omega)$, which is dominated by the capacitance C_{sol} but still slightly perturbed by R_{sol} , C_{ins} and C_{DL} (see Section 2.4(a)), into an output voltage.

Voltage-controlled oscillators (VCO)

To perform the capacitance-to-voltage conversion, a voltage-controlled oscillator (VCO) can be used in a phase-locked loop (PLL), synchronizing the VCO output frequency with an input frequency (Fig. 4.3(a)) [93, 244]. In this case, the VCO consists of a NMOS differential pair with on-chip inductors. Since a single VCO suffers from temperature sensitivity and low-frequency noise [244], the same principle can be applied to a reference and sensing VCOs [93], whose inputs are differentiated and expressed as an digital output by an ADC. This enables a more accurate permittivity measurement.

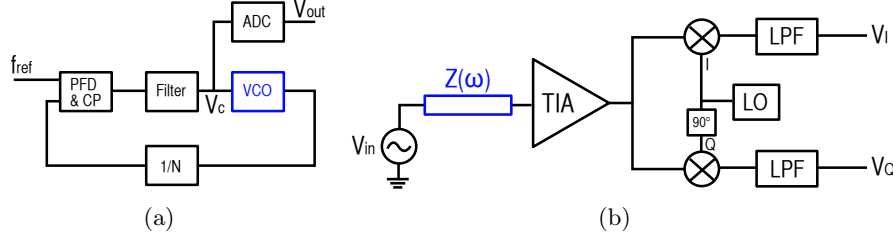


Figure 4.3 – Readout interfaces for the semi-capacitive impedance $Z(\omega)$: (a) voltage-controlled oscillator (VCO) consisting of a NMOS differential pair within a phase-locked loop (PLL) [93, 244] and (b) coherent detection using two multiplexers to extract real and imaginary parts of the voltage [92]. PFD, CP, TIA, LO and LPF refer to phase-frequency detector, charge pump, transimpedance amplifier, local oscillator and low-pass filter, respectively. The model for $Z(\omega)$ is described in Fig. 2.4(a).

Coherent detection technique

To evaluate both the capacitive and parasitic parts of the impedance $Z(\omega)$, the real and imaginary parts of $Z(\omega)$ can be estimated by using the coherent detection technique [92]. As shown in Fig. 4.3(b), a sinusoidal voltage applied on one electrode side triggers an electrical current on the other side, which is then magnified by a transimpedance amplifier (TIA). The outputs are eventually multiplied by orthogonal signals (I and Q) and followed by low-pass filters (LPFs) to remove high-order harmonics, resulting in the following admittance $Y(\omega) = Z(\omega)^{-1}$:

$$\|Y(\omega)\| = \frac{\sqrt{V_I^2 + V_Q^2}}{A \cdot \|V_{in}\|} \quad \text{and} \quad \theta_Y(\omega) = \tan^{-1} \left(\frac{V_Q}{V_I} \right) \quad (4.1)$$

Capacitance-to-frequency converters (CFC)

The generation of a square waveform featuring a frequency inversely proportional to the input capacitance has the big advantage to involve no ADC, since the frequency can be converted to a digital signal by simple counters. The most common implementation of capacitance-to-frequency converters (CFC) consists in charging and discharging the impedance $Z(\omega)$ with current sources delivering reference currents I_{ref} , controlled by the switching of a comparator between reference voltages V_{ref} [82, 139, 235] (see Fig. 4.4(a) and 4.4(b)). The output frequency is inversely proportional to C_{sol} , but quite imperfectly because of the

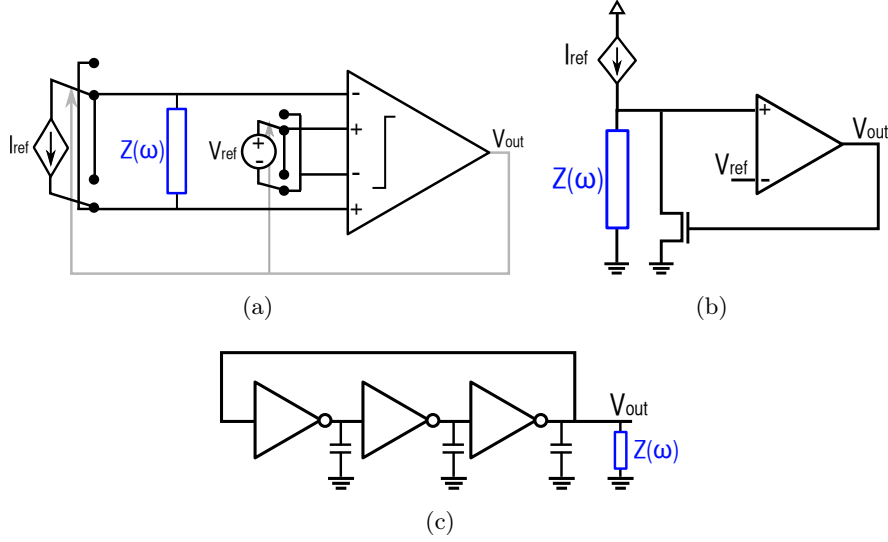


Figure 4.4 – Capacitive-to-frequency converters (CFC) for the semi-capacitive impedance $Z(\omega)$: (a) (b) oscillator based on a comparator [82, 139, 235] and (c) based on a ring oscillator [247]. The model for $Z(\omega)$ is described in Fig. 2.4(a).

small resistance R_{sol} inducing a non-linear behavior:

$$\frac{1}{f} = 2R_{sol}C_{sol} \cdot \ln \left(\frac{1}{1 - \frac{V_{ref}}{R_{sol}I_{ref}}} \right) \simeq \frac{2C_{sol}V_{ref}}{I_{ref}} \quad (4.2)$$

where the last approximation holds only if $\frac{V_{ref}}{R_{sol}I_{ref}} \ll 1$. Another possibility is the use of a ring oscillator as VCO, featuring the sensor impedance at its output and whose output frequency is inversely proportional to the sensor capacitance [247] (Fig. 4.4(c)):

$$f \simeq \frac{I_{avg}}{2V \cdot (3C_{load} + C_{sense})} \quad (4.3)$$

where I_{avg} is the average current provided by one inverter, C_{load} the load capacitance at each inverter node and C_{sense} the sense capacitance related to the impedance $Z(\omega)$.

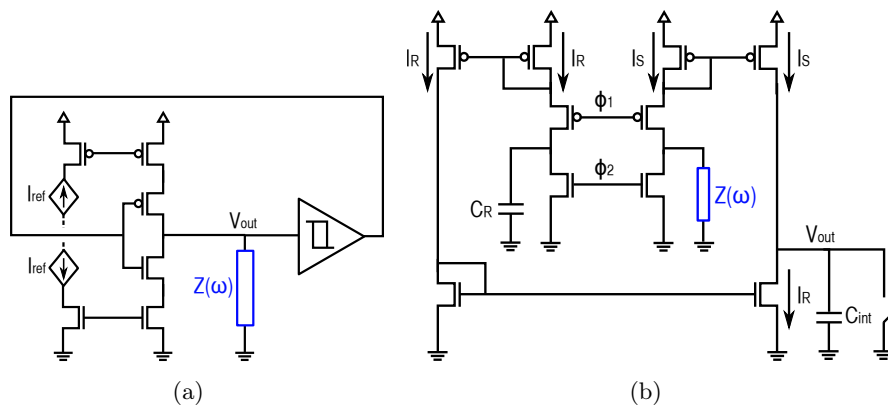


Figure 4.5 – Readout interfaces for the semi-capacitive impedance $Z(\omega)$: (a) current-controlled oscillator (CCO) generating capacitance-dependent triangular waveforms [234, 248] and (b) charge-based capacitance measurement (CBCM) performing differential measurements [154, 228, 246, 249, 250]. The model for $Z(\omega)$ is described in Fig. 2.4(a).

Temporal triangular waveforms

The evaluation of lumped elements at the electrode-electrolyte interface can be performed by analyzing the shape of generated triangular waveforms, avoiding the tedious extraction of the impedance phase and modulus [234, 248]. It is typically implemented by a non-differential current-controlled oscillator (CCO) charging and discharging the sensor impedance $Z(\omega)$. A triangular waveform voltage (TWV) can be generated to measure the stepwise current [234], or inversely a square current can be applied to generate a triangular output voltage [248] (Fig. 4.5(a)). Again, the sensitivity of passivated electrodes drops in high-conductive solutions because of the extremely low values of time constant $\tau \triangleq R_{sol}C_{sol}$ and asymptotic voltage $\xi = R_{sol}I_0$ [248]. For unpassivated electrodes, the sensing can still be performed through the DL capacitance C_{DL} [234].

Charge-based capacitance measurement (CBCM)

Initially introduced to measure interconnect capacitances down to 10 aF [251], the charge-based capacitance measurement (CBCM) is a high sensitive differential technique that integrates the subtraction between a reference current I_R and the sensing current I_S through an inte-

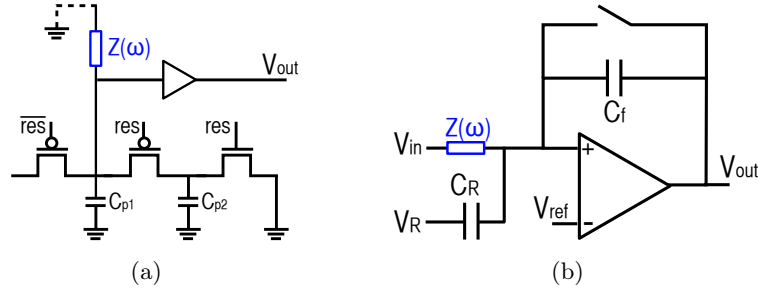


Figure 4.6 – Readout interfaces for the semi-capacitive impedance $Z(\omega)$: (a) charge sharing principle [153] and (b) switched capacitor implementation [231]. The model for $Z(\omega)$ is described in Fig. 2.4(a).

gration capacitance C_{int} . Used for biosensing in low-conductive solutions [154, 228, 246, 249, 250], its CMOS implementation consists in differential pairs (Fig. 4.5(b)) giving the following output voltage:

$$V_{out} \simeq \frac{C_{sol} - C_R}{C_{int}} \cdot A_I \cdot V_{dd} + V_{off} \quad (4.4)$$

where C_R is the reference capacitance, A_I is a design-dependent constant and V_{off} an offset voltage accounting for the mismatch between current mirrors. For high-conductive fluids, the time constant $\tau_1 = R_{sol}C_{ins}$ is smaller than the sampling time and V_{out} is independent of C_{sol} [250]:

$$V_{out} \simeq \frac{C_{ins}}{C_{int}} \cdot A_I \cdot V_{dd} + V_{off} \quad (4.5)$$

since $C_{ins} \gg C_R$. However, when performing fully differential measurements thanks to two distinct microfluidic channels [228, 232], C_{sol} can be sensed in series with C_{ins} thanks to the high sensitivity of CBCM technique. In the case of pseudo-differential measurement, a calibration circuit is required to match I_R with I_S [250].

Switched capacitors and charge sharing principle

The sensor capacitance can be evaluated by using charge redistribution. The first method, known as the *charge sharing principle*, is non-differential and redistributes stored charges in the sensed capacitor to another fixed capacitor, thanks to controlled switches. The voltage across

these capacitors is almost proportional to the sensed capacitor [153]:

$$V_{out} = \frac{(C_{p1} + C_{sol}) \cdot V_{dd} + C_{p2}V_{ss}}{C_{p1} + C_{p2} + C_{sol}} \quad (4.6)$$

where C_{p1} and C_{p2} are parasitic capacitances (Fig. 4.6(a)). Another implementation uses *switched capacitors* at the negative input of an amplifier, featuring a feedback capacitance C_f and a reference capacitance C_R that can be used for calibration purposes [231]. After double sampling to remove imperfections and subtract a programmable offset (for DR purposes), the output voltage V_{out} is given by:

$$V_{out} \simeq \frac{C_{sol}\Delta V_{in} - C_R\Delta V_R}{C_f} \quad (4.7)$$

Comparison and chapter innovations

An exhaustive comparison between CMOS capacitive biosensors is provided in Table 4.1. Because of the different sensor sizes, biospecies, resuspension media and interfaces, it is extremely hard to provide an objective comparison of these works. However, some key conclusions can be drawn:

- Very low intrinsic LoD ($\sim 10 - 20$ aF) are achieved by differential architectures [231, 232]. Detection of single beads or cells featuring a minimal diameter of $10 \mu\text{m}$ are reported [82, 231].
- For capacitance-to-voltage conversion, the typical intrinsic sensitivity is $200 - 400$ mV/fF, achieved with differential techniques [231, 232]. For capacitance-to-frequency conversion, the highest intrinsic sensitivity is 223 kHz/fF [82].
- Most works perform biosensing in high-conductive solutions such as growth medium [226, 228], PBS-like solutions [22, 234, 238] or other solutions [92, 139]. However, among these studies, only [226, 228] use passivated electrodes but for growth monitoring (no direct detection), while other use gold coatings atop the CMOS chip. Other passivated chips perform direct detection in low-conductive solutions such as water or mannitol solution [231, 237].
- Most arrays feature fairly large pixels, typically with a side on the order of $100 - 200 \mu\text{m}$. Two works report smaller pixels with side of $20 \mu\text{m}$ [226, 231], but carry detection of $10\text{-}\mu\text{m}$ cells whose volumes are three orders of magnitude larger than bacteria.

In this chapter, we develop two architectures for capacitive sensors to go beyond the state of the art. The first is a capacitance-to-frequency converter working at very-high frequency (~ 575 MHz) to provide sensitive detection of bacteria in high-conductive solutions, despite the use of passivated electrodes, thanks to the monitoring of volume properties [22] (see Section 4.2). The second architecture is a 16×16 capacitive biosensor array with small pixels ($14 \mu\text{m} \times 16 \mu\text{m}$) targeting detection of single bacterium in low-conductive solutions [23] (see Section 4.3).

Table 4.1 – CMOS capacitive biosensors from the state of the art. Blue-highlighted results are those reported in this Chapter.

Ref.	Techno.	# sens. [†]	Sensor size	IC area	Principle	Biospecies	Medium	LoD	Power	Sensitivity	Input range
[231]	0.35- μm CMOS	320 x 320	20 μm x 20 μm	NA	18-T C2V (D); SC + ADC	10 μm beads	280 mM mannitol	21 aF (Single bead)	NA	345 mV/ff 145 mV/ff/bead	NA
[139]	0.5- μm CMOS	8 x 16	200 μm x 200 μm	28.8 mm ²	26-T C2f (D); CB-oscillator	DNA	0.3 M NaCl	NA	NA	23 Hz/pF @ 7.5 kHz @ 330 pF	330 pF - 10 nF
[226]	0.5- μm CMOS	28	20 μm x 20 μm	0.16 mm ²	(>8)-T C2V (ND); Charge sharing	Cancer cells	Growth medium	~ 5 fF (10 ⁵ cells/mL)	NA	NA	NA
[232]	0.5- μm CMOS	6 x 6	NA	3 mm ²	4-T C2V (D); CBCM	-	-	15 aF (NA)	2.6 mW	200 mV/ff	± 25 fF
[228]	0.18- μm CMOS	1	100 μm x 100 μm	2 mm ²	(>25)-T C2V (D); CBCM	<i>E. coli</i>	LB medium	NA (10 ⁷ CFU/mL)	NA	255 mV/ff ^{††}	NA
[234]	0.35- μm CMOS	16 x 8	170 μm x 80 μm	10 mm ²	C2f (ND); TIE	DNA	PBS- Tween	5 pF (10 nM)	NA	NA	5 pF - 5 nF
[92]	0.35- μm CMOS	10 x 10	100 μm x 100 μm	4 mm ²	32-T C2V (ND); TIA + coher.	DNA	4xSSC	10 nS (10 ⁵)	85 mW	NA	NA
[235]	0.35- μm CMOS	5 x 5	200 μm x 200 μm	NA	(>9)-T C2f (ND); CB-oscillator	Neurotrans. polydop.	NA	NA (0.1 fM)	NA	21 kHz/ff @ 4.9 MHz @ 123 ff	12 ff - 700 ff
[237]	0.18- μm CMOS	3 x 3	100 μm x 100 μm	1.8 mm ²	4-T C2V (ND); CBCM	0.5-2 μm beads	DI water	1ff (NA)	NA	10 ff/mV	NA
[238]	0.13- μm CMOS	4 x 4	200 μm x 300 μm	1.68 mm ²	FRA (ND)	DNA	PPB with Fe(CN) ₆ ^{3-/4-}	0.42 fF (NA)	1.7 mW	NA	0.13 fF - 53 pF
[82]	0.35- μm CMOS	8 x 8	100 μm x 100 μm	NA	(>9)-T C2f (ND); CB-oscillator	10- μm beads	Air	2.5 fF (Single bead)	NA	223 kHz/ff @ 5.2 MHz @ 23 ff	NA
[22]	0.25- μm CMOS	1	220 μm x 230 μm	0.05 mm ²	(>25)-T C2f (ND); CB-oscillator	<i>S. epi-dermidis</i>	PBS	50 fF (10 ⁷ CFU/mL)	29 mW	16 kHz/ff @ 254 MHz @ 17.5 pF	NA
[23]	0.25- μm CMOS	16 x 16	14 μm x 16 μm	0.1 mm ²	7-T C2V (ND); Charge sharing	<i>S. epi-dermidis</i>	PBS 1:1000	450 aF (~ 7 bact.)	29 μW	55 mV/ff 2.2 mV/bact.	0.45 fF -57 ff ^{†††}

[†]: Arrays are in bold, ^{††}: Only simulated value, ^{†††}: Tunable by t_{int} and V_{ref} .

4.2 A CFC for bacterial sensing in conductive buffers

4.2.1 Motivations

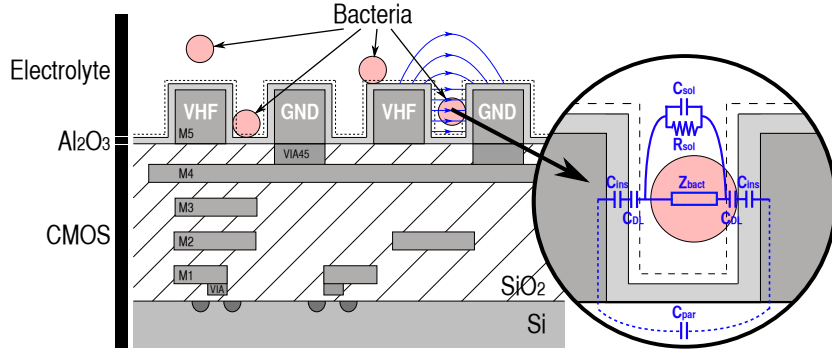
It is highly desirable to perform capacitive biosensing directly in the initial conductive sample to maximize biological affinity with bioreceptors and avoid time-consuming centrifugation and washing steps with low-conductive solutions. As previously explained in Section 2.1.7, the largest sensitivity to bacterial cells in high-conductive buffers is typically obtained through changes of the double-layer capacitance C_{DL} . However, the passivation layer of capacitive biosensors screens C_{DL} so that bacteria must preferably be sensed through R_{sol} and/or C_{sol} (see Section 2.2.2 for explanation and Section 2.2.3 for experimental results). Many interfaces for capacitive biosensors use this principle in low-conductive solutions (see Section 4.1.3) but fail to deliver a sufficient sensitivity in high-conductive solutions, since very high frequencies ($\sim 100\text{--}500$ MHz) are required. To do so, avoiding bulky impedance analyzers, large parasitics and tedious calibration steps, co-integrating sensing and readout parts on the same chip requires the use of CMOS process, which further provides portability, miniaturization and affordability.

To address this challenge, this section presents a CMOS capacitance-to-frequency converter (CFC) interfacing on-chip Al/Al₂O₃ IDE up to 575 MHz, thus enabling sensing in high-conductive solutions [22] and extending the use of the biosensor built in Chapter 2. In Section 4.2.2, the design of the CFC is described. In Section 4.3.4, we discuss experimental results in solutions with various $\varepsilon_{r,sol}$ and σ_{sol} and in physiological buffers containing whole-cell *Staphylococcus epidermidis*.

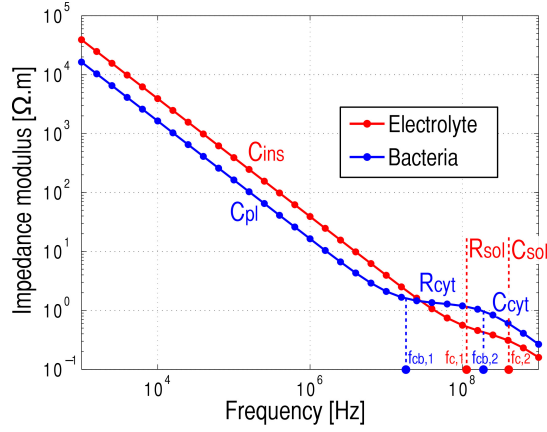
4.2.2 System architecture

Model of the sensing part

To optimize the IC design for high bacterial sensitivity, the metal-insulator-electrolyte (MIE) dielectric behavior of the Al/Al₂O₃ IDE, subjected to alternating voltages of frequency f_{IDE} , needs to be understood in bacterial solution (Fig. 4.7(a)). The equivalent model is identical to the one reported in Section 2.2.3, but with slightly different parameters: $t_{ins} = 25$ nm, $\sigma_{sol} = 1.8$ S/m, $\lambda_D \simeq 0.8$ nm, $d_e = w_e = 1.5$ μm and $t_e = 1.8$ μm (see next sections for justification). In this case, the



(a)



(b)

Figure 4.7 – Bacterial sensing principle: (a) schematic cross-section (not at scale) of the integrated circuit including on-chip sensing parts, whose equivalent electrical circuit is depicted, and (b) Bode diagram of the electrolyte and the bacterial cell alone, based on expressions given in Section 2.2.

geometrical constant G is equal to 1 and the medium cutoff frequencies are given by Eq. 2.12 and 2.13:

$$f_{c,1} \simeq \frac{1}{\pi} \cdot \frac{t_{ins}}{d_e} \cdot \frac{\sigma_{sol}}{\varepsilon_0 \varepsilon_{r,ins}} \cdot G \simeq 120 \text{ MHz} \quad (4.8)$$

$$f_{c,2} \simeq \frac{1}{2\pi} \cdot \frac{\sigma_{sol}}{\varepsilon_0 \varepsilon_{r,sol}} \simeq 405 \text{ MHz} \quad (4.9)$$

The bacterial cell features quite similar cutoff frequencies as those given in Section 2.2.3: $f_{cb,1} \simeq 13.7 \text{ MHz}$ (different because of the smaller R_{wall}

value) and $f_{cb,2} \simeq 200$ MHz. The whole system is then described by the following succession of cutoff frequencies $f_{cb,1} < f_{c,1} < f_{cb,2} < f_{c,2}$, where each interval corresponds to a specific behavior (Fig. 4.7(b)). At $f_{IDE} < f_{c,1}$, C_{ins} dominates in series whatever the outer capacitance C_{pl} (if $f_{IDE} < f_{cb,1}$) or the cytoplasm resistance R_{cyt} (if $f_{IDE} > f_{cb,1}$) values. Between $f_{c,1}$ and $f_{cb,2}$, the bacterial cytoplasmic resistance governs and slightly increases the whole medium resistance. At $f_{IDE} > f_{c,2}$, bacterial cytoplasm decreases the medium capacitance. Thus, the largest bacterial sensitivity is expected around frequencies $f_{cb,2}$ and $f_{c,2}$ where volume effects (R_{sol} & C_{sol}) dominate. A sensor interface must thus be designed to operate at such very high frequencies (VHF) beyond $f_{c,1} \simeq 120$ MHz.

CFC architecture

To achieve VHF operation, the full IDE sensor is divided into five sub-interdigitated microelectrodes (sIDE), each connected to an internal node of a ring oscillator (Fig. 4.8). Once the *en* signal is enabled, the oscillation starts and establishes at a frequency:

$$f_{IDE} \simeq I_{on}/(2N_{inv}C_{inv}V_{dd}) \quad (4.10)$$

where V_{dd} is the supply voltage, I_{on} the drive current provided by one inverter, N_{inv} is the number of inverters and C_{inv} the inverter output capacitance. The sIDE impedance, approximated by a global capacitance C_{sIDE} , dominates C_{inv} as detailed in next sections. In other words, f_{IDE} is inversely proportional to the whole electrode capacitance $C_{IDE} \simeq N_{inv} \cdot C_{sIDE}$, and thus provides an easy way to quantify it.

For a given total electrode area and inverter design, the number of inverters must be odd and minimal to maximize f_{IDE} and the sensitivity to C_{IDE} , by reducing parasitic capacitances at each sIDE node. Post-layout simulations of a three-stage ring oscillator presented attenuation of oscillations at low R_{sol} , i.e., for high-conductive buffers, due to detrimental combination of parasitic line resistances and R_{sol} . A five-stage ring oscillator was thus designed to reach the specifications.

A frequency divider is added at the oscillator output to reduce the output frequency f_{out} below 600 kHz, thus minimizing the effect of external parasitic couplings and enabling read-out by standard scopes or microcontrollers. The frequency divider is a 10-stage Johnson counter with identical closed-loop flipflops composed of two latches and one inverter, and its division factor is $2^{10} = 1024$.

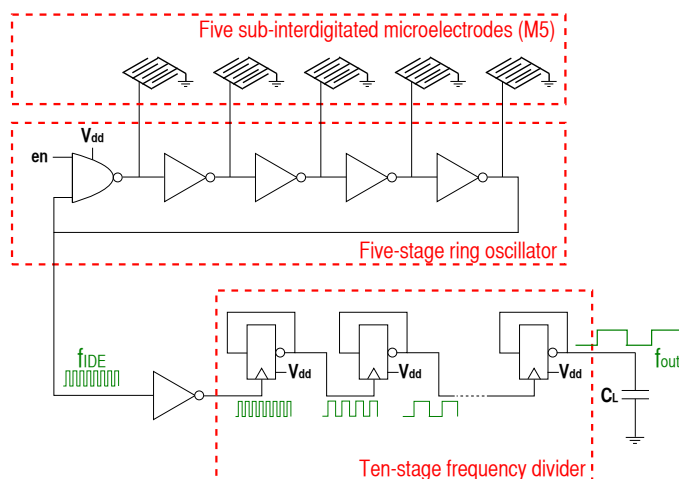


Figure 4.8 – Architecture of the capacitance-to-frequency converter (CFC) composed of a five-stage ring oscillator and a ten-stage frequency divider. Each oscillator node is connected to one on-chip sub-interdigitated microelectrodes (sIDE). A load capacitance C_L of 10 pF is assumed to mimic BNC cables.

CMOS manufacturing, post-processing and design

The CMOS fabrication, post-processing and encapsulation of capacitance-to-frequency converters (CFC) with their own on-chip IDE are detailed in Appendix A.4. For the inverter design, native- V_t NMOS and PMOS transistors, with $(W/L)_N = 5 \times (5 \mu\text{m}/0.24 \mu\text{m})$ and $(W/L)_P = 5 \times (12.5 \mu\text{m}/0.24 \mu\text{m})$ were used. Their large W/L ratio were chosen to provide enough I_{on} to achieve VHF oscillation up to 300 MHz for the 100 μm -sided CFC and 575 MHz for the 200 μm -sided CFC on $C_{sIDE} \sim \text{pF}$ at $V_{dd} = 2.5 \text{ V}$ (see Appendix D.4). In contrast, NMOS/PMOS transistors in flipflops are medium- V_t with smaller sizes $(W/L)_N = (1 \mu\text{m}/0.35 \mu\text{m})$ and $(W/L)_P = (2.5 \mu\text{m}/0.35 \mu\text{m})$, respectively. Two CFC systems were designed with the same electrical circuit but different total sensing areas: 100 $\mu\text{m} \times 100 \mu\text{m}$ versus 200 $\mu\text{m} \times 200 \mu\text{m}$ IDE patterned in M5. Microelectrode width and gap were fixed to the minimal allowable size (1.5 μm) to maximize sensitivity to 1.2 μm -diameter bacteria [180]. Consequently, each of the five sIDE has a total number of fingers of 7 and 13 for the 100 μm - and 200 μm -sided electrodes, respectively (Fig. 4.9). Also, the oscillator layout protects sensitive tracks from VHF voltages on microelectrodes. In particular, a large mass shield was patterned in the fourth metal layer (M4) to reduce clock feedthrough effects between upper and lower CMOS metal layers (Fig. 4.7(a)).

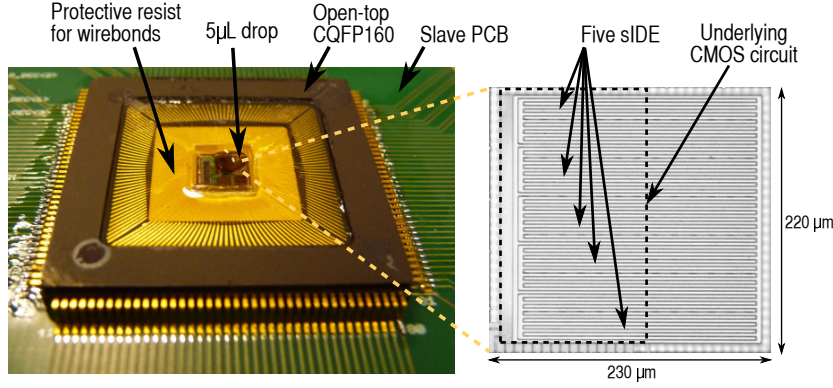


Figure 4.9 – Packaged chip and die microphotograph of the 200 μm -sided CFC.

4.2.3 Experimental validation

To improve readability, experimental results are expressed in term of f_{IDE} , obtained by multiplying the measured output frequency f_{out} by the frequency divider factor $2^{10} = 1024$. Details on the measurement setup is provided in Appendix A.5.

Circuit functionality

The frequency f_{IDE} depends on V_{dd} following the I_{on} trend from sub-threshold to strong inversion operation (Fig. 4.10(a)), in agreement to SPICE post-layout simulations where DI water was modeled by lumped elements as in Fig. 4.7(a). Wide operating ranges of f_{IDE} are available in DI water when V_{dd} spanned from 0.3 V to 2.5 V: [11 kHz, 574 MHz] and [8 kHz, 291 MHz] for the 100 μm - and 200 μm -sided IDE, respectively. In the whole V_{dd} range, the ratio between f_{IDE} of 100 μm - to 200 μm -sided IDE is $\simeq 2$, differing from the IDE area ratio $\simeq 4$. Indeed, parasitic capacitances at each sIDE node are not negligible, as shown by the 1st term in the next expressions extracted from post-layout simulations:

$$100 \mu\text{m CFC: } f_{IDE} \sim (0.8 \text{ pF} + 0.77 \cdot C_{sol,100\mu\text{m}})^{-1} \quad (4.11)$$

$$200 \mu\text{m CFC: } f_{IDE} \sim (1 \text{ pF} + 0.77 \cdot C_{sol,200\mu\text{m}})^{-1} \quad (4.12)$$

The factor 0.77 comes from insulator capacitance C_{ins} twice in series with C_{sol} , and featuring $C_{ins}/C_{sol} = \frac{\epsilon_{r,ins}}{\epsilon_{r,sol}} \cdot \frac{d_e}{t_{ins}} \cdot \frac{1}{G} \simeq 6.75$. Based on 3D FEM simulations with Comsol multiphysics[®] giving $C_{sol,100\mu\text{m}} = 1 \text{ pF}$ and $C_{sol,200\mu\text{m}} = 3.5 \text{ pF}$ for each sIDE, Eqs. (4.11) and (4.12) demonstrate that f_{IDE} decreases only by a factor 2 when the electrode area

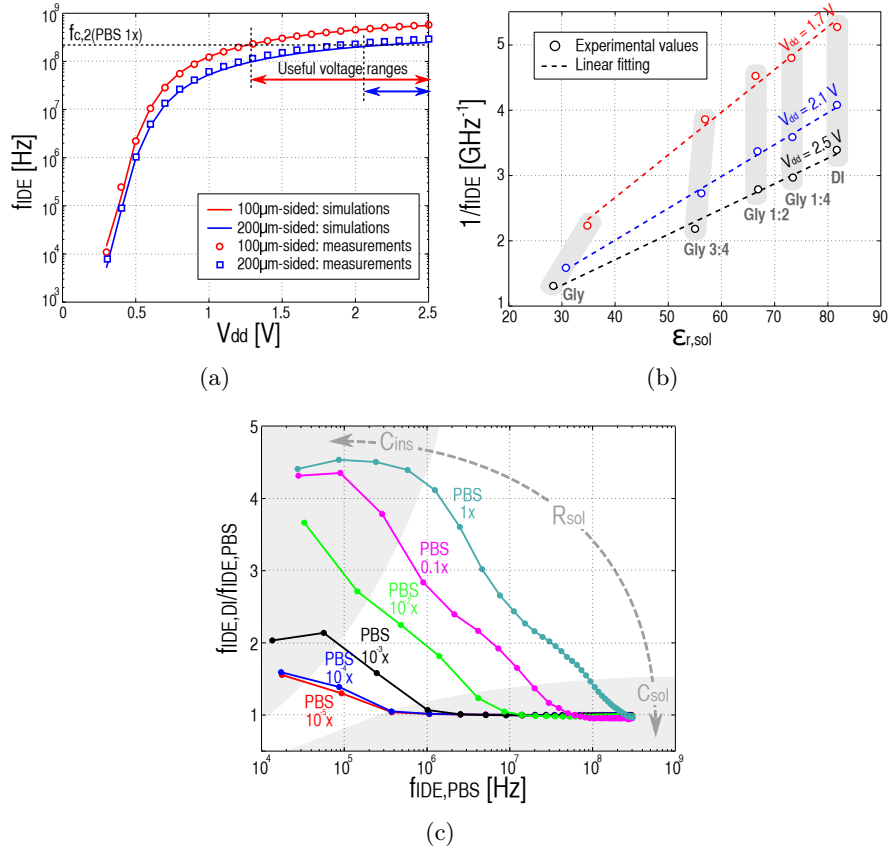


Figure 4.10 – (a) Measurements and post-layout simulations of f_{IDE} versus V_{dd} in DI water, (b) experimental dependence of $f_{IDE,200\mu m}$ with the relative permittivity of glycerol (Gly) dilutions by volume in DI water at distinct V_{dd} and (c) experimental ($f_{IDE,DI}/f_{IDE,PBS}$) ratio versus $f_{IDE,PBS}$ for different PBS dilutions with σ_{sol} ranging from 18 $\mu\text{S}/\text{m}$ (PBS 10 ^{-5}x) to 1.8 S/m (PBS 1x), characterized on the 200 μm -sided IDE. Similar results for (b) and (c) holds for the 100 μm -sided IDE.

is multiplied by a factor 4. To experimentally check the proportionality between f_{IDE}^{-1} and C_{sol} , serial Glycerol dilutions were performed in DI water and pipetted atop the chip. Their permittivities $\epsilon_{r,sol}$ were characterized at each f_{IDE} by a VNA (Agilent N5242A) connected to a dielectric probe (Agilent 85070E). Demonstrating the inverse proportionality between f_{IDE} and $\epsilon_{r,sol}$, measurements feature a mean error inferior to 2% compared to linear least squares regressions (Fig. 4.10(b)), which is in the same range that [93, 243, 244, 252].

Influence of the electrolyte conductivity σ_{sol}

The ratio between the measured frequency in DI water ($f_{IDE,DI}$) to the one in various tenfold PBS dilutions ($f_{IDE,PBS}$) was extracted for the 200 μm -sided IDE (Fig. 4.10(c)). When the ionic strength increases with related conductivities σ_{sol} from 18 $\mu\text{S}/\text{m}$ to 1.8 S/m (checked with a conductimeter), the low-frequency ($f_{IDE} < 1$ MHz) capacitance gets larger and saturates to approximately 4.5 times the capacitance in DI water. As indicated in Fig. 4.10(c), this can be interpreted as a progressive transition from $(0.77 \cdot C_{sol})$ to $(C_{ins}/2) \simeq 3.37 \cdot C_{sol}$ in Eq. 4.11–4.12, because both $f_{c,1}$ and $f_{c,2}$ increase proportionally to σ_{sol} and eventually exceed f_{IDE} . At high frequencies ($f_{IDE} > 200$ MHz), the capacitance value stays stable from PBS 10^{-5}x to pure PBS, since $f_{c,2} < f_{IDE}$ for all $\sigma_{sol} \leq 1.8$ S/m. In this case, C_{sol} dominates the CFC response, demonstrating volume monitoring in saline buffers.

It is important to mention that the capacitive behavior remains dominant for all σ_{sol} up to 1.8 S/m (either through $C_{ins}/2$ or C_{sol}) since the maximal phase of the electrolyte in the Bode diagram of Fig. 4.7(b) is -52° , which is smaller than -45° . This is quite important since it guarantees the proper operation of the CFC.

Bacteria sensing in high-conductive solutions

The preparation of *S. epidermidis* sample is fully described in Appendix A.3. A 5 μL drop of bacterial resuspension was pipetted above the two CFC IC and the package lid was then closed during the incubation time of 20 min to avoid drop evaporation. Measurements of f_{IDE} in fresh sterile PBS for each V_{dd} were performed before and after this bacterial incubation, and the chip surface observed by optical microscopy. Results were repeated for a second independent experiment (Fig. 4.11(a)).

After the incubation time, the random *S. epidermidis* binding to the sensor surface (see [180] for details on biological variations) leads to number of captured bacteria of ca. 1200 (i.e. 13.57% coverage, see Fig. 4.11(b)) and 4614 (i.e. 13% coverage) for the 100 μm - and the 200 μm -sided IDE of the second experiment, respectively. These numbers come from the second experiment in Fig. 4.11(a), since the first experiment gives underestimated bacteria numbers because of the rough undesired wash that occurred before visualization. Achieved around 150 MHz ($> f_{c,1} \simeq 120$ MHz) where volume properties dominate, the corresponding maximal sensitivities were 5.3% and 12.7%, respectively, differing by a factor 2 despite similar bacterial coverages. Indeed, a small vari-

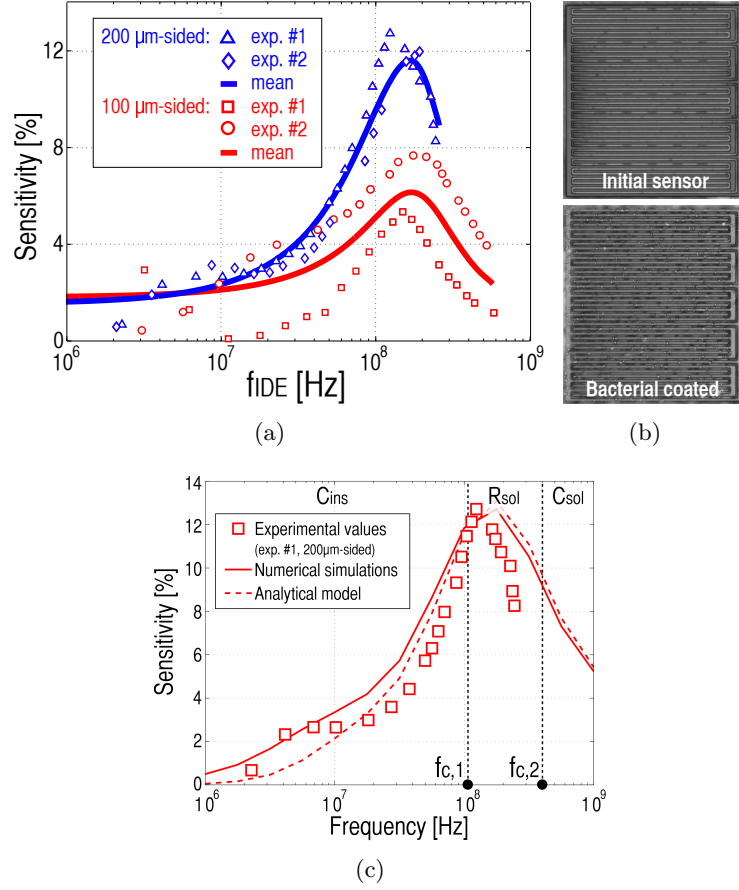


Figure 4.11 – (a) Experimental sensitivity $S \triangleq (\Delta f_{IDE})/f_{IDE}$ to *S. epidermidis* in pure PBS versus f_{IDE} for the two CFC circuits, repeated by one independent experiment. Δf_{IDE} and f_{IDE} are mean values of 100 successive temporal measurements (standard deviation at each point is $< 0.5\%$). (b) Illustration of the bacterial coverage for the 100- μm sided CFC of the second experiment. (c) Matching between experimental values, numerical simulations of Section 2.4 and analytical model of Section 2.2 having the following parameters $t_{ins} = 25$ nm, $\sigma_{sol} = 1.8$ S/m, $d_e = w_e = 1.5$ μm and $t_e = 1.8$ μm . The factor K to match 2D with 3D data is equal to 0.89.

ation $\Delta C_{sol,200\mu\text{m}} \simeq 3.5 \cdot \Delta C_{sol,100\mu\text{m}}$ will not impact f_{IDE} proportionally due to parasitic capacitances expressed in Eqs. (4.11) and (4.12). At the optimal frequency of 150 MHz, f_{IDE} experimentally increases and highlights the larger and lower values for R_{sol} and C_{sol} , respectively, since $\varepsilon_{r,cyt} < \varepsilon_{r,sol}$ and $\sigma_{cyt} < \sigma_{sol}$. Excellent matching with numerical simulations developed in Section 2.4 and with the analytical

model provided in Section 2.2 was obtained (Fig. 4.11(c)). Unlike Fig. 2.23(b), there is no significant difference between analytical and simulated curves since R_{wall} becomes negligible at $\sigma_{sol} = 1.8$ S/m. Since the nominal $SNR \triangleq 20 \cdot \log_{10}(\overline{f_{out}}/\sigma_{f_{out}})$ were 60 dB and 65 dB respectively, the minimal detectable sensitivities defined as five times the noise were 0.5% (i.e. 25 fF for the whole IDE) and 0.28% (i.e. 50 fF for the whole IDE), corresponding to 113 and 102 bacteria for the 100 μm - and 200 μm -sided IDE, respectively. In term of concentration, the LOD is estimated to 10^7 CFU/ml of whole-cell *S. epidermidis* in pure PBS, after 20 min of incubation on the sensor.

It is important to mention that the temperature rise of the chip and liquid did not exceed 2 to 3°C at the maximum power consumption of 29 mW, as characterized with a macro lens (FLIR Macro 1X) mounted on an infrared camera (FLIR SC660). This small temperature drift guarantees the viability of bacteria, the stability of f_{IDE} (variation $< 0.5\%$ were obtained by SPICE simulations) and the stability of σ_{sol} (variation $< 0.6\%$ as characterized). More details are provided in Appendix D.5.

4.2.4 Comparison with relevant works

To compare this work objectively with the literature, two sets of detailed comparison are provided in Tables 4.2 and 4.3. A wider comparison including much works can be found in Tables 2.1 and 4.1.

When considering only impedimetric detection of bacteria (Table 4.2), this work provides the smallest chip, which additionally comprises both sensor and electrical readout. The LoD is slightly higher than other works which use either non-saline buffers [79, 94] or larger sample volumes [120]. To decrease the LoD, several strategies can be combined with the CFC such as electrokinetics (see Chapter 3), sensor arrays (see Section 4.3), or magnetic beads [94]. Selectivity can also be obtained with lytic enzymes (see Section 2.3) or using grafted antibodies [104].

When considering GHz oscillators designed to probe chemical solutions [93, 243, 244, 252] (Table 4.3), our CFC is more suitable for biological sensing thanks to the large active area, provided by the small electrode width and gap, and to electrode robustness against corrosion provided by Al_2O_3 . This leads to a much higher capacitance ($C_{IDE} \sim 14$ pF) but for a similar power consumption (29 mW). Hence, our design features the best value for the figure of merit $FoM \triangleq \frac{\text{power}}{C_{IDE} \cdot f_{IDE} \cdot V_{dd}^2} \simeq 1.14$ at $V_{dd} = 2.5$ V. At 29 mW, the CFC output provides $2.5 \cdot 10^5$ samples per sec and can be duty-cycled to reduce the energy consumption.

4.2. A CFC for bacterial sensing in conductive buffers 145

Table 4.2 – Comparison of relevant works on impedimetric detection of bacteria.

	[94]	[120]	[79]	This work* [22]
Readout	Off-chip IA	Off-chip IA	Off-chip IA	On-chip CFC
Techno.	Passive IDE	Passive IDE	Passive IDE	0.25 μm CMOS
V_{dd}	-	-	-	0.3 - 2.5 V
Range	10 Hz - 1 MHz	100 Hz - 100 kHz	1 Hz - 100 kHz	8 kHz - 291 MHz
Power	-	-	-	29 mW @ 2.5V, 250 kS/s
Area**	7.5 mm ²	2.25 mm ²	0.09 mm ²	0.05 mm ²
Material	Au	Au	Au	Al/Al ₂ O ₃
Bacteria	<i>E. coli</i>	<i>E. coli</i>	<i>S. typhimur.</i>	<i>S. epiderm.</i>
Labeling	Yes	No	No	No
σ_{sol}	$\simeq 200 \mu\text{S/m}$	$\simeq 1 \text{ S/m}$	$\simeq 6 \mu\text{S/m}$	$\simeq 1.8 \text{ S/m}$
Sensing	R_{sol}	C_{DL}	R_{sol}	R_{sol}/C_{sol}
LOD	10 ⁵ CFU/ml	10 ⁴ CFU/ml	3 · 10 ⁶ CFU/ml	10 ⁷ CFU/ml
Sample	2 μL	1000 μL	25 μL	5 μL
t_{detect.}	35 min	40 min @ 37°C	60 min	20 min

IA: Impedance Analyzer. *: for the 200 μm -sided CFC
 **: including the sensor and readout, if integrated.

Table 4.3 – Comparison of relevant works on very-high-frequency CFC.

	[244]	[252]	[243]	[93]	This work* [22]
CMOS process	90 nm	0.35 μm	65 nm	90 nm	0.25 μm
V_{dd}	1.3 V	1.5 V	NA	0.45 V	2.5 V
IC area	6.25 mm ²	9 mm ²	1.2 mm ²	2.15 mm ²	0.05 mm ²
Power	16.5 mW	9 mW	114 mW	22 mW	29 mW
Frequency	9 GHz	2 GHz	25 GHz	10.4 GHz	291 MHz
$\varepsilon_{r,sol}$	30	9	4	30	80
C_{sense}	0.4 pF	0.24 pF	3.5 fF	0.12 pF	14 pF
Power FoM	2.71	8.44	NA	87	1.1
Accuracy on $\varepsilon_{r,sol}$	< 3.5%	< 1%	1%	1.5%	< 2%

C_{sense} is the sensed capacitance including the C_{ins}^* capacitance.
 FoM $\triangleq Power/(C_{IDE} \cdot f_{IDE} \cdot V_{dd}^2)$.

4.2.5 Conclusions

In this first chapter part, capacitive biosensing at VHF ~ 575 MHz was analytically, numerically and experimentally assessed to increase sensitivity to bacteria in high-conductive buffers [22]. To this end, a CMOS capacitance-to-frequency converter (CFC) connected to on-chip Al/Al₂O₃ IDEs was designed and tested with various solutions. The results showed excellent matching with simulations and ability to

accurately sense volume properties instead of surface properties in high-conductive buffers ($\sigma_{sol} \simeq 1.8 \text{ S/m}$). As a proof-of-concept towards bacterial point-of-care (PoC) diagnostics, detection of whole-cell *S. epidermidis* was successfully performed in pure PBS demonstrating a maximal sensitivity in the 100 MHz – 250 MHz range and a detection limit of approximately 10^7 CFU/ml after 20 min of bacterial incubation. The 0.05 mm^2 area, the 29 mW consumption at 250 kS/s, and the sensor/circuit co-integration makes this biochip very suitable for PoC applications.

4.3 A biosensor array towards single bacterium sensing

4.3.1 Motivations

Integrated biosensor arrays are unique platforms combining thousands biosensors on a single chip. Many studies have highlighted the huge medical potential of charged-based multi-electrode arrays (MEA) to sequence bacterial and human genome in few hours [67] and record real-time activities of electrogenic cells from the brain and heart [158, 253].

Such array can also be envisioned for PoC detection of pathogen bacteria, where the huge amount of parallel detectors provides multiplexing and reduces the sample size, diagnosis time, cumbersomeness and cost [1]. Another key advantage is that pixels can be shrunk to the μm -size while keeping the same total sensing area by increasing their number. When close to the bacterial size ($\sim \mu\text{m}$), each sensing unit increases its sensitivity and can envision detection of single bacterium. In this case, the biosensor array can thus enhance its detection limit in term of number of bacteria per mm^2 [240], substituting to concentration techniques such as dielectrophoresis [220] or magnetic beads [94].

As previously established in Section 4.1.3, capacitive biosensor arrays have been reported for detection of cells [231], DNA [92, 139, 234, 238], proteins [235] or $10 \mu\text{m}$ polystyrene or magnetic beads [82, 231], but not for whole-cell bacteria to the best knowledge of the authors. In the case of nanometer biospecies such as proteins and DNA, the on-chip sensors monitor a change of C_{DL} . In contrast, cells and beads that are larger than $10 \mu\text{m}$ typically exceed the pixel size, so that sensors evaluate their volumic dielectric properties through R_{sol} or C_{sol} . The same principle can be used for bacteria but the modified volume between electrodes is three orders of magnitude smaller because of their $1 \mu\text{m}$ diameter. In this case, sensitivity is then the key performance to enhance.

In this second part of the chapter, we report the first CMOS capacitive biosensor array for detection of whole-cell bacteria [23]. Built in a $0.25 \mu\text{m}$ mixed-signal CMOS process, a 16×16 array comprises pixels of $14 \mu\text{m} \times 16 \mu\text{m}$ whose sensing parts include two Al_2O_3 -passivated microelectrodes in the last CMOS metal layer. The in-pixel readout circuit uses a non-differential charge sharing principle combined with a gain transistor in subthreshold operation to enhance the sensitivity to bacterial cells, achieving a LoD of ca. 7 single bacteria.

The work is organized as follows. In Section 4.3.2, the challenges of

capacitance conversion inside micrometer-sized pixels towards biosensing are addressed. In Section 4.3.3, the designs of the electrical circuit and sensing parts are detailed. In Section 4.3.4, experimental performances achieved by the capacitive array are described in dry condition and in solutions with and without bacterial cells. Finally, a discussion with regards to literature is provided in Section 4.3.5.

4.3.2 Challenges of in-pixel capacitance conversion

Capacitive readout interfaces convert in-pixel capacitances into either analog voltages, which then require ADC, or square voltages with a frequency inversely proportional to the pixel capacitance. When the readout circuit is integrated inside each pixel, the main challenges arise from the small pixel area required to boost sensitivity to bacteria and the next issues must be considered to design the readout interface:

- Sensed capacitances are typically extremely small (~ 10 fF) despite the large value of $\varepsilon_{r,sol}$. Parasitic capacitances and kT/C noise can thus possibly deteriorate sensing performance.
- When electrodes are protected by a passivation layer [82, 226, 228, 231, 232, 235, 237], the sensed capacitance C_{sol} is partially screened.
- For high-conductive solutions, the low resistance R_{sol} can alter the capacitance conversion.
- Mismatch (FPN) between small pixels must be reduced.

As previously described in Section 4.1.2, differential methods are not suitable for biosensor arrays because of the need for a proper control value for each pixel. On the other hand, pseudo-differential methods consisting in subtracting the sensed capacitance from an fixed on-chip capacitance [231, 242] are not versatile since the fixed capacitance is calibrated for a given liquid featuring fixed $\varepsilon_{r,sol}$ and σ_{sol} .

Among single-ended methods, capacitance-to-frequency converters feature output voltages inversely proportional to C_{sol} , charging time constants extremely small at high σ_{sol} and no implemented compensation techniques for FPN (see Section 4.1.3). Capacitor dividers are not recommended since one electrode side is floating and then presents trap charges that strongly increases FPN. Coherent detection requires complex electrical circuitry and can hardly be integrated within a micrometer-sized pixel (see Section 4.1.3).

Charge sharing principle or switched capacitors seem thus the most appropriate techniques for the targeted application because of the possible FPN compensation and the linear dependence between the output voltage and the input capacitance (see Section 4.1.2). Depending on the switching frequency, they can be used with high-conductive solutions.

4.3.3 Implementation

System architecture

The biosensor array is divided in five parts: the row and column decoders, pixel array, column amplifiers and output stage. The analog-to-digital conversion is performed off-chip with a dedicated instrument (see Appendix A.5). The 4:16 decoders use two 2:4 decoders built with inverters and NAND gates, while other blocks are implemented as depicted in Fig. 4.12. The readout is controlled by digital signals synchronized on a 40 MHz-clock and features four phases: initialization, reset, integration and readout. The supply voltage V_{dd} is fixed to 2.5 V.

Each pixel comprises both sensing and readout parts. The sensor is implemented by miniaturized IDE patterned in the last CMOS metal layer and covered with a thin post-processed passivation layer. The underlying electrical circuit uses charge sharing principle to convert the in-pixel IDE capacitance C_{IDE} into a proportional output voltage. One row of the capacitive array is read at a time and controlled by row decoders. The critical in-pixel nodes V_{IDE} and V_{gT} are first initialized to ground during the initialization phase. During the reset phase, the transistor M_R sets the voltage V_{pix} to its reset value and switches M_{C1} and M_{C2} load the voltage V_{gT} to a value proportional to C_{IDE} :

$$V_{gT} = \left(\frac{C_{IDE}}{\underbrace{C_{IDE} + C_D + C_{gT}}_{\beta}} \right) \cdot V_{ref} \quad (4.13)$$

$$\simeq \left(\frac{C_{IDE}}{C_D + C_{gT}} \right) \cdot V_{ref}$$

with C_{gT} the gate capacitance of M_T , C_D the in-pixel capacitance of fixed value and V_{ref} the reference voltage supplied off-chip and applied to all pixels. This conversion comes from the charge redistribution between C_{IDE} , first loaded to V_{ref} when M_{c1} is asserted by V_{c1} , and the fixed capacitance $C_D + C_{gT}$ when M_{c2} is enabled by V_{c2} . By placing M_T in subthreshold inversion, the small value of V_{ref} enables maximizing the

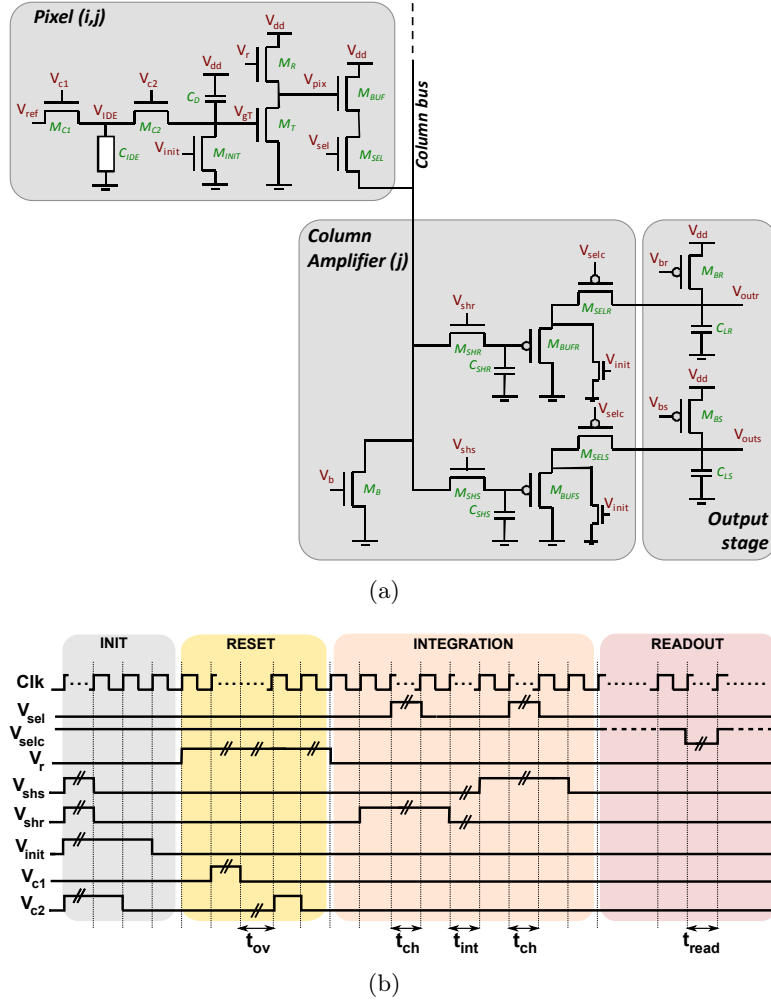


Figure 4.12 – System architecture of the pixel, column amplifier and output stage. The temporal diagram illustrates the digital controls for the readout of a single row, where annotations // refer to durations longer than the clock period. Four main phases are highlighted: the initialization, reset, integration and readout phases. The clock frequency is 40 MHz and the supply voltage V_{dd} is 2.5 V.

relative sensitivity S_r , defined as:

$$S_r \triangleq \frac{1}{V_{out}} \cdot \frac{\partial V_{out}}{\partial C_{sol}} \quad (4.14)$$

where V_{out} is the output voltage defined by Eq. 4.15 and C_{sol} the medium capacitance, which is slightly different from C_{IDE} as explained in the

4.3. A biosensor array towards single bacterium sensing 151

next section. To maximize S_r , V_{gT} is amplified by an exponential transfer function (see Appendix C.2), provided by the subthreshold operation of M_T . SPICE simulations give a subthreshold slope of 98 mV/dec for M_T , corresponding to $\alpha = \frac{98 \text{ mV}}{\ln 10} = 42 \text{ mV}$ in Appendix C.2. The subthreshold transfer function thus enhances S_r when $V_{gT} > 42 \text{ mV}$.

During the integration phase, V_{gT} remains fixed to the value given by Eq. 4.13 since M_{c1} and M_{c2} are both disabled. The drain current of M_T progressively discharges V_{pix} during an integration period t_{int} , reducing its temporal noise. Both reset and signal values on V_{pix} , chosen at the start and end of integration period, are stored on column-based amplifiers. Eventually, for each in-row pixels selected by the column decoder, the readout phase successively sends reset and signal values stored in column amplifiers to the output stage, resulting in voltages V_{outr} and V_{outs} , respectively. These are then converted to digital values by the off-chip ADC and subtracted to implement the CDS, which reduces FPN and kT/C noise [241]:

$$\begin{aligned} V_{out} &\triangleq V_{outr} - V_{outs} \\ &\propto \exp(V_{gT}) \\ &\propto \exp(C_{IDE}) \end{aligned} \tag{4.15}$$

where the two last relationships hold when M_T is in weak inversion. The dependence of the voltage V_{out} with V_{gT} is depicted in Fig. 4.13. The operating range is defined as the region where M_T goes from weak to strong inversion, i.e. $V_{gT} \in [0.1 \text{ V}, 0.32 \text{ V}]$. When $V_{gT} < 0.1 \text{ V}$, the output voltage mostly depends on the mismatch between V_{outs} and V_{outr} . When $V_{gT} > 0.32 \text{ V}$, both the signal V_{outs} and reset V_{outr} saturate and V_{out} drops consequently. This dependence of the reset level with V_{gT} is due to the CDS implementation, since V_{pix} must be sampled *after that* M_R is cut off. The drop of V_{outr} compared to its value at $V_{gT} = 0$ is ca. 10 times smaller than for V_{outs} when $V_{gT} \in [0 \text{ V}, 0.3 \text{ V}]$ and does not alter the circuit working principle. However, it slightly reduces the sensitivity of V_{out} to V_{gT} by ca. 10%.

The major contributions of our circuit with regards to the charge sharing implementation proposed in [226] are the additional subthreshold gain stage, the calibration capability with V_{ref} and the large on-chip capacitance C_D , providing a better linearity between V_{gT} and C_{IDE} .

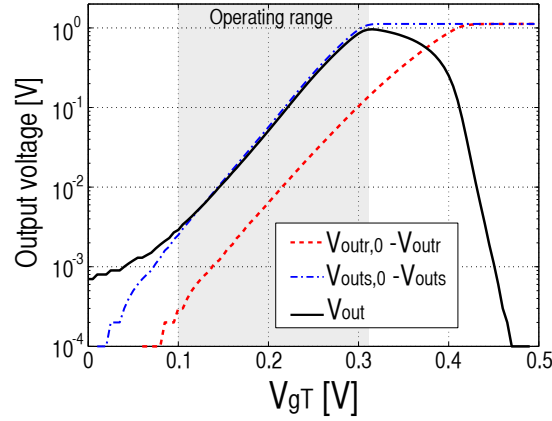


Figure 4.13 – SPICE simulations showing the impact of V_{gT} on the output reset voltage $V_{out,r}$, the output signal voltage $V_{out,s}$ and the differential output $V_{out} = V_{out,r} - V_{out,s}$. The voltages $V_{out,r,0}$ and $V_{out,s,0}$ correspond to the values of $V_{out,r}$ and $V_{out,s}$ at $V_{gT} = 0$, respectively.

Design of the pixel sensing part

Each pixel comprises two electrodes patterned in the last CMOS metal layer and connected to V_{IDE} and ground, respectively. They are designed to maximize the sensitivity to adherent bacteria on the given pixel area (Fig. 4.14(a)), fixed by the underlying readout circuit to $14 \mu\text{m} \times 16 \mu\text{m}$ (see Section 4.3.3). Gaps $d_e = 2 \mu\text{m}$, widths $w_e = 2 \mu\text{m}$ and lengths $L_e = 14 \mu\text{m}$ provide a maximal active area, a regular pattern and enough place to let bacteria bind between microelectrodes, where electric field is maximal. The capacitance C_{IDE} of these electrode configuration is impacted mainly by the interaction between the electrode at V_{IDE} and its counterpart at ground, but also by ground electrodes of neighborless pixels which result in fill factors $\geq 100\%$.

Another key design parameter is the insulating layer covering these electrodes and protecting them from electrochemical corrosion in biological buffers. The electrical equivalent model of one pixel is similar to the one reported in Section 2.2.2, by accounting for an additional stray capacitance C_{stray} (Fig. 4.14(b)). Compared to the model of Section 2.2.2, the following parameters are different: $d_e = w_e = 2 \mu\text{m}$, $t_{ins} = 25 \text{ nm}$, $t_e = 1.8 \mu\text{m}$ and $G = 1$. Since the sensing principle is based on the linear change of C_{sol} with the number of adherent bacteria (see Section 2.2.3), it is important to quantify the reduction of sensitivity caused by lumped elements R_{sol} , C_{ins} , C_{DL} , C_{ox} and C_{stray} .

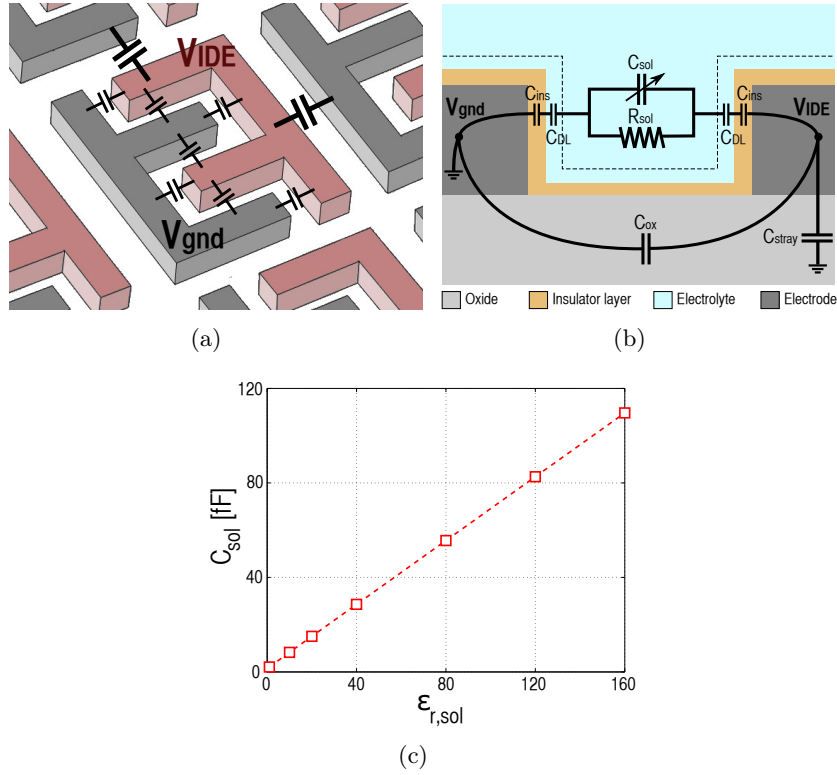


Figure 4.14 – Sensing part of the pixel: (a) 3D representation of the last metal layer (M5) of one pixel with the neighborless pixels highlighting the concerned capacitances, (b) 2D schematic cross-section of adjacent electrodes with their equivalent electrical circuit and (c) simulation results of the dependence of capacitance $C_{ox} + C_{sol}$ with the solution relative permittivity $\epsilon_{r,sol}$, based on the 3D representation of Fig. 4.14(a).

The resistance R_{sol} hardly perturbs the C_{sol} -to- V_{gT} conversion because the corresponding time constant is evaluated to $\tau \simeq \frac{\epsilon_{r,sol}\epsilon_0}{\sigma_{sol}} = 400$ ns, which is far larger than the 25 ns clock period between V_{c1} and V_{c2} . Furthermore, the ratio $C_{DL}/C_{ins} \simeq \frac{\epsilon_{r,sol}}{\epsilon_{r,ins}} \cdot \frac{t_{ins}}{\lambda_D} \simeq 9.3$ shows that C_{ins} dominates C_{DL} in series, while $(C_{ins}/2)/C_{sol} \simeq \frac{\epsilon_{r,ins}}{\epsilon_{r,sol}} \cdot \frac{d_e}{2t_{ins}} \cdot \frac{1}{G} \simeq 4.5$ demonstrates that C_{ins} cannot be neglected in series with C_{sol} . By assuming C_{ox} and C_{stray} far smaller than C_{sol} in parallel (see next paragraph and Section 4.3.3 for justification), C_{IDE} is approximated to:

$$C_{IDE} \simeq (2C_{ins}^{-1} + C_{sol}^{-1})^{-1} \simeq 0.82 \cdot C_{sol} \quad (4.16)$$

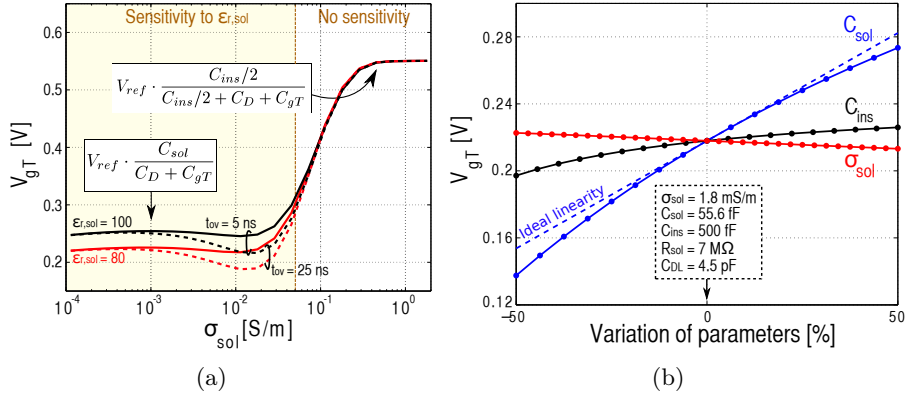


Figure 4.15 – SPICE simulation results of (a) the impact of the electrolyte conductivity σ_{sol} on the gate voltage V_{gT} of M_T for several values of t_{ov} and $\varepsilon_{r,sol}$ and (b) the impact of variation of C_{sol} , C_{ins} and σ_{sol} (thus impacting R_{sol} and C_{DL}) within $\pm 50\%$ of their nominal value on V_{gT} . V_{ref} is fixed at 0.9 V and the lumped elements shown in Fig. 4.14(b) are used in SPICE.

To accurately estimate C_{sol} , 3D finite-element simulations of the electrode design in Fig. 4.14(a) were performed with Comsol Multiphysics[®], by assuming no insulator and double layers. It highlights the following linear dependence of C_{sol} with $\varepsilon_{r,sol}$ (Fig. 4.14(c)): $C_{sol} = 2 \text{ fF} + 0.68 \text{ fF} \cdot \varepsilon_{r,sol}$. In typical electrolyte featuring $\varepsilon_{r,sol} = 80$, the solution capacitance is then equal to $C_{sol} = 55.6 \text{ fF}$. By setting $\varepsilon_{r,sol} = 0$, the capacitance corresponds to C_{ox} and is equal to 2 fF, which is far smaller than C_{sol} , as expected. The cell constant κ_{cell} is equal to $(\varepsilon_0 \varepsilon_{r,sol}) / C_{sol} = 127 \text{ cm}^{-1}$, giving the following value for the solution resistance: $R_{sol} = \kappa_{cell} \sigma_{sol}^{-1} \simeq 7 \text{ M}\Omega$.

Design of the pixel circuit

The charge sharing circuit is designed to obtain a gate voltage V_{gT} proportional to C_{sol} , free of non-linearities and independent of C_{ins} , C_{DL} and R_{sol} (see Eq. 4.13). Switches M_{C1} , M_{C2} and M_{INIT} are high- V_{th} transistors with minimal widths and channel lengths to reduce clock feedthrough and charge injection. The type of switches (low- versus high- V_{th}) impacts by only 16 % the on-resistance R_{on} of switches, so that high- V_{th} is preferred for low leakages. Based on sizes given in Table 4.4, the stray capacitance C_{stray} has a simulated value of 4 fF, which

4.3. A biosensor array towards single bacterium sensing 155

is far smaller than $C_{sol} = 55.6$ fF. The transition t_{ov} between V_{c1} and V_{c2} must be sufficiently small to have a proper and stable operation at $\sigma_{sol} \leq 0.05$ S/m (Fig. 4.15(a)). In this work, t_{ov} was fixed to the clock period (25 ns) to limit the V_{gT} drop around $\sigma_{sol} \simeq 0.01$ S/m below 15% of the V_{gT} value at $t_{ov} = 5$ ns and to provide a sufficient sensitivity at $\sigma_{sol} < 0.05$ S/m. At $\sigma_{sol} > 0.05$ S/m, the insulator capacitance dominates ($C_{IDE} \simeq C_{ins}/2$) and results in $V_{gT} \simeq V_{ref} \cdot \frac{C_{ins}/2}{C_{ins}/2 + C_D + C_{gT}}$ from Eq. 4.13, which is thus insensitive to $\varepsilon_{r,sol}$ whatever the t_{ov} -value. Around the nominal operating point where $\sigma_{sol} = 1.8$ mS/m, $\varepsilon_{r,sol} = 80$ and $\varepsilon_{r,ins} = 9$, V_{gT} predominantly depends on C_{sol} with a maximum non-linearity of 10% at $\pm 50\%$ of its variation (Fig. 4.15(b)). Furthermore, V_{gT} is almost insensitive to variations of C_{ins} and σ_{sol} , featuring maximal deviations of 9% and 2% on V_{gT} . The sensing principle is thus mainly impacted by dielectric medium properties, and immune to unexpected corrosion of the insulator layer [161] or ionic contamination of the electrolyte buffer (see Section 2.2.3), both inexistent in this work anyway.

To provide the high linearity between V_{gT} and C_{sol} , the capacitance C_D has been chosen constant and sufficiently larger than C_{sol} , but with moderation to limit degradation of the pixel area and sensitivity (see Eq. 4.13). A MIM capacitance cannot be used since microelectrodes are patterned in the last metal layer. Since V_{gT} is typically small to place M_T in weak inversion, a PMOS capacitor was used and features a maximal variation of 1.5% when V_{gT} spans from 0 to 0.5 V, thanks to its strong inversion regime. A $3.95 \mu\text{m} \times 3.95 \mu\text{m}$ size gives $C_D \simeq 100$ fF, therefore two times larger than C_{sol} . In addition, M_T is also designed with large width and channel length ($W/L = (5.5 \mu\text{m}/5.5 \mu\text{m})$) to increase its gate capacitance C_{gT} to 45 fF, reduce its Early effect and reduce the local mismatch on I_{dT} , detrimental for FPN. Finally, V_{ref} is chosen to boost S_r thanks to the experimental procedure described in Section 4.3.4.

The pixel source follower is designed to load a column bus capacitance $C_{col} \simeq 1$ pF in 6 clock periods (150 ns) and consists of a buffer transistor M_{BUF} , a row switch M_{SEL} and a biasing transistor M_B included in a column amplifier. For noise and timing constraints, the g_m/I_d of M_{BUF} is maximized to a high value of 22 V^{-1} (weak inversion) thanks to a low- V_{th} feature. To have a settling error smaller than the 1-mV resolution of the off-chip ADC, the charging time t_{ch} must be 8 times larger than the time constant $\tau_{ch} = \frac{C_{col}}{g_m}$. Since t_{ch} is limited to 6 clock periods (i.e. 150 ns) and $C_{col} \simeq 1$ pF, the g_m value of M_{BUF}

Table 4.4 – Transistor sizing for the circuit shown in Fig. 4.12(a)

Transistor	Type	(W/L) sizing
M_{C1}	NMOS high- V_{th}	(0.58 $\mu\text{m}/0.24 \mu\text{m}$)
M_{C2}	NMOS high- V_{th}	(0.58 $\mu\text{m}/0.24 \mu\text{m}$)
M_{INIT}	NMOS high- V_{th}	(0.58 $\mu\text{m}/0.24 \mu\text{m}$)
M_T	NMOS high- V_{th}	(5.5 $\mu\text{m}/5.5 \mu\text{m}$)
M_R	NMOS high- V_{th}	(0.58 $\mu\text{m}/0.24 \mu\text{m}$)
M_{BUF}	NMOS low- V_{th}	(3.86 $\mu\text{m}/0.5 \mu\text{m}$)
M_{SEL}	NMOS low- V_{th}	(0.58 $\mu\text{m}/0.5 \mu\text{m}$)
C_D	PMOS capacitance (100 fF)	(3.95 $\mu\text{m}/3.95 \mu\text{m}$)
M_B	NMOS high- V_{th}	(0.8 $\mu\text{m}/2 \mu\text{m}$)
$M_{SHR} - M_{SHS}$	NMOS high- V_{th}	(0.58 $\mu\text{m}/0.7 \mu\text{m}$)
$M_{BUFR} - M_{BUFS}$	PMOS high- V_{th}	(9.5 $\mu\text{m}/1 \mu\text{m}$)
$M_{SELR} - M_{SELS}$	PMOS high- V_{th}	(0.58 $\mu\text{m}/0.35 \mu\text{m}$)
$C_{SHR} - C_{SHS}$	NMOS capacitance (300 fF)	(6.82 $\mu\text{m}/6.82 \mu\text{m}$)
$M_{BR} - M_{BS}$	PMOS high- V_{th}	3 x (13 $\mu\text{m}/12 \mu\text{m}$)

Available values of threshold voltages V_{th0} in the 0.25- μm CMOS technology:
 NMOS: 60 mV, 180 mV and 480 mV; PMOS: 290 mV and 600 mV.

is fixed to 60 μS and the drive current therefore to 2.7 μA . Based on the g_m/I_d method [254], the biasing voltage V_b and the (W/L) ratio are found to be 0.7 V and 7.7, respectively, which results in sizes mentioned in Table 4.4 by minimizing the channel length for reduction of the pixel area. For the design of M_B , high- V_{th} NMOS is chosen with $g_m/I_d = 7.3 \text{ V}^{-1}$ (moderate inversion) to reduce noise. Giving (W/L) = 0.4, a large L is chosen to reduce the column FPN. Because of the non-zero body source voltages of M_{BUF} and M_{SEL} , the source follower suffers from a non-linearity of 3% per unit voltage when V_{pix} goes from 0.5 V to 2 V.

Design of the column amplifier circuit

The storage of the reset and signal values are ensured by large capacitances C_{SHR} and C_{SHS} . Designed to fill the column amplifier width with a squared shape, the capacitances have a value of 300 fF that enable only 3 mV shift after 100 μs of storage, thanks to high- V_{th} transistors M_{SHR} and M_{SHS} featuring low leakages in OFF state.

The two source followers are identically sized and next developments are only focused on the part storing the reset value. It consists of three transistors M_{BUFR} , M_{SELR} and M_{BR} , which have large widths and channel lengths to minimize the column-based FPN (which was not

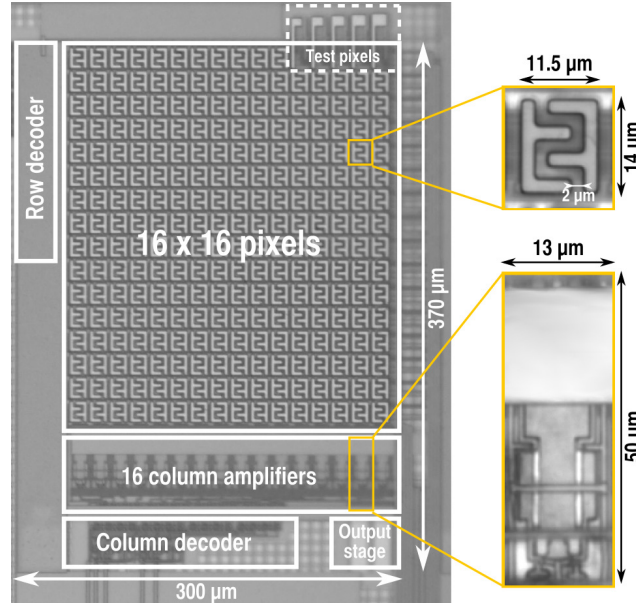


Figure 4.16 – Chip microphotograph with pixel and column amplifier zoom.

compensated by the delta-difference sampling (DDS) scheme such as in [255]). It is crucial for M_{SELR} to be high- V_{th} in order to reduce its drain leakage current and avoid the drain voltage of M_{BUFR} to increase with time, and perturb the storage node by capacitive coupling. The same methodology as the pixel source follower is used to size M_{BUFR} and M_{BR} and provides biasing voltage $V_{br} = 1.55$ V. However, the body of PMOS transistors is connected to the source to limit non-linearity from body effect, which was not possible in pixels for size constraint due to triple well. With $C_{LR} = C_{LS} \simeq 100$ pF, the maximal charging time t_{read} is 8 μ s. With the sizes provided in Table 4.4, the source follower achieves a non-linearity of 6.9% per unit voltage from 0 to 1.4 V.

4.3.4 Experimental validation

In this section, experimental tests performed with the fabricated chip are detailed. Firstly, functionality of the capacitive array is confirmed at dry condition and with basic solutions without bacterial cells. Secondly, the real-time detection of bacterial cells is demonstrated. The chip fabrication, post-processing and encapsulation is described in Appendix A.4, while the measurement setup is provided in Appendix A.5.

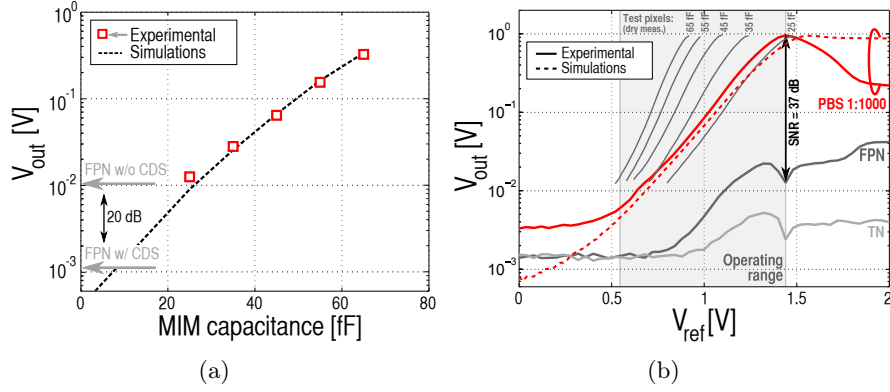


Figure 4.17 – (a) Experimental and simulated characteristics of V_{out} of test pixels versus their MIM capacitance values at $V_{ref} = 0.8$ V and at dry condition, showing the FPN values with and without CDS. (b) Experimental and simulated mean pixel output V_{out} versus V_{ref} in PBS 1:1000 with corresponding measured FPN and temporal noise (TN) levels, including comparison with measured characteristics of test pixels at dry condition. SPICE simulations account for the model in Fig. 4.14(b).

Circuit functionality

At dry condition, the readout time t_{read} was first adjusted to 20 μ s to let V_{outr} and V_{outs} achieve their steady state values. The time t_{ov} was fixed to the clock period (25 ns), while t_{int} to 2 μ s (see Appendix D.6 for the impact of t_{ins}). Test pixels with known MIM capacitance values ranging from 25 fF to 65 fF by step of 10 fF (Fig. 4.16) feature output voltages V_{out} that exponentially depend on MIM capacitances (as expected from Eq. 4.15) and that perfectly match post-layout simulations at dry condition (Fig. 4.17(a)). FPN levels at $V_{ref} = 0.8$ V with and without CDS were computed from the difference $V_{outr} - V_{outs}$ (Eq. 4.15) and from the voltage V_{outs} only, respectively, on all except edge pixels. Thanks to CDS, the FPN was reduced by a factor 9, close to 20 dB of improvement (Fig. 4.17(a)). The array consumes 29 μ W at a frame rate of 37 frames per sec, corresponding to an energy efficiency of 3 nJ/(frame.pixel) (see Appendix D.6 for the full characterization).

To validate sensing capabilities of all pixels, a 10 μ L drop of PBS 1:1000 was pipetted atop the capacitive array and the package lid closed to avoid drop evaporation and to work under dark condition. The mean output voltage computed on all except edge pixels highlights three different regions of operation depending on V_{ref} (Fig. 4.17(b)). At

4.3. A biosensor array towards single bacterium sensing 159

$V_{ref} < 0.6$ V, the output voltage is dominated by parasitics and noise. The operating range spans from 0.6 V to 1.3 V, where M_T progressively goes from weak to strong inversion and provides V_{out} dependent on V_{ref} and C_{IDE} according to Eq. 4.13. At each V_{ref} , ca. 10 successive temporal measurements were acquired and FPN was computed as the standard deviation of the mean temporal values of each pixel, while the temporal noise (TN) as the average of the standard deviations obtained on successive temporal values of each pixel. As shown in Fig. 4.17(b), FPN and TN have close values and both increase with V_{ref} , because mismatch and noise from M_T in subthreshold are not compensated by CDS. Operating in the subthreshold region of M_T thus enables to reduce both FPN and noise. Also, for this reason, FPN in water ($\varepsilon_{r,sol} = 80$, Fig. 4.17(b)) features larger values than FPN in air ($\varepsilon_{r,sol} = 1$, Fig. 4.17(a)), where M_T is cut off thanks to small $C_{IDE} \simeq 2$ fF and does not add FPN. The measured noise figure follows the same evolution versus V_{ref} as that given by SPICE simulations, but is larger by a factor 3 due to the use of external ADC that adds uncorrelated noise of 1-mV characterized amplitude on V_{outtr} and V_{outs} . The maximal signal-to-noise ratio (SNR) accounting for both FPN and noise is 37 dB at $V_{ref} = 1.44$ V (Fig. 4.17(b)). By comparing the measured characteristics V_{out} versus V_{ref} of the different test pixels at dry condition, the slopes are different because of the different values of β expressed in Eq. 4.13. The larger the MIM capacitance, the larger the value of β and therefore the steeper the slope. In solution, the effective capacitance C_{IDE} is also slightly smaller than C_{sol} (see Eq. 4.16), so that β is smaller compared to a fixed MIM capacitance of the same value. By considering this slope difference and comparing V_{out} values at the start of the subthreshold operation of M_T ($V_{ref} \simeq 0.7$ V), C_{IDE} in PBS 1:1000 can be approximated to 40-45 fF (Fig. 4.17(b)), which is ca. 80% of the simulated C_{sol} value of (55 fF), as expected by Eq. 4.16. SPICE simulations including the IDE model of Fig. 4.14(b) confirms the good matching in the operating range.

To assess that pixel outputs depend on dielectric medium properties, the capacitive array was subject to several glycerol dilutions, featuring different relative permittivities characterized with a VNA (Agilent N5242A) connected to a dielectric probe (Agilent 85070E) at 419 MHz: 35.5, 55.6, 66.9, 73.5 and 81.6 for glycerol, glycerol 3:4, glycerol 1:2, glycerol 1:4 and DI water, respectively. These permittivity values can be considered as good approximations for DC permittivities, since dielectric dispersion occurs beyond 419 MHz. Within the operating range, the mean pixel output and its slope both increase for larger $\varepsilon_{r,sol}$ (Fig.

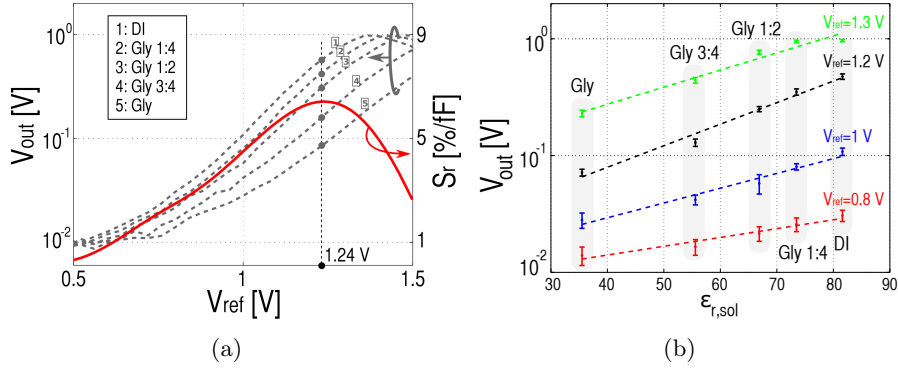


Figure 4.18 – Experimental dependence of V_{out} with (a) V_{ref} for several glycerol dilutions and with (b) the solution permittivity $\epsilon_{r,sol}$ of these dilutions for several V_{ref} , considering all except edge pixels for mean and standard deviation. For (a), the relative sensitivity S_r is also shown and is identical for all glycerol dilutions.

4.18(a)) for the same reasons as test pixels. At fixed V_{ref} , V_{out} is shown to be exponentially dependent on $\epsilon_{r,sol}$ (Fig. 4.18(b)) and confirms Eq. 4.15. Since C_{sol} changes by 1 fF when $\epsilon_{r,sol}$ goes from 80 to 78.5, the sensitivity $S \triangleq \frac{\partial V_{out}}{\partial C_{sol}}$ computed around $\epsilon_{r,sol} = 80$ has a maximal value of 55 mV/fF at $V_{ref} = 1.36$ V. On the other hand, the relative sensitivity defined by Eq. 4.14 has been extracted from the curves of different $\epsilon_{r,sol}$ (Fig. 4.18(a)) and has a maximal value of 6.3%/fF at $V_{ref} = 1.24$ V. As expected, S_r is maximized in the subthreshold slope at estimated gate voltage $V_{gT} \simeq 0.3$ V, thus well beyond $\alpha = 42$ mV (cfr Section 4.3.3 and Appendix C.2). Since the noise σ_n at $V_{ref} = 1.36$ V has a value of 5 mV (Fig. 4.17(b)), the LoD corresponding to $5 \cdot \sigma_n$ is evaluated to 450 aF. Accordingly, the dynamic range is $20 \cdot \log_{10}(\frac{55.6 \text{ fF}}{0.45 \text{ fF}}) \simeq 42$ dB.

Sensing of bacterial cells

In this section, the response of the biosensor array to bacterial cells contained in a low-conductive buffer is investigated. In contrast to the previous experimentation with simple solutions, all pixels are not supposed to give the same output voltage anymore, since bacterial cells can preferably adhere to some pixels. Protocols for preparation of the bacteria are provided in Appendix A.3.

The capacitive array was first measured under sterile PBS 1:1000 with V_{ref} spanning from 0 to 2.5 V. Then, a real-time experiment on the

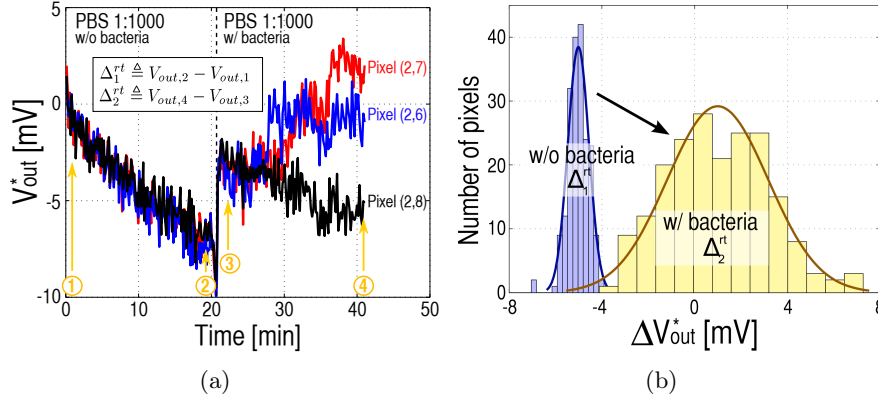


Figure 4.19 – Experimental biosensing of real-time *S. epidermidis* binding on the sensor surface: (a) temporal evolution of the output voltages V_{out}^* of three different pixels, set identical at $t = 0$ s, (b) statistical evolution of $\Delta_1^{rt} \triangleq V_{out,2}^* - V_{out,1}^*$ and $\Delta_2^{rt} \triangleq V_{out,4}^* - V_{out,3}^*$ on all pixels. V_{ref} is set to 1.06 V.

capacitive array was performed based on the following protocol. The reference buffer, the bacterial solution and the reference buffer again were successively incubated on the array surface, 20 min each time with lid closed and under electrical measurements at $V_{ref} = 1.06$ V, a midrange value in the subthreshold slope. The chip surface was then dried and observed by optical microscopy to localize bacterial binding. Then, the capacitive array was measured again in PBS 1:1000 with V_{ref} spanning from 0 to 2.5 V to find the best conditions achieving the maximal sensitivity with regards to the initial measurement. Because the bacterial-covered surface can hardly be cleaned without damaging the array, the biochip was discarded after a single experiment to avoid any interference. More generally, the chip was not designed to be reused because the Al_2O_3 layer would be strongly etched by chlorine solutions employed to remove adherent bacteria.

The temporal evolution of the three distinct pixel outputs (2,6), (2,7) and (2,8) during the two first incubation phases is described in term of $V_{out}^*(t) = V_{out}(t) - V_{out}(0)$ to suppress pixel mismatch and facilitate comparison (Fig. 4.19(a)). During the first 20 min, the three pixel outputs present a similar drift of approximately 5 mV (Fig. 4.19(a)), occurring because of the slight drop evaporation or possibly the accumulating charges in the DL because no reference electrodes is used. The voltage difference at times $[t_1, t_2] = [3, 19]$ min defines the shift

$\Delta_1^{rt} \triangleq V_{out,2}^* - V_{out,1}^* = V_{out,2} - V_{out,1}$, which has a Gaussian distribution computed on all pixels with a -5 -mV mean and 0.45 -mV standard deviation (Fig. 4.19(b)). When the solution with bacterial cells is pipetted, the pixel values recover instantaneously and approximately their initial levels (the previous drift due to evaporation is suppressed by the new drop, but a small difference in conductivity between PBS 1:1000 without and with bacteria explains the slight negative values of V_{out}^* as the new drop is pipetted) but each pixel presents different temporal evolutions (Fig. 4.19(a)). To quantify this, a second shift $\Delta_2^{rt} \triangleq V_{out,4}^* - V_{out,3}^* = V_{out,4} - V_{out,3}$ is defined with $t_3 = 24$ min and $t_4 = 40$ min, and features a broader distribution centered around 1 mV with a standard deviation of 2.2 mV (Fig. 4.19(b)). Compared to Δ_1^{rt} , the mean value increased by 6 mV because bacterial binding induces an increase of pixel capacitances, as previously demonstrated in [18, 22, 180]. Indeed, the bacterial impedance is dominated by the large outer shell capacitance, thus increasing the global capacitance between electrodes [19]. The large dispersion of Δ_2^{rt} is due to the fact that all pixels do not have the same number of bacteria and that their positions affect the capacitance value [180]. The bacteria could then be indirectly detected through the enlargement of the pixel distribution.

To quantify the voltage shift per bacterium, the number of adherent bacteria on each pixel was estimated from microscope images taken after the real-time experiment. Bacterial cells appear black (type 1) or white (type 2) depending on their respective positions between or atop microelectrodes (Fig. 4.20(a)). This distinction is important since the positions of adherent bacterial cells slightly affect the capacitive shift [180]. Pixel outputs with the same number of bacteria can then exhibit non-negligible variability arising from these random bacterial positions. 3D simulations of the pixel represented in Fig. 4.14(a) demonstrates that both pixel capacitance and output voltage increase with the bacteria number N_b , but with a large variability (Fig. 4.20(c)): $\Delta V_{out} \simeq (2.6 \pm 0.6 \text{ mV}) \cdot N_b$ and $\Delta C_{sol} \simeq (61 \pm 14 \text{ aF}) \cdot N_b$. Despite the exponential transfer function of M_T (see Eq. 4.13), a linear dependence between the mean ΔV_{out} and N_b is observed because of the very small capacitance shifts ($< 1\%$ of the nominal value at $N_b < 10$). In these simulations, the SNR achieves a peak value of 13 dB at $N_b = 10$ showing that biological noise established in [180] and independent of V_{ref} strongly limits the biosensor performance. It is also confirmed that S_r is strongly enhanced by the weak inversion of M_T , from 1% at the input capacitance level to 3.6% at the output voltage. Experimentally, since

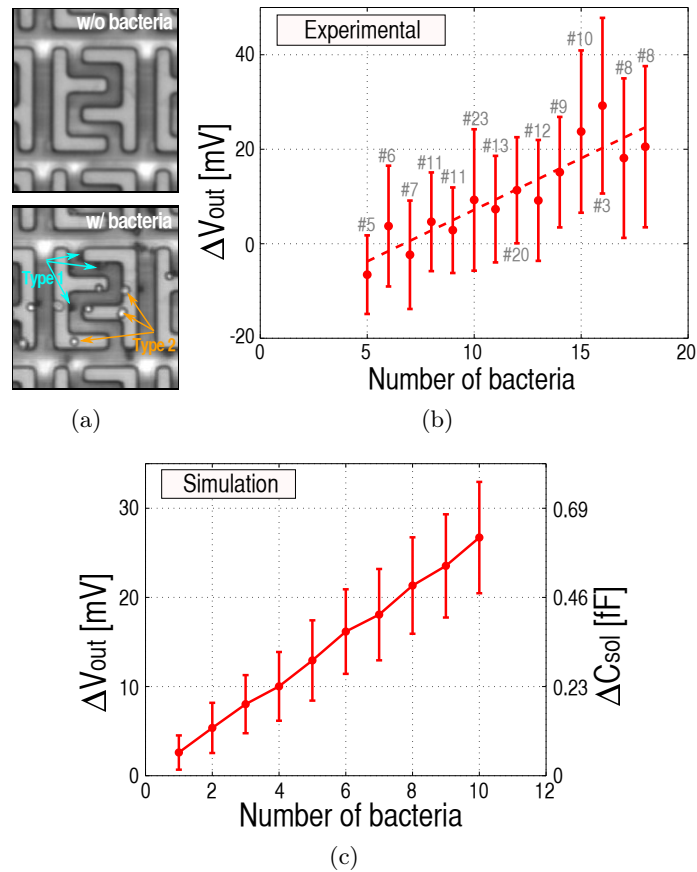


Figure 4.20 – Impact of the number of bacteria per pixel on the pixel output: (a) microphotographs of one pixel before and after the bacterial binding. Two types of adherent bacteria are found: type 1 corresponds to bacteria between electrodes, while type 2 to bacteria atop electrodes. (b) Experimental V_{out} after wash versus the number of adherent bacteria, computed on all countable pixels of the array at the optimum $V_{ref} = 1.24$ V. The number of pixels used for each error bar is indicated by the symbol #. Edge pixels and pixels where the number of bacteria cannot accurately be estimated were discarded. (c) 3D simulation results of random bacterial deposition on the 3D structure of Fig. 4.14(a) at $V_{ref} = 1.24$ V. Each error bar is obtained by averaging 200 independent simulation results involving different bacterial positions.

it was not possible to optically observe bacteria binding during the real-time incubation, only V_{out} measured for each V_{ref} before and after the bacterial incubation are compared. The maximal sensitivity to bacterial cells is obtained at $V_{ref} = 1.24$ V (data not shown), as expected from Fig. 4.18(a). The pixel output voltage V_{out} is shown to increase with the number of adherent bacterial cells (Fig. 4.20(b)), and presents the following dependence on N_b : $\Delta V_{out} \simeq -14.6$ mV + 2.18 mV $\cdot N_b$. The negative value at $N_b = 0$ is due to the slight difference in σ_{sol} between the initial and final wash, because it is very likely for low-conductive electrolytes ($\sigma_{sol} \simeq 1.8$ mS/m). There is a good matching between experimental data and 3D simulations since the sensitivity to bacteria is fairly the same, i.e. 2.18 versus 2.6 mV/bacteria, respectively. Based on the sensitivity of 35.3 mV/fF at $V_{ref} = 1.24$ V (see Section 4.3.4), one bacterium is then represented by a capacitance increase of 62 aF, which is the same order of magnitude as in [18]. Since the detection limit is 450 aF, the minimal detectable number of bacteria is approximately 7.

4.3.5 Comparison with relevant works

A comparison of performances from relevant CMOS capacitive biosensors is provided in Table 4.1. Among biosensor arrays, our work is the first to focus on bacterial detection, while others deal with protein [235], DNA [92, 139, 234, 238] and cells/beads [82, 231, 237]. To our best knowledge, this capacitive biosensor array is also the first CMOS array for bacterial detection, whatever the transduction mechanism (capacitive, impedance, field-effect, etc.). In particular, [232] only shows functionality with on-chip capacitances, and not in biological solutions. Contrasting with these works, a more advanced CMOS technology ($0.25 \mu\text{m}$) and smaller pixels ($16 \mu\text{m} \times 14 \mu\text{m}$) were required to enhance the sensitivity to bacteria without using differential measurements. For the same reason, miniaturized interdigitated electrodes with micrometer gap ($2 \mu\text{m}$) were used instead of single squared/disk electrodes. Similarly to [22, 82, 235], a thin passivated layer was post-processed on the last CMOS metal layer to protect it from corrosion. As in [22], the thickness (25 nm) was one order of magnitude smaller than in [82, 235] (~ 300 nm) to boost the sensitivity. While most work used differential measurements to boost the sensitivity [139, 228, 232, 234], an innovative gain stage in subthreshold region was included along with a charge sharing capacitance-to-voltage conversion within the pixel to enlarge the sensitivity by a factor 4. Compared to the best reported LoD ~ 20

4.3. A biosensor array towards single bacterium sensing 165

aF [231, 232], the value achieved by this work is one order of magnitude larger (450 aF) but obtained without differential or pseudo-differential architectures. For the same reason, the sensitivity (55 mV/fF) is 4 to 5 times smaller as well compared to the best reported ones. However, the pixel size ($14 \mu\text{m} \times 16 \mu\text{m}$) and power consumption ($29 \mu\text{W}$) are the smallest and then provide benefits in term of IC area, costs and portability. Finally, thanks to the non-differential circuit, the design of this biosensor array can still be scaled in more advanced technology to eventually achieve single bacterial detection. The selectivity can also easily be provided with lytic enzymes in volume (see Section 2.3) or with antibodies on the sensor surface [104].

4.3.6 Conclusion

The design and fabrication of a 16×16 capacitive biosensor array in a $0.25 \mu\text{m}$ mixed-signal CMOS process has been reported towards detection of single bacterial cell [23]. Each pixel features two miniaturized IDE and a readout circuit based on the charge sharing principle that enables a linear capacitance-to-voltage conversion. To boost the bacterial sensitivity without differential measurements, a gain stage consisting of a single transistor operating in the subthreshold region was added after the linear capacitance-to-voltage conversion. Thanks to the non-differential architecture, the array offers possibilities for miniaturization and fonctionnalization. Experimental results demonstrate excellent matching with simulations, and confirm the sensing principle based on medium dielectric properties, featuring a maximal sensitivity of 55 mV/fF and a LoD of 450 aF. When *S. epidermidis* bind on pixels in real-time, their output values were shown to be correlated to the number of adherent bacteria on each pixel. Each bacterial cell was shown to induce a 62-aF capacitance shift, corresponding to 2.18 mV in output.

4.4 Conclusions

In this chapter, we have presented two distinct CMOS interfaces for the capacitive biosensor presented in Chapter 2. In addition to convert the sensor capacitance into a readable output voltage, these implementations provide additional functionalities hardly achievable without co-integrating the capacitive biosensor with the CMOS circuit:

- **Ability to sense bacteria in high-conductive solutions [22]:** the screening by the passivation layer is avoided by exciting the electrodes with a very-high-frequency ($\sim 200 - 500$ MHz) voltage, generated by a five-stage ring oscillator. The designed capacitance-to-frequency converter (CFC) generates a square signal whose frequency is lower than 1 MHz thanks to a frequency divider and inversely proportional to the on-chip IDE. Owing to the VHF stimuli, bacterial cells are detected in PBS buffer characterized by an electrical conductivity of 1.8 S/m.
- **Ability to sense few bacteria [23]:** the sensor is downscaled to $14 \mu\text{m} \times 16 \mu\text{m}$ and replicated 16×16 times to form a whole capacitive biosensor array. Each pixel unit features two tiny electrodes and a proper electrical circuit implementing capacitance-to-voltage conversion with an innovative subthreshold gain stage. As a result, the sensing of ~ 7 bacteria per pixel with a maximal sensitivity of 55 mV/fF is achieved.

Conclusions and perspectives

Thesis conclusion

In this thesis, three key aspects of capacitive biosensors towards the detection of whole-cell bacteria have been investigated:

1. the transducer consisting in interdigitated passivated microelectrodes and its transduction mechanism [18–20] (Chapter 2).
2. the electrokinetic effects that can be integrated along with such capacitive biosensors, and their mechanisms [21] (Chapter 3).
3. the CMOS readout interfaces enabling conversion of the biosensor capacitance into an analog or digital signal [22, 23] (Chapter 4).

For each aspect, notable innovations have been proposed and studied through analytical models, numerical simulations, innovative designs and experiments. These innovations address known problems or challenges related to capacitive biosensors for bacterial detection; the most important being:

- *Avoiding significant sample pre-treatments and the effects of non-specific bindings*: a method using lytic enzymes has been developed to selectively detect target bacteria in relatively complex matrixes such as urine [18] (Chapter 2).
- *Optimizing and understanding capacitive biosensors*: analytical models have been proposed and provide a cutoff-frequency analysis of the metal-insulator-electrolyte (MIE) interface with and without bacterial cells. In addition, 2D numerical simulations have been implemented to accurately quantify the impact of key system parameters on the sensitivity [19] (Chapter 2).
- *Combining multi-range electrokinetics with capacitive biosensors*: an innovative design using macroelectrodes surrounding capacitive biosensors has been demonstrated for simultaneous short and long-range trapping of bacterial cells on capacitive biosensors [21] (Chapter 3). In addition, an electromagnetic resonance effect has been identified to strongly improve the bacterial short- and long-range trapping.

- *Understanding the electrokinetics of passivated electrodes*: new analytical formulae have been proposed to quantify electrokinetic effects generated by contactless electrodes [21] (Chapter 3). Numerical simulations of contactless dielectrophoresis (c-DEP) have also been implemented to explain experimental results.
- *Capacitive biosensing in high-conductive buffers*: to bypass the screening of the double layer capacitance by the insulating capacitance, a capacitance-to-frequency converter (CFC) with on-chip IDEs and working at very high frequency has been designed towards sensing of the solution capacitance. Detection of bacterial cells has been demonstrated in solutions featuring electrical conductivities up to 1.8 S/m [22] (Chapter 4).
- *Sensing single bacterial cells*: a 16×16 capacitive biosensor array with $14 \mu\text{m} \times 16 \mu\text{m}$ pixels has been designed towards single bacteria detection. Experimental results have demonstrated a detection limit of 7 bacteria per pixel, thanks to an innovative in-pixel capacitance-to-voltage architecture [23] (Chapter 4).

The table 4.5 provides a comparison of the four different sensing devices developed in this thesis. Due to the different sensor geometries, the nominal medium capacitance in DI water ranges from 55 fF (single pixel in the biosensor array) to 17.5 pF (IDE of the CFC). As described in Chapter 4, this has obviously lead to different design considerations for the readout interfaces. On the other hand, two different solutions (PBS and PBS 1:1000) featuring extreme conductivities (1.8 S/m and 1.8 mS/m, respectively) were used both in fluidic (Chapters 2 and 3) or steady state conditions (Chapter 4). Detection limits range from 10^5 to 10^7 CFU/mL after 20 minutes of sample incubation, depending on whether electrokinetic effects are used or not. The related figures of merit, FoM_1 and FoM_2 , feature best values of $5 \cdot 10^3$ CFU and 10^5 CFU.min, respectively. On the other hand, the intrinsic limits of detection (iLoD) range from 450 aF to 10 fF, mainly driven by the sensor area. For the two CMOS interfaces, the intrinsic sensitivities are respectively equal to 16 kHz/fF and 55 mV/fF.

Performances expressed in function of the bacteria number, e.g. the sensitivity and the iLoD in Table 4.5, must only be interpreted as rough approximations because of:

- *The unaccuracy of the bacteria number*: precise counting of bacteria is hardly possible because of the low resolution of micropho-

Table 4.5 – Comparison of the different works performed in this thesis.

	IDE [18]	IDE+EK [21]	CFC [22]	Array [23]
Sensor	#	1		16 × 16
	Techno	Winfab (Home made)		0.25- μm CMOS
	d_e	4 μm		2 μm
	w_e	2 μm		2 μm
	t_e	1 μm		1.8 μm
	t_{ins}	33 nm		25 nm
	Unit area	0.05 mm ²		224 μm^2
	Voltage	50 mV		0.3 - 0.8 V
	Frequency	1 MHz		-
	C_{sol}	~ 3 pF		~ 55 fF
Solution	Type	PBS 1:1000**		PBS 1:1000
	σ_{sol}	1.8 mS/m		1.8 S/m
	Selectivity	Lytic enz.	-	-
	Total vol.	20 μL	100 μL	10 μL
	Flow rate	1 $\mu\text{L}/\text{min}$	5 $\mu\text{L}/\text{min}$	-
Performances	Time	20 min		20 min
	iLoD	5 fF (~ 50 bact.)		50 fF (~ 102 bact.)
	LoD	5 · 10 ⁶ CFU/mL	10 ⁵ CFU/mL	10 ⁷ CFU/mL
	FoM ₁	10 ⁵ CFU	5 · 10 ³ CFU	-
	FoM ₂	2 · 10 ⁶ CFU.min	10 ⁵ CFU.min	10 ⁶ CFU.min
	iSensitivity	-		16 kHz/fF
	Sensitivity	$\sim 80 - 100$ aF/bacteria		~ 8 kHz/bact*
	Input range	-		55 mV/fF
	Power	-		~ 2.2 mV/bact [†]
	consump.	-		0.45 fF - 57 fF
			29 mW	29 μW

*: corresponds to ~ 490 aF/bacteria; †: corresponds to ~ 60 aF/bacteria

**.: for IDE, urine was used as the resuspension medium for bacteria but measurements were performed in PBS 1:1000.

topographs, the hidden bacteria atop electrodes (in the case of the inverted microscope) and in 3D clusters, and the uncertainty of the algorithmic or manual counting methods. In Chapter 4, bacteria are also numbered *after* the experiment so that their amount possibly slightly differs from the real number *during* experiments.

- *The unaccuracy of physical and biological properties*: the dielectric properties and sizes of the bacterial components can vary from batch to batch (different cultures and manipulations) and inside a given batch (mutations, clusters and biofilm formation). In addition, the bacteria dielectric and dimension values in this work are

taken from [30], and must be considered only as an approximation.

- *The unaccuracy of the transduction mechanism:* a universal relationship between the sensor output and the number of bacteria does not exist, since it depends on the bacteria position, the possible 3D agglomeration of bacteria, the kind of stimuli (e.g. DC versus AC) and the simulation framework (e.g. 2D versus 3D).

With these notices in mind, the sensitivity were evaluated to $\sim 80 - 100$ aF/bacteria, ~ 490 aF/bacteria and ~ 60 aF/bacteria for the IDE, the CFC and the pixel array, respectively. The two last figures are still more imprecise than the first, because they were indirectly obtained from the measurement results by the means of post-layout simulations and the number of bacteria was evaluated *after* the experiment. The larger bacterial sensitivity of the CFC compared to the IDE is due to the smaller electrode gap ($1.5 \mu\text{m}$ versus $4 \mu\text{m}$) that partially compensates the loss of sensitivity at VHF, as confirmed by numerical simulations of Section 2.4 (more details in Appendix D.3). The smaller sensitivity of the pixel array (~ 60 aF/bacteria) despite the small electrode gap of $2 \mu\text{m}$ probably originates from the transient stimuli applied on electrodes, which are different from the AC stimuli applied on the IDE and CFC, and from the larger number of unfavourable random bacteria positions on the electrode configuration. Unfortunately, it is not possible to compare with simulation results, since no numerical simulation were implemented when considering transient stimuli.

As a general guideline, the detection principle must be chosen to maximize the difference of dielectric properties between the bacterial cytoplasm and the electrolyte medium. In particular, the maximal sensitivity in low-conductive electrolytes is achieved thanks to the significantly larger electrical conductivity of the bacterial cytoplasm. In high-conductive electrolytes, the detection should rely on the smaller conductance and capacitance of the cytoplasm compared to the outer electrolyte. Finally, for a detection after drying the sensor surface, both the very small permittivity and conductivity of the air will be strongly impacted by the bacterial cell.

In conclusion, this thesis has opened some unexplored research directions in the field of capacitive biosensors towards bacterial detection. Owing to their miniaturization and integration capabilities, it has been shown that capacitive biosensors can potentially be used for point-of-care testing of bacteria because it provides competitive sensitivity and selectivity means. However, the technology still requires 5 to 10 years

of applied research to converge towards a competitive commercialized product in the area of point-of-care diagnosis tools. For instance, even though it is more cumbersome, expensive and non-portable, MALDI-TOF analysis can perform analysis of urine samples ($> 10^5$ CFU/mL) in less than 30 min (see Section 1.2.4), while more time is required with our method. Similarly, the limit of detection must still be decreased down to smaller bacterial loads, such as 10^3 CFU/mL in milk samples. Besides the reported innovations, some interesting perspectives can be highlighted. The two next sections thus develop the main outlooks regarding CMOS capacitive biosensing of bacteria cells.

Next generation of capacitive biosensors for PoC diagnosis

Because each of the four devices developed in this thesis provides interesting features (see Table 4.5), the big question is:

Which device should be selected?

The answer is none of them. Indeed, each device targets specific and isolated goals. The best option is thus to rethink the whole system by trying to cleverly integrate most innovations present in these proof-of-concept devices. The new PoC device should address the four following targets at the same time, with their proper solutions:

- *High sensitivity*: the device should include small pixels and electrokinetics, in order to cumulate their respective benefits in term of sensitivity.
- *Rapidity and simplicity*: the device should avoid pre-treatment steps, by using on-chip concentration means and by performing the analysis in real-time.
- *Multiplexing*: the device should perform parallel detection of bacteria from a single sample, through innovative selectivity means.
- *Portable and miniaturized*: all electronic and sensing parts should be integrated on a CMOS chip.

Based on these criteria and on the four devices of Table 4.5, the next generation of capacitive biosensors for PoC diagnosis can be envisioned (Fig. 4.21(a)). It consists in a CMOS biosensor array with pixel sides of $\sim 3 \mu\text{m}$ and surrounded by a circularly-shaped macroelectrode that enables bacteria volume trapping. The circular shape of the array is required to uniformly concentrate bacterial cells by electrokinetics. Each pixel features a single pair of miniaturized electrodes spaced by $\sim 1 \mu\text{m}$ to increase the sensitivity close to 1 fF per bacteria, thus enabling sensing of single bacterium and rendering the device very sensitive as only one adherent bacteria per 0.1 mm^2 could potentially be detected. Even if different sensor answers can be obtained for different bacteria, a sufficiently small signal threshold can be settled to encompass most bacteria under test. The in-pixel circuit should use VHF stimuli on the *ns*-order to enable sensing in high-conductive buffers, thus avoiding washing or centrifugation steps. In that case, the challenge resides in the non-overlap

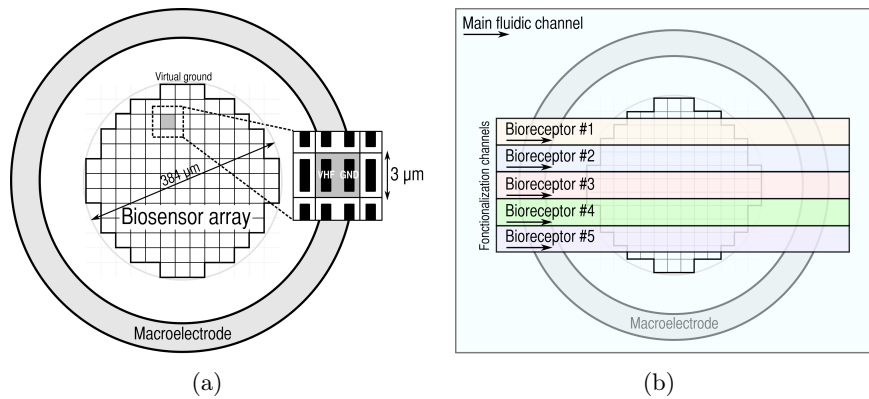


Figure 4.21 – (a) Next generation of capacitive biosensor arrays (not at scale) and (b) its related microfluidics.

of digital command signals. An on-chip control can be provided with larger electrodes that sense only the solution conductivity. To achieve small geometric features as well as fast and compact in-pixel circuits, the use of nanometer CMOS technologies (~ 65 nm) is advised. The multiplexing capabilities can be provided by patterning several parts of the array by specific bioreceptors (e.g. antibodies or lytic enzymes) prior to biosensing thanks to a dedicated microfluidic clamp, as shown by conceptual linear fluidic channels in Fig. 4.21(b). It can then be withdrawn and replaced by the main microfluidic channel enabling the flow of a larger sample volume atop the sensor. It is important to note that selectivity through volume-based methods (Chapter 2) would require permanent multi-channels atop the biosensor array, which can possibly trouble electrokinetic effects.

Other outlooks

Besides this big picture, other important aspects can further be explored:

- *Challenges for extreme scaling of pixels*: shrinking pixels is required to enhance the sensitivity to bacterial cells. Some important tradeoffs must be considered: a more advanced CMOS technology, a smaller number of transistors within the pixel circuit, a higher mismatch between sensing parts, a more problematic kT/C noise and a smaller size of the column amplifier.
- *Combining different transducers inside the biosensor array*: including different sensing sites within the biosensor array can lead to innovative applications:
 - *e-Nose sensor array*: the design of a generic in-pixel circuit to interface optical, impedance, field-effect and temperature sensors can provide pixels with identical dimensions and terminals but including different transducers, enabling multi-type sensing of various chemical and biological parameters.
 - *Multi-function pixels*: several kind of sensors can be integrated inside each pixel, which thus features larger sizes but multi-sensing capabilities. This could enable statistical consideration and improvement of sensitivity and selectivity.
 - *Multi-signal pixels*: a single in-pixel sensor can be interrogated differently with different interface circuits located inside each pixel. For instance, the capacitance of capacitive biosensors could be converted both into voltage and frequency at different operating frequencies to retrieve complementary information. This could possibly enhance detection limits and physical information on bacteria binding.
- *Combining capacitive sensing with droplet microfluidics*: profiting from the electrowetting-on-dielectric (EWD) technology for droplet microfluidics, capacitive biosensors can directly be integrated on the metal-insulator-electrolyte (MIE) interface and thus benefit from the bacterial confinement inside well-controlled drops.
- *Capacitive biosensors for biofilm monitoring*: another very important application of capacitive biosensors is their ability to monitor biofilm formation [89, 90], several hours after that bacterial cells

have bound. This ability is critical for healthcare system and water and food industry, where biofilm prevention can save lives and money, respectively [7]. Many challenges and possible innovations can be identified: early biofilm detection, differentiation of the biofilm type (e.g. 2D or 3D) and EPS-destructive enzymes use.

- *Screening drug resistance of bacteria*: identifying the bacterial species is important, but determining resistance factors to antibiotics and drugs is still more critical for medical diagnoses [61]. Strategies using local spotting or flow of antibiotics can be used on capacitive biosensors to obtain new generations of antibiograms, enabling massive screening of drugs on target bacteria.
- *Combining magnetic particles (MP) with dielectrophoresis (DEP)*: an interesting method can be envisioned. The first step aims at mixing the bacterial sample with antibody (Ab)-coated MP for selective trapping. Then, an external magnetic field is applied to separate conjugates (target bacteria + Ab-MP) from the rest of the sample. Finally, the resuspension is flown on the capacitive sensor where DEP is applied similarly to Chapter 3 to attract only bacterial conjugates, and not excessive MP that are repelled by n-DEP since $\varepsilon_{r,p} \ll \varepsilon_{r,sol}$ and $\sigma_p \ll \sigma_{sol}$ (Fig. 4.22). A fine tuning of the MP diameter and electrokinetics could optimize the opposition between the two forces.
- *Combining the biosensor array with coils*: to attract magnetic par-

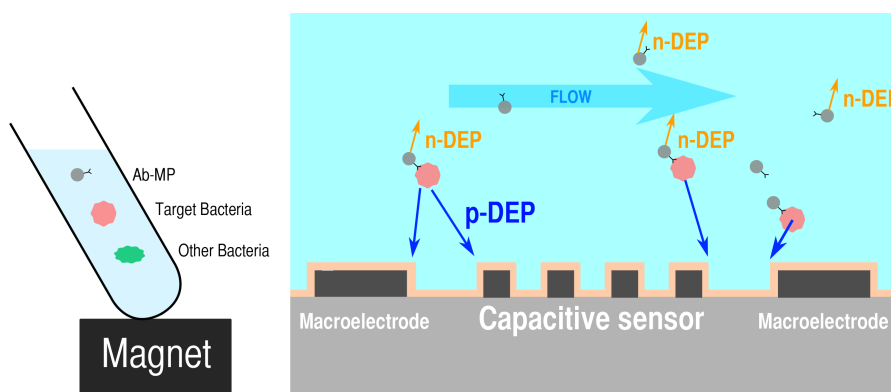


Figure 4.22 – Scheme combining magnetic particles (MP) and dielectrophoresis (DEP) for selective detection of bacteria.

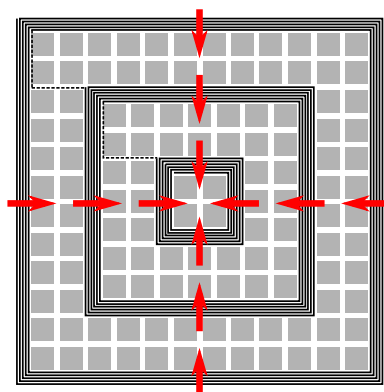


Figure 4.23 – Optimal combination of a sensor array with several coils.

ticles (MP) conjugated to bacterial cells to the sensor surface, it is possible to adopt the arrangement shown in Fig. 4.23, avoiding losing too much spaces by integrating coils inside each pixels such as [82]. The space and number of pixels between each coil must be optimized to enhance the trapping of MP.

- *Non-linear impedance spectroscopy for bacterial detection*: using voltage amplitudes far larger than 10 – 50 mV could lead to interesting results for detection of bacterial cells. Some effects would change the system behavior: the electrical double layer would be strongly different because of steric effects, harmonics could not be neglected anymore and could contain information on bacterial cells and finally, electrokinetic effects could appear at the same time as the real-time detection.
- *Combining lytic enzymes and antibodies*: when the sample matrix contains many parasitic components, such as other bacteria, cells, proteins, etc., it could be very interesting to combine surface functionalization using antibodies with a volume-based selective method using lytic enzymes. Indeed, without an antibody layer, the surface can be mainly covered by parasitic components so that target bacteria have no place to bind the sensor surface. The sensitivity is then strongly impacted. This combination results in a more costly and intricate selective method, but which is more sensitive and selective in return.

Besides these novel aspects, many optimizations regarding the work performed in this thesis can still be realized:

- *Optimizing the microfluidic chamber:* the design of the microfluidic chamber could be optimized to increase the number of trapped bacteria per unit time. Geometric factors such as the channel width and height could be tuned with regards to the bacterial diameter, flow rate and sensor dimensions [96]. It is also possible to imagine vertical channel inlets atop the sensor to maximize the number of bacteria coming into contact with the sensor surface.
- *Improving the biosensor array architecture:* several features could be added at the circuit level to enhance the performances of the biosensor array:
 - A digital interface could be implemented to control the read-out and avoid loss of power. A calibration procedure can also be included to automatically set tuning factors such as V_{ref} and t_{int} .
 - A cancelling scheme for the column-based FPN could be implemented by using double delta sampling (DDS) [255].
 - For pixels sufficiently large, the kT/C noise can be neglected and the NCDS could then be implemented instead of the CDS to increase the frame rate and alleviate storage capabilities.
 - Methods should be implemented to compensate noise and mismatch of the in-pixel capacitive sensor and transistor M_T . For instance, increasing the integration time, modifying the pixel architecture, bringing a differential low-noise ADC on-chip, performing an averaging procedure on-chip and implementing the DDS for column FPN can all provide noise and/or mismatch reduction.
 - Analog-to-digital conversion should be added inside each pixel, e.g. by using capacitance-to-frequency conversion, or inside each column amplifier with differential ADCs.
- *Ability to measure dozens of capacitive biosensors in parallel:* a characterization platform should be built to enable simultaneous measurements of dozens capacitive biosensors similar to those in Chapter 2.

- *Investigating the optimal insulating material:* Al_2O_3 used in this thesis could be replaced by a more resistant oxide withstanding corrosion in electrolytes during several months, because it is required for long-term testing with biofilms for instance. This material should be biocompatible, present a high relative permittivity and be deposited by ALD. The best candidate seems to be TiO_2 , because of its biocompatibility and its high relative permittivity.
- *Optimizing sticking coatings:* other coatings as Polydopamine improving the adhesion of bacterial cells can be studied and optimized, such as poly-L-lysine.
- *Investigating different bacterial species under electrokinetics:* by quantifying the effects shown in Chapter 3 for different bacterial species, it is possible to assess whether the attraction speed, resonance and electrokinetic effects are different or not. It can potentially lead to a selectivity means since electrokinetic effects slightly depend on physical properties of bacterial cells.

Bibliography

- [1] American Academy of microbiology, "Bringing the lab to the patient," pp. 1–24, July 2012.
- [2] H. P. Dwivedi and L.-A. Jaykus, "Detection of pathogens in foods: the current state-of-the-art and future directions," *Crit Rev Microbiol*, vol. 37, pp. 40–63, Feb. 2011.
- [3] J. J. Theron and T. E. T. Cloete, "Emerging waterborne infections: contributing factors, agents, and detection tools," *Crit Rev Microbiol*, vol. 28, pp. 1–26, Dec. 2001.
- [4] I. Raad, A. Alrahwan, and K. Rolston, "Staphylococcus epidermidis: emerging resistance and need for alternative agents.," *Clin. Infect. Dis.*, vol. 26, pp. 1182–1187, May 1998.
- [5] M. L. Cohen, "Changing patterns of infectious disease," *Nature*, vol. 406, no. 6797, pp. 762–767, 2000.
- [6] O. Lazcka, F. J. D. Campo, and F. X. Muñoz, "Pathogen detection: A perspective of traditional methods and biosensors," *Biosensors and Bioelectronics*, vol. 22, pp. 1205–1217, Feb. 2007.
- [7] L. Hall-Stoodley, J. W. Costerton, and P. Stoodley, "Bacterial biofilms: from the Natural environment to infectious diseases," *Nat Rev Micro*, vol. 2, pp. 95–108, Feb. 2004.
- [8] A. K. Deisingh and M. Thompson, "Biosensors for the detection of bacteria," *Can. J. Microbiol.*, vol. 50, pp. 69–77, Feb. 2004.
- [9] Y. Lei, W. Chen, and A. Mulchandani, "Microbial biosensors," *Analytica Chimica Acta*, vol. 568, pp. 200–210, May 2006.
- [10] A. Ahmed, J. V. Rushworth, N. A. Hirst, and P. A. Millner, "Biosensors for whole-cell bacterial detection.," *Clin. Microbiol. Rev.*, vol. 27, pp. 631–646, July 2014.
- [11] C.-C. Lin, J.-L. Hsu, and G.-B. Lee, "Sample preconcentration in microfluidic devices," *Microfluid Nanofluid*, vol. 10, no. 3, pp. 481–511, 2011.
- [12] J. Kretzer and M. Biebl, "Sample Preparation—An Essential Prerequisite for High-Quality Bacteria Detection," *Principles of Bacterial Detection: Biosensors, Recognition Receptors and Microsystems*, 2008.
- [13] A. Donahue and M. Albitar, "Antibodies in Biosensing," *Recognition Receptors in Biosensors*, pp. 221–248, 2010.
- [14] Y. Haik, R. Sawafta, I. Ciubotaru, A. Qablan, E. Tan, and K. Ong, "Magnetic Techniques for Rapid Detection of Pathogens," *Principles of Bacterial Detection: Biosensors, Recognition Receptors and Microsystems*, pp. 415–458, 2008.
- [15] J. Ambrose, B. Bearzatto, A. Robert, B. Govaerts, B. Macq, and J.-L. Gala, "Impact of the spotted microarray preprocessing method on fold-change compression and variance stability," *BMC Bioinformatics*, vol. 12, p. 413, Oct. 2011.
- [16] F. Götz, "Staphylococcus and biofilms," *Mol. Microbiol.*, vol. 43, no. 6, pp. 1367–1378, 2002.

- [17] X. Tang, D. Flandre, J.-P. Raskin, Y. Nizet, L. Moreno-Hagelsieb, R. Pampin, and L. A. Francis, "A new interdigitated array microelectrode-oxide-silicon sensor with label-free, high sensitivity and specificity for fast bacteria detection," *Sensors & Actuators: B. Chemical*, vol. 156, no. 2, pp. 578–587, 2011.
- [18] N. Couniot, T. Vanzieleghem, J. Rasson, N. Van Overstraeten-Schlögel, O. Poncelet, J. Mahillon, L. A. Francis, and D. Flandre, "Lytic enzymes as selectivity means for label-free, microfluidic and impedimetric detection of whole-cell bacteria using ALD-Al₂O₃ passivated microelectrodes," *Biosensors and Bioelectronics*, vol. 67, pp. 154–161, May 2015.
- [19] N. Couniot and A. Afzalian, "Capacitive biosensing of bacterial cells: Analytical model and numerical simulations," *Sensors and Actuators B*, vol. 211, pp. 428–438, 2015.
- [20] N. Couniot, A. Afzalian, N. Van Overstraeten-Schlögel, L. A. Francis, and D. Flandre, "Capacitive biosensing of bacterial cells: sensitivity optimization," *Sensors & Actuators: B. Chemical*, Apr. 2015.
- [21] N. Couniot, L. A. Francis, and D. Flandre, "Resonant dielectrophoresis and electrohydrodynamics for high-sensitivity impedance detection of whole-cell bacteria," *Lab on a Chip*, Apr. 2015.
- [22] N. Couniot, D. Bol, O. Poncelet, L. A. Francis, and D. Flandre, "A Capacitance-to-Frequency Converter With On-Chip Passivated Microelectrodes for Bacteria Detection in Saline Buffers Up to 575 MHz," *Circuits and Systems II: Express Briefs, IEEE Transactions on*, vol. 62, no. 2, pp. 159–163, 2015.
- [23] N. Couniot, L. A. Francis, and D. Flandre, "A 16 x 16 CMOS Capacitive Biosensor Array towards Detection of Single Bacterial Cell," *IEEE Transactions on Biomedical Circuits and Systems*, Apr. 2015.
- [24] T. Love and B. Jones, "Introduction to Pathogenic Bacteria," *Principles of Bacterial Detection: Biosensors, Recognition Receptors and Microsystems*, pp. 3–13, 2008.
- [25] D. Ivnitiski, I. Abdel-Hamid, and P. Atanasov, "Biosensors for detection of pathogenic bacteria," *Biosensors and Bioelectronics*, vol. 14, pp. 599–624, 1999.
- [26] M. Häggström, "Medical gallery of Mikael Häggström 2014." Wikiversity Journal of Medicine.
- [27] H.-C. Flemming, "The perfect slime," *Colloid Surface B*, vol. 86, pp. 251–259, Sept. 2011.
- [28] V. Harden, "The isoelectric point of bacterial cells," *J. Bacteriol.*, 1953.
- [29] G. Markx, Y. Huang, and X. Zhou, "Dielectrophoretic characterization and separation of micro-organisms," *Microbiology*, vol. 140, pp. 585–591, 1994.
- [30] A. Sanchis, A. P. Brown, M. Sancho, G. Martínez, J. L. Sebastián, S. Muñoz, and J. M. Miranda, "Dielectric characterization of bacterial cells using dielectrophoresis," *Bioelectromagnetics*, vol. 28, no. 5, pp. 393–401, 2007.
- [31] R. G. Eagon, "Pseudomonas natriegens, a marine bacterium with a generation time of less than 10 minutes," *J. Bacteriol.*, vol. 83, pp. 736–737, Apr. 1962.
- [32] V. A. Fischetti, "Bacteriophage lytic enzymes: novel anti-infectives," *Trends in Microbiology*, vol. 13, pp. 491–496, Jan. 2005.

- [33] M. Zasloff, "Antimicrobial peptides of multicellular organisms.," *Nature*, vol. 415, pp. 389–395, Jan. 2002.
- [34] ECDC, "Surveillance Report. Antimicrobial resistance surveillance in Europe 2013," pp. 1–211, Nov. 2014.
- [35] Y. Le Loir, F. Baron, and M. Gautier, "Staphylococcus aureus and food poisoning.," *Genet. Mol. Res.*, vol. 2, no. 1, pp. 63–76, 2003.
- [36] A. K erouanton, J. A. Hennekinne, C. Letertre, L. Petit, O. Chesneau, A. Brisabois, and M. L. De Buyser, "Characterization of Staphylococcus aureus strains associated with food poisoning outbreaks in France.," *Int. J. Food Microbiol.*, vol. 115, pp. 369–375, Apr. 2007.
- [37] Y.-C. Chang, C.-Y. Yang, R.-L. Sun, Y.-F. Cheng, W.-C. Kao, and P.-C. Yang, "Rapid single cell detection of Staphylococcus aureus by aptamer-conjugated gold nanoparticles.," *Sci. Rep.*, vol. 3, p. 1863, 2013.
- [38] J. J. Curtin and R. M. Donlan, "Using Bacteriophages To Reduce Formation of Catheter-Associated Biofilms by Staphylococcus epidermidis.," *Antimicrob. Agents Chemother.*, vol. 50, pp. 1268–1275, Mar. 2006.
- [39] P. Yagupsky and F. S. Nolte, "Quantitative aspects of septicemia.," *Clin. Microbiol. Rev.*, vol. 3, pp. 269–279, July 1990.
- [40] N. Nicolaou, Y. Xu, and R. Goodacre, "Fourier Transform Infrared and Raman Spectroscopies for the Rapid Detection, Enumeration, and Growth Interaction of the Bacteria Staphylococcus aureus and Lactococcus lactis ssp. cremoris in Milk.," *Anal. Chem.*, vol. 83, pp. 5681–5687, July 2011.
- [41] Northern Ireland Environment Agency, "European and National Drinking Water Quality Standards," pp. 1–12, Sept. 2014.
- [42] A. C. Thomsen, T. Espersen, and S. Maigaard, "Course and treatment of milk stasis, noninfectious inflammation of the breast, and infectious mastitis in nursing women.," *Am. J. Obstet. Gynecol.*, vol. 149, pp. 492–495, July 1984.
- [43] J. B. Lee and G. H. Neild, "Urinary tract infection.," *Medicine*, vol. 35, no. 8, pp. 423–428, 2007.
- [44] A. Wieser, L. Schneider, J. Jung, and S. Schubert, "MALDI-TOF MS in microbiological diagnostics—identification of microorganisms and beyond (mini review).," *Appl Microbiol Biotechnol*, vol. 93, pp. 965–974, Dec. 2011.
- [45] A. Yousef, "Detection of bacterial pathogens in different matrices: Current practices and challenges.," *Principles of Bacterial Detection: Biosensors*, 2008.
- [46] M.-F. Lartigue, "Matrix-assisted laser desorption ionization time-of-flight mass spectrometry for bacterial strain characterization.," *Infect. Genet. Evol.*, vol. 13, pp. 230–235, Jan. 2013.
- [47] J. O. Lay, "MALDI-TOF mass spectrometry of bacteria.," *Mass Spectrom. Rev.*, vol. 20, no. 4, pp. 172–194, 2001.
- [48] S. Biswas and J.-M. Rolain, "Use of MALDI-TOF mass spectrometry for identification of bacteria that are difficult to culture.," *Journal of Microbiological Methods*, vol. 92, pp. 14–24, Jan. 2013.

- [49] A. Turner, I. Karube, and G. S. Wilson, *Biosensors: fundamentals and applications*. Oxford Science Publications, 1987.
- [50] G. A. Zelada-Guillén, J. L. Sebastián-Avila, P. Blondeau, J. Riu, and F. X. Rius, “Label-free detection of *Staphylococcus aureus* in skin using real-time potentiometric biosensors based on carbon nanotubes and aptamers,” *Biosensors and Bioelectronics*, vol. 31, pp. 226–232, Jan. 2012.
- [51] V. Escamilla-Gómez, S. Campuzano, M. Pedrero, and J. M. Pingarrón, “Electrochemical immunosensor designs for the determination of *Staphylococcus aureus* using 3, 3-dithiodipropionic acid di (N-succinimidyl ester)-modified gold electrodes,” *Talanta*, vol. 77, no. 2, pp. 876–881, 2008.
- [52] B. Mirhabibollahi, J. L. Brooks, and R. G. Kroll, “Development and performance of an enzyme-linked amperometric immunosensor for the detection of *Staphylococcus aureus* in foods,” *J. Appl. Bacteriol.*, vol. 68, pp. 577–585, June 1990.
- [53] M. D. Morales, B. Serra, A. Guzmán-Vázquez de Prada, A. J. Reviejo, and J. M. Pingarrón, “An electrochemical method for simultaneous detection and identification of *Escherichia coli*, *Staphylococcus aureus* and *Salmonella choleraesuis* using a glucose oxidase-peroxidase composite biosensor,” *Analyst*, vol. 132, pp. 572–578, June 2007.
- [54] F. Tan, P. H. M. Leung, Z.-b. Liu, Y. Zhang, L. Xiao, W. Ye, X. Zhang, L. Yi, and M. Yang, “A PDMS microfluidic impedance immunosensor for *E. coli* O157:H7 and *Staphylococcus aureus* detection via antibody-immobilized nanoporous membrane,” *Sensors & Actuators: B. Chemical*, vol. 159, pp. 328–335, Nov. 2011.
- [55] M. Braiek, K. Rokbani, A. Chrouda, B. Mrabet, A. Bakhrouf, A. Maaref, and N. Jaffrezic-Renault, “An Electrochemical Immunosensor for Detection of *Staphylococcus aureus* Bacteria Based on Immobilization of Antibodies on Self-Assembled Monolayers-Functionalized Gold Electrode,” *Biosensors*, vol. 2, pp. 417–426, Dec. 2012.
- [56] D. K. Corrigan, H. Schulze, G. Henihan, I. Ciani, G. Giraud, J. G. Terry, A. J. Walton, R. Pethig, P. Ghazal, J. Crain, C. J. Campbell, A. R. Mount, and T. T. Bachmann, “Biosensors and Bioelectronics,” *Biosensors and Bioelectronics*, vol. 34, pp. 178–184, Apr. 2012.
- [57] J. H. Yoon, Y. D. Han, P. C. Lee, and H. C. Yoon, “Lysostaphin-mediated fragmentation of microbial peptidoglycans for label-free electrochemical impedance immunanalysis of *Staphylococcus aureus*,” *BioChip J*, vol. 7, pp. 344–352, Dec. 2013.
- [58] R. A. Villamizar, A. Maroto, F. X. Rius, I. Inza, and M. J. Figueras, “Fast detection of *Salmonella Infantis* with carbon nanotube field effect transistors,” *Biosensors and Bioelectronics*, vol. 24, pp. 279–283, Oct. 2008.
- [59] A. Taylor, J. Ladd, J. Homola, and S. Jiang, “Surface Plasmon Resonance (SPR) Sensors for the Detection of Bacterial Pathogens,” *Principles of Bacterial Detection: Biosensors, Recognition Receptors and Microsystems*, pp. 83–108, 2008.
- [60] N. Tawil, E. Sacher, R. Mandeville, and M. Meunier, “Surface plasmon resonance detection of *E. coli* and methicillin-resistant *S. aureus* using bacteriophages,” *Biosensors and Bioelectronics*, vol. 37, pp. 24–29, Aug. 2012.
- [61] W.-S. Chan, B. S. F. Tang, M. V. Boost, C. Chow, and P. H. M. Leung, “Detection of methicillin-resistant *Staphylococcus aureus* using a gold nanoparticle-based colourimetric polymerase chain reaction assay,” *Biosensors and Bioelectronics*, vol. 53, pp. 105–111, Mar. 2014.

- [62] N. Moll, E. Pascal, D. H. Dinh, J.-P. Pillot, B. Bennetau, D. Rebière, D. Moynet, Y. Mas, D. Mossalayi, J. Pistré, and C. Déjous, "A Love wave immunosensor for whole E. coli bacteria detection using an innovative two-step immobilisation approach," *Biosensors and Bioelectronics*, vol. 22, pp. 2145–2150, Apr. 2007.
- [63] Y. Lian, F. He, H. Wang, and F. Tong, "A new aptamer/graphene interdigitated gold electrode piezoelectric sensor for rapid and specific detection of Staphylococcus aureus," *Biosensors and Bioelectronics*, vol. 65C, pp. 314–319, Oct. 2014.
- [64] D. R. Thévenot, K. Toth, R. A. Durst, and G. S. Wilson, "Electrochemical biosensors: recommended definitions and classification," *Biosensors and Bioelectronics*, vol. 16, pp. 121–131, Jan. 2001.
- [65] S. Arya, S. Singh, and B. Malhotra, "Electrochemical Techniques in Biosensors," *Handbook of Biosensors and Biochips*, 2007.
- [66] Y. Miyahara, T. Sakata, and A. Matsumoto, "Microbial genetic analysis based on field effect transistors," *Principles of Bacterial Detection: Biosensors, Recognition Receptors and Microsystems*, pp. 313–339, 2008.
- [67] J. M. Rothberg, W. Hinz, T. M. Rearick, J. Schultz, W. Mileski, M. Davey, J. H. Leamon, K. Johnson, M. J. Milgrew, M. Edwards, J. Hoon, J. F. Simons, D. Marran, J. W. Myers, J. F. Davidson, A. Branting, J. R. Nobile, B. P. Puc, D. Light, T. A. Clark, M. Huber, J. T. Branciforte, I. B. Stoner, S. E. Cawley, M. Lyons, Y. Fu, N. Homer, M. Sedova, X. Miao, B. Reed, J. Sabina, E. Feierstein, M. Schorn, M. Alanjary, E. Dimalanta, D. Dressman, R. Kasinskas, T. Sokolsky, J. A. Fianza, E. Namsaraev, K. J. McKernan, A. Williams, G. T. Roth, and J. Bustillo, "An integrated semiconductor device enabling non-optical genome sequencing," *Nature*, vol. 475, pp. 348–352, July 2011.
- [68] P. Georgiou and C. Toumazou, "An adaptive CMOS-based PG-ISFET for pH sensing," *Circuits and Systems, 2009. ISCAS 2009. IEEE International Symposium on*, pp. 557–560, 2009.
- [69] C. Z. D. Goh, P. Georgiou, T. G. Constandinou, T. Prodromakis, and C. Toumazou, "A CMOS-Based ISFET Chemical Imager With Auto-Calibration Capability," *IEEE Sensors J.*, vol. 11, pp. 3253–3260, Dec. 2011.
- [70] W. C. Chan, "Quantum Dot Bioconjugates for Ultrasensitive Nonisotopic Detection," *Science*, vol. 281, pp. 2016–2018, Sept. 1998.
- [71] L. P. Choo-Smith, K. Maquelin, T. van Vreeswijk, H. A. Bruining, G. J. Puppels, N. A. N. Thi, C. Kirschner, D. Naumann, D. Ami, A. M. Villa, F. Orsini, S. M. Doglia, H. Lamfarraj, G. D. Sockalingum, M. Manfait, P. Allouch, and H. P. Endtz, "Investigating Microbial (Micro)colony Heterogeneity by Vibrational Spectroscopy," *Applied and Environmental Microbiology*, vol. 67, pp. 1461–1469, Apr. 2001.
- [72] D. Naumann, D. Helm, and H. Labischinski, "Microbiological characterizations by FT-IR spectroscopy," *Nature*, vol. 351, pp. 81–82, May 1991.
- [73] N. Nicolaou and R. Goodacre, "Rapid and quantitative detection of the microbial spoilage in milk using Fourier transform infrared spectroscopy and chemometrics," *Analyst*, vol. 133, no. 10, p. 1424, 2008.
- [74] E. Olsen, A. Vainrub, and V. Vodyanoy, "Acoustic Wave (TSM) Biosensors: Weighing Bacteria," *Principles of Bacterial Detection: Biosensors, Recognition Receptors and Microsystems*, pp. 255–298, 2008.

- [75] H. Xia, F. Wang, Q. Huang, J. Huang, M. Chen, J. Wang, C. Yao, Q. Chen, G. Cai, and W. Fu, "Detection of Staphylococcus epidermidis by a Quartz Crystal Microbalance Nucleic Acid Biosensor Array Using Au Nanoparticle Signal Amplification," *Sensors*, vol. 8, pp. 6453–6470, Jan. 2008.
- [76] D. Le, F.-j. He, T. J. Jiang, L. Nie, and S. Yao, "A goat-anti-human IgG modified piezoimmunosensor for Staphylococcus aureus detection," *Journal of Microbiological Methods*, vol. 23, no. 2, pp. 229–234, 1995.
- [77] L. Bao, H. Tan, Q. Duan, X. Su, and W. Wei, "A rapid method for determination of Staphylococcus aureus based on milk coagulation by using a series piezoelectric quartz crystal sensor," *Analytica Chimica Acta*, vol. 369, no. 1, pp. 139–145, 1998.
- [78] M.-I. Rocha-Gaso, C. March-Iborra, Á. Montoya-Baides, and A. Arnau-Vives, "Surface Generated Acoustic Wave Biosensors for the Detection of Pathogens: A Review," *Sensors*, vol. 9, pp. 5740–5769, Dec. 2009.
- [79] L. Yang, "Electrical impedance spectroscopy for detection of bacterial cells in suspensions using interdigitated microelectrodes," *Talanta*, vol. 74, pp. 1621–1629, Feb. 2008.
- [80] T. DeCory, R. A. Durst, S. Zimmerman, L. Garringer, G. Paluca, H. DeCory, and R. Montagna, "Development of an immunomagnetic bead-immunoliposome fluorescence assay for rapid detection of Escherichia coli O157: H7 in aqueous samples and comparison of the assay with a standard microbiological method," *Applied and Environmental Microbiology*, vol. 71, no. 4, p. 1856, 2005.
- [81] L. Yang and Y. Li, "Detection of viable Salmonella using microelectrode-based capacitance measurement coupled with immunomagnetic separation," *Journal of Microbiological Methods*, vol. 64, pp. 9–16, Jan. 2006.
- [82] A.-Y. Chang and M. S. C. Lu, "A CMOS magnetic microbead-based capacitive biosensor array with on-chip electromagnetic manipulation," *Biosensors and Bioelectronics*, vol. 45, pp. 6–12, July 2013.
- [83] A. Ramos, H. Morgan, N. G. Green, and A. Castellanos, "AC electrokinetics: a review of forces in microelectrode structures," *J. Phys. D: Appl. Phys.*, vol. 31, no. 18, p. 2338, 1998.
- [84] J. Suehiro, R. Yatsunami, R. Hamada, and M. Hara, "Quantitative estimation of biological cell concentration suspended in aqueous medium by using dielectrophoretic impedance measurement method," *J. Phys. D: Appl. Phys.*, vol. 32, no. 21, p. 2814, 1999.
- [85] K. F. Hoettges, M. P. Hughes, A. Cotton, N. A. Hopkins, and M. B. McDonnell, "Optimizing particle collection for enhanced surface-based biosensors," *IEEE Eng Med Biol Mag*, vol. 22, pp. 68–74, Oct. 2003.
- [86] R. Gomez-Sjoberg, D. T. Morissette, and R. Bashir, "Impedance microbiology-on-a-chip: microfluidic bioprocessor for rapid detection of bacterial metabolism," *J. Microelectromech. Syst.*, vol. 14, pp. 829–838, Aug. 2005.
- [87] J. Suehiro, G. Zhou, M. Imamura, and M. Hara, "Dielectrophoretic filter for separation and recovery of biological cells in water," *IEEE Trans. on Ind. Appl.*, vol. 39, pp. 1514–1521, Sept. 2003.
- [88] J. Q. Boedicker, L. Li, T. R. Kline, and R. F. Ismagilov, "Detecting bacteria and determining their susceptibility to antibiotics by stochastic confinement in nanoliter droplets using plug-based microfluidics," *Lab on a Chip*, vol. 8, no. 8, p. 1265, 2008.

- [89] J. Paredes, S. Becerro, F. Arizti, A. Aguinaga, J. L. Del Pozo, and S. Arana, "Real time monitoring of the impedance characteristics of Staphylococcal bacterial biofilm cultures with a modified CDC reactor system.," *Biosensors and Bioelectronics*, vol. 38, no. 1, pp. 226–232, 2012.
- [90] J. Paredes, S. Becerro, F. Arizti, A. Aguinaga, J. L. Del Pozo, and S. Arana, "Interdigitated microelectrode biosensor for bacterial biofilm growth monitoring by impedance spectroscopy technique in 96-well microtiter plates," *Sensors & Actuators: B. Chemical*, vol. 178, pp. 663–670, Mar. 2013.
- [91] E. Stern, J. F. Klemic, D. A. Routenberg, P. N. Wyrembak, D. B. Turner-Evans, A. D. Hamilton, D. A. LaVan, T. M. Fahmy, and M. A. Reed, "Label-free immunodetection with CMOS-compatible semiconducting nanowires," *Nature*, vol. 445, pp. 519–522, Feb. 2007.
- [92] A. Manickam, A. Chevalier, M. McDermott, A. D. Ellington, and A. Hassibi, "A CMOS Electrochemical Impedance Spectroscopy (EIS) Biosensor Array," *IEEE Transactions on Biomedical Circuits and Systems*, vol. 4, pp. 379–390, Dec. 2010.
- [93] O. Elhadidy, M. Elkholy, A. A. Helmy, S. Palermo, and K. Entesari, "A CMOS Fractional- PLL-Based Microwave Chemical Sensor With 1.5Accuracy," *Microwave Theory and Techniques, IEEE Transactions on*, vol. 61, no. 9, pp. 3402–3416, 2013.
- [94] M. Varshney, "Interdigitated array microelectrode based impedance biosensor coupled with magnetic nanoparticle–antibody conjugates for detection of Escherichia coli O157:H7 in food samples," *Biosensors and Bioelectronics*, vol. 22, pp. 2408–2414, 2007.
- [95] P. S. Dittrich and A. Manz, "Lab-on-a-chip: microfluidics in drug discovery," *Nat Rev Drug Discov*, vol. 5, pp. 210–218, Mar. 2006.
- [96] T. M. Squires, R. J. Messinger, and S. R. Manalis, "Making it stick: convection, reaction and diffusion in surface-based biosensors," *Nat Biotechnol*, vol. 26, no. 4, pp. 417–426, 2008.
- [97] D. A. Routenberg and M. A. Reed, "Microfluidic probe: a new tool for integrating microfluidic environments and electronic wafer-probing," *Lab on a Chip*, vol. 10, no. 1, p. 123, 2010.
- [98] R. B. Fair, "Digital microfluidics: is a true lab-on-a-chip possible?," *Microfluid Nanofluid*, vol. 3, pp. 245–281, Mar. 2007.
- [99] M. Abdelgawad and A. R. Wheeler, "The Digital Revolution: A New Paradigm for Microfluidics," *Adv. Mater.*, vol. 21, pp. 920–925, Feb. 2009.
- [100] H. Norian, R. M. Field, I. Kymissis, and K. L. Shepard, "Lab on a Chip," *Lab on a Chip*, pp. 1–9, Aug. 2014.
- [101] J. Piehler, A. Brecht, K. E. Geckeler, and G. Gauglitz, "Surface modification for direct immunoprobes.," *Biosensors and Bioelectronics*, vol. 11, no. 6-7, pp. 579–590, 1996.
- [102] A. Bange, H. B. Halsall, and W. R. Heineman, "Microfluidic immunosensor systems.," *Biosensors and Bioelectronics*, vol. 20, pp. 2488–2503, June 2005.
- [103] J. S. Daniels and N. Pourmand, "Label-Free Impedance Biosensors: Opportunities and Challenges," *Electroanalysis*, vol. 19, pp. 1239–1257, June 2007.
- [104] N. Van Overstraeten-Schlögel, O. Lefèvre, N. Couniot, and D. Flandre, "Assessment of different functionalization methods for grafting a protein to an alumina-covered biosensor.," *Biofabrication*, vol. 6, p. 035007, May 2014.

- [105] J. Suehiro, A. Ohtsubo, T. Hatano, and M. Hara, "Selective detection of bacteria by a dielectrophoretic impedance measurement method using an antibody-immobilized electrode chip," *Sensors & Actuators: B. Chemical*, vol. 119, pp. 319–326, Nov. 2006.
- [106] D. K. Aswal, S. Lenfant, D. Guerin, J. V. Yakhmi, and D. Vuillaume, "Self assembled monolayers on silicon for molecular electronics," *Analytica Chimica Acta*, vol. 568, pp. 84–108, May 2006.
- [107] L. Shriver-Lake, B. Donner, R. Edelstein, K. Breslin, S. K. Bhatia, and F. S. Ligler, "Antibody immobilization using heterobifunctional crosslinkers.," *Biosensors and Bioelectronic*, vol. 12, no. 11, pp. 1101–1106, 1997.
- [108] S. M. Radke and E. C. Alocilja, "A high density microelectrode array biosensor for detection of *E. coli* O157:H7," *Biosensors and Bioelectronics*, vol. 20, pp. 1662–1667, Feb. 2005.
- [109] A. Shabani, M. Zourob, B. Allain, C. A. Marquette, M. F. Lawrence, and R. Mandeville, "Bacteriophage-Modified Microarrays for the Direct Impedimetric Detection of Bacteria," *Anal. Chem.*, vol. 80, pp. 9475–9482, Dec. 2008.
- [110] M. Labib, A. S. Zamay, O. S. Kolovskaya, I. T. Reshetneva, G. S. Zamay, R. J. Kibbee, S. A. Sattar, T. N. Zamay, and M. V. Berezovski, "Aptamer-Based Viability Impedimetric Sensor for Bacteria," *Anal. Chem.*, vol. 84, pp. 8966–8969, Oct. 2012.
- [111] R. M. Iost and F. N. Crespilho, "Layer-by-layer self-assembly and electrochemistry: Applications in biosensing and bioelectronics," *Biosensors and Bioelectronics*, vol. 31, pp. 1–10, Jan. 2012.
- [112] M. Zourob and S. Ripp, "Bacteriophage-based biosensors," *Recognition Receptors in Biosensors*, pp. 415–448, 2010.
- [113] T. C. Chang, H. C. Ding, and S. Chen, "A Conductance Method for the Identification of *Escherichia coli* O157:H7 Using Bacteriophage AR1," *Journal of Food Protection*®, 2002.
- [114] T. C. D. Huang, S. Sorgenfrei, P. Gong, R. Levicky, and K. L. Shepard, "A 0.18-um CMOS Array Sensor for Integrated Time-Resolved Fluorescence Detection," *IEEE J. Solid-State Circuits*, vol. 44, no. 5, pp. 1644–1654, 2009.
- [115] J. Zhang, Y. Huang, N. Trombly, C. Yang, and A. Mason, "Electrochemical array microsystem with integrated potentiostat," *Sensors, 2005 IEEE*, 2005.
- [116] P. M. Levine, P. Gong, R. Levicky, and K. L. Shepard, "Real-time, multiplexed electrochemical DNA detection using an active complementary metal-oxide-semiconductor biosensor array with integrated sensor electronics," *Biosensors and Bioelectronics*, vol. 24, pp. 1995–2001, Nov. 2008.
- [117] A. Gore, S. Chakrabartty, S. Pal, and E. C. Alocilja, "A multichannel femtoampere-sensitivity potentiostat array for biosensing applications," *Circuits and Systems I: Regular Papers, IEEE Transactions on*, vol. 53, no. 11, pp. 2357–2363, 2006.
- [118] J. Ripp, "Analytical Detection Limit Guidance & Laboratory Guide for Determining Method Detection Limits," 1996.
- [119] L. A. Currie, "Detection and quantification limits: origins and historical overview," *Analytica Chimica Acta*, vol. 391, no. 2, pp. 127–134, 1999.

- [120] O. Laczka, E. Baldrich, F. X. Muñoz, and F. J. del Campo, "Detection of Escherichia coli and Salmonella typhimurium using interdigitated microelectrode capacitive immunosensors: the importance of transducer geometry," *Anal. Chem.*, vol. 80, pp. 7239–7247, Oct. 2008.
- [121] L. Yang, C. Ruan, and Y. Li, "Detection of viable Salmonella typhimurium by impedance measurement of electrode capacitance and medium resistance," *Biosensors and Bioelectronics*, vol. 19, pp. 495–502, Dec. 2003.
- [122] M. Varshney and Y. Li, "Double interdigitated array microelectrode-based impedance biosensor for detection of viable Escherichia coli O157:H7 in growth medium," *Talanta*, vol. 74, pp. 518–525, Jan. 2008.
- [123] A. Hassibi, S. Zahedi, R. Navid, R. W. Dutton, and T. H. Lee, "Biological shot-noise and quantum-limited signal-to-noise ratio in affinity-based biosensors," *J. Appl. Phys.*, vol. 97, no. 8, p. 084701, 2005.
- [124] N. K. Rajan, D. A. Routenberg, and M. A. Reed, "Optimal signal-to-noise ratio for silicon nanowire biochemical sensors," *Appl. Phys. Lett.*, vol. 98, no. 26, p. 264107, 2011.
- [125] J. Vessman, R. I. Stefan, J. F. van Staden, K. Danzer, W. Lindner, D. T. Burns, A. Fajgelj, and H. Müller, "Selectivity in analytical chemistry (IUPAC Recommendations 2001)," *Pure Appl. Chem.*, vol. 73, no. 8, pp. 1381–1386, 2001.
- [126] H. Li and R. Bashir, "Dielectrophoretic separation and manipulation of live and heat-treated cells of Listeria on microfabricated devices with interdigitated electrodes," *Sensors & Actuators: B. Chemical*, vol. 86, pp. 215–221, 2002.
- [127] S. S. Ghoreishizadeh, C. Baj-Rossi, A. Cavallini, S. Carrara, and G. De Micheli, "An Integrated Control and Readout Circuit for Implantable Multi-Target Electrochemical Biosensing," *IEEE Transactions on Biomedical Circuits and Systems*, June 2014.
- [128] E. Hall, "Glucose Measurement Within Diabetes via Traditional Electrochemical Biosensors," *Central Asia*, vol. 2, no. 856, p. 803, 2007.
- [129] G. Barbero, A. L. Alexe-Ionescu, and I. Lelidis, "Significance of small voltage in impedance spectroscopy measurements on electrolytic cells," *J. Appl. Phys.*, vol. 98, no. 11, p. 113703, 2005.
- [130] L. Yang, Y. Li, and G. F. Erf, "Interdigitated Array Microelectrode-Based Electrochemical Impedance Immunosensor for Detection of Escherichia coli O157:H7," *Anal. Chem.*, vol. 76, pp. 1107–1113, Feb. 2004.
- [131] F. C. B. Fernandes, A. Santos, D. C. Martins, M. S. Góes, and P. R. Bueno, "Comparing label free electrochemical impedimetric and capacitive biosensing architectures," *Biosensors and Bioelectronics*, vol. 57, pp. 96–102, July 2014.
- [132] A. J. Bard and L. R. Faulkner, "Electrochemical methods: fundamentals and applications," vol. 2, 1980.
- [133] C. Ruan, L. Yang, and Y. Li, "Immunobiosensor Chips for Detection of Escherichia coli O157:H7 Using Electrochemical Impedance Spectroscopy," *Anal. Chem.*, vol. 74, pp. 4814–4820, Sept. 2002.
- [134] R. Maalouf, C. Fournier-Wirth, J. Coste, H. Chebib, Y. Saïkali, O. Vittori, A. Er-rachid, J.-P. Cloarec, C. Martelet, and N. Jaffrezic-Renault, "Label-Free Detection of Bacteria by Electrochemical Impedance Spectroscopy: Comparison to Surface Plasmon Resonance," *Anal. Chem.*, vol. 79, pp. 4879–4886, July 2007.

- [135] A. Ahmed, J. V. Rushworth, J. D. Wright, and P. A. Millner, "Novel Impedimetric Immunosensor for Detection of Pathogenic Bacteria *Streptococcus pyogenes* in Human Saliva," *Anal. Chem.*, vol. 85, pp. 12118–12125, Dec. 2013.
- [136] Y. Li, R. Afrasiabi, F. Fathi, N. Wang, C. Xiang, R. Love, Z. She, and H.-B. Kraatz, "Biosensors and Bioelectronics," *Biosensors and Bioelectronics*, vol. 58, pp. 193–199, Aug. 2014.
- [137] R. Gómez and R. Bashir, "Microscale electronic detection of bacterial metabolism," *Sensors & Actuators: B. Chemical*, vol. 86, pp. 198–208, 2002.
- [138] S. M. Radke and E. C. Alocilja, "Design and Fabrication of a Microimpedance Biosensor for Bacterial Detection," *IEEE Sensors J.*, vol. 4, pp. 434–440, Aug. 2004.
- [139] C. Stagni, C. Guiducci, L. Benini, B. Ricco, S. Carrara, B. Samori, C. Paulus, M. Schienle, M. Augustyniak, and R. Thewes, "CMOS DNA Sensor Array With Integrated A/D Conversion Based on Label-Free Capacitance Measurement," *IEEE J. Solid-State Circuits*, vol. 41, pp. 2956–2964, Dec. 2006.
- [140] H. Etayash, K. Jiang, T. Thundat, and K. Kaur, "Impedimetric Detection of Pathogenic Gram-Positive Bacteria Using an Antimicrobial Peptide from Class IIa Bacteriocins," *Anal. Chem.*, vol. 86, pp. 1693–1700, Feb. 2014.
- [141] K. Settu, C.-J. Chen, J.-T. Liu, C.-L. Chen, and J.-Z. Tsai, "Biosensors and Bioelectronics," *Biosensors and Bioelectronics*, vol. 66, pp. 244–250, Apr. 2015.
- [142] G.-J. Yang, J.-L. Huang, W.-J. Meng, M. Shen, and X.-A. Jiao, "A reusable capacitive immunosensor for detection of *Salmonella* spp. based on grafted ethylene diamine and self-assembled gold nanoparticle monolayers," *Analytica Chimica Acta*, vol. 647, pp. 159–166, Aug. 2009.
- [143] P. Van Gerwen, W. Laureyn, W. Laureys, G. Huyberechts, M. Op De Beeck, K. Baert, J. Suls, W. Sansen, P. Jacobs, L. Hermans, and R. Mertens, "Nanoscaled interdigitated electrode arrays for biochemical sensors," *Sensors & Actuators: B. Chemical*, vol. 49, pp. 73–80, 1998.
- [144] Z. Zou, J. Kai, M. J. Rust, J. Han, and C. Ahn, "Functionalized nano interdigitated electrodes arrays on polymer with integrated microfluidics for direct bio-affinity sensing using impedimetric measurement," *Sensors and Actuators A: Physical*, vol. 136, pp. 518–526, May 2007.
- [145] M. Varshney and Y. Li, "Interdigitated array microelectrodes based impedance biosensors for detection of bacterial cells," *Biosensors and Bioelectronics*, vol. 24, pp. 2951–2960, June 2009.
- [146] H. Wu, Y. Zuo, C. Cui, W. Yang, H. Ma, and X. Wang, "Rapid Quantitative Detection of *Brucella melitensis* by a Label-Free Impedance Immunosensor Based on a Gold Nanoparticle-Modified Screen-Printed Carbon Electrode," *Sensors*, vol. 13, pp. 8551–8563, July 2013.
- [147] J. Wu, Y. Ben, D. Battigelli, and H.-C. Chang, "Long-Range AC Electroosmotic Trapping and Detection of Bioparticles," *Ind. Eng. Chem. Res.*, vol. 44, pp. 2815–2822, Apr. 2005.
- [148] M. S. Mannoor, S. Zhang, A. J. Link, and M. C. McAlpine, "Electrical detection of pathogenic bacteria via immobilized antimicrobial peptides," *Proc. Natl. Acad. Sci. U.S.A.*, vol. 107, no. 45, pp. 19207–19212, 2010.

- [149] M. Tolba, M. U. Ahmed, C. Tlili, F. Eichenseher, M. J. Loessner, and M. Zourob, "A bacteriophage endolysin-based electrochemical impedance biosensor for the rapid detection of *Listeria* cells," *Analyst*, vol. 137, no. 24, p. 5749, 2012.
- [150] J. Suehiro, T. Hatano, M. Shutou, and M. Hara, "Improvement of electric pulse shape for electroporation-assisted dielectrophoretic impedance measurement for high sensitive bacteria detection," *Sensors & Actuators: B. Chemical*, vol. 109, pp. 209–215, Sept. 2005.
- [151] V. Gorodokin and D. Zemlyanov, "Metallic contamination in silicon processing," in *Electrical and Electronics Engineers in Israel, 2004. Proceedings. 2004 23rd IEEE Convention of*, pp. 157–160, IEEE, 2004.
- [152] S.-W. Wang and M.-C. Lu, "CMOS Capacitive Sensors With Sub- μm Microelectrodes for Biosensing Applications," *IEEE Sensors J.*, vol. 10, no. 5, pp. 991–996, 2010.
- [153] S. B. Prakash and P. Abshire, "On-Chip Capacitance Sensing for Cell Monitoring Applications," *IEEE Sensors J.*, vol. 7, pp. 440–447, Mar. 2007.
- [154] E. Ghafar-Zadeh and M. Sawan, "A Core-CBCM sigma delta capacitive sensor array dedicated to lab-on-chip applications," *Sensors and Actuators A: Physical*, vol. 144, pp. 304–313, June 2008.
- [155] A. Manickam, R. Singh, N. Wood, B. Li, A. Ellington, and A. Hassibi, "A fully-electronic charge-based DNA sequencing CMOS biochip," *VLSI Circuits (VLSIC), 2012 Symposium on*, pp. 126–127, 2012.
- [156] C. Christensen, R. de Reus, and S. Bouwstra, "Tantalum oxide thin films as protective coatings for sensors," *J. Micromech. Microeng.*, vol. 9, no. 2, p. 113, 1999.
- [157] F. Hofmann, B. Eversmann, M. Jenkner, A. Frey, M. Merz, T. Birkenmaier, P. Fromherz, M. Schreiter, R. Gabl, K. Plehnert, M. Steinhauser, G. Eckstein, and R. Thewes, "Technology aspects of a CMOS neuro-sensor: back end process and packaging," *Audio, Transactions of the IRE Professional Group on*, pp. 167–170, Sept. 2003.
- [158] A. Hierlemann, U. Frey, S. Hafizovic, and F. Heer, "Growing cells atop microelectronic chips: interfacing electrogenic cells in vitro with CMOS-based microelectrode arrays," *Proc. IEEE*, vol. 99, no. 2, pp. 252–284, 2011.
- [159] D. S. Finch, T. Oreskovic, K. Ramadurai, C. F. Herrmann, S. M. George, and R. L. Mahajan, "Biocompatibility of atomic layer-deposited alumina thin films," *J. Biomed. Mater. Res.*, vol. 87A, pp. 100–106, Oct. 2008.
- [160] X. Tang, A. M. Jonas, B. Nysten, S. Demoustier-Champagne, F. Blondeau, P.-P. Prévot, R. Pampin, E. Godfroid, B. Iñiguez, J.-P. Colinge, J.-P. Raskin, D. Flandre, and V. Bayot, "Direct protein detection with a nano-interdigitated array gate MOS-FET," *Biosensors and Bioelectronics*, vol. 24, pp. 3531–3537, Aug. 2009.
- [161] A. I. Abdulagatov, Y. Yan, J. R. Cooper, Y. Zhang, Z. M. Gibbs, A. S. Cavanagh, R. G. Yang, Y. C. Lee, and S. M. George, "Al₂O₃ and TiO₂ Atomic Layer Deposition on Copper for Water Corrosion Resistance," *ACS Appl. Mater. Interfaces*, vol. 3, pp. 4593–4601, Dec. 2011.
- [162] L. Moreno-Hagelsieb, B. Fouttier, G. Laurent, R. Pampin, J. Remacle, J. P. Raskin, and D. Flandre, "Electrical detection of DNA hybridization: Three extraction techniques based on interdigitated Al/Al₂O₃ capacitors," *Biosensors and Bioelectronics*, vol. 22, pp. 2199–2207, Apr. 2007.

- [163] B. Reddy, B. R. Dorvel, J. Go, P. R. Nair, O. H. Elibol, G. M. Credo, J. S. Daniels, E. K. C. Chow, X. Su, M. Varma, M. A. Alam, and R. Bashir, "High-k dielectric Al₂O₃ nanowire and nanoplate field effect sensors for improved pH sensing," *Biomed Microdevices*, vol. 13, pp. 335–344, Jan. 2011.
- [164] S. Chen, J. G. Bomer, E. T. Carlen, and A. van den Berg, "Al₂O₃/silicon nanoISFET with near ideal nernstian response.," *Nano Lett.*, vol. 11, pp. 2334–2341, June 2011.
- [165] J. Y. Oh, H.-J. Jang, W.-J. Cho, and M. S. Islam, "Highly sensitive electrolyte-insulator-semiconductor pH sensors enabled by silicon nanowires with Al₂O₃/SiO₂ sensing membrane," *Sensors & Actuators: B. Chemical*, vol. 171-172, pp. 238–243, June 2012.
- [166] F. David, M. Hebeisen, G. Schade, E. Franco-Lara, and M. Di Berardino, "Viability and membrane potential analysis of *Bacillus megaterium* cells by impedance flow cytometry," *Biotechnol. Bioeng.*, vol. 109, pp. 483–492, Oct. 2011.
- [167] K. C. Cheung, M. Di Berardino, G. Schade-Kampmann, M. Hebeisen, A. Pierzchalski, J. Bocsi, A. Mittag, and A. Tárnok, "Microfluidic impedance-based flow cytometry," *Cytometry*, vol. 77A, pp. 648–666, May 2010.
- [168] T. Sun and H. Morgan, "Single-cell microfluidic impedance cytometry: a review," *Microfluid Nanofluid.*, vol. 8, pp. 423–443, Mar. 2010.
- [169] N. Haandbæk, O. With, S. C. Bürgel, F. Heer, and A. Hierlemann, "Resonance-enhanced microfluidic impedance cytometer for detection of single bacteria," *Lab on a Chip*, vol. 14, p. 3313, June 2014.
- [170] C. Küttel, E. Nascimento, N. Demierre, T. Silva, T. Braschler, P. Renaud, and A. G. Oliva, "Label-free detection of *Babesia bovis* infected red blood cells using impedance spectroscopy on a microfabricated flow cytometer," *Acta Tropica*, vol. 102, pp. 63–68, Apr. 2007.
- [171] C. Bernabini, D. Holmes, and H. Morgan, "Micro-impedance cytometry for detection and analysis of micron-sized particles and bacteria," *Lab on a Chip*, vol. 11, no. 3, pp. 407–412, 2011.
- [172] N. Haandbæk, S. C. Bürgel, F. Heer, and A. Hierlemann, "Characterization of sub-cellular morphology of single yeast cells using high frequency microfluidic impedance cytometer," *Lab on a Chip*, vol. 14, no. 2, pp. 369–377, 2014.
- [173] B. W. Peterson, P. K. Sharma, H. C. van der Mei, and H. J. Busscher, "Bacterial Cell Surface Damage Due to Centrifugal Compaction," *Applied and Environmental Microbiology*, vol. 78, pp. 120–125, Dec. 2011.
- [174] J. Suehiro, "Selective detection of specific bacteria using dielectrophoretic impedance measurement method combined with an antigen–antibody reaction," *Journal of Electrostatics*, vol. 58, pp. 229–246, June 2003.
- [175] P. Pham, M. Howorth, A. Planat-Chrétien, and S. Tardu, "Numerical Simulation of the Electrical Double Layer Based on the Poisson-Boltzmann Models for AC Electroosmosis Flows," *Excerpt from the Proceedings of the COMSOL Users Conference 2007 Grenoble*, 2007.
- [176] R. Van Hal, J. Eijkel, and P. Bergveld, "A general model to describe the electrostatic potential at electrolyte oxide interfaces," *Advances in colloid and interface science*, vol. 69, no. 1-3, pp. 31–62, 1996.

- [177] A. Hassibi, R. Navid, R. W. Dutton, and T. H. Lee, "Comprehensive study of noise processes in electrode electrolyte interfaces," *J. Appl. Phys.*, vol. 96, no. 2, p. 1074, 2004.
- [178] B.-Y. Chang and S.-M. Park, "Electrochemical Impedance Spectroscopy," *Annual Review of Analytical Chemistry*, vol. 3, pp. 207–229, June 2010.
- [179] W. Olthuis, W. Streekstra, and P. Bergveld, "Theoretical and experimental determination of cell constants of planar-interdigitated electrolyte conductivity sensors," *Sensors & Actuators: B. Chemical*, vol. 24, no. 1-3, pp. 252–256, 1995.
- [180] N. Couniot, D. Flandre, L. A. Francis, and A. Afzalian, "Signal-to-noise ratio optimization for detecting bacteria with interdigitated microelectrodes," *Sensors & Actuators: B. Chemical*, vol. 189, pp. 43–51, Dec. 2013.
- [181] C. Jungreuthmayer, G. M. Birnbaumer, J. Zanghellini, and P. Ertl, "3D numerical simulation of a lab-on-a-chip—increasing measurement sensitivity of interdigitated capacitors by passivation optimization," *Lab on a Chip*, vol. 11, no. 7, p. 1318, 2011.
- [182] T. Lederer, S. Clara, B. Jakoby, and W. Hilber, "Integration of impedance spectroscopy sensors in a digital microfluidic platform," *Microsyst Technol*, vol. 18, pp. 1163–1180, Mar. 2012.
- [183] W. Laureyn, D. Nelis, P. Van Gerwen, K. Baert, L. Hermans, R. Magnée, J. J. Pireaux, and G. Maes, "Nanoscaled interdigitated titanium electrodes for impedimetric biosensing," *Sensors & Actuators: B. Chemical*, vol. 68, pp. 360–370, 2000.
- [184] M. A. Rampi, O. J. A. Schueller, and G. M. Whitesides, "Alkanethiol self-assembled monolayers as the dielectric of capacitors with nanoscale thickness," *Appl. Phys. Lett.*, vol. 72, no. 14, pp. 1781–1783, 1998.
- [185] E. Boubour and R. B. Lennox, "Insulating Properties of Self-Assembled Monolayers Monitored by Impedance Spectroscopy," *Langmuir*, vol. 16, pp. 4222–4228, May 2000.
- [186] R. Pethig and D. B. Kell, "The passive electrical properties of biological systems: their significance in physiology, biophysics and biotechnology," *Phys Med Biol*, vol. 32, pp. 933–970, Aug. 1987.
- [187] G. Markx and C. L. Davey, "The dielectric properties of biological cells at radiofrequencies: applications in biotechnology," *Enzyme and Microbial Technology*, vol. 25, pp. 161–171, 1999.
- [188] M. Webster, I. Timoshkin, S. MacGregor, and M. Matthey, "Computer aided modelling of an interdigitated microelectrode array impedance biosensor for the detection of bacteria," *Dielectrics and Electrical Insulation, IEEE Transactions on*, vol. 16, no. 5, pp. 1356–1363, 2009.
- [189] T.-T. Ngo, H. Shirzadfar, D. Kourtiche, and M. Nadi, "A Planar Interdigital Sensor for Bio-impedance Measurement: Theoretical analysis, Optimization and Simulation," *Journal of Nano- and Electronic Physics*, vol. 6, no. 1, 2014.
- [190] F. Pittino, L. Selmi, and F. Widdershoven, "Numerical and analytical models to investigate the AC high-frequency response of nanoelectrode/SAM/electrolyte capacitive sensing elements," *Solid-State Electronics*, vol. 88, pp. 82–88, Oct. 2013.
- [191] F. Pittino and L. Selmi, "Use and comparative assessment of the CVFEM method for Poisson-Boltzmann and Poisson-Nernst-Planck three dimensional simulations of impedimetric nano-biosensors operated in the DC and AC small signal regimes," *Comput. Methods Appl. Mech. Engrg.*, vol. 278, pp. 902–923, Aug. 2014.

- [192] F. Pittino, P. Palestri, P. Scarbolo, D. Esseni, and L. Selmi, "Models for the use of commercial TCAD in the analysis of silicon-based integrated biosensors," *Solid-State Electronics*, vol. 98, pp. 63–69, Aug. 2014.
- [193] A. T. Poortinga, R. Bos, W. Norde, and H. J. Busscher, "Electric double layer interactions in bacterial adhesion to surfaces," *Surface Science Reports*, vol. 47, no. 1, pp. 1–32, 2002.
- [194] van der Wal A, M. Minor, W. Norde, A. Zehnder, and J. Lyklema, "Conductivity and Dielectric Dispersion of Gram-Positive Bacterial Cells," *Journal of Colloid and Interface Science*, vol. 186, pp. 71–79, Feb. 1997.
- [195] H. Lee, S. M. Dellatore, W. M. Miller, and P. B. Messersmith, "Mussel-Inspired Surface Chemistry for Multifunctional Coatings," *Science*, vol. 318, pp. 426–430, Oct. 2007.
- [196] M. Flury and T. F. Gimmi, "6.2 Solute Diffusion," *Methods of Soil Analysis: Part 4 Physical Methods*, pp. 1323–1351, 2002.
- [197] L. Højgaard Olesen, M. Bazant, and H. Bruus, "Strongly nonlinear dynamics of electrolytes in large ac voltages," *Phys. Rev. E*, vol. 82, p. 011501, July 2010.
- [198] M. Z. M. Bazant, K. K. Thornton, and A. A. Ajdari, "Diffuse-charge dynamics in electrochemical systems.," *Phys Rev E Stat Nonlin Soft Matter Phys*, vol. 70, pp. 021506–021506, July 2004.
- [199] F. Pittino, F. Passerini, L. Selmi, and F. Widdershoven, "Numerical simulation of the position and orientation effects on the impedance response of nanoelectrode array biosensors to DNA and PNA strands," *Microelectronics Journal*, vol. 45, no. 12, pp. 1695–1700, 2014.
- [200] J.-C. Chou and L. P. Liao, "Study on pH at the point of zero charge of TiO₂ pH ion-sensitive field effect transistor made by the sputtering method," *Thin Solid Films*, vol. 476, pp. 157–161, Apr. 2005.
- [201] R. Rodriguez, M. A. Blesa, and A. E. Regazzoni, "Surface complexation at the TiO₂ (anatase)/aqueous solution interface: chemisorption of catechol," *Journal of Colloid and Interface Science*, vol. 177, pp. 122–131, 1996.
- [202] H.-C. Chang and L. Y. Yeo, *Electrokinetically driven microfluidics and nanofluidics*. Cambridge University Press Cambridge, UK;, 2010.
- [203] Y. Huang, K. L. Ewalt, M. Tirado, R. Haigis, A. Forster, D. Ackley, M. J. Heller, J. P. O'Connel, and M. Krihak, "Electric Manipulation of Bioparticles and Macromolecules on Microfabricated Electrodes," *Anal. Chem.*, vol. 73, pp. 1549–1559, Apr. 2001.
- [204] K. Khoshmanesh, S. Nahavandi, S. Baratchi, A. Mitchell, and K. Kalantar-zadeh, "Biosensors and Bioelectronics," *Biosensors and Bioelectronic*, vol. 26, pp. 1800–1814, Jan. 2011.
- [205] T. Z. Jubery, S. K. Srivastava, and P. Dutta, "Dielectrophoretic separation of bioparticles in microdevices: A review," *Electrophoresis*, vol. 35, pp. 691–713, Feb. 2014.
- [206] A. Castellanos, A. Ramos, A. Gonzalez, N. G. Green, and H. Morgan, "Electrohydrodynamics and dielectrophoresis in microsystems: scaling laws," *J. Phys. D: Appl. Phys.*, vol. 36, no. 20, p. 2584, 2003.
- [207] X. Wang, X.-B. Wang, and P. R. Gascoyne, "General expressions for dielectrophoretic force and electrorotational torque derived using the Maxwell stress tensor method," *Journal of Electrostatics*, vol. 39, no. 4, pp. 277–295, 1997.

- [208] N. G. Green, A. Ramos, A. Gonzalez, A. Castellanos, and H. Morgan, "Electrothermally induced fluid flow on microelectrodes," *Journal of Electrostatics*, vol. 53, no. 2, pp. 71–87, 2001.
- [209] N. G. Green, A. Ramos, A. Gonzalez, A. Castellanos, and H. Morgan, "Electric field induced fluid flow on microelectrodes: the effect of illumination," *J. Phys. D: Appl. Phys.*, vol. 33, no. 2, p. L13, 2000.
- [210] J. Gao, M. L. Y. Sin, T. Liu, V. Gau, J. C. Liao, and P. K. Wong, "Hybrid electrokinetic manipulation in high-conductivity media," *Lab on a Chip*, vol. 11, no. 10, p. 1770, 2011.
- [211] P. K. Wong, C.-Y. Chen, T.-H. Wang, and C.-M. Ho, "Electrokinetic Bioprocessor for Concentrating Cells and Molecules," *Anal. Chem.*, vol. 76, pp. 6908–6914, Dec. 2004.
- [212] P. Sabounchi, A. M. Morales, P. Ponce, L. P. Lee, B. A. Simmons, and R. V. Davalos, "Sample concentration and impedance detection on a microfluidic polymer chip," *Biomed Microdevices*, vol. 10, pp. 661–670, May 2008.
- [213] H. Shafiee, J. L. Caldwell, M. B. Sano, and R. V. Davalos, "Contactless dielectrophoresis: a new technique for cell manipulation," *Biomed Microdevices*, vol. 11, pp. 997–1006, May 2009.
- [214] J. Gimsa, T. Muller, T. Schnelle, and G. Fuhr, "Dielectric spectroscopy of single human erythrocytes at physiological ionic strength: dispersion of the cytoplasm," *Biophys. J.*, vol. 71, pp. 495–506, July 1996.
- [215] Z. Gagnon, J. Gordon, S. Sengupta, and H.-C. Chang, "Bovine red blood cell starvation age discrimination through a glutaraldehyde-amplified dielectrophoretic approach with buffer selection and membrane cross-linking," *Electrophoresis*, vol. 29, pp. 2272–2279, June 2008.
- [216] Z. Gagnon and H.-C. Chang, "Aligning fast alternating current electroosmotic flow fields and characteristic frequencies with dielectrophoretic traps to achieve rapid bacteria detection," *Electrophoresis*, vol. 26, pp. 3725–3737, Oct. 2005.
- [217] B. H. Lapizco-Encinas, B. A. Simmons, E. B. Cummings, and Y. Fintschenko, "Dielectrophoretic concentration and separation of live and dead bacteria in an array of insulators," *Anal. Chem.*, vol. 76, pp. 1571–1579, Mar. 2004.
- [218] M. Castellarnau, A. Errachid, C. Madrid, A. Juárez, and J. Samitier, "Dielectrophoresis as a Tool to Characterize and Differentiate Isogenic Mutants of *Escherichia coli*," *Biophys. J.*, vol. 91, pp. 3937–3945, Nov. 2006.
- [219] J. Suehiro, M. Shutou, T. Hatano, and M. Hara, "High sensitive detection of biological cells using dielectrophoretic impedance measurement method combined with electroporabilization," *Sensors & Actuators: B. Chemical*, vol. 96, pp. 144–151, Nov. 2003.
- [220] R. Hamada, H. Takayama, Y. Shonishi, L. Mao, M. Nakano, and J. Suehiro, "A rapid bacteria detection technique utilizing impedance measurement combined with positive and negative dielectrophoresis," *Sensors & Actuators: B. Chemical*, vol. 181, pp. 439–445, May 2013.
- [221] F. Grom, J. Kentsch, T. Muller, T. Schnelle, and M. Stelzle, "Accumulation and trapping of hepatitis A virus particles by electrohydrodynamic flow and dielectrophoresis," *Electrophoresis*, vol. 27, pp. 1386–1393, Apr. 2006.
- [222] R. Pethig, "Dielectrophoresis: Status of the theory, technology, and applications," *Biomicrofluidics*, vol. 4, no. 2, p. 022811, 2010.

- [223] C. A. Mack, "Fifty Years of Moore's Law," *Semiconductor Manufacturing, IEEE Transactions on*, vol. 24, no. 2, pp. 202–207, 2011.
- [224] A. B. Kahng, "Scaling: More than Moore's law.," *IEEE Design & Test of Computers*, vol. 27, no. 3, pp. 86–87, 2010.
- [225] H. Baltes, O. Brand, A. Hierlemann, D. Lange, and C. Hagleitner, "CMOS MEMS - present and future," in *Micro Electro Mechanical Systems, 2002. The Fifteenth IEEE International Conference on*, pp. 459–466, 2002.
- [226] S. B. Prakash and P. Abshire, "Tracking cancer cell proliferation on a CMOS capacitance sensor chip," *Biosensors and Bioelectronics*, vol. 23, pp. 1449–1457, May 2008.
- [227] M. Ali-Bakhshian and G. W. Roberts, "A semi-digital interface for capacitive sensors," *Circuits and Systems, 2009. ISCAS 2009. IEEE International Symposium on*, pp. 1957–1960, 2009.
- [228] E. Ghafar-Zadeh, M. Sawan, V. P. Chodavarapu, and T. Hosseini-Nia, "Bacteria Growth Monitoring Through a Differential CMOS Capacitive Sensor," *IEEE Transactions on Biomedical Circuits and Systems*, vol. 4, pp. 232–238, Aug. 2010.
- [229] N. Samanta, O. Kundu, and C. R. Chaudhuri, "A Simple Low Power Electronic Read-out for Rapid Bacteria Detection with Impedance Biosensor," *IEEE Sensors J.*, vol. 13, no. 12, pp. 4716–4724, 2013.
- [230] B. Eversmann, M. Jenkner, F. Hofmann, C. Paulus, R. Brederlow, B. Holzapfl, P. Fromherz, M. Merz, M. Brenner, M. Schreiter, R. Gabl, K. Plehnert, M. Steinhauser, G. Eckstein, D. Schmitt-Landsiedel, and R. Thewes, "A 128 x 128 cmos biosensor array for extracellular recording of neural activity," *IEEE J. Solid-State Circuits*, vol. 38, pp. 2306–2317, Dec. 2003.
- [231] A. Romani, N. Manaresi, L. Marzocchi, G. Medoro, A. Leonardi, L. Altomare, M. Tartagni, and R. Guerrieri, "Capacitive sensor array for localization of bioparticles in CMOS lab-on-a-chip," in *Solid-State Circuits Conference, 2004. Digest of Technical Papers. ISSCC. 2004 IEEE International*, pp. 224–225, IEEE, 2004.
- [232] S. B. Prakash and P. Abshire, "A fully differential rail-to-rail CMOS capacitance sensor with floating-gate trimming for mismatch compensation," *Circuits and Systems I: Regular Papers, IEEE Transactions on*, vol. 56, no. 5, pp. 975–986, 2009.
- [233] B. Jang, P. Cao, A. Chevalier, A. Ellington, and A. Hassibi, "A CMOS fluorescent-based biosensor microarray," in *Solid-State Circuits Conference - Digest of Technical Papers, 2009. ISSCC 2009. IEEE International*, pp. 436–437, 2009.
- [234] K.-H. Lee, J.-O. Lee, M.-J. Sohn, B. Lee, S.-H. Choi, S. K. Kim, J.-B. Yoon, and G.-H. Cho, "One-chip electronic detection of DNA hybridization using precision impedance-based CMOS array sensor," *Biosensors and Bioelectronics*, vol. 26, pp. 1373–1379, Dec. 2010.
- [235] M. S. C. Lu, Y.-C. Chen, and P.-C. Huang, "5 x 5 CMOS capacitive sensor array for detection of the neurotransmitter dopamine.," *Biosensors and Bioelectronics*, vol. 26, pp. 1093–1097, Nov. 2010.
- [236] L. Li, X. Liu, W. A. Qureshi, and A. J. Mason, "CMOS Amperometric Instrumentation and Packaging for Biosensor Array Applications.," *IEEE Transactions on Biomedical Circuits and Systems*, vol. 5, pp. 439–448, Oct. 2011.

- [237] M. A. Miled, G. Massicotte, and M. Sawan, "Dielectrophoresis-based integrated Lab-on-Chip for nano and micro-particles manipulation and capacitive detection.," *IEEE Transactions on Biomedical Circuits and Systems*, vol. 6, pp. 120–132, Apr. 2012.
- [238] H. Mazhab-Jafari, L. Soleymani, and R. Genov, "16-channel CMOS impedance spectroscopy DNA analyzer with dual-slope multiplying ADCs.," *IEEE Transactions on Biomedical Circuits and Systems*, vol. 6, pp. 468–478, Oct. 2012.
- [239] J. Musayev, Y. Adlguzel, H. Klah, S. Eminoglu, and T. Akln, "Label-Free DNA Detection Using a Charge Sensitive CMOS Microarray Sensor Chip," *IEEE Sensors J.*, vol. 14, no. 5, pp. 1608–1616, 2014.
- [240] N. Couniot, A. Afzalian, and D. Flandre, "Scaling laws and performance improvements of integrated biosensor microarrays with multi-pixel per spot," *Sensors & Actuators: B. Chemical*, vol. 166-167, pp. 184–192, May 2012.
- [241] A. El Gamal and H. Eltoukhy, "CMOS image sensors," *Circuits and Devices Magazine, IEEE*, vol. 21, no. 3, pp. 6–20, 2005.
- [242] G. Nabovati, E. Ghafar-Zadeh, M. Mirzaei, G. Ayala-Charca, F. Awwad, and M. Sawan, "A New Fully Differential CMOS Capacitance to Digital Converter for Lab-on-Chip Applications.," *IEEE Transactions on Biomedical Circuits and Systems*, Aug. 2014.
- [243] J.-C. Chien, M. Anwar, E.-C. Yeh, L. P. Lee, and A. M. Niknejad, "A 1–50 GHz dielectric spectroscopy biosensor with integrated receiver front-end in 65nm CMOS," in *Microwave Symposium Digest (IMS), 2013 IEEE MTT-S International*, pp. 1–4, IEEE, 2013.
- [244] A. A. Helmy, H.-J. Jeon, Y.-C. Lo, A. J. Larsson, R. Kulkarni, J. Kim, J. Silva-Martinez, and K. Entesari, "A Self-Sustained CMOS Microwave Chemical Sensor Using a Frequency Synthesizer," *IEEE J. Solid-State Circuits*, vol. 47, no. 10, pp. 2467–2483, 2012.
- [245] U. Frey, J. Sedivy, F. Heer, R. Pedron, M. Ballini, J. Mueller, D. Bakkum, S. Hafizovic, F. D. Faraci, F. Greve, K. U. Kirstein, and A. Hierlemann, "Switch-matrix-based high-density microelectrode array in CMOS technology," *IEEE J. Solid-State Circuits*, vol. 45, no. 2, pp. 467–482, 2010.
- [246] E. Ghafar-Zadeh, M. Sawan, and V. P. Chodavarapu, "Micro-Organism-on-Chip: Emerging Direct-Write CMOS-Based Platform for Biological Applications.," *IEEE Transactions on Biomedical Circuits and Systems*, vol. 3, pp. 212–219, Aug. 2009.
- [247] C.-L. Dai, "A capacitive humidity sensor integrated with micro heater and ring oscillator circuit fabricated by CMOS–MEMS technique," *Sensors & Actuators: B. Chemical*, vol. 122, pp. 375–380, Mar. 2007.
- [248] S. Druart, D. Flandre, and L. A. Francis, "A Self-Oscillating System to Measure the Conductivity and the Permittivity of Liquids within a Single Triangular Signal," *Journal of Sensors*, vol. 2014, 2014.
- [249] E. Ghafar-Zadeh and M. Sawan, "A Hybrid Microfluidic/CMOS Capacitive Sensor Dedicated to Lab-on-Chip Applications," *IEEE Transactions on Biomedical Circuits and Systems*, vol. 1, pp. 270–277, Dec. 2007.
- [250] E. Ghafar-Zadeh, M. Sawan, and D. Therriault, "A 0.18- μm CMOS capacitive sensor Lab-on-Chip," *Sensors and Actuators A: Physical*, vol. 141, pp. 454–462, Feb. 2008.

-
- [251] D. Sylvester, J. C. Chen, and C. Hu, "Investigation of interconnect capacitance characterization using charge-based capacitance measurement (CBCM) technique and three-dimensional simulation," *IEEE J. Solid-State Circuits*, vol. 33, no. 3, pp. 449–453, 1998.
- [252] M. Bakhshiani, M. A. Suster, and P. Mohseni, "A broadband biosensor interface IC for miniaturized dielectric spectroscopy from MHz to GHz," in *Custom Integrated Circuits Conference (CICC), 2013 IEEE*, pp. 1–4, IEEE, 2013.
- [253] A. H. D. Graham, J. Robbins, C. R. Bowen, and J. Taylor, "Commercialisation of CMOS Integrated Circuit Technology in Multi-Electrode Arrays for Neuroscience and Cell-Based Biosensors," *Sensors*, vol. 11, pp. 4943–4971, May 2011.
- [254] F. Silveira, D. Flandre, and P. Jespers, "A gm/ID based methodology for the design of CMOS analog circuits and its application to the synthesis of a silicon-on-insulator micropower OTA," *IEEE J. Solid-State Circuits*, vol. 31, no. 9, pp. 1314–1319, 1996.
- [255] S. Mendis, S. Kemeny, R. Gee, B. Pain, C. Staller, Q. Kim, and E. R. Fossum, "CMOS active pixel image sensors for highly integrated imaging systems," *IEEE J. Solid-State Circuits*, vol. 32, no. 2, pp. 187–197, 1997.
- [256] W. Thielicke and E. J. Stamhuis, "PIVlab – Towards User-friendly, Affordable and Accurate Digital Particle Image Velocimetry in MATLAB," *Journal of Open Research Software*, vol. 2, pp. 1–10, Sept. 2014.
- [257] R. D. Keane and R. J. Adrian, "Theory of cross-correlation analysis of PIV images," *Applied scientific research*, vol. 49, no. 3, pp. 191–215, 1992.

APPENDIX **A**

Protocols and setups

A.1 Sensor microfabrication

The process is detailed in Table A.1 and sketched in Fig. A.1. The main steps are the following:

1. The 3-inch 400 μm -thick Pyrex wafer is immersed in a fresh Piranha solution ($\text{H}_2\text{O}_2:\text{H}_2\text{SO}_4$, 2:5) during 10 min for cleaning, followed by two continuously renewed immersions in DI water baths during 20 min.
2. Aluminum is evaporated in a rotate mode to deposit a 1 μm -thick layer. A first optical lithography with positive photoresist AZ6612 (Microchemicals) and developer AZ726MIF (Microchemicals) then provides finger masking during the subsequent Al plasma etching in RD600 equipment. After removing the photoresist with an oxygen plasma, the whole wafer is covered with 33 nm of plasma enhanced ALD Al_2O_3 at room temperature (RT) with trimethylaluminum and oxygen as precursor. The argon flow through plasma source is 200 sccm and the oxygen flow for the plasma step is 30 sccm during 20 sec.

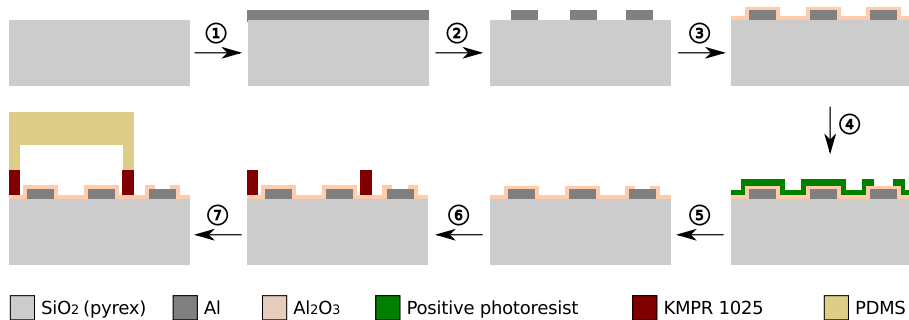


Figure A.1 – Sensor micro-fabrication steps: (1) aluminum deposition, (2) positive optical lithography followed by aluminum plasma etching, (3) deposition of an ALD Al_2O_3 layer, (4) positive optical lithography to open pads, (5) etching Al_2O_3 with IPA:HF 70% (3:1), (6) positive optical lithography to define thick KMPR walls and (7) PDMS cap pressure.

Table A.1 – Process sheet for the fabrication of the IDE devices.

Sequence	Parameters	Thickness
1	Cleaning without HF	
2	Metallization e-gun Varian	Rotate, Front, Al
3	Lithography Positive	<i>Metal</i> LFi, exposition of 2.6 s
4	Etching Al Plasma	RD-600
5	Photoresist barrel stripping	500 W prog, 10 min
6	Measurement Dektak	
7	Custom	ALD, Front, Al ₂ O ₃
8	Measurement ellipsometer	Al ₂ O ₃
9	Custom	HMDS layer, LP-III
10	Lithography Positive	<i>Contact</i> DFi, exposition of 3.5 s
11	Custom	Etching Al ₂ O ₃ with HF:IPA
12	Photoresist barrel stripping	500 W prog, 10 min
13	Custom	HMDS layer, LP-III
14	Lithography Positive	<i>RemoveAl</i> DFi, exposition of 5.5 s
15	Etching Al wet	H ₃ PO ₄ , 65°C
16	Photoresist barrel stripping	500 W prog, 10 min
17	Lithography Positive	<i>Microfluidics</i> DFi, KMPR 1025
18	Dicing	

LFi: Light Field, DFi: Dark Field, HMDS: hexamethyldisilazane
 Italic names are the masks used for photolithography

3. A second optical lithography with positive photoresist AZ6612 and developer AZ726MIF is used to define pad area and etch the subsequent Al₂O₃ layer after 15 sec immersion in IPA:HF 70% (3:1), presenting a characterized etch rate of $\simeq 0.5 \mu\text{m}/\text{min}$ for Al₂O₃. The photoresist is then removed with an oxygen plasma.
4. A third positive lithography with positive photoresist AZ6612 and developer AZ726MIF is performed to open central aluminum lines, connecting all the sensors together. These lines were included to further enable a potential anodization step, instead of using atomic layer deposition (ALD). These lines are removed by subsequent immersion in H₃PO₄ at 65°C during approximately 3 min since the etch rate is ca. 300 nm/min.
5. A last optical lithography with negative photoresist KMPR 1025 defines 30 μm -thick walls to support the microfluidic cap. The parameters of this non-standard photolithography step are detailed:
 - (a) Coating at 1500 RPM and 1000 RPM/s during 60 s.

- (b) Soft bake during 30 min at 100°C, followed by a cleaning with acetone on the wafer backside.
 - (c) Exposure during 120 s with a soft contact at a distance of 100 μm .
 - (d) Post exposure bake of 6 min at 100°C.
 - (e) Development in SU-8 Developer during 6 min, using two different baths and ending with 20 sec of ultrasounds.
6. The wafer is then diced into 8 mm x 8 mm chips, each containing 3 to 12 individual sensors (Fig. A.2(b)).

To define the microfluidic cap, a 270 μm -thick KMPR 1050 layer is patterned by optical lithography on a clean 3-inch silicon wafer (Fig. A.2(a)). The following parameters are used to achieve this thick patterned photoresist:

1. Coating at 600 RPM and 1000 RPM/s during 80 s.
2. Soft bake: 15 min at 40°C, followed by 15 min at 65°C and 260 min at 100°C. After, the wafer must cool down overnight. The plate level must also be tightly controlled.
3. Exposure during 100 s with a soft contact.
4. Post exposure bake: 5 min at 40°C, followed by 10 min at 65°C and 15 min at 100°C.
5. Development in SU-8 Developer during 25 min, using two different baths and ending with 3 min of ultrasounds.

This mold is then covered with a thin hexamethyldisilazane (HMDS) layer to easily take off the polydimethylsiloxane (PDMS) cap subsequently. Inside a Petri dish, the PDMS is flown on the mold wafer and incubated at 60°C overnight. Every microfluidic caps are then cut individually with a cutter blade. To improve the sticking, an oxygen plasma (25 W during 35 s) was performed on both the PDMS and chip faces, that are next pressed against each other (Fig. A.2(c)). Microfluidic tubes are then plugged manually through the device. To ensure the watertight sealing of the system during several hours, a transparent pressure tool has also been used (Fig. A.5).

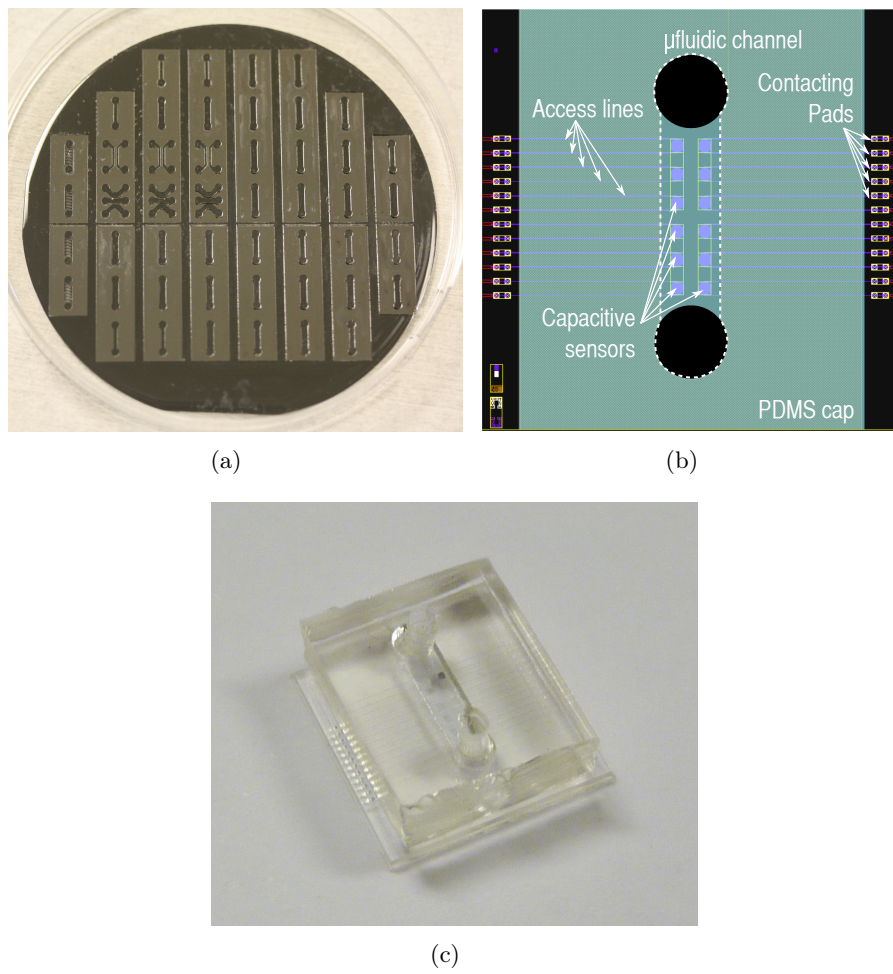


Figure A.2 – (a) Molding wafer to define the PDMS caps and (b)(c) packaged sensor (die + PDMS cap): (b) top view from *Cadence* design and (c) photograph.

A.2 Materials

PBS tablet, creatinine, Na_2HPO_4 , CaCl_2 , dopamine hydrochloride and lysostaphin were purchased at Sigma-Aldrich (Diegem, Belgium). Urea, KCl, MgSO_4 and Tris were purchased at Merck (Overijse, Belgium). NaCl, NaHCO_3 , NaCl and glycerol were purchased at VWR (Leuven, Belgium). $(\text{NH}_4)_2\text{SO}_4$ was purchased from UCB (Brussels, Belgium).

- **PBS dilutions** : 0.01 M phosphate buffer saline (PBS) at pH 7.4 was obtained by diluting one tablet in 200 mL of milliQ water. PBS 1:1000, PBS 1:100 and PBS 1:10 were prepared by adequately diluting PBS in milliQ water by volume. PBS and all PBS dilutions were autoclaved 15 min at 121°C before use.
- **Culture media** : Tryptic Soy Broth (TSB), Tryptic Soy Agar (TSA) and Lysogeny broth (LB) were prepared standardly and autoclaved 15 min at 121°C.
- **Synthetic urine** : Synthetic urine was made as follows (w/v): urea 2%, KCl 1.2%, creatinine 0.1%, $(\text{NH}_4)_2\text{SO}_4$ 0.1%, Na_2HPO_4 0.1%, MgSO_4 0.01%, CaCl_2 0.01% and NaHCO_3 0.01%. These compounds were diluted in 1 L of milliQ water, the pH was then adjusted at 7 using 1M HCl. Synthetic urea was sterilized using 0.22 μm porosity Millipore filters in PES (Filter service, Eupen, Belgium) before use.
- **Polydopamine solution** : A Tris-NaCl buffer contains Tris 50 mM, NaCl 150 mM dissolved in milliQ water, adjusted to pH=9.2 with HCl 1 M and autoclaved prior to use. The polydopamine solution was prepared by dissolving 4 mg/mL of dopamine hydrochloride in the Tris-NaCl buffer. The solution was left 1 hour in the dark to polymerize before being injected in the microfluidic channel.
- **Lysostaphin solution** : commercialized lysostaphin, sold as 1 mg powder where 55% of the total mass is lysostaphin, was diluted in 1 mL of PBS supplemented with 30% of glycerol, and transferred into 50 μL aliquots stored at -20°C. Working solutions were prepared by adding 950 μL of PBS to 50 μL of stock solution (20 μM) yielding a 1 μM lysostaphin.

A.3 Bacterial handling

- **Section 2.2.3 (IDE for real-time bacterial sensing):** *S. epidermidis* ATCC 35984 (purchased from LGC standards, Molsheim, France) was used as reference Gram-positive bacteria. Following overnight culture on TSA plates at 37°C, liquid cultures were performed in 250 mL Erlenmeyer flasks containing 50 mL of TSB. Stationary phase cultures were obtained after overnight incubation at 37°C at 120 RPM. Two 2mL tubes of stationary phase culture of *S. epidermidis* were centrifuged 10 min at RT at 5500 g. The supernatant was then discarded and both pellets were resuspended in 1 mL of synthetic urine. The centrifugation, supernatant removal and resuspension steps were repeated twice for both tubes. Suspensions from both tubes were pooled and the optical density (OD_{600nm}) was adjusted from $OD_{600nm} = 3$ ($\simeq 10^9$ CFU/mL) to $OD_{600nm} = 0.003$ ($\simeq 10^6$ CFU/mL), by adequately diluting the concentrated suspension in PBS 1:1000.
- **Section 2.3.2 (IDE with lytic enzymes):** *E. faecium* ATCC 19434 (purchased from LGC standards, Molsheim, France) was used as negative control. The culture and resuspension steps use the same protocol as in Section 2.2.3, but the optical density was adjusted to $OD_{600nm} = 1$ ($\sim 5 \cdot 10^8$ CFU/mL). For exponential-state *S. epidermidis*, an exponential phase culture was obtained by inoculating 50 mL of fresh medium with 500 μ L of the stationary phase culture and incubating at 37°C, 120 RPM until an OD_{600nm} of 0.5 was reached. One 50 mL tube was then centrifuged 10 min at 4°C with an acceleration of 5500 g and the pellet was resuspended in 2 mL of synthetic urine. This step was repeated two times in two 2 mL tubes. The suspension was adjusted to an $OD_{600nm} = 1$ ($\sim 5 \cdot 10^8$ CFU/mL) in order to be injected into the setup. The bacterial concentration was determined by plate count technique and expressed in colony forming units per milliliter (CFU/mL).
- **Section 3.5 and 3.6 (IDE + EK):** *Staphylococcus epidermidis* ATCC 35984 was cultivated overnight at 37°C on Tryptic Soy Agar (TSA) plates. One single colony was then scraped and brought into Tryptic Soy Broth (TSB) medium for overnight culture at 37°C. From this culture, 2 mL was extracted and centrifuged at 7000 RPM during 10 min. The supernatant was discarded and the pellet resuspended in PBS 1:1000. The centrifugation and resus-

pension steps were repeated two times to remove any remaining ions from the initial culture medium. The bacterial sample in PBS 1:1000 was diluted 100 times in sterile PBS 1:1000, and the number of viable bacteria was estimated to $7 \cdot 10^6$ colony forming unit (CFU)/mL after plate counting.

- **Section 4.2.3 (CFC):** *S. epidermidis* ATCC 35984 was cultivated on agar plates and incubated at 37°C overnight. Then, one single colony was suspended in 50 mL of Tryptic Soy Broth (TSB) and incubated overnight at 37°C to obtain a stationary phase bacterial culture. Afterwards, the culture was centrifugated and bacterial cells were resuspended in pure PBS. This step was repeated two times. The bacterial concentration was c.a. $5 \cdot 10^8$ CFU/ml, as determined by surface plate counting.
- **Section 4.3.4 (capacitive biosensor array):** After cultivated on agar plates at 37°C overnight, one single colony of *S. epidermidis* ATCC 35984 was suspended in 50 mL of Tryptic Soy Broth (TSB) and incubated overnight at 37°C . Afterwards, the culture was centrifugated and bacterial cells were resuspended in PBS 1:1000. This step was repeated two times. The bacterial concentration was evaluated to $5 \cdot 10^8$ CFU/ml by surface plate counting.

A.4 CMOS chip fabrication, post-processing and encapsulation

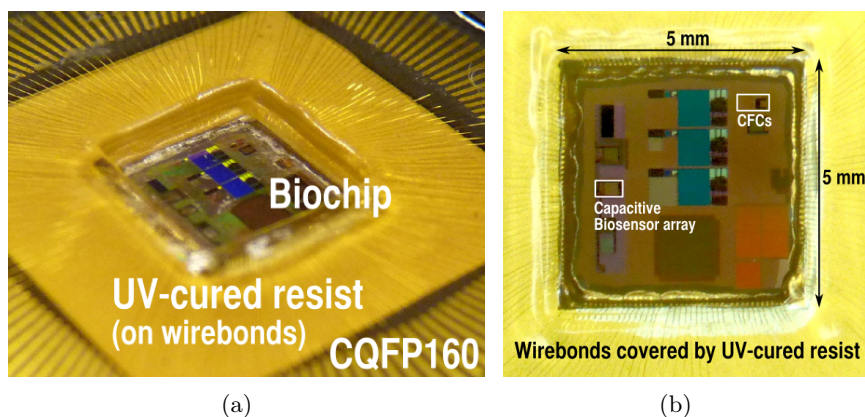


Figure A.3 – Photograph of (a) the packaged biochip in the ceramic package CQFP160, highlighting protected wirebonds, and (b) the biochip with locations of the capacitive biosensor array and capacitance-to-frequency converters (CFCs).

The CMOS chips were fabricated in an industrial $0.25\ \mu\text{m}$ 2.5-V multi- V_{th} 1P5M Mixed-Signal CMOS process, comprising a $1.8\ \mu\text{m}$ -thick Al 99.5%/Cu 0.5% last metal layer (M5) used for patterning sensing parts. The CMOS dies were not covered by the thick $\text{SiO}_2/\text{Si}_3\text{N}_4$ passivation layer and were encapsulated in open-top CQFP160 packages. The wirebonds were covered by epoxy resin to avoid contact with liquid during experiments (Figs. A.3(a) and A.3(b)). As characterized by ellipsometry, a $25 \pm 0.25\ \text{nm}$ -thick Al_2O_3 layer was deposited by plasma-enhanced atomic layer deposition (PE-ALD) at room temperature with trimethylaluminum (TMA) and oxygen as precursor. The argon flow through plasma source was 200 sccm and the oxygen flow for the plasma step was 30 sccm during 20 sec. Compared to the conventional $1\text{-}\mu\text{m}$ thick CMOS passivation layer in Si_3N_4 , the ALD-deposited Al_2O_3 passivation layer is much thinner ($\sim 25\ \text{nm}$), features a higher relative permittivity (9 versus 7.5) and is positively charged in physiological buffers (see Fig. 2.21(a)), so that negatively-charged bacteria (see Fig. 2.21(b)) adhere more easily. Besides these advantages, a TiO_2 passivation layer should have been better because it is more resistant to corrosion [161], features a very large relative permittivity (~ 160) and can also be deposited by ALD.

A.5 Measurement setup

- **Section 2.2.2 (IDE in simple solutions):** the device is positioned on probe station (PA200, Karl Suss, Germany) and contacted by electrical probes to an impedance analyzer (LCR 4284A, Agilent, USA), which is remotely controlled by LabVIEW[®] to perform sweep the applied frequency from 100 Hz to 1 MHz, at voltage amplitude of 50 mV (Fig. A.4). Samples were flown through the microfluidic channel by a peristaltic pump.
- **Section 2.2.3 (IDE + bacteria):** the device was positioned on an inverted microscope (DMI6000, Leica, Belgium) enabling real-time imaging of the sensor surface during electrical measurements (Fig. A.5). Samples were flown through the microfluidic channel by a peristaltic pump. An impedance analyzer (LCR 4284A, Agilent, USA) was connected to electrical probes and remotely controlled through LabVIEW[®] to perform an automatic sweep from 100 Hz to 1 MHz, at voltage amplitude of 50 mV. Before impedance measurement, an open calibration was performed by positioning electrical probes above aluminum pads, without any electrical contacts.

Once electrical probes contacted to pads, the sensor was first rinsed

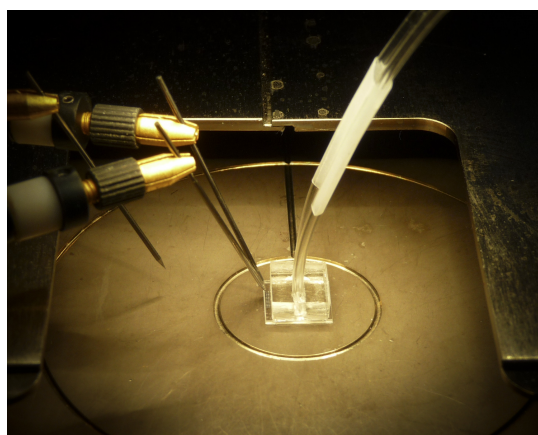


Figure A.4 – Measurement setup with electrical probes of the sensor encapsulated in a microfluidic package. Electrical probes are connected to a LCR meter and the microfluidic flow is imposed by the peristaltic pump.

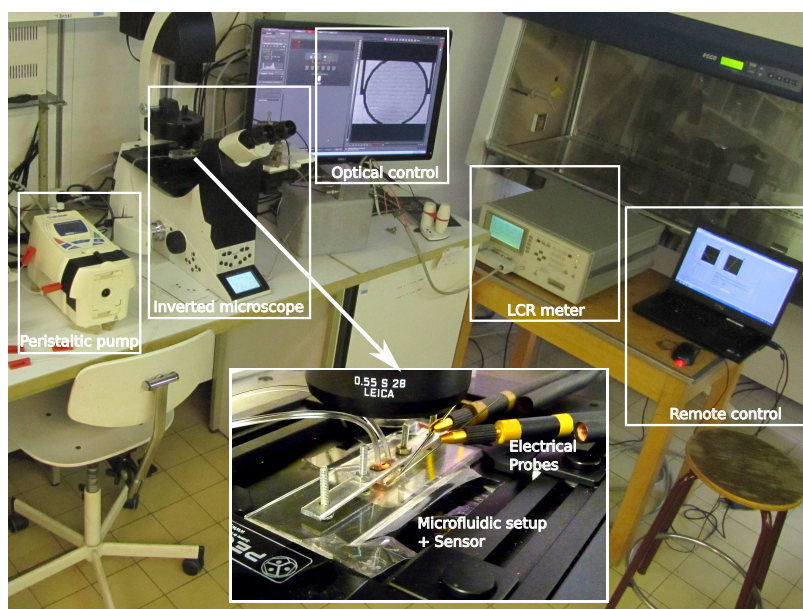


Figure A.5 – Measurement setup enabling real-time optical and electrical monitoring. The encapsulated sensor is positioned on an inverted microscope and contacted through electrical probes to the LCR meter. The microfluidic flow is imposed by the peristaltic pump.

and measured in PBS 1:1000 at $125 \mu\text{L}/\text{min}$, during 10 min at RT. Then, a polydopamine solution, known as biological glue [195], was incubated during 30 min at dark condition, without flow and electrical measurements. Afterwards, the sensor was washed with PBS 1:1000 during 5 min at $250 \mu\text{L}/\text{min}$ followed by 5 min at $125 \mu\text{L}/\text{min}$ under electrical measurements to reach a constant value. At this point, the sensor is ready to be experimented with bacterial cells.

- **Sections 3.5 and 3.6 (IDE + EK):** the device described in Section 3.2 was contacted to instruments by electrical probes connected to $50\text{-}\Omega$ BNC cables. The IDEs impedance was measured by a LCR meter (Agilent 4284A) between 1 kHz and 1 MHz, with an amplitude of 50 mV. The LCR was calibrated in open position (electrical probes ca. $250 \mu\text{m}$ above electrical pads) before use. A $14\text{-}V_{pp}$ sinusoidal voltage, with tuneable frequency comprised between 1 kHz and 80 MHz, was applied on the macroelectrode by

a function waveform generator (Agilent 33250A), having the same ground as the LCR and an input impedance of 50Ω . Simultaneous optical and electrical monitoring was performed by placing the microfluidic transparent device on an inverted microscope (Leica DMI6000), as illustrated in Fig. A.5.

The S_{11} parameter of the previous setup, i.e. BNC cables and electrical probe contacting the macroelectrode immersed in PBS 1:1000 without bacteria while microelectrodes are grounded, was measured by a vector network analyser (VNA Agilent ENA 5061B) between 10 kHz and 300 MHz. The VNA power and input impedance are 0 dBm and 50Ω , respectively. Furthermore, the VNA port was calibrated with the calibration kit 85032F in a standard SOLT (Short-Open-Load-Thru) calibration method.

- **Sections 4.2.3 and 4.3.4 (CMOS biochips)**

The open-top CQFP160 packages were soldered on slave PCBs, each successively mounted in a master PCB to enable multiple purpose measurements (Fig. A.6(a)). The measurement setup is slightly different for the two following circuits (Fig. A.6(b)):

- **Section 4.2.3 (CFC):** a LabVIEW[®] program was implemented to automatically sweep V_{dd} , generated by a Keithley K2400, and accordingly measure the mean $\overline{f_{out}}$ and the standard deviation $\sigma_{f_{out}}$ on 100 repeated measurements of f_{out} from the two circuits, whose outputs were connected to scope channels (Agilent MSO8104A).
- **Section 4.3.4 (capacitive biosensor array):** digital signals were generated by the National Instruments[®] (NI) PXI-6552 card while analog output signals from the chip were converted to digital signals by the NI PXI-5105 card. Supply and biasing voltages were provided by the N6715B and K2400 equipments. All the setup and data acquisition were controlled through LabVIEW.

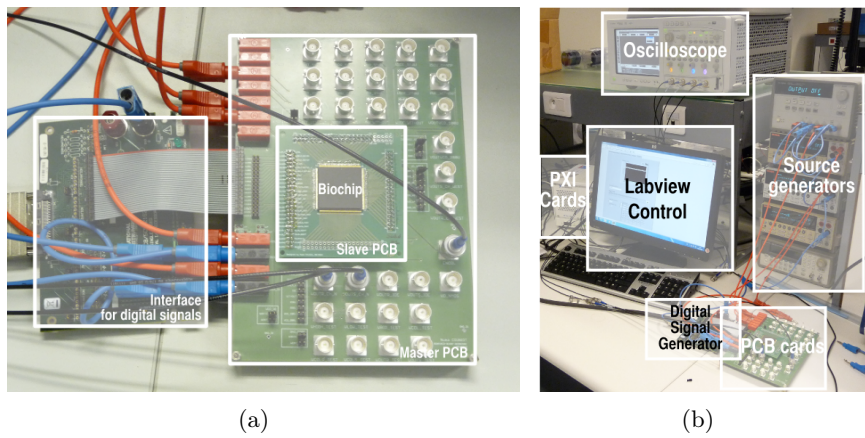


Figure A.6 – (a) Measurement setup for the CFC and biosensor array and (b) related slave and master PCBs to interface the packaged chip.

APPENDIX **B**

Programs

B.1 Matlab algorithm for automatic bacterial counting

Based on microscope images, a MATLAB[®] program was implemented to automatically count the number of attached bacteria on the sensor surface. A mask was first obtained from an image of the sensor surface with almost no bacteria (Fig. B.1(a)) after black and white (B&W) conversion and electrode dilatation (Fig. B.1(c)), compensating the blur effect on IDE edges. Using the mask, the electrode region was set to a zero value and the whole image (Fig. B.1(d)) was converted to B&W with an optimal threshold to distinguish bacteria (Fig. B.1(f)). Finally, the number of pixel clusters was automatically counted to estimate the total number of bacteria on the picture, and subsequently the bacterial density (in # per mm²). Two important remarks must be drawn:

- The bacteria density takes into account the mask area by removing it from the active surface when computing the ratio.
- When the mask is not dilated at the sensor edges (Fig. B.1(b)), the inaccuracy is very high because edges are wrongly numbered as bacteria (Fig. B.1(e)).

B.2 PIVlab for bacterial speed extraction

To extract the speed of attracted bacterial cells based on videos taken by the inverted microscope, the graphical user interface (GUI) open-source tool *PIVlab* was used in MATLAB [256]. Performing digital particle image velocimetry (DPIV), the speed extraction is based on the analysis of the cross correlation for a particle group in several successive images, giving the most probable displacement for the considered particles [256, 257].

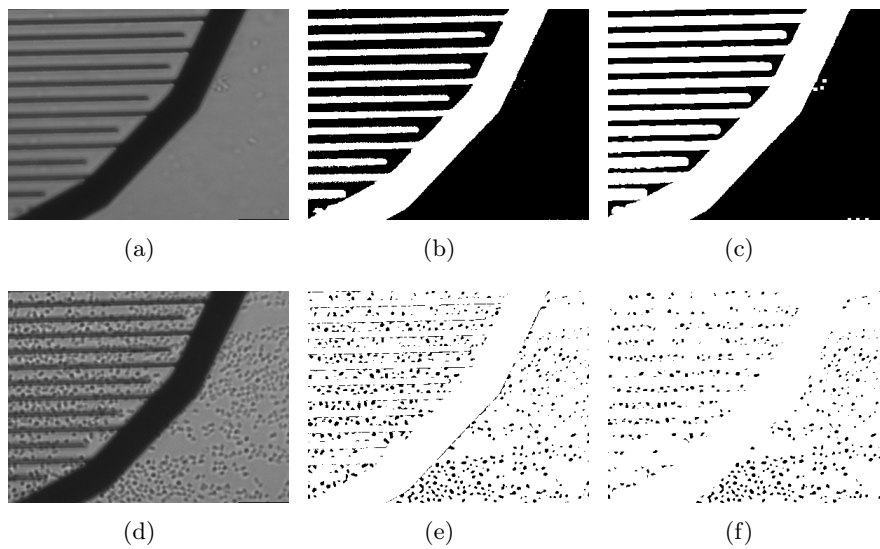


Figure B.1 – Results of the MATLAB algorithm on microphotographs of the sensor surface: (a) original image used for the mask, (b) obtained mask without dilatation and (c) obtained mask with dilatation, (d) original image with bacterial cells, (e) bacterial numbering without dilatation and (f) bacterial numbering with dilatation.

APPENDIX C

Mathematical developments

C.1 Analytical expression of the sensitivity to bacteria

We simplified the spherical bacterial cell and the semi-planar electrodes by the situation shown in Fig. C.1. The bacterial cell is modelled as a square with the same area as the spherical one: $d_{eq} = \frac{\sqrt{\pi}}{2} \cdot d_{bact}$. Two single electrodes are assumed and the capacitances are expressed in 2D.

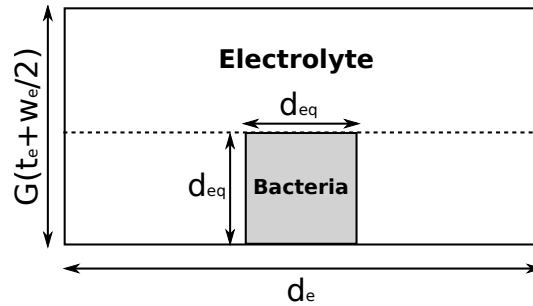


Figure C.1 – Schematic of the simplified geometry for bacterial sensitivity computation

For the bacterial impedance, we assume that the two capacitances of outer shells dominate, i.e. $C_{out} = \frac{\epsilon_{out}^* d_{eq}}{t_{out}^*}$. We thus have the following

expressions:

$$\begin{aligned}
C_{ins} &= \frac{\varepsilon_{ins}}{t_{ins}} \cdot \left(t_e + \frac{w_e}{2}\right) \\
&= \frac{\varepsilon_{sol}}{d_e} \cdot \left(t_e + \frac{w_e}{2}\right) \cdot \underbrace{\left(\frac{d_e}{t_{ins}} \cdot \frac{\varepsilon_{ins}}{\varepsilon_{sol}}\right)}_Q \\
C_{sol,0} &= \frac{\varepsilon_{sol}}{d_e} \cdot \left(t_e + \frac{w_e}{2}\right) \cdot G \\
C_{sol,1} &= C_{sol,up} + C_{sol,down} \\
&= \left(\varepsilon_{sol} \frac{G(t_e + w_e/2) - d_{eq}}{d_e}\right) + \left(\left(\frac{\varepsilon_{sol} d_{eq}}{d_e - d_{eq}}\right)^{-1} + \left(\frac{\varepsilon_{out}^* d_{eq}}{2t_{out}^*}\right)^{-1}\right)^{-1} \\
&= \left(\varepsilon_{sol} \frac{G(t_e + w_e/2) - d_{eq}}{d_e}\right) + \left(\frac{\varepsilon_{sol} \varepsilon_{out}^* d_{eq}}{(d_e - d_{eq}) \varepsilon_{out}^* + 2t_{out}^* \varepsilon_{sol}}\right) \\
&= \frac{\varepsilon_{sol} \left(t_e + \frac{w_e}{2}\right)}{d_e} \cdot \left[G + \frac{d_{eq}}{(t_e + w_e/2)} \left(\frac{1}{(1 - d_{eq}/d_e) + 2 \frac{t_{out}^*}{d_e} \frac{\varepsilon_{sol}}{\varepsilon_{out}^*}} - 1 \right) \right] \\
&= \frac{\varepsilon_{sol} \left(t_e + \frac{w_e}{2}\right)}{d_e} \cdot \left[G + \frac{d_{eq}}{(t_e + w_e/2)} \left(\frac{1 - 2 \cdot \frac{t_{out}^*}{d_e} \cdot \frac{\varepsilon_{sol}}{\varepsilon_{out}^*} \cdot \frac{d_e}{d_{eq}}}{\frac{d_e}{d_{eq}} - 1 + 2 \cdot \frac{t_{out}^*}{d_e} \cdot \frac{\varepsilon_{sol}}{\varepsilon_{out}^*} \cdot \frac{d_e}{d_{eq}}} \right) \right] \\
&= \frac{\varepsilon_{sol} \left(t_e + \frac{w_e}{2}\right)}{d_e} \cdot \underbrace{\left[G + \frac{d_{eq}}{(t_e + w_e/2)} \left(\frac{1 - 2T}{\frac{d_e}{d_{eq}} - 1 + 2T} \right) \right]}_P
\end{aligned}$$

with $T = \frac{t_{out}^*}{d_e} \cdot \frac{\varepsilon_{sol}}{\varepsilon_{out}^*} \cdot \frac{d_e}{d_{eq}}$ and $C_{sol,0}$ and $C_{sol,1}$ are the system capacitances without and with bacterial cell, respectively. The following steps are required to obtain the maximal sensitivity:

$$\begin{aligned}
S_{max}^{2D} &\triangleq \frac{C_{sol,0}^{-1} - C_{sol,1}^{-1}}{2C_{ins}^{-1} + C_{sol,1}^{-1}} \\
&= \frac{G^{-1} - (G + P)^{-1}}{2Q^{-1} + (G + P)^{-1}} \\
&= \frac{P}{G} \cdot \frac{1}{1 + 2 \cdot \frac{G+P}{Q}}
\end{aligned}$$

In our case, we have $G \simeq 1.28$, $T = 0.06$, $P = 0.17$ and $Q = 15$. Therefore $S_{max} \simeq 11.4$ %.

C.2 Linear versus exponential sensitivity

Let A_{in} be a quantity subject to variation and A_{out} its value through a transfer function, either linear $A_{out}^{lin} = KA_{in}$ or exponential $A_{out}^{exp} = K \exp(A_{in}/\alpha)$, with fixed-value constants K and α . For a change ΔA_{in} , the respective relative sensitivities in linear and exponential modes are respectively:

$$S_{r,lin} \triangleq \frac{1}{A_{out}^{lin}} \cdot \frac{\partial A_{out}^{lin}}{\partial A_{in}} = \frac{1}{A_{in}} \quad (\text{C.1})$$

$$S_{r,exp} \triangleq \frac{1}{A_{out}^{exp}} \cdot \frac{\partial A_{out}^{exp}}{\partial A_{in}} = \frac{1}{\alpha} \quad (\text{C.2})$$

Consequently, the following relationship is obtained: $S_{r,exp} = (\frac{A_{in}}{\alpha}) \cdot S_{r,lin}$. The exponential relative sensitivity $S_{r,exp}$ is then always larger than $S_{r,lin}$ if $A_{in} > \alpha$.

C.3 Analytical models of electrokinetic effects with passivated electrodes

In this section, electrokinetic effects for passivated electrodes are modelled. Compared to Section 3.3, the mathematical and physical development are fully described.

Generalities

To derive expression of electrokinetic effects for passivated electrodes, we use similar developments as those indicated in [83] and [206]. The situation is represented in Fig. C.2, where cylindrical coordinates are used. All parameters are defined in Table 3.2 and the friction factor is

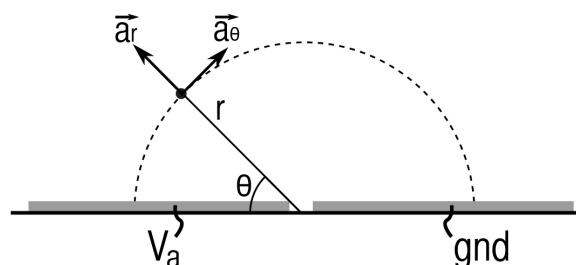


Figure C.2 – Schematic cross section of the electrodes and point of observation.

defined as $f_v = 6\pi\eta r_{bact}$. Some important expressions will be used in following developments:

- **Gradient:** $\vec{\nabla}a = \frac{\partial a}{\partial r} \cdot \vec{a}_r + \frac{1}{r} \cdot \frac{\partial a}{\partial \theta} \cdot \vec{a}_\theta + \frac{\partial a}{\partial z} \cdot \vec{a}_z$
- **RMS AC voltage:** $V_{a,RMS} \triangleq \sqrt{\langle V(t)^2 \rangle} = \frac{1}{\sqrt{2}} \cdot V_a$
- **RMS electric field:** $E_{sol,RMS} \triangleq \sqrt{\langle E_{sol}(t)^2 \rangle} = \frac{1}{\sqrt{2}} \cdot E_{sol}$

Expression of the electric field between passivated electrodes

Let \vec{E}_{ins} and \vec{E}_{sol} be the electric field contained in the insulating layers of thickness t_{ins} and in the electrolyte, respectively. The current conservation at the insulator-electrolyte interface gives the following relationship: $\varepsilon_{ins}\vec{E}_{ins} = (\varepsilon_{sol} + \frac{\sigma_{sol}}{j\omega})\vec{E}_{sol}$. The applied AC electric potential V_a is thus expressed as:

$$\begin{aligned} V_a &= - \int_0^{t_{ins}} E_{ins} dx - \int_{t_{ins}}^{\pi r + t_{ins}} E_{sol} dx - \int_{\pi r + t_{ins}}^{\pi r + 2t_{ins}} E_{ins} dx \\ &= 2t_{ins}E_{ins} + \pi r E_{sol} \\ &= \left[\frac{2t_{ins}}{\varepsilon_{ins}} \cdot \left(\varepsilon_{sol} + \frac{\sigma_{sol}}{j\omega} \right) + \pi r \right] \cdot E_{sol} \end{aligned}$$

The quantity πr is simply obtained by integrating the circular path from the left to the right electrode (θ goes from 0° to 180°). Consequently, the electric field \vec{E}_{sol} can be expressed as:

$$\vec{E}_{sol} = \frac{V_a}{\pi r} \cdot \underbrace{\left(\frac{1}{1 + 2 \cdot \left(\frac{\varepsilon_{sol}}{\varepsilon_{ins}} + \frac{\sigma_{sol}}{j\omega\varepsilon_{ins}} \right) \cdot \frac{t_{ins}}{\pi r}} \right)}_{H(\omega, r)} \cdot \vec{a}_\theta$$

It can be noticed that the electric field depends on the frequency when $t_{ins} \neq 0$, unlike gold electrodes ($t_{ins} = 0$) immersed in solution where the electric field $\vec{E}_{sol} = \frac{V_a}{\pi r} \cdot \vec{a}_\theta$ is constant [83, 206]. The modulus of $H(\omega, r)$ and \vec{E}_{sol} are equal to:

$$\begin{aligned} \|H(\omega, r)\|^2 &= \frac{1}{\left(1 + 2 \frac{\varepsilon_{sol} \cdot t_{ins}}{\varepsilon_{ins} \cdot \pi r}\right)^2 + \left(\frac{2\sigma_{sol} \cdot t_{ins}}{\omega\varepsilon_{ins} \cdot \pi r}\right)^2} \\ \|E_{sol}\|^2 &= \frac{V_a^2}{\pi^2} \cdot \frac{1}{\left(r + \frac{2\varepsilon_{sol} t_{ins}}{\varepsilon_{ins} \pi}\right)^2 + \left(\frac{2\sigma_{sol} t_{ins}}{\omega\varepsilon_{ins} \pi}\right)^2} \end{aligned}$$

Expression of the dielectrophoresis

The dielectrophoresis force can generally be expressed as [83, 206]:

$$F_{DEP}(t) = (\vec{m}(t) \cdot \vec{\nabla}) \vec{E}_{sol}(t)$$

The time-average dielectrophoresis force $\langle \vec{F}_{DEP} \rangle$ is thus equal to:

$$\begin{aligned} \langle \vec{F}_{DEP} \rangle &= \frac{1}{2} \cdot \mathbb{R}[(\vec{m}(\omega) \cdot \vec{\nabla}) \vec{E}_{sol}^*] \\ &= \frac{1}{2} \cdot \mathbb{R}[(4\pi\epsilon_{sol} \cdot r_{bact}^3 f_{CM}(\omega) \vec{E}_{sol} \cdot \vec{\nabla}) \vec{E}_{sol}(\omega)^*] \\ &= 2\pi\epsilon_{sol} r_{bact}^3 \cdot \mathbb{R} \left[f_{CM}(\omega) \frac{\vec{\nabla} \{ \vec{E}_{sol} \cdot \vec{E}_{sol}^* \}}{2} \right] \\ &= \pi\epsilon_{sol} r_{bact}^3 \cdot \mathbb{R} \left[f_{CM}(\omega) \vec{\nabla} |\vec{E}_{sol}|^2 \right] \end{aligned}$$

where r_{bact} is the bacterial radius and $f_{CM}(\omega)$ the Clausius-Mossoti factor. As $|\vec{E}_{sol}|^2$ is always a real number (even if \vec{E}_{sol} is complex), we get:

$$\begin{aligned} \langle \vec{F}_{DEP} \rangle &= \pi\epsilon_{sol} r_{bact}^3 \cdot \mathbb{R}\{f_{CM}(\omega)\} \cdot \vec{\nabla} |\vec{E}_{sol}|^2 \\ &= \pi\epsilon_{sol} r_{bact}^3 \cdot \mathbb{R}\{f_{CM}(\omega)\} \cdot \frac{\partial |\vec{E}_{sol}|^2}{\partial r} \cdot \vec{a}_r \\ &= -\frac{2r_{bact}^3 V_a^2 \epsilon_{sol}}{\pi} \cdot \mathbb{R}\{f_{CM}(\omega)\} \cdot \left(\frac{r + 2\frac{\epsilon_{sol} t_{ins}}{\epsilon_{ins} \pi}}{r^4} \right) \cdot \|H(\omega, r)\|^4 \cdot \vec{a}_r \end{aligned}$$

The resulting speed is computed as follows:

$$\begin{aligned} \langle \vec{v}_{DEP} \rangle &= \frac{\langle \vec{F}_{DEP} \rangle}{f_v} \\ &= -\frac{r_{bact}^2 V_a^2 \epsilon_{sol}}{3\pi^2 \eta} \cdot \mathbb{R}\{f_{CM}(\omega)\} \cdot \left(\frac{r + 2\frac{\epsilon_{sol} t_{ins}}{\epsilon_{ins} \pi}}{r^4} \right) \cdot \|H(\omega, r)\|^4 \cdot \vec{a}_r \\ &= -\frac{r_{bact}^2 V_a^2 \epsilon_{sol} \cdot \mathbb{R}\{f_{CM}(\omega)\} \cdot \left(r + 2\frac{\epsilon_{sol} t_{ins}}{\epsilon_{ins} \pi} \right)}{3\pi^2 \eta \cdot \left[\left(r + 2\frac{\epsilon_{sol} t_{ins}}{\epsilon_{ins} \pi} \right)^2 + \left(\frac{2\sigma_{sol} t_{ins}}{\omega \epsilon_{ins} \pi} \right)^2 \right]^2} \cdot \vec{a}_r \\ &= -\frac{r_{bact}^2 V_a^2 \epsilon_{sol} \cdot \mathbb{R}\{f_{CM}(\omega)\}}{3\pi^2 \eta \cdot \left(r + 2\frac{\epsilon_{sol} t_{ins}}{\epsilon_{ins} \pi} \right)^3 \left[1 + \left(\frac{2\sigma_{sol} t_{ins}}{\omega \left(r \epsilon_{ins} \pi + 2\epsilon_{sol} t_{ins} \right)} \right)^2 \right]^2} \cdot \vec{a}_r \end{aligned}$$

As $\mathbb{R}\{f_{CM}(\omega)\}$ is positive, the speed is directed towards the sensor centre and positive dielectrophoresis then occurs.

Expression of the AC-electroosmosis

Based on Fig. C.3 and the expression of the series capacitance $C_s = [C_{ins}^{-1} + C_{DL}^{-1}]^{-1}$, the voltage drop across one double layer is:

$$\begin{aligned}
 \Delta\phi_{DL} &= \frac{\Delta\phi_{DL}^*}{2} \\
 &= \frac{1}{2} \cdot \frac{I_{tot}}{j\omega C_{DL}/2} \\
 &= \frac{1}{2} \cdot \frac{\left[(G_{sol} + j\omega C_{sol})^{-1} + (j\omega C_s/2)^{-1} \right]^{-1}}{j\omega C_{DL}/2} \cdot V_a \\
 &= \frac{1}{2} \cdot \frac{1}{C_{DL}/C_s} \cdot \frac{V_a}{1 + \frac{j\omega C_s/2}{G_{sol} + j\omega C_{sol}}} \\
 &= \frac{1}{2} \cdot \frac{1}{C_{DL}/C_s} \cdot \frac{V_a}{1 + \frac{j\omega C_s/2 \cdot (G_{sol} - j\omega C_{sol})}{G_{sol}^2 + \omega^2 C_{sol}^2}} \\
 &= \frac{1}{2} \cdot \frac{1}{C_{DL}/C_s} \cdot \frac{V_a}{(1 + \omega^2 \tau_1 \tau_2) + j\omega \tau_1}
 \end{aligned}$$

with $\tau_1 \triangleq \frac{G_{sol} C_s/2}{G_{sol}^2 + \omega^2 C_{sol}^2} = \frac{\pi r \cdot \sigma_{sol} C_s/2}{\sigma_{sol}^2 + \omega^2 \varepsilon_{sol}^2}$ and $\tau_2 \triangleq \frac{C_{sol}}{G_{sol}} = \frac{\varepsilon_{sol}}{\sigma_{sol}}$, since $C_{DL} = \frac{\varepsilon_{sol}}{\lambda_D}$, $C_{ins} = \frac{\varepsilon_{ins}}{t_{ins}}$, $C_{sol} = \frac{\varepsilon_{sol}}{\pi r}$, $G_{sol} = \frac{\sigma_{sol}}{\pi r}$, $C_s = \frac{\varepsilon_{sol} \varepsilon_{ins}}{t_{ins} \varepsilon_{sol} + \lambda_D t_{ins}}$. Thus,

$$|\Delta\phi_{DL}|^2 = \frac{1}{4(C_{DL}/C_s)^2} \cdot \frac{V_a^2}{\omega^2 \tau_1^2 + (1 + \omega^2 \tau_1 \tau_2)^2}$$

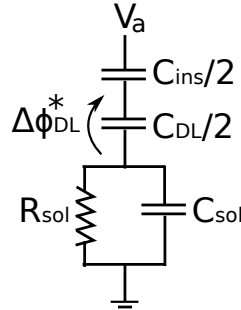


Figure C.3 – Schematic view of the situation.

Therefore:

$$\begin{aligned} \frac{\partial |\Delta\phi_{DL}|^2}{\partial r} &= \frac{\partial |\Delta\phi_{DL}|^2}{\partial \tau_1} \cdot \frac{\partial \tau_1}{\partial r} \\ &= -\frac{V_a^2 \omega^2}{2(C_{DL}/C_s)^2 r} \cdot \frac{(\tau_1 + \tau_2)\tau_1 + \omega^2 \tau_1^2 \tau_2^2}{(\omega^2 \tau_1^2 + (1 + \omega^2 \tau_1 \tau_2))^2} \end{aligned}$$

Finally, the slip velocity inside the electrical double layer is approximated by [206]:

$$\begin{aligned} \vec{v}_{slip} &\triangleq \frac{\varepsilon_{sol}}{2\eta} \cdot \Lambda \cdot \Re\{\Delta\phi_{DL} \cdot \vec{E}_t^*\} \\ &= -\frac{\varepsilon_{sol}}{2\eta} \cdot \Lambda \cdot \Re\left\{\Delta\phi_{DL} \cdot \frac{\partial \Delta\phi_{DL}^*}{\partial r}\right\} \cdot \vec{a}_r \end{aligned}$$

Because $c \cdot \partial c^*/\partial r = c^* \cdot \partial c/\partial r = 0.5 \cdot \partial(c \cdot c^*)/\partial r = 0.5 \cdot \partial|c|^2/\partial r$ for all complex c , the following formula is finally obtained:

$$\begin{aligned} \vec{v}_{slip} &= -\frac{\varepsilon_{sol}}{4\eta} \cdot \Lambda \cdot \Re\left\{\frac{\partial |\Delta\phi_{DL}|^2}{\partial r}\right\} \cdot \vec{a}_r \\ &= -\frac{\varepsilon_{sol}}{4\eta} \cdot \Lambda \cdot \frac{\partial |\Delta\phi_{DL}|^2}{\partial r} \cdot \vec{a}_r \\ &= \frac{V_a^2 \omega^2 \varepsilon_{sol} \Lambda}{8\eta (C_{DL}/C_s)^2 r} \cdot \frac{(\tau_1 + \tau_2)\tau_1 + \omega^2 \tau_1^2 \tau_2^2}{(\omega^2 \tau_1^2 + (1 + \omega^2 \tau_1 \tau_2))^2} \cdot \vec{a}_r \end{aligned}$$

It is important to remember that \vec{v}_{slip} is only a slip velocity which exists only at the electrode surface, so that \vec{a}_r is parallel to \vec{a}_x .

Expression of the electrothermal flow

To estimate the electrothermal flow, it is required to evaluate the increase of the local temperature induced by the electric field \vec{E}_{sol} . The Poisson equation gives: $-\sigma_{sol} E_{sol}(t)^2 = -k \vec{\nabla}^2 T(t)$. Since $E_{sol}(t) = E_{sol} \cdot \cos(\omega t)$, we have: $E_{sol}(t)^2 = \frac{E_{sol}^2}{2} \cdot (1 + \cos(2\omega t)) = E_{sol,RMS}^2 \cdot (1 + \cos(2\omega t))$. The following relationship is obtained by neglecting AC terms:

$$\begin{aligned} -\sigma_{sol} E_{sol,RMS}^2 &= k \vec{\nabla}^2 T \\ &= \frac{k}{r} \frac{\partial}{\partial r} \left(r \frac{\partial T}{\partial r} \right) + \frac{k}{r^2} \frac{\partial^2 T}{\partial \theta^2} \end{aligned}$$

with $E_{sol,RMS} = \frac{V_{a,RMS}}{\pi r} \cdot H(\omega, r)$. A particular solution $T(r, \theta)$ to this equation was not found, mainly because of the dependence of $H(\omega, r)$ with r . By assuming $H(\omega, r) = H(\omega)$, it is possible to find a particular solution: $T(\theta) = -\frac{\sigma_{sol}}{k} \cdot \frac{V_{a,RMS}^2 \cdot H(\omega)^2}{2\pi} (\frac{\theta^2}{\pi} - \theta)$. The correctness of the approximation $H(\omega, r) = H(\omega)$ was numerically verified between $f = 1$ kHz and 1 GHz at $\sigma_{sol} = 1$ mS/m and 10 mS/m. However, it does not hold anymore for $f < 10$ kHz at $\sigma_{sol} = 0.1$ S/m and for $f < 100$ kHz at $\sigma_{sol} = 1$ S/m since $\frac{k}{r} \frac{\partial}{\partial r} (r \frac{\partial T}{\partial r}) \gg \frac{k}{r^2} \frac{\partial^2 T}{\partial \theta^2}$. No conclusion can thus be drawn in these two cases.

With this assumption, $\vec{\nabla} T = \frac{1}{r} \cdot \frac{\partial T(\theta)}{\partial \theta} \vec{a}_\theta = -\frac{\sigma_{sol}}{kr} \cdot \frac{V_{a,RMS}^2 \cdot H(\omega, r)^2}{2\pi} (\frac{2\theta}{\pi} - 1) \cdot \vec{a}_\theta$. Starting from Coulomb equation like in [83], the force exerted on the fluid can be expressed as:

$$\begin{aligned}
\langle \vec{f}_E \rangle &= \frac{1}{2} \Re \left\{ \left[\left(\frac{\sigma_{sol} \vec{\nabla} \varepsilon_{sol} - \varepsilon_{sol} \vec{\nabla} \sigma_{sol}}{\sigma_{sol} + j\omega \varepsilon_{sol}} \right) \vec{E}_0 \right] \vec{E}_0^* \right\} - \frac{1}{4} \vec{E}_0 \cdot \vec{E}_0^* \vec{\nabla} \varepsilon_{sol} \\
&= \left[\frac{1}{2} \frac{\sigma_{sol} \cdot (\sigma_{sol} \vec{\nabla} \varepsilon_{sol} - \varepsilon_{sol} \vec{\nabla} \sigma_{sol})}{\sigma_{sol}^2 + \omega^2 \varepsilon_{sol}^2} - \frac{1}{4} \vec{\nabla} \varepsilon_{sol} \right] \cdot E_0^2 \\
&= \frac{1}{2} \left[\left(\frac{\frac{1}{\varepsilon_{sol}} \vec{\nabla} \varepsilon_{sol} - \frac{1}{\sigma_{sol}} \vec{\nabla} \sigma_{sol}}{1 + (\omega \varepsilon_{sol} / \sigma_{sol})^2} - \frac{1}{2\varepsilon_{sol}} \vec{\nabla} \varepsilon_{sol} \right) \cdot \varepsilon_{sol} E_0^2 \right] \\
&= - \underbrace{\left[\frac{\frac{T}{\sigma_{sol}} \frac{\partial \sigma_{sol}}{\partial T} - \frac{T}{\varepsilon_{sol}} \frac{\partial \varepsilon_{sol}}{\partial T}}{1 + (\omega \varepsilon_{sol} / \sigma_{sol})^2} + \frac{T}{2\varepsilon_{sol}} \frac{\partial \varepsilon_{sol}}{\partial T} \right]}_{M(\omega, T)} \cdot \frac{\varepsilon_{sol} E_{RMS}^2}{T} \cdot \vec{\nabla} T \\
&= -M(\omega, T) \cdot \frac{\varepsilon_{sol} \sigma_{sol} V_{a,RMS}^4 H(\omega, r)^4}{2k\pi^3 r^3 T} \cdot \left(1 - \frac{2\theta}{\pi} \right) \cdot \vec{a}_\theta \\
&= -M(\omega, T) \cdot \frac{\varepsilon_{sol} \sigma_{sol} V_a^4 H(\omega, r)^4}{8k\pi^3 r^3 T} \cdot \left(1 - \frac{2\theta}{\pi} \right) \cdot \vec{a}_\theta
\end{aligned}$$

To compute the fluid speed, we use the Stokes equation $\vec{v}_E \approx 0.13 \cdot \langle \vec{F}_E \rangle r^2 / \eta$, as Eq. 32 in [83]:

$$\begin{aligned}
\vec{v}_E(\theta) &= -0.13 \cdot M(\omega, T) \cdot \frac{\varepsilon_{sol} \sigma_{sol} V_a^4 H(\omega)^4}{8k\pi^3 r \eta T} \cdot \left(1 - \frac{2\theta}{\pi} \right) \cdot \vec{a}_\theta \\
&\approx -5 \cdot 10^{-4} \cdot M(\omega, T) \cdot \frac{\varepsilon_{sol} \sigma_{sol} V_a^4 H(\omega)^4}{k\eta r T} \cdot \left(1 - \frac{2\theta}{\pi} \right) \cdot \vec{a}_\theta
\end{aligned}$$

APPENDIX D

Supplementary results

D.1 2D-to-3D sensitivity conversion

This section investigates the difference of sensitivity to bacteria between 2D and 3D numerical simulations. Physics is described by the Maxwell equations in the whole system, thus neglecting the ion transport equations provided in Section 2.4. The 2D and 3D geometries are identical, except that the bacterial cell is spherical in 3D (while virtually cylindrical in 2D) and that the electrode length is set to $10\ \mu\text{m}$ in 3D (Fig. D.1(b)). To enable a visual comparison between 2D and 3D sensitivity, the 2D sensitivity is multiplied by the factor $K = S_{max}^{3D}/S_{max}^{2D}$.

The two curves of the sensitivity versus the frequency are similar in amplitudes, but present slight differences in the transitions around 100 kHz and 100 MHz, which reduces the frequency range in 3D where the sensitivity is the highest (Fig. D.1(a)). On the other hand, the bump around 10 kHz due to C_{pl} is strongly attenuated in 3D because of the slight differences of the cutoff frequencies.

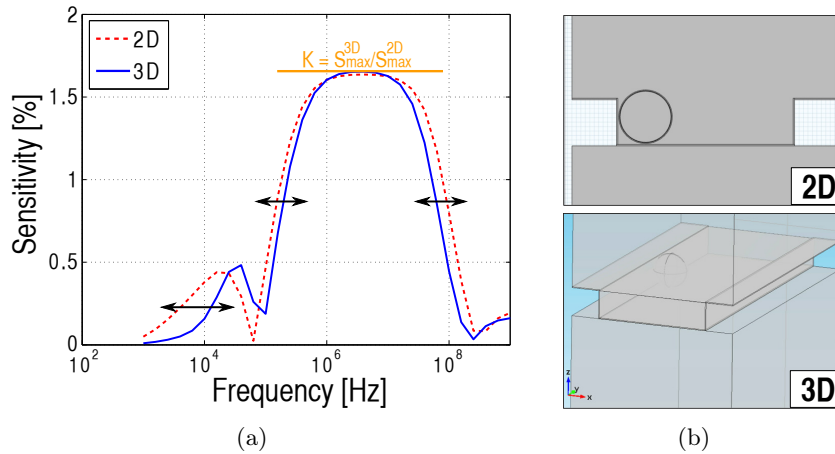


Figure D.1 – (a) Comparison between the 2D and 3D sensitivities versus the applied frequency. The 2D sensitivity is multiplied by the frequency-independent constant $K = S_{max}^{3D}/S_{max}^{2D} \simeq 0.1$. (b) Representation of the 2D and 3D geometries used for numerical simulations in Comsol Multiphysics.

D.2 Characterization of the permittivity of different solutions

To evaluate how frequency impacts the relative permittivity of different solutions, a dielectric probe (Agilent 85070E) was immersed in each solution and connected to a VNA (Agilent N5242A) that performs dielectric measurements. Several volume dilutions of glycerol in DI water were measured. For instance, 100 mL of Gly 25 % is a mixture between 25 mL of Gly 100 % and 75 mL of DI water.

The extraction of the relative permittivity between 20 MHz and 20 GHz is shown in Fig. D.2. It is clearly observable that DI water and Gly 25 % features a constant relative permittivity up to 1 GHz. However, the other solutions present a relative permittivity value that begins to change below 1 GHz. Dispersion of the permittivity occurs from ca. 4 GHz in DI water to 100 MHz in pure Glycerol.

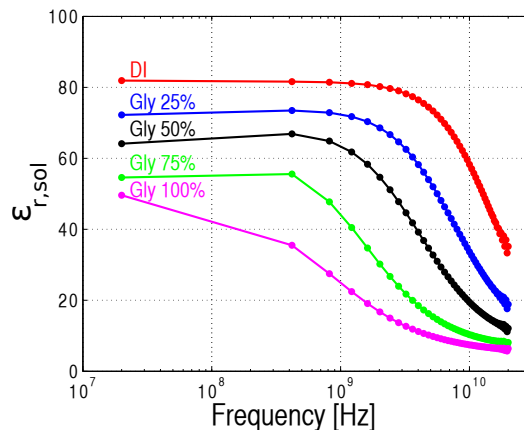


Figure D.2 – Experimental characterization of the relative permittivity of glycerol dilutions in DI water.

D.3 Performance comparison between reference and CFC IDEs

In this Section, the difference of performance between the IDEs of Chapter 2, called the *reference IDE*, and Chapter 4, called the *CFC IDE*, is explained with regards to their different design and conditioning properties (see Table D.1).

D.3. Performance comparison between reference and CFC IDEs

221

As shown in, it is required to duplicate the CFC IDE to compare devices with identical bacterial surface coverages. 2D numerical simulations show that the capacitive shift ΔC induced by one bacterial cell for the CFC IDE is 4.4 times larger than for the reference IDE. This confirms why experimentally, the capacitive shift is 490 aF for the CFC while it is only 80-100 aF for the reference IDE (see Table D.1). However, the nominal capacitance C_0 of the CFC is almost 10 times larger than for the reference IDE. Consequently, the 2D maximal sensitivity is only 7% for the CFC IDE, while it achieves 16% for the reference IDE, which makes a factor $S_{max,ref}^{2D}/S_{max,CFC}^{2D} \sim 2.3$ of difference. We find approximately the same factor by considering experimental sensitivities normalized to bacterial surface coverages, both mentioned in Table D.1: $\frac{S_{max,ref}/S_{b,ref}}{S_{max,CFC}/S_{b,CFC}} \approx 2.5$. The lower simulated sensitivity of the CFC IDE is thus experimentally balanced by a higher bacterial surface coverage. To understand the relationship between K factors, the previous equation $\frac{S_{max,CFC}^{2D}}{S_{max,ref}^{2D}} \simeq \frac{S_{max,CFC}/S_{b,CFC}}{S_{max,ref}/S_{b,ref}}$ results in:

$$S_{max,CFC} \simeq \underbrace{(K_0 S_{b,CFC})}_{2K_{CFC}} \cdot S_{max,CFC}^{2D} \quad (\text{D.1})$$

$$S_{max,ref} \simeq \underbrace{(K_0 S_{b,ref})}_{K_{ref}} \cdot S_{max,ref}^{2D} \quad (\text{D.2})$$

where a factor 2 must be considered for K_{CFC} since 2D sensitivity is divided by 2 by duplicating the simulated structure (see Fig. D.3). This leads to $K_{CFC}/K_{ref} = \frac{1}{2} \cdot S_{b,CFC}/S_{b,ref} \simeq 1.8$, which is almost verified since $K_{CFC} = 0.89$ and $K_{ref} = 0.58$.

Table D.1 – Comparison between the design, conditioning and experimental performance of IDEs from Chapters 2 and 4.

	Reference IDE (Chapter 2)	CFC IDE (Chapter 4)
w_e	2 μm	1.5 μm
d_e	4 μm	1.5 μm
t_e	1 μm	1.8 μm
t_{ins}	33 nm	25 nm
Electrolyte	PBS 1/1000	Pure PBS
Bacterial coverage S_b	$3.2 \cdot 10^4 \text{ \#/mm}^2$	$1.15 \cdot 10^5 \text{ \#/mm}^2$
Maximal sensitivity S_{max}	$\sim 9 \%$	12.7 %
Bacterial sensitivity	80-100 aF/bact.	490 aF/bact.
Factor K	0.58	0.89
Theoretical factor K^{th}	0.32	0.44

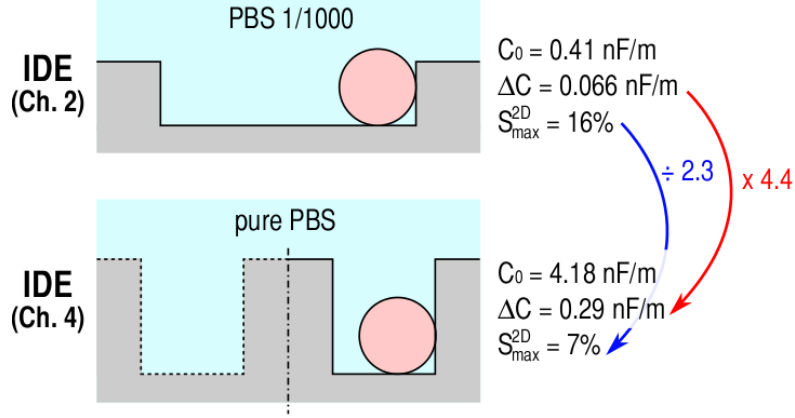


Figure D.3 – Schematic representation (at scale) of the IDEs from Chapter 2 and 4 with indicated nominal capacitance C_0 , capacitance shift ΔC and 2D maximal sensitivity S_{max}^{2D} for identical bacterial surface coverages, all obtained from 2D numerical simulations of Section 2.4.

The theoretical factor K^{th} is defined as the ratio of the measured bacterial surface coverage to the bacterial surface coverage in the 2D plane: $K^{th} \triangleq \frac{S_b}{1/[d_e \cdot (t_e + \frac{w_e}{2}) \cdot G]}$. As indicated in Table D.1, K^{th} is equal to 0.32 and 0.44 for the reference and CFC IDEs, respectively. Their ratio is $K_{CFC}^{th}/K_{ref}^{th} = 1.38$, which is close to the experimental ratio $K_{CFC}/K_{ref} = 1.53$. The smaller values of K_{CFC}^{th} and K_{ref}^{th} with regards to K_{CFC} and K_{ref} can be explained by the uncertainties on both the bacteria number and the bacterial dielectric properties.

D.4 CFC inverter sizing

The Figure D.4 shows how the (W/L) ratio of inverters increases the IDE frequency f_{IDE} . A transistor width $W_n = 5 \mu\text{m}$ ensures an oscillation frequency of ca. 300 MHz on the 200 μm -sided CFC. The figure also shows that the increase of parasitic capacitances with W_n can be neglected versus the sIDE capacitance.

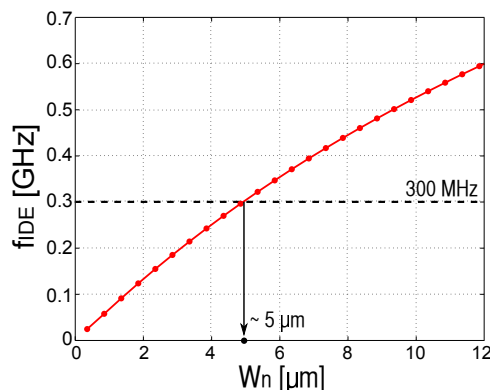


Figure D.4 – SPICE simulations of the frequency f_{IDE} versus the inverter NMOS width W_n for the 200 μm -sided CFC, as $L_n = L_p = 0.24 \mu\text{m}$ and $W_p = 2.5 \cdot W_n$.

D.5 Temperature impact on CFC

As the 200- μm CFC is activated, the temperature at the chip/liquid surface increases by 0.5°C and 1°C in air and PBS condition, respectively (Fig. D.5(a)). The difference comes from the difference of power (10 mW versus 29 mW) consumes by the CFC in air and PBS. During the ca. 10 min of incubation, a temperature slope can be noticed for the PBS, while inexistent in air. Indeed, as the drop progressively evaporates (see Fig. D.5(c)), the underlying aluminum tracks from the CMOS chip are more apparent and thus cause an incorrect temperature increase because of the higher aluminum reflectivity. Furthermore, the drop also heats quicker because of its smaller volume owing to evaporation.

Post-layout simulations on the 200- μm sided IDE demonstrate that f_{IDE} decreases from 293.1 MHz to 291.8 MHz as the temperature increases from 25°C to 28°C. Indeed, the propagation delays of inverters increase with the temperature since the electron mobility decreases so that the drain current as well.

The impact of temperature on the electrical conductivity σ_{sol} of PBS has also been characterized, by using a conductimeter indicating both σ_{sol} and the temperature (Fig. D.5(c)). It can be seen that σ_{sol} spans from 1.8 S/m to 1.66 S/m as the temperature goes from 10°C to 36°C. It corresponds to 0.1 % of variation per °C between 22°C and 36°C. The stagnation after 36°C is mostly due to the partial evaporation of the fluid, resulting in indirect σ_{sol} increase.

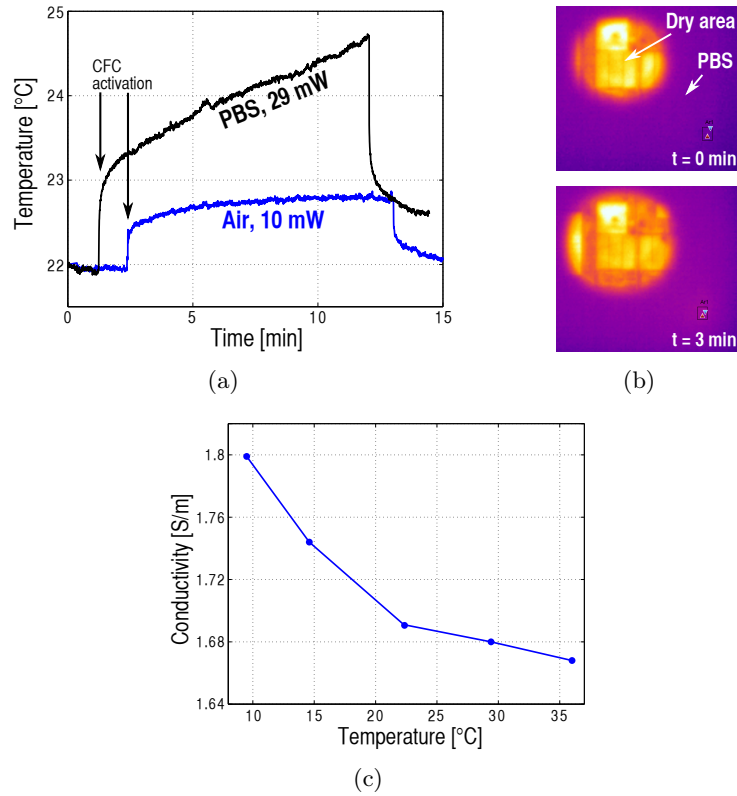


Figure D.5 – (a) Real-time increase of the temperature monitored at the chip/liquid surface by the infrared camera in PBS and air condition, (b) infrared image at two different sampling time in (a), and (c) conductivity of PBS versus the temperature as characterized by a conductimeter in stirred solution.

D.6 Characterization of the biosensor array

The biosensor array has been characterized more extensively to provide information on the following parameters:

- **The integration time** t_{int} is shown to strongly impact the output voltage V_{out} (Fig. D.6(a)). Furthermore, V_{out} is well proportional to t_{int} (Fig. D.6(b)), as expected since V_{pix} decreases linearly with time during the integration phase.
- **The electrical conductivity** σ_{sol} impacts the V_{out} versus V_{ref} curve by featuring a strong evolution from C_{sol} to C_{ins} , as PBS 1:100 is replaced by PBS 1:10. However, the electrical conductivity

does not strongly impact the curves in these two different regions.

- **The power consumption** P of the capacitive biosensor array at different frame rate is provided in Fig. D.6(d). It can be seen that the power P linearly depends on the frame rate FR , and that the energy efficiency is $E_{pix} \triangleq \frac{P}{FR \cdot N^2} \simeq 3 \text{ nJ}/(\text{frame.pixel})$, with N^2 the total number of pixels.
- **The experimental output noise** is compared to the SPICE simulation results in Fig. D.6(e). These curves demonstrate that the maximal noise is approximately three times larger in measurements compared to simulations, mainly because of the additional uncorrelated noise sources introduced by off-chip ADCs. Its suppression or mitigation can be obtained by reducing the reference voltage V_{ref} to lower values. It is also possible to use on-chip low-noise ADC instead of off-chip ADCs.

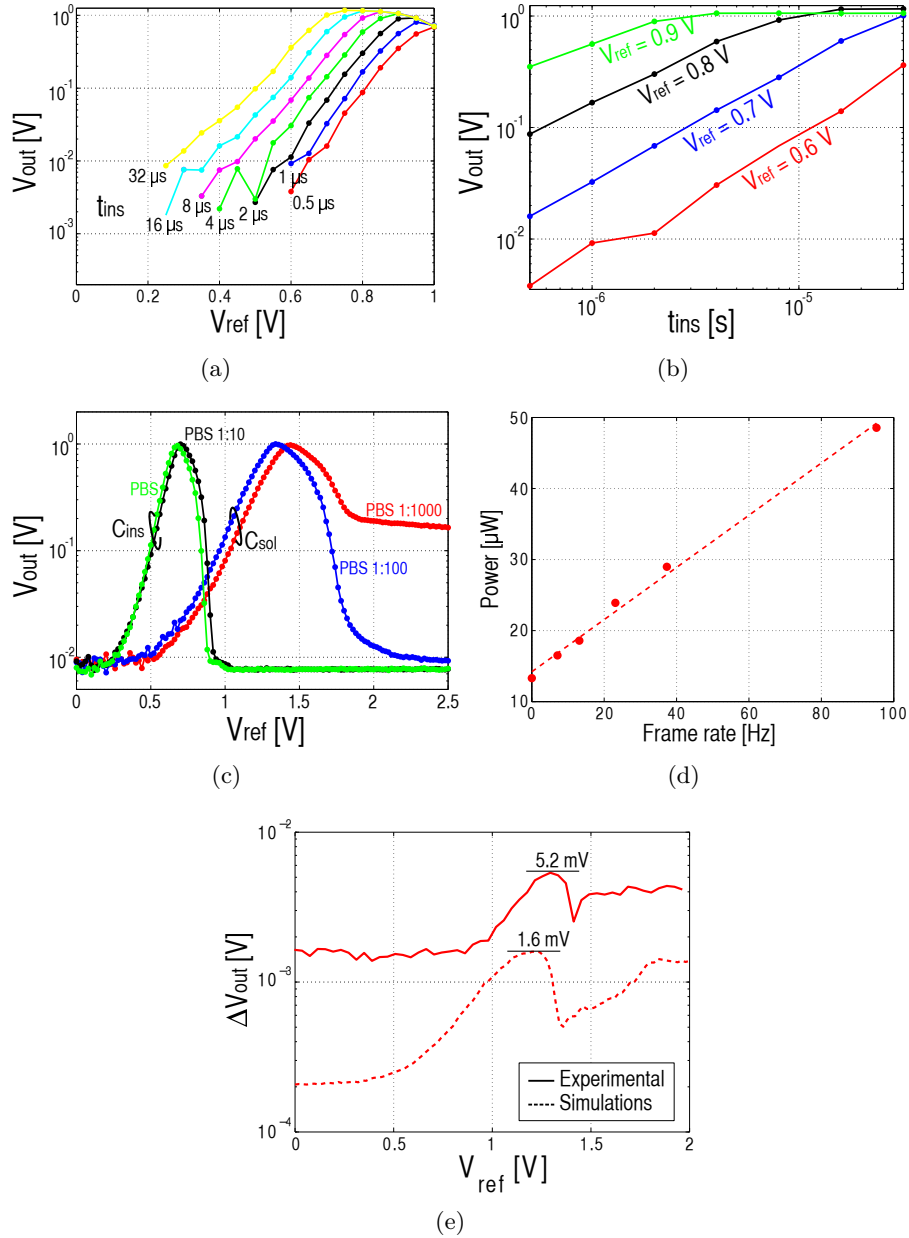


Figure D.6 – Additional experimental characterization of the capacitive biosensor array: (a) (b) impact of the integration time t_{int} and the reference voltage V_{ref} for the test pixel featuring a MIM capacitance of 65 fF, (c) dependence of the V_{out} versus V_{ref} characteristics with σ_{sol} , (d) power versus the frame rate and (e) comparison between measurements and SPICE simulations of the output noise.